Laser cooling of YbF molecules

for an improved measurement of the electron electric dipole moment

James Robert Almond

A thesis submitted for the degree of Doctor of Philosophy

Department of Physics
Imperial College London

April 2017

Abstract

Cold molecules are attractive for a wide range of scientific applications, including quantum computation, the study of chemical reactions, and tests of fundamental physics. Laser cooling has proved to be an invaluable technique in the cooling of atoms. This technique was once thought to be infeasible for molecules, because it is difficult to find a closed cycling transition due to their vibrational structure. Recently, laser cooling of several diatomic species has been demonstrated. These molecules possess electronic transitions with highly diagonal Franck-Condon matrices, which make it possible to drive a quasi-closed cycling transition.

Ytterbium fluoride (YbF) molecules are amenable to laser cooling and are especially interesting because they are used to measure the electron's electric dipole moment (eEDM). Measurements of the eEDM test the prediction of theories that extend the Standard Model of particle physics. The sensitivity of an eEDM experiment could be greatly increased by using ultracold molecules produced by direct laser cooling.

This thesis presents work done towards producing a laser-cooled beam of YbF for an eEDM experiment. This work includes the construction of the cooling experiment, a novel method for efficiently combining laser beams of very similar frequencies, results of spectroscopic measurements to find the required transitions for laser cooling, the results of initial optical cycling experiments, and the first laser cooling results of YbF.

Using a one-dimensional optical molasses, a beam of molecules is Doppler cooled in one transverse direction to a temperature of approximately 70 mK. Preliminary evidence of cooling to lower temperatures through a Sisyphus mechanism is also presented. Finally, paths towards improving the laser cooling are suggested. The work opens the door to improved measurements of the eEDM using ultracold YbF molecules.

Declaration

I declare that this thesis is my own work. Where I have used the work of others, the sources are appropriately acknowledged and referenced.

Acknowledgements

During the work described in this thesis, I have been fortunate to work with a terrific bunch of people whom I would like to thank. For the majority of the experiments discussed here, I have worked with Jongseok, who has been a brilliant colleague and teacher, and has become a good friend. I have also enjoyed and benefited from working closely with t'other James, Noah, and recently, μMike, who is doing an excellent job moving forward with the experiment.

To my supervisors Mike and Ed, thank you for your expert guidance, and your oversight of the experiment. I would additionally like to thank Mike, for providing very helpful and detailed comments on the draft of this thesis. Thank you Ben for your considered suggestions, help with all things technical, and uplifting remarks. You have helped to make the CCM a fun place to work.

To the other members of the group, I have enjoyed working alongside all of you, and have especially appreciated the lunchtime conversation. Particularly, I would like to thank; Jack, for valuable discussions, Izzie, for thesis writing motivation, Pete, for help in the lab, and Anne, for help on a spectroscopy experiment. Thank you Jon, Steve, Gio and Val for the wonderful equipment you have built, and thank you Sanja for your support, hard work, and outstanding parties.

Finally, I would like to thank my family and friends for their interest (or perhaps, well concealed boredom) when discussing my research. To Samantha, thank you for your constant encouragement and patience over the last few fantastic years, and especially for putting up with me whilst I have been writing this thesis. To my mum and dad, thank you for the innumerable things you have done for me, and for inspiring my interest in science. To you, I dedicate this thesis.

"You never hear about the dolphins that drag people out to sea."

— B. Sauer *on survival bias*
one lunchtime, 2016

Contents

Chapter 1

Introduction

This thesis discusses an experiment to laser cool a beam of ytterbium fluoride (YbF) molecules in one transverse dimension. In future, a transverse cooled beam of YbF molecules can be used in an experiment to make an improved measurement of the permanent electric dipole moment of the electron (eEDM).

In this chapter, laser cooling and the motivation for measuring the eEDM is discussed, as is the way in which transverse laser cooling can be used to improve an eEDM measurement. Chapter 2 explains how laser cooling may be applied to the YbF molecule, and makes some predictions about the scattering rates in the multi-level cycling transitions used for laser cooling. Chapter 3 describes the molecular source which is used for the majority of experiments in this thesis. Chapter 4 describes the laser systems that are used, and also presents the results of an experiment to efficiently combine laser beams using a novel method. Chapter 5 presents the results of spectroscopy experiments which have enabled us to locate the transitions we require for laser cooling. It also presents the result of the optical cycling experiments which were stepping stones towards laser cooling. Chapter 6 presents and discusses our laser cooling results. Chapter 7 discusses improvements that will be made to this experiment, and its future direction.

1.1 Laser cooling atoms

Laser cooling molecules is very similar to laser cooling atoms, except with molecules there are usually more lasers and transitions involved. It is therefore appropriate to start off by reviewing atomic laser cooling, before discussing the extension of this technique to molecules.

1.1.1 The principle of laser cooling

Radiation pressure

Photons carry momentum $\boldsymbol{p} = \hbar\boldsymbol{k}$, where $|\boldsymbol{k}| = k = \frac{2\pi}{\lambda}$, and λ is the wavelength of light. When a photon is absorbed or emitted by an atom, the momentum of the atom is changed by $\pm\hbar\boldsymbol{k}$. An atom may absorb a photon emitted by a laser, and receive a momentum kick $\hbar\boldsymbol{k}$. The atom will later emit a photon via stimulated or spontaneous emission. For stimulated emission, the emitted photon's momentum is $\hbar\boldsymbol{k}$, and the recoil momentum of the atom is $-\hbar\boldsymbol{k}$, so no net transfer of momentum to the atom. If the emission is spontaneous, then the direction of the emitted photon is random. Over many absorption and spontaneous emission cycles, the average momentum transfer through spontaneous emission tends to zero, whereas the momentum kicks from absorption are cumulative. The atom is therefore accelerated by the laser beam. This force is the product of the rate at which the atom undergoes spontaneous emission (the scattering rate) R_γ, and the momentum change per scattered photon, $\hbar k$,

$$F = \hbar k R_\gamma. \tag{1.1}$$

For a two-level atom, the interaction between the atom and laser electric field may be treated semiclassically to determine the steady state population of the excited state. The scattering rate is then the product of the excited state population and the decay rate,

$$R_\gamma = \frac{\Gamma}{2}\frac{I/I_{\text{sat}}}{1 + I/I_{\text{sat}} + 4(\delta/\Gamma)^2}, \tag{1.2}$$

where Γ is the spontaneous emission rate of the excited state, δ is the laser detuning from the atomic resonance, I is the laser intensity, and the saturation intensity is $I_{\text{sat}} \equiv \frac{\pi hc\Gamma}{3\lambda^3}$. Here, the ratio $I/I_{\text{sat}} = 2(\Omega/\Gamma)^2$, where Ω is the Rabi frequency.

The first experimental observation of this force on free atoms was made in 1933 by Frisch, who demonstrated that a beam of sodium atoms could be deflected by the resonant light from a sodium vapour lamp [1].[1]

Laser cooling

In 1970 Ashkin suggested that the scattering force could be used to slow down and trap atoms [5], and in 1975 Hänsch and Schawlow pointed out that it could also be used to cool them. This can be done as follows. A cloud of atoms moves towards a laser source,

[1] Although the first experimental measurement of the radiation pressure force was made in around 1900 by Lebedev [2], followed shortly afterwards by an improved measurement by Nichols and Hull [3]. They measured the force exerted by light reflected from a mirror using a kind of torsion balance, and the result obtained was in close agreement with the theoretical prediction of Maxwell [4].

which is red detuned with respect to the mean Doppler shifted resonance frequency of the atoms. The cloud is slowed by radiation pressure. Additionally, the distribution of forward speeds of the atoms is narrowed, because the Doppler shift brings the light closer to resonance for atoms travelling at higher speeds, and so the slowing force is larger for faster atoms. This compression of the velocity distribution is called 'Doppler cooling' and the effect can be considered as a reduction of the translational temperature of the beam in one direction.[2]

Doppler cooling was demonstrated in 1981 by Andreev *et al* [6]. In this experiment, sodium atoms in a thermal beam were slowed and cooled to 1.5 K by laser light propagating in the opposite direction to their motion. The slowest velocity attainable by these methods was limited, because, as the atoms are slowed, the Doppler shift no longer brings the light close to resonance. This problem could be solved by either ramping the laser frequency to keep up with the decelerating of the atoms, or applying a spatially varying magnetic field which changes the resonant frequency of the atoms via the Zeeman interaction such that the atoms remain on resonance as they are slowed (Zeeman slowing). Zeeman slowing was first demonstrated by Phillips and Metcalf in 1982, where a sodium beam was decelerated to 40 % of its initial velocity.

The development of these techniques enabled atoms to be slowed to rest. It then became desirable to confine the slowed atomic cloud, and cool it in the other spatial dimensions to reveal the new phenomena that were expected to occur in clouds of bosons and fermions at high phase space density. This 3D cooling can be done by applying the frictional scattering force in all three dimensions by using additional laser beams, in an arrangement called an 'optical molasses'.

1.1.2 Optical molasses

Here we will consider the optical molasses force in one dimension. If an atom is illuminated by two (low-intensity) laser beams which counterpropagate, and have the same frequency, intensity, and polarisation, the net force is approximately the sum of the force from each beam in isolation. The force exerted by each beam is

$$F_{\pm} = \pm \hbar k \frac{\Gamma}{2} \frac{s_0}{1 + s_0 + 4(\delta \mp vk)^2/\Gamma^2}, \tag{1.3}$$

where v is the velocity of the atom in the propagation axis of the lasers, and the saturation parameter is defined as $s_0 \equiv I/I_{\mathrm{sat}}$. The total force, $F_{\mathrm{M}} = F_+ + F_-$, and the forces exerted by each beam $F_{\pm}$ are plotted in Fig. 1.1 for red detuning. For small v, this force can be written as $F_{\mathrm{M}} \simeq -\beta v$, where β is found from the Taylor expansion of F_{M} about $v = 0$,

[2] Although the temperature of the beam does not conform to the strict definition in thermodynamics, where temperature is only defined for a closed system in thermal equilibrium with its surroundings.

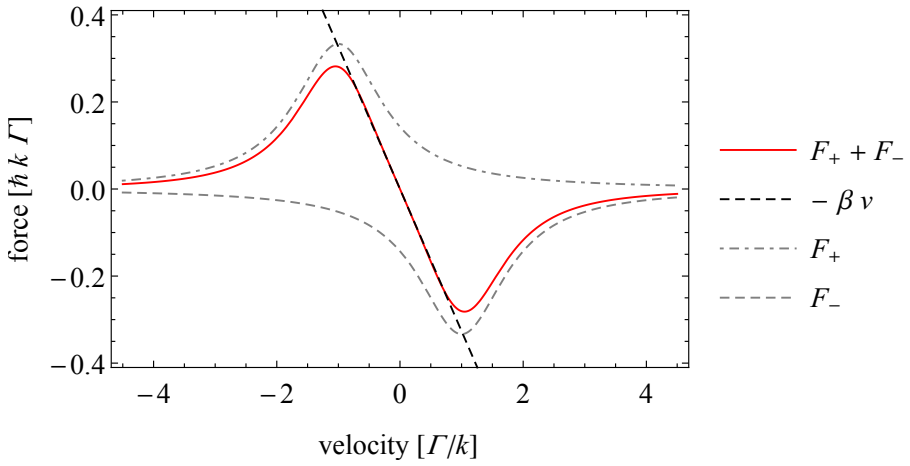

Figure 1.1: The velocity dependent damping force for a 1D optical molasses, plotted for $s_0 = 2$ and $\delta = -\Gamma$. Reproduced from [7].

neglecting terms of order v^3 and higher,

$$\beta = \frac{8\hbar k^2 \delta s_0}{\Gamma(1 + s_0 + 4(\delta/\Gamma)^2)^2}. \tag{1.4}$$

For red detuning β is positive, and the force viscously damps motion in the laser propagation axis. For blue detuning, β is negative, and the velocity distribution is expanded by the force.

A three dimensional optical molasses was first demonstrated by Chu *et al.* in 1985 [8]. In this experiment sodium atoms in a thermal beam were decelerated by using a chirped laser. They were confined and cooled in an optical molasses to $\sim 240\,\mu\text{K}$. This is close to the predicted minimum temperature that was expected to be obtainable via Doppler cooling [9], called the 'Doppler temperature'.

With the correct choice of laser polarisations, and the addition of a spatially inhomogeneous magnetic field the optical molasses can become a magneto-optical trap for atoms which have angular momentum in their excited state. Here, in addition to the friction force, there is a position dependent trapping force, preventing atoms from diffusing out of the optical molasses. In this arrangement, the magnetic field Zeeman shifts transitions driven by laser beams exerting a restoring radiation pressure closer to resonance, and Zeeman shifts those driven by anti-restoring beams away from resonance. This technique was first demonstrated by Raab *et al.* in 1987 [10].

The Doppler temperature

From the above equations for F_{M} for an optical molasses, it would appear that a cloud of atoms could be continuously cooled towards zero velocity and therefore zero temperature, however this cannot be the case. The force which cools the atoms is delivered in discrete,

randomly directed momentum kicks, with each kick delivering an energy of $E_\mathrm{R} = \frac{\hbar^2 k^2}{2m}$, and therefore the velocity distribution cannot be made narrower than that corresponding to particles having this average energy. The lowest obtainable temperature must therefore be greater than

$$T_\mathrm{R} = \frac{\hbar^2 k^2}{2k_\mathrm{B} m}, \tag{1.5}$$

which is called the 'recoil temperature'. However, for most atomic transitions used in laser cooling experiments, the heating rate due to the momentum kicks is greater than the rate at which atoms can be cooled via Doppler cooling. Therefore, the minimum temperature that can be obtained by this process is significantly higher than T_R. To find this minimum, we must find the mean kinetic energy of the atoms in the steady state, when the heating and cooling rates have become equal.

The kinetic energy change when an atom absorbs a photon is the recoil energy, E_R, and this is also the energy change on spontaneous emission, and so the energy change per scatter is $2E_\mathrm{R}$. The heating rate is thus the product of this energy change and the scattering rate. In a 1D molasses, there are two laser beams each generating scattering rate R_γ, therefore the heating rate is

$$\frac{\mathrm{d}E_\mathrm{heat}}{\mathrm{d}t} = 2\frac{\hbar^2 k^2}{2m}(2R_\gamma). \tag{1.6}$$

The cooling rate is the rate of energy change due to the cooling force, $\boldsymbol{F} \cdot \boldsymbol{v}$, which we can write as

$$\frac{\mathrm{d}E_\mathrm{cool}}{\mathrm{d}t} = -\beta v^2. \tag{1.7}$$

The sum of these rates is equal in the steady state; to find the root mean squared velocity of the atoms, we may solve for v,

$$v_\mathrm{RMS} = 2\sqrt{\frac{\hbar^2 k^2}{2m}\frac{R_\gamma}{\beta}}. \tag{1.8}$$

For a 1D thermal distribution, the root-mean-square velocity is $\sqrt{\frac{k_\mathrm{B}T}{m}}$. Substituting, taking R_γ for $v \to 0$, and solving for the temperature, one obtains

$$T = -\frac{\hbar\Gamma^2}{8k_\mathrm{B}\delta}(1 + s_0 + 4(\delta/\Gamma)^2), \tag{1.9}$$

which is valid only for $\delta < 0$. The minimum of this function is for $\delta = -\Gamma/2$ and $s_0 \to 0$, which give a minimum obtainable temperature of

$$T > \frac{\hbar\Gamma}{2k_\mathrm{B}} = T_\mathrm{D}. \tag{1.10}$$

This temperature is called the Doppler temperature, or the Doppler limit. In a situation where only 1D cooling is applied, atoms would be heated by photon scattering in the non-cooled transverse dimensions. For sodium, cooled on the transition used in [8], the Doppler temperature is 235 µK. However, it was soon found that the temperature of the atomic cloud in an optical molasses could become much lower than this [11].

1.1.3 Sub-Doppler cooling

In optical moalasses experiments, it was found that there were other stong cooling forces which became dominant after a period of Doppler cooling, for atoms travelling with low velocity. Dalibard and Cohen-Tannoidji, as well as Ungar *et al.*, developed the first models for the observed sub-Doppler cooling forces in 1989 [12, 13]. These were for experiments in which there are polarisation gradients (where the net polarisation of electric field of the light changes with position).

In a 3D optical molasses, there must always be polarisation gradients due to the transverse wave-like nature of light [7]. And in a 1D molasses, these polarisation gradients can be formed by using counterpropogating beams which have either orthogonal linear polarisations, a configuration called π_x-π_y or lin⊥lin, or orthogonal circular polarisations, σ^+-σ^-.

There are also sub-Doppler processes that do not rely on polarisation gradients. Three sub-Doppler processes are qualitatively discussed here. It is possible for these processes to cool molecules to T_R. It should also be noted that it is possible to cool atoms below T_R via a process called 'velocity selective coherent population trapping', which was first demonstrated in 1988 by the group of Cohen-Tannoudji [14]. In this process, atoms are pumped into a coherent superposition of ground states which cannot absorb light in a velocity selective manner.

Sisyphus cooling, π_x-π_y

For the π_x-π_y configuration, the cooling mechanism relies on the light shift, also known as the alternating current (AC) Stark shift. This effect was first discovered by Autler and Townes in 1955 for radio frequency transitions [15]. In addition to the radiation pressure force, there was also significant interest in using the force that could be exerted by this effect for the slowing and trapping af atoms. This was following the suggestion by Askaryan that light shifts could be used to exert a strong force on atoms in intensity gradients of laser fields [16].

When the polarisations of the opposing lasers are π_x-π_y, the net polarisation of the electric field changes over the length scale of the laser wavelength. Regions of σ^+ polarisation, are separated by regions of σ^- polarisation by a distance of $\lambda/4$, and at the midpoints

between these regions the polarisation is linear. Because the polarisation changes in space, transitions between different pairs of excited and ground states driven at different locations in the laser field, and ground and excited states are subject to spatially dependent light shifts.

For this effect, the ground state must have $F \geq 1/2$, as there must be at least two ground eigenstates that are shifted in energy relative to one another. To understand how this can result in a cooling force, a qualitative argument can be made for a simple system. Here we consider a $F' = 3/2 \rightarrow F = 1/2$ system, where F is the total angular momentum of each state, and the prime goes with the excited state. The states involved in the transition are shown in Fig. 1.2(a).

A description of the mechanism of the cooling force goes as follows [7]. The atom begins at zero in Fig. 1.2(b) in a region of σ^+ polarised light, where it is optically pumped into $m_F = +1/2$. As the atom moves to the right, it must climb a potential hill and lose kinetic energy. At the top of the hill, the light is σ^- polarised and so the atom is optically pumped into $m_F = -1/2$. This state has lower energy, and so the potential energy that the atom gained when climbing the hill is lost. The atom must continuously climb potential hills as it moves across the polarisation gradients. This type of process is often called the Sisyphus effect, named after the unfortunate king of Greek mythology.

The Sisyphus cooling force produces the strongest cooling forces for atoms travelling a distance $\lambda/4$ in the optical pumping time. The friction coefficient is greatest for relatively large detuning, and it may be larger by a factor $2|\delta|/\Gamma$ than the maximum friction coefficient for Doppler cooling [7].

σ^+-σ^- polarisation gradient cooling

In the σ^+-σ^- arrangement, the net polarisation is linear at all positions and so light shifts are constant and the atom does not climb potential hills. However, the orientation of the linearly polarised field corkscrews in position. The polarisation rotates through 2π over a distance of λ. This cooling process at work requires the atom's ground state to have an orientation and so a ground state with at least $F \geq 1$ is required [7]. In this situation, an atom moving through the rotating polarisation gradient aquires a velocity dependent imbalance in the populations of its ground states. In the case of a $F' = 2 \rightarrow F = 1$ transition, the imbalance in population is produced between the $m_F = \pm 1$ sub-levels, which was shown in [12]. This imbalance leads to a difference in the relative scattering rates from the σ^+ and σ^- beams, generating a restoring force.

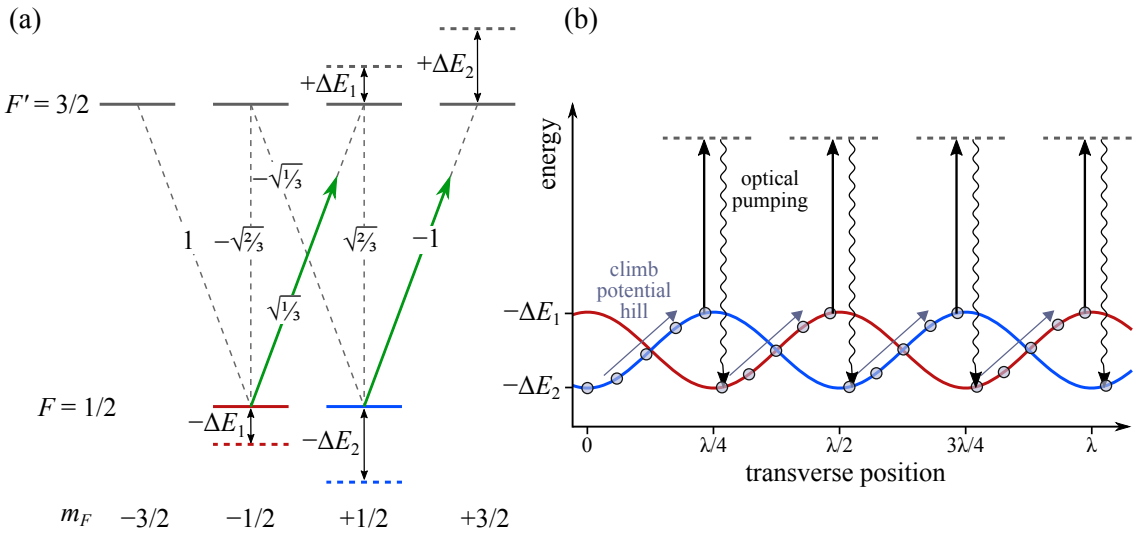

Figure 1.2: Polarisation gradient cooling in an $F' = 3/2 \rightarrow F = 1/2$ system, where m_F is the magnetic quantum number. (a): Here, the transition is driven with red detuned σ^+ polarised light. The energies of the ground states are light shifted by an energy that is proportional to the Clebsch-Gordan coefficients of the driven transitions. The shifted energy levels are shown as dotted lines. (b): At zero, the light is σ^+ polarised and atoms are in $m_F = +1/2$ as they move to the right, the polarisation oscillates between σ^+ and σ^- with position causing the light shift of the $m_F = \pm 1/2$ states to oscillate out of phase with one another.

Magnetically assisted Sisyphus cooling

Another sub-Doppler process is a type of Sisyphus cooling, which does not rely on polarisation gradients, but does require the presence of a small magnetic field. It is sometimes called the magnetically assisted Sisyphus effect,[3] and was first observed in 1D optical molasses experiments for $F' = F + 1$ ($F > 0$) type transitions [17, 18] . However, because this force is particularly relevant in experiments where molecules are laser cooled, it is discussed here for $F' = F - 1$ type transitions as this is more relevant to molecule cooling experiments.

So far, we have only discussed the type of transitions, where the angular momentum of the upper state is greater that of the lower state. These are often called 'type-I' systems, as opposed to 'type-II' systems, where $F' = F$ or $F' = F + 1$. Where available, type-I systems tend to be used in laser cooling experiments because there are no ground angular momentum eigenstates from which transitions cannot be driven for any choice of laser polarisation. Ground states which cannot couple to the laser polarisation (dark states) are generally bad for laser cooling, because population is optically pumped into these states. Without a mechanism to redistribute population, scattering ceases. However, in experiments where molecules are laser cooled such as ours, transitions with dark states must be used ('type-II' systems), as discussed in Sec. 2.3.5.

[3] It has also been called magnetically induced laser cooling [7], or just, 'a Sisyphus force'.

For type-II systems it was found that cooling is obtained for blue laser detuning and heating for red detuning for this Sisyphus force (it is the opposite in type-I systems). This was first observed in a one dimensional molasses experiment using caesium [19]. These results were reproduced using the 2^3S_1-2^3P_1 transition in metastable helium, and discussed in detail in [20]. The effect has also been investigated in a 2D atomic beam laser cooling experiment in [21], and laser cooling in these types of systems has been modelled in 3D in [22].

A qualitative picture of the mechanism responsible for the Sisyphus force is shown in Fig. 1.3 for a $F = 1 \rightarrow F' = 0$ system. The transition is driven by two counterpropagating beams of π polarised light, whose polarisations are both oriented in the same direction. The $m_F = \pm 1$ states are therefore dark. The light is blue detuned, and forms a standing wave, such that $m_F = 0$ and $m'_F = 0$ experience an attractive light shift, whose size depends upon the position relative to the nodes of the standing wave. Additionally, a small magnetic field is applied at an angle to the laser polarisation. Consider a molecule in the $m_F = 0$ state which begins at a node in the standing wave, at the bottom left of Fig. 1.3(b), and moves to the right. As it moves towards an antinode it must climb a potential hill, and lose kinetic energy. As it climbs the potential hill, the molecule is optically pumped into either of the $m_F = \pm 1$ states and the potential energy it gained climbing the hill is lost to the spontaneously emitted photon. Around the next node, the magnetic field may cause the dark state to precess into the bright $m_F = 0$ state, and the molecule must again climb a potential hill as it moves towards the next antinode. This process is repeated as molecules travel across the standing wave. The situation is reversed for red detuning, as the $m_F = 0$ and $m'_F = 0$ states are repelled, and the molecule gains kinetic energy as it moves towards a node. The picture is slightly more complicated in systems with higher degeneracy such as those using $F = 1 \rightarrow F' = 1$ and $F = 2 \rightarrow F' = 1$ transitions, however the effect may be explained in a similar way. Because the velocity dependent force has an opposite sign to that of Doppler cooling, these forces compete at low velocity. For red detuning this can result in there being a non-zero speed towards which atoms are cooled.

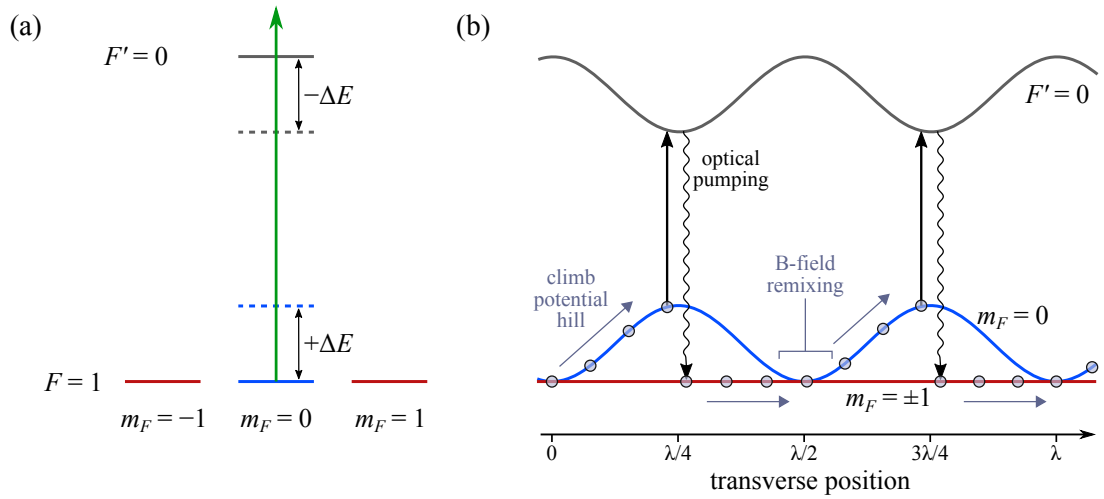

Figure 1.3: A qualitative picture of the magnetically assisted Sisyphus effect for a $F = 1 \rightarrow F' = 0$ system, similar to that discussed in [23]. (a): Solid lines are the zero field energy levels, dashed lines are the light shifted levels in the presence of a blue detuned, linearly polarised laser field. (b): The energy levels and motion of molecules in a blue detuned standing wave. Molecules must continuously climb potential hills, and lose kinetic energy.

1.2 Laser cooling molecules

The ability to produce cold, dense atomic clouds by laser cooling has brought significant advances in physics. It has improved the accuracy of timekeeping and has led to the realisation of Bose-Einstein condensation. It has also enabled the precise control of atoms that is required to make tests of fundamental physics through the use of methods such as atom interferometry. This technique also promises technological advancement through the delivery of incredibly precise accelerometers and rotation sensors.

The production of cold, dense diatomic molecular clouds offers to deliver its own scientific advancements. These include quantum computation using polar molecules [24], and the study of chemical reactions at low temperature [25]. Additional applications are reviewed in [26, 27]. Another application is the use of cold molecules in tests of fundamental physics, which is the purpose of the experiment discussed in this thesis.

In this section, experiments to laser cool molecules are reviewed. It should also be noted that in addition to laser cooling, there are many other routes by which cold molecules may be produced. Many other techniques are reveiwed in [27, 28, 29].

1.2.1 Extending laser cooling to molecules

In addition to the energy level structure of an atom, a molecule has rotational and vibrational structure. This additional structure is one of the reasons why cold molecules are scientifically interesting, but also presents a problem for laser cooling. Laser cooling relies

on the scattering of thousands of photons from the species that is to be cooled, which requires a transition which is closed – meaning that the excited state of the transition quickly decays back to the ground state, with a low probability of the atom decaying to a long-lived metastable state. Around 20 elements have transitions which have been found suitable for laser cooling.

The presence of the rotational and vibrational structure of molecules generally means that there are a large number of electronic ground states to which they are likely to decay. These states are long-lived and transitions from all of them cannot be driven using a single laser frequency. In general, to laser cool a molecule, one would require an unfeasibly large number of lasers.

In 1996, Bahns *et al.* put forward a technique to cool the vibrational, rotational and translational degrees of freedom of molecules [30]. Whilst this technique was perhaps less demanding than the use of many independent laser sources to address these states, it was still too experimentally complex to be realised.

It is particularly the vibrational structure of a molecule which makes laser cooling troublesome. This is because there are no selection rules which govern the change in vibrational quantum state in an electronic transition. The probability of decay to a particular vibrational state depends upon the overlap between the excited and ground state vibrational wavefunctions.

DiRosa considered this problem, and in 2004, explained that there were several diatomic molecular species that were suitable for laser cooling and identified 10 such species (including BeH, CaH, BH, AlF and AlCl). Theses were molecules whose vibrational potentials in the excited state were very similar to the potentials in the ground state, which causes the overlap between pairs of wavefunctions corresponding to the same vibrational quantum number, v, to be large, and others to be small. He proposed that suitable molecules could be cooled using transitions of this type by driving a $v = 0 \rightarrow v' = 0$ transition, and using only a small number of additional lasers to drive transitions from $v = 1, 2, ...n$ (where typically $n \sim 2$) in order to return stray population to the cycling transition.

Rotational branching is governed by angular momentum selection rules, and so does not present such a large problem. Generally, an excited state can decay into two or three ground rotational states. This would mean that more than one laser frequency is required per vibrational ground state to address rotational structure. It was pointed out by Stuhl *et al.* that this can be avoided by driving a transition which has rotational quantum number $R = 1$ in the ground state and $R' = 0$ in the excited state [31], because $R' = 0 \rightarrow R = 1$ is the only allowed transition from the excited state. This reduces the experimental complexity, but requires there to be dark ground eigenstates as the angular momentum of the excited state is smaller than that of the ground state.

By following these criteria, the laser cooling of molecules became feasible. In 2009, Shuman *et al.* of the DeMille group demonstrated the deflection of a beam of strontium fluoride radicals (SrF) [23], and in 2010, the same group reported the first molecule laser cooling results [23]. Here it was demonstrated that a beam of SrF could be transversely cooled in one dimension by either Doppler cooling or the magnetically assisted Sisyphus effect. The beam's initial transverse temperature was 50 mK, and final temperatures < 15 mK and < 5 mK could be obtained when the experiment operated in either Doppler or Sisyphus regimes respectively. This experiment was followed by an experiment where an SrF beam was slowed via radiation pressure [32]. In this experiment, molecules in a $140\,\mathrm{m\,s^{-1}}$ beam could be slowed to $\lesssim 50\,\mathrm{m\,s^{-1}}$ by scattering $\sim 10^4$ photons over a distance of 1.35 m. From these numbers, it may be apparent to the reader familiar with atomic laser cooling experiments that the scattering rates and forces that may be obtained in molecule cooling experiments are substantially lower than their typical atomic counterparts. This is primarily due to the large ratio of ground to excited states involved in the cycling transition, which is discussed in Sec. 2.4.

These results were followed by demonstrations of laser cooling, and two dimensional magneto optical trapping of YO by Hummon *et al.* [33], and the longitudinal slowing of a CaF beam by Zhelyazkova *et al.* of the Imperial group [34].

Because the change in electronic state always causes some perturbation to the vibrational potential, laser cooling will never be as efficient for molecules as for atoms, because the length of time for which a molecular sample can be cooled and trapped by the scattering force will be limited by decays to non-addressed vibrational levels. Additionally, the molecular species which are appropriate for laser cooling appear to be highly reactive radical species, which must be produced by an often inefficient chemical reaction as part of the experiment. However, these disadvantages are often outweighed by the benefits that the use of a molecule can bring to an experiment.

1.2.2 Current experiments

In 2014, Barry *et al.* demonstrated magneto-optical trapping (MOT) of SrF [35]. The application of this powerful technique to molecules promises to deliver higher densities and lower temperatures of molecular samples for experiments. In this first experiment, ~ 400 molecules at approximately 2.5 mK could be trapped, with a trap lifetime of ~ 40 ms. Due to the $R = 1 \rightarrow R' = 0$ transition used, molecule MOTs operate on type-II transitions. In atomic MOTs, type-I transitions are typically used, and where type-II MOTs have been experimentally studied, it was found that they typically have higher temperatures ($2 \rightarrow 20$ mK), larger cloud sizes, and lower densities [36, 37].

Following some relatively simple modelling of type-I and type-II systems [38], an im-

proved design of the SrF MOT was demonstrated [39], as well as a radio-frequency (RF) molecular MOT [40]. In the RF MOT, the directions of the laser polarisations and magnetic field are rapidly reversed at $\sim 1\,\mathrm{MHz}$ frequencies. With the use of this technique the temperature to which an SrF cloud could be cooled and trapped was reduced to $400\,\mu\mathrm{K}$. Recently, further progress has also been made in modelling and understanding the effects produced by the complex cycling transitions that are used in these types of experiments [22, 38].

In 2015, Yeo *et al.* used a scheme in which microwave transition between rotational states were driven simultaneously with the electronic transition for improved optical cycling in YO to slow molecules to $\lesssim 10\,\mathrm{m\,s^{-1}}$ [41]. This scheme was used because YO has a complicated structure in the first excited state, and decays via an intermediate state that distributes population across additional rotational ground states.

Recently, Truppe *et al.* have shown the slowing of CaF to the capture velocity of a MOT, using a particularly efficient choice of cycling scheme [42]. In this experiment an average of $\sim 3 \times 10^4$ photons could be scattered by the molecule with 50 % probability of the molecule remaining in the cycling transition. The slowing of CaF has also been demonstrated by the Doyle group [43].

The Doyle group have also presented evidence of magnetically assisted Sisyphus laser cooling for a triatomic molecule [44]. As the number of atoms in a molecule increases, so does the number of vibrational and rotational modes the molecule can support. This leads to increasingly complex energy structures, which would appear to make laser cooling impractical, due to the increased probability of vibrational branching. Recently, it was explained by Isaev and Berger that some polyatomic molecules should possess a structure that make them amenable to laser cooling [45], and the Doyle group have published a proposal for an experiment to cool molecules consisting of many atoms. This interesting development could open the door for new directions of research in physics and chemistry [46, 47].

1.2.3 Novel cooling techniques

In addition to the 'conventional' methods of laser cooling so far discussed, there are suggestions that some other methods of laser cooling can have a significant advantage to the photon scattering force and the sub-Doppler forces, for certain applications.

Vuletić and Chu explained that atoms, molecules or ions inside an optical cavity may be cooled by light that is at low saturation and a large detuning from their resonances [48]. In this technique, a molecule is coupled to the light field inside a cavity, as the particle moves, it modifies the field inside the cavity and the field acts upon it via the light shift. The effect on the light field is delayed with respect to the position of the moving particle

due to the finite response time of the cavity. This process leads to a dissipative force for light that is red detuned with respect to the cavity resonance. The authors explain that this force should also work for an ensemble of particles. Crucially, the force is independent of the particles' internal energy level structure, and scattering is coherent, making this particularly interesting for molecule cooling.

The bichromatic force is a coherent effect which may be produced by a pair of counterpropagating laser beams which each contain two similar frequencies $\omega \pm \delta$, where δ is a two level resonance frequency for a molecular transition. Each beam may be considered as a train of beat notes. The power in the beams is tuned so that each beat is approximately a π pulse. If the counterpropagating beat notes have the correct relative phase, this can produce a large force due to the alternating cycles of absorbtion and stimulated emission in the molecule. Recently, Aldridge *et al.* have modelled this effect for the CaF molecule, and have found that it should be effective for rapid slowing and cooling [49]. There had been some controversy surrounding cooling via this method, as it was not clear how a force due to stimulated processes only can be dissipative. This was resolved by Corder *et al.* who demonstrate and discuss cooling via this method in atoms [50].

A technique named Zeeman-Sisyphus deceleration has been proposed by Fitch and Tarbutt which may increase the efficiency with which a molecular beam may be decelerated [51]. The technique can also achieve some compression of the forward velocity distribution. In this method the molecular beam travels through a tunnel of magnets, and there is a laser beam, directed opposite to the direction of motion of the molecules. The laser contains two frequency components. The magnetic field varies with longitudinal position, and the ground state levels are shifted via the Zeeman interaction. A molecule in a weak field seeking state moves towards a region of high field and must climb a potential hill. Close to the top of the potential hill, it is Zeeman shifted into resonance with the lower laser frequency, and is optically pumped into a strong field seeking state. As the molecule continues its journey, it returns to a region of strong field and again climbs a potential hill. Upon becoming shifted into resonance with the higher laser frequency, it is optically pumped back into a weak field seeking state. Compared with radiation pressure slowing, molecular species may be slowed by scattering $\lesssim 1/10$ of the number of photons, making it an attractive technique for slowing molecules with moderately favourable Franck-Condon factors. This technique can also provide some transverse confinement of the molecular beam.

1.3 Measuring the electron electric dipole moment

1.3.1 Symmetry

Until the early 1950s it had been assumed that all interactions respected three symmetries; charge conjugation (C), parity inversion (P), and time reversal (T). The C-transformation replaces particles with their antiparticle, so all charges become opposite, $q \to -q$. P inverts space through an arbitrary coordinate origin, $(x, y, z) \to (-x, -y, -z)$. T reverses all directions of motion, and inverts quantities associated with time, $t \to -t$.

In 1950, Purcell and Ramsey challenged these assumptions by suggesting that elementary particles might have permanent electric dipole moments (EDM) [52]. The presence of these EDMs would be a violation of both P and T symmetries. They went on to make a measurement of the neutron EDM, but within the precision of their experiment, they found it to be consistent with zero [53]. Parity violation by the weak force was suggested by Lee and Yang in 1956 [54], and observed soon after (1957) in the measurement by Wu *et al.* of the directional preference for emitted electrons in the β-decay of spin polarised ^{60}Co nuclei [55].

It was quickly proposed that interactions should be symmetric under combined CP operations, with the main argument for this being that it seemed peculiar for nature to reject spatial symmetry entirely [56]. But, in 1964 it was found that the weak force violates CP symmetry in decays of the neutral K meson [57], and, more recently, in decays of the B meson and D meson [58, 59, 60].

Symmetry is not entirely abandoned, as it is thought that the combined CPT-transformation is most likely a symmetry operation. This idea is from CPT theorem [61], which states that any Lorentz invariant field theory which obeys locality, must obey the combined symmetries of C, P and T [62]. This leads to the assumption that because CP is violated, T must be violated in the right way to make the combined CPT-transformation symmetric. Direct evidence that T symmetry was violated was reported in 1998 by the CPLEAR collaboration by comparing the probabilities of forward and reverse $\mathrm{K}^0 \leftrightarrow \overline{\mathrm{K}}^0$ transformations [63], and also more recently in decays of B mesons [64].

1.3.2 Permanent electric dipole moments

To see why an elementary particle with an EDM violates P and T symmetry, we will consider the effects of the symmetry operations on such a particle. Here we consider a spin-$1/2$ particle (for example, a proton, neutron or electron).

The relative orientations of the particle's EDM, $\boldsymbol{d}_\mathrm{e}$, and spin angular momentum $\boldsymbol{S}$ are constrained by the Wigner-Eckart theorem [65], such that a meaningful $\boldsymbol{d}_\mathrm{e}$ must lie along the same axis as $\boldsymbol{S}$, so $\boldsymbol{d}_\mathrm{e} = d_\mathrm{e}\frac{\boldsymbol{S}}{|\boldsymbol{S}|}$. The P-transformation reverses $\boldsymbol{d}_\mathrm{e}$ but leaves

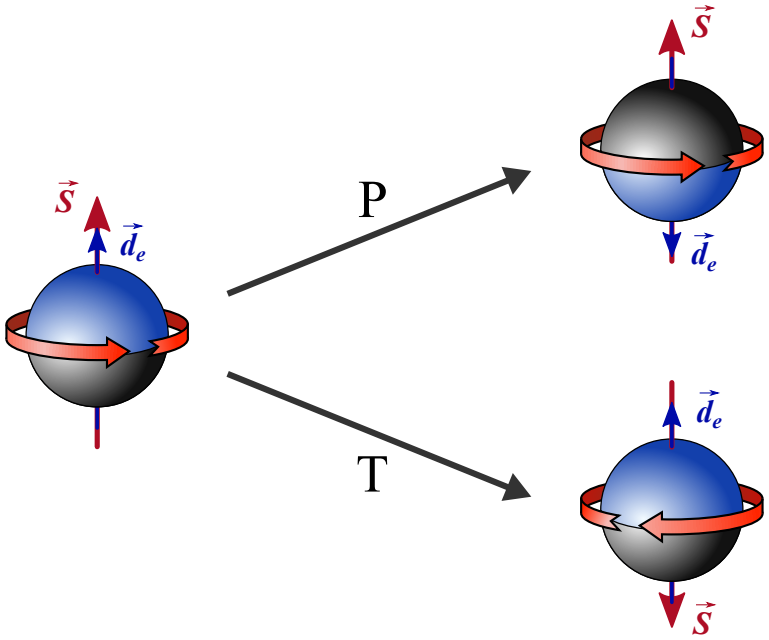

Figure 1.4: P and T transformations on a particle which has a spin, $\boldsymbol{S}$, and an EDM, $\boldsymbol{d}_{\mathrm{e}}$. Assuming that the $\boldsymbol{d}_{\mathrm{e}}$ and $\boldsymbol{S}$ are initially aligned.

$\boldsymbol{S}$ unchanged. The T-transformation reverses $\boldsymbol{S}$ but not $\boldsymbol{d}_{\mathrm{e}}$. These transformations are shown in Fig. 1.4. For both transformations, the particle will not interact in the same way as the original. Considering the particle to be an electron, we know that it does not exist in both quantum states, $\pm d_{\mathrm{e}}$ from our knowledge of atomic physics; the number of internal states of the electron is consistent with its spin being the only degree of freedom. Therefore, either the EDM is zero, or the electron has an EDM which has only one relative orientation. This violates P and T symmetry. Under the CPT theorem, this violation in T is equivalent to violation of CP.

Since the existence of permanent particle EDMs was first suggested by Purcell and Ramsey, they have been searched for in a wide range of systems, including neutrons, muons and mercury atoms [66]. So far an EDM has not been detected, but there is good reason to think that they should exist.

The Standard Model has been incredibly successful in explaining and predicting a wide range of phenomena [67, 68], however it can not explain the observations of dark matter, or the accelerating expansion of the universe [69]. Nor does it contain enough CP violation to explain the matter-antimatter imbalance in the universe [70]. These (and other) failings have led theorists to develop theories beyond the Standard Model. These theories generally contain additional particles, and additional sources of CP violation. The new particles must either have a large mass or interact very weakly, or they would have been observed previously in high energy particle physics experiments. One method of testing these theories is to continue searching for new particles at higher energies. A

second approach, is to look for the predicted CP violating effects of the new particles on more familiar particles such as the electron.

The standard model predicts a very small value for the eEDM of $|d_e| \simeq 10^{-38}$ e cm,[4] which is very much smaller than the current experimental limit $|d_e| < 8.7 \times 10^{-29}$ e cm (90 % confidence) [71]. However, many extensions to the Standard Model, predict eEDMs in the range $10^{-25} \rightarrow 10^{-31}$ e cm [72, 73], (with some these theories already being effectively ruled out by eEDM measurements). An improved measurement of the eEDM consistent with zero would constrain or rule out more of these theories, whereas a measurement of an eEDM would be proof of physics beyond the Standard Model [74].

1.3.3 Measuring the eEDM using molecules

To measure the eEDM, we would like to measure the interaction energy of the EDM with an electric field (E-field),[5] $-\boldsymbol{d}_e \cdot \boldsymbol{E}$. It would be difficult to do this experiment using a free electron in an E-field, as the electron would be rapidly accelerated. Instead, we might consider looking for an energy shift experienced by a paramagnetic atom in an E-field. Schiff considered this effect for nuclear EDMs, and showed that for any non relativistic quantum system of charged point particles there is no energy shift that is first order in particle EDMs [77]. A qualitative explanation of Schiff's theorem is as follows [78]: A neutral system of charges is not accelerated by a homogeneous external E-field. Therefore, the average force on each particle must be zero, and the average E-field experienced by each particle must also be zero, since in the non-relativistic limit there are only electrostatic forces. This means that the charges must rearrange themselves such that the average E-field experienced by each is cancelled.

Schiff went on to point out that in a real atom, this does not strictly apply for nuclear EDMs because the nucleus is not a point particle. Additionally, in heavy atoms, electrons do move relativistically. In 1965, Sandars investigated the effect of relatavistic motion of electrons, and in 1965 showed that for increasingly heavy atomic species the atom can have an effective EDM due to the eEDM of the unpaired electron, and that this can actually be considerably larger than that of the free electron [79, 80]. The ratio of the effective dipole moment of the atom, d_a, to that of the electron is usually called the 'enhancement factor' $R \equiv d_a/d_e$, and for the ground states of the alkali atoms, $|R| \approx 10Z^3\alpha^2$ [78], where Z is the atomic number, and α is the fine structure constant. This led to a series of experiments on the heavy atoms, rubidium [81], caesium [82], and thallium [83], which set new limits on the size of the eEDM.

A possible intuitive explanation for the evasion of Schiff's theorem in heavy atoms is as follows [84]: The valence electron moves relativistically, and it moves at different speeds

[4] For historical reasons, EDMs are quoted in units of electron charge multiplied by length in centimetres.
[5] Although this is not the only possible approach [75, 76].

depending upon its distance from the nucleus. In the rest frame of the atom, the 'length' of the electric dipole experiences a velocity dependent Lorentz contraction. Therefore, although the time averaged interaction between the E-field and the charge is zero, the average interaction energy between the EDM and the E-field may be non-zero. It is possible for $R > 1$ because the E-field strength inside the polarised atom reaches magnitudes much larger than the externally applied field, and so the time averaged interaction between the EDM and the internal field can be larger than the interaction between the EDM of a bare electron and the applied E-field.

The strength of the eEDM interaction is proportional to the polarisation of the atomic system by the applied E-field. The degree of polarisation of a polar molecule can be far greater than that of an atom in any realisable E-field, and so molecules offer an advantage [85, 86, 87]. For a large enhancement, a molecule containing a heavy atom bonded to an electronegative species is required. An applied E-field is still required, but its role is not to polarise the heavy atom, but to align the molecule [88]. The increase in the interaction strength with the eEDM due to the internal electric field of a polar molecule may be of the order 10^4, [87, 89]. For molecules, both the relativistic enhancement and the increase in interaction strength due to the internal polarisation can be quantified by an effective electric field, $\boldsymbol{E}_{\text{eff}}$ that interacts with $\boldsymbol{d}_{\text{e}}$, where,

$$\boldsymbol{E}_{\text{eff}} = E_{\text{eff}}^{\text{max}} \eta(E) \boldsymbol{z}. \tag{1.11}$$

Here, $E_{\text{eff}}^{\text{max}}$ is the maximum effective electric field for a molecule fully aligned with the applied electric field $E\boldsymbol{z}$, where $\boldsymbol{z}$ is a unit vector. The alignment of the molecule with the field is $\eta(E) = \langle \boldsymbol{n} \cdot \boldsymbol{z} \rangle$, where $\boldsymbol{n}$ is a unit vector along the internuclear axis of the molecule, pointing from the negative ion to the positive ion.

For eEDM sensitive states of various molecules, $\boldsymbol{E}_{\text{eff}}$ has been calculated. For three molecular species, values of $E_{\text{eff}}^{\text{max}}$ are given in the table below. Experiments to measure the eEDM have been performed using molecules including YbF [90], PbO [91] and ThO [71].

molecule	$E_{\text{eff}}^{\text{max}}$	
YbF	$-25\,\text{GV cm}^{-1}$	[92]
PbO	$26\,\text{GV cm}^{-1}$	[93]
ThO	$84\,\text{GV cm}^{-1}$	[94]

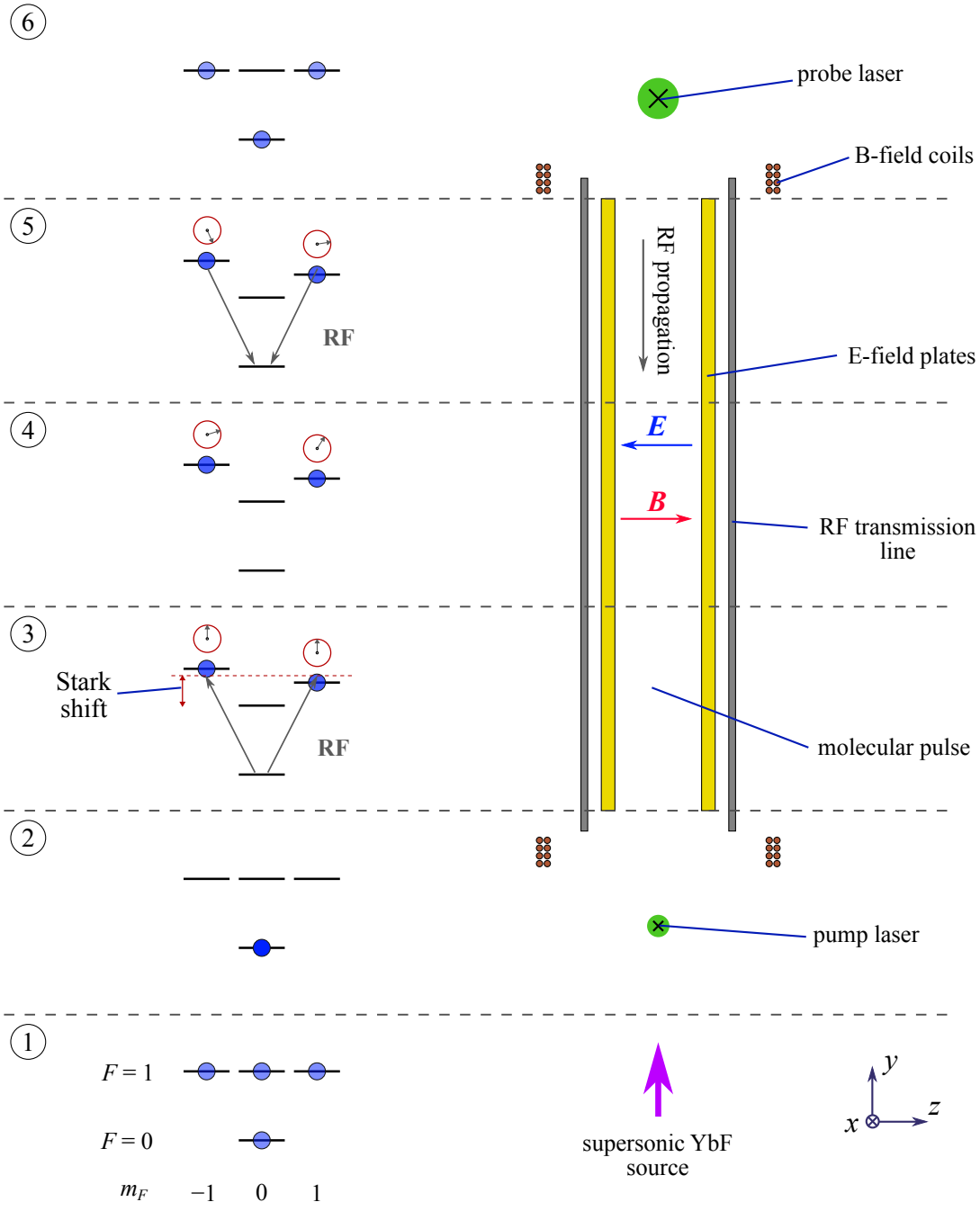

Figure 1.5: An overview of theYbF eEDM experiment, as in [95]. 1: Molecules are emitted from the supersonic source with equal population in the four sublevels. 2: Population is optically pumped out of the $F = 1$ sublevels. 3: The first RF pulse prepares molecules in a coherent superposition of $m_F = \pm 1$ states. 4: A phase difference accumulates due to the applied E- and B-fields. 5: The second RF pulse transfers population back to $F = 0$ with a probability which depends upon the phase difference. 6: The population in $F = 0$ is probed by laser-induced fluorescence.

1.3.4 The YbF eEDM experiment

Over the past ~ 20 years, members of this group (E. Hinds and co-workers) have worked on, or towards, an experiment which measures the eEDM using YbF molecules. Essentially, the experiment measures the change in the spin precession frequency of the electron in an applied magnetic field due to the interaction between $\boldsymbol{d}_\mathrm{e}$, and the effective electric field $\boldsymbol{E}_\mathrm{eff}$. The experiment is done by interferometry; the molecules are put into a coherent superposition of states which have different eEDM sensitive energy shifts, and the relative precession frequency of these states is measured.

Here I will give a brief overview of the basic principles of the experiment following that in [95], in order to discuss how laser cooling can be used to improve its precision. More detailed discussions of the experiment can be found in [95, 96].

Fig. 1.5 is a simplified schematic of the current experiment. In the experiment, only ^{174}YbF molecules which are in the $\mathrm{X}^2\Sigma^+(v = 0, N = 0)$ state are used. This is the lowest rotational, vibrational and electronic state. It contains two hyperfine sub-states with $F = 0, 1$. First, a pulse of YbF molecules is produced by a supersonic source. The molecules travel vertically upwards at $590\,\mathrm{m\,s^{-1}}$. They then travel through a pump laser beam which optically pumps molecules from the $F = 1$ states into $F = 0$ (some molecules are pumped into other rotational and vibrational states and lost from the experiment). The molecules pass between a pair of electric field plates which are 750 mm long and separated by 12 mm.

Between the field plates there is a uniform electric field, $E\boldsymbol{z}$, and magnetic field, $B\boldsymbol{z}$, where $\boldsymbol{z}$ is a unit vector in the z-axis. The applied electric field causes the ground state of the molecule to shift down in energy, the hyperfine splitting to increase, and causes the $|F, m_F\rangle = |1, 0\rangle$ level to split from the $|1, \pm1\rangle$ levels. If $d_\mathrm{e} = 0$ and $B = 0$, $|1, \pm1\rangle$ are degenerate. The magnetic field shifts the energy of the $|1, \pm1\rangle$ levels by $\pm\mu_\mathrm{B} B m_F$ due to the Zeeman interaction, and a non-zero eEDM produces an energy shift $\mp d_\mathrm{e} E_\mathrm{eff} m_F$. Typically, $B = \pm14\,\mathrm{nT}$, and $E = \pm10\,\mathrm{kV\,cm^{-1}}$, which makes $E_\mathrm{eff} = \mp14.5\,\mathrm{GV\,cm^{-1}}$.

An RF pulse whose magnetic field is linearly polarised in $\boldsymbol{x}$ is applied via a transmission line parallel to the electric field plates. The duration and amplitude of the pulse is chosen such that it drives a π-pulse to the coherent superposition state $|c\rangle = \frac{1}{\sqrt{2}}(|1, +1\rangle + |1, -1\rangle)$. As the molecules travel through the E-field plates, this state evolves for a time $\tau = 650\,\mu\mathrm{s}$ into $\frac{1}{\sqrt{2}}\left(\mathrm{e}^{\mathrm{i}\phi}|1, +1\rangle + \mathrm{e}^{-\mathrm{i}\phi}|1, -1\rangle\right)$, where $\phi = (\mu_\mathrm{B} B - d_\mathrm{e} E_\mathrm{eff})\tau/\hbar$. A second, identical RF pulse is then applied, coupling $|c\rangle$ to $|0, 0\rangle$. The final state is then $\cos\phi\,|0, 0\rangle + \mathrm{i}\sin\phi\,|u\rangle$, where $|u\rangle = \frac{1}{\sqrt{2}}(|1, +1\rangle - |1, -1\rangle)$.

The population in $F = 0$ is then probed via laser-induced fluorescence, and is proportional to $\cos^2\phi$, enabling d_e to be extracted. The magnetic field is used to set $\phi \approx \mu_\mathrm{B} B\tau/\hbar \approx \pm\pi/4$, which is the steepest part of the interference curve, such that the ex-

periment is most sensitive to d_e. To measure d_e, the relative directions of the electric and magnetic field are reversed. In order to find and quantify various sources of systematic error many more parameters are modulated, including the direction of the magnetic field and the RF propagation direction.

The statistical uncertainty in d_e is [72]

$$\sigma_d = \frac{\hbar}{2E_{\text{eff}}\tau\sqrt{N}}, \tag{1.12}$$

where N is the total number of molecules detected in the experiment.

1.3.5 Improving eEDM measurement sensitivity using laser cooling

To make a more precise measurement of the eEDM, we must reduce the statistical uncertainty in d_e. From Eq. (1.12), we see that there are three parameters available, E_{eff}, N and τ. In the current eEDM experiment, E_{eff} is half of $E_{\text{eff}}^{\text{max}}$, and increasing the applied electric field further has diminishing returns in saturating E_{eff}. Current upgrades to the eEDM experiment are concerned with increasing N, and these upgrades are detailed in [96, 97]. First, a pumping scheme will be used to pump molecules, which are in other rotational states, into the $F = 0$ rotational ground state before they begin the interferometry experiment.[6] Second, the probability of detecting each molecule at the end of the experiment is being significantly improved through the use of pumping and optical cycling in the detection region, and through the detection of the molecules remaining in $F = 1$. These improvements should result in an increased sensitivity of 11.4 over the previous YbF result in 2011 [90, 97].

The remaining parameter that can be increased to improve the sensitivity is the interaction time of molecules with the electric and magnetic fields, τ. Improving τ could be done by either increasing the length of the interferometer, or using a slower molecular beam. Increasing the length of the current interferometer would do little to change the sensitivity; the interaction time increases linearly with length, but, due to the divergence of the molecular beam, the number of molecules arriving at the detector decreases proportional to the square of the propagation distance.

To deliver a similar number of molecules to the detector, but increase the interaction length, transverse laser cooling could be used to significantly reduce the divergence of the beam. The transverse cooling would be done immediately after the molecular source. In addition, the current supersonic source would be replaced with a buffer gas source with a forward velocity of $180\,\text{m}\,\text{s}^{-1}$ rather than the $590\,\text{m}\,\text{s}^{-1}$ supersonic source.

To see the benefit of transverse cooling, we consider a simple model for the sensitivity: First, we assume that the cooled molecular beam has a Gaussian position distribution in

[6] This pumping scheme is done using lasers, radio-frequency and microwaves.

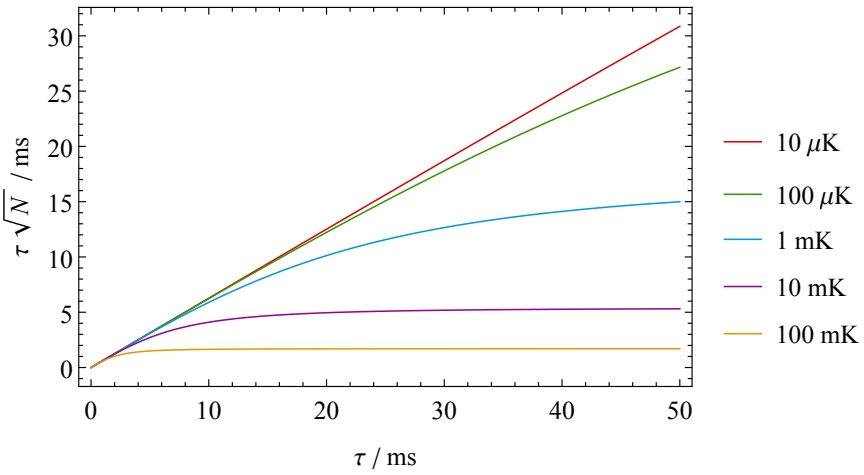

Figure 1.6: Plots of $\tau\sqrt{N}$ as a function of τ for $R_{\mathrm{det}} = 5\,\mathrm{mm}$, $\sigma_0 = 5\,\mathrm{mm}$ and $m = 193\,\mathrm{u}$.

its radial coordinate, r with standard deviation σ_r,

$$f(r) = \frac{1}{2\pi\sigma_r^2} \exp\left(-\frac{r}{2\sigma_r^2}\right). \tag{1.13}$$

The beam also has a Gaussian transverse velocity distribution characterised by a temperature T. The position distribution grows with time, τ, from its initial standard deviation $\sigma_{r,0}$ according to

$$\sigma_r(\tau) = \sqrt{\sigma_{r,0}^2 + \frac{k_{\mathrm{B}}T}{m}\tau^2}, \tag{1.14}$$

where m is the molecular mass. The molecules travel through the interferometer to a detector, which detects molecules within a radius, R_{det} in the transverse direction. The fraction of molecules detected is

$$N = 2\pi \int_0^{R_{\mathrm{det}}} r f(r) \mathrm{d}r = 1 - \exp\left(-\frac{R_{\mathrm{det}}^2}{2\sigma_r^2}\right). \tag{1.15}$$

The eEDM sensitivity, $1/\sigma_d$, is proportional to $\tau\sqrt{N}$, which is plotted as a function of τ for different molecular beam temperatures in Fig. 1.6. In limit of large τ, the maximum sensitivity is proportional to

$$\lim_{\tau\to\infty} \tau\sqrt{N} = R_{\mathrm{det}}\sqrt{\frac{m}{2k_{\mathrm{B}}T}}. \tag{1.16}$$

Therefore, the maximum sensitivity of the experiment scales as $1/\sqrt{T}$. If molecules leaving from the current supersonic source have a transverse temperature of 1 K, reducing the transverse temperature to 1 mK can increase the sensitivity a factor of ~ 30. To do this experiment using the buffer gas source with forward velocity $180\,\mathrm{m\,s^{-1}}$ we would want a travel length of $\sim 5\,\mathrm{m}$ through the interferometer. If it were to be much longer, there

would not be space in the laboratory!

In future, it should be possible to slow a YbF beam to rest, and capture molecules in a 3D magneto-optical trap (MOT). The captured molecules could then be launched in a molecular fountain, in which the eEDM experiment is performed. This idea is discussed in [72]. Using this method, the useful interaction time would be limited only by the temperature of the molecules rather than space constraints, and a sensitivity increase of a factor ~ 100 should be realisable. We have so far been unable to find a practical method of efficiently decelerating molecules produced from an available molecular beam source to the capture velocity of a MOT (which we calculate to be $\sim 10\,\mathrm{m\,s^{-1}}$). Further discussion of a YbF fountain can be found in Sec. 7.3.

1.4 Other tests of fundamental physics using molecules

As well as measuring the eEDM, there are other questions in fundamental physics which cold molecules may help us to answer. Here, two of these applications are briefly discussed.

1.4.1 Time variation of fundamental constants

A fundamental constant is a parameter that appears in a theory of fundamental physics whose value is not predicted by the theory; they must therefore be measured experimentally. It has been the goal of theoreticians to devise theories which are consistent with experimental measurement and contain ever fewer of these free parameters. The Standard Model of particle physics has 22 such parameters, and in Lorentz invariant theories, these parameters are constant, meaning that dynamics of an interaction is unaffected by the time or position at which the interaction happens in the Universe. However, many extensions to the Standard Model predict that these constants may vary with time, position or the local density of matter [98, 99]. Such theories aim to explain the nature of dark energy or unify gravity with the other forces.

The energy spectra of atoms and molecules depend upon the fine structure constant, α, and the electron-to-proton mass ratio, μ. Measuring these spectra to high precision provides a method by which these variations in these constants can be found since the different energy scales (gross, fine, and hyperfine structure) have different dependencies on α and μ. The rotational and vibrational transitions in molecules have yet different dependences, and in certain circumstances can have greatly increased sensitivity to these constants [100].

Astronomical data enables comparison of molecular and atomic spectra over 10^{10} year timescales. This may be done by comparing the emission and absorption spectra of atoms and molecules in distant gas clouds with different redshifts which are in the line of sight

of even more distant quasars. The analyses of these data have thus far yielded conflicting results, with some measuring a variation in α across the Universe [101, 102], and others finding no variation [103, 104]. Comparisons between laboratory data and astronomical measurements of certain transitions have also been used to place limits on the variation of μ and α [105, 106]. Variations in constants over ~ 1 year timescales can be measured in the lab by making multiple precise measurements of a system at different times [107], or by comparing atomic clocks whose frequencies have different dependencies on the constants [108]. Recently, a molecular fountain of NH_3 has been demonstrated, which will be used to make high precision measurements of the inversion, rotational, and vibrational transitions in NH_3, each of which has a different dependence upon μ [109].

1.4.2 Parity violations

A chiral molecule is one whose mirror image cannot be superimposed upon itself. Due to the parity-violating weak interaction between the electrons and nuclei, the left and right-handed versions of a chiral molecule (called 'enantiomers') are expected to have slightly different energy structures. Calculations have been done to find molecules with large enantiomer dependent energy differences [110, 111], however measurements have so far lacked the required sensitivity to detect these differences [112]. An experiment is currently under way to measure these differences using molecules which are cooled in a buffer gas source [113]. It has also been suggested that it is possible to laser cool complex polyatomic species, including chiral molecules [44].

Biomolecules (sugars, peptides, amino acids, *etc.*) of the same compound all have the same chirality, and enantiomers frequently have very different biological effects. Intrestingly, it has been suggested that these tiny, $\sim 10\,\mathrm{mHz}$ energy differences between enantiomers may have been responsible for enantiomer selection in nature [114, 115].

Chapter 2

YbF structure and laser cooling scheme

2.1 Diatomic molecule energy level structure and notation

In a molecule, the presence of multiple nuclei introduce additional degrees of freedom that are not present in atomic systems. In particular, the nuclei may oscillate relative to one another, or rotate about one another. This gives molecules rotational and vibrational structure. Here, I will only give a brief explanation of the definitions and labelling of the quantum states that will be used in this thesis, considering only diatomic molecules (those containing two nuclei). Fig. 2.1 illustrates the energy level structure of a diatomic molecule.

2.1.1 Electronic structure

The largest energy scale in a molecule corresponds to its electronic states, these intervals are of the order of 100 - 1000 THz. Currently, laser sources are usually available to address transitions between these states. The states are typically labelled using letters, with X for the ground state, and A, B, C, ... for the first, second, third, etc. excited states which have the same multiplicity as the ground state. Lower case letters, a, b, c, ..., are used where the excited state has a different multiplicity.

As in atoms, it is possible to label the electronic states of molecules with a term symbol. For atoms this is written in the form

$$^{2S+1}L_J, \tag{2.1}$$

where S is the total spin, L is the orbital angular momentum, and J is the total angular momentum. In atoms the Coulomb force experienced by the electrons is spherically sym-

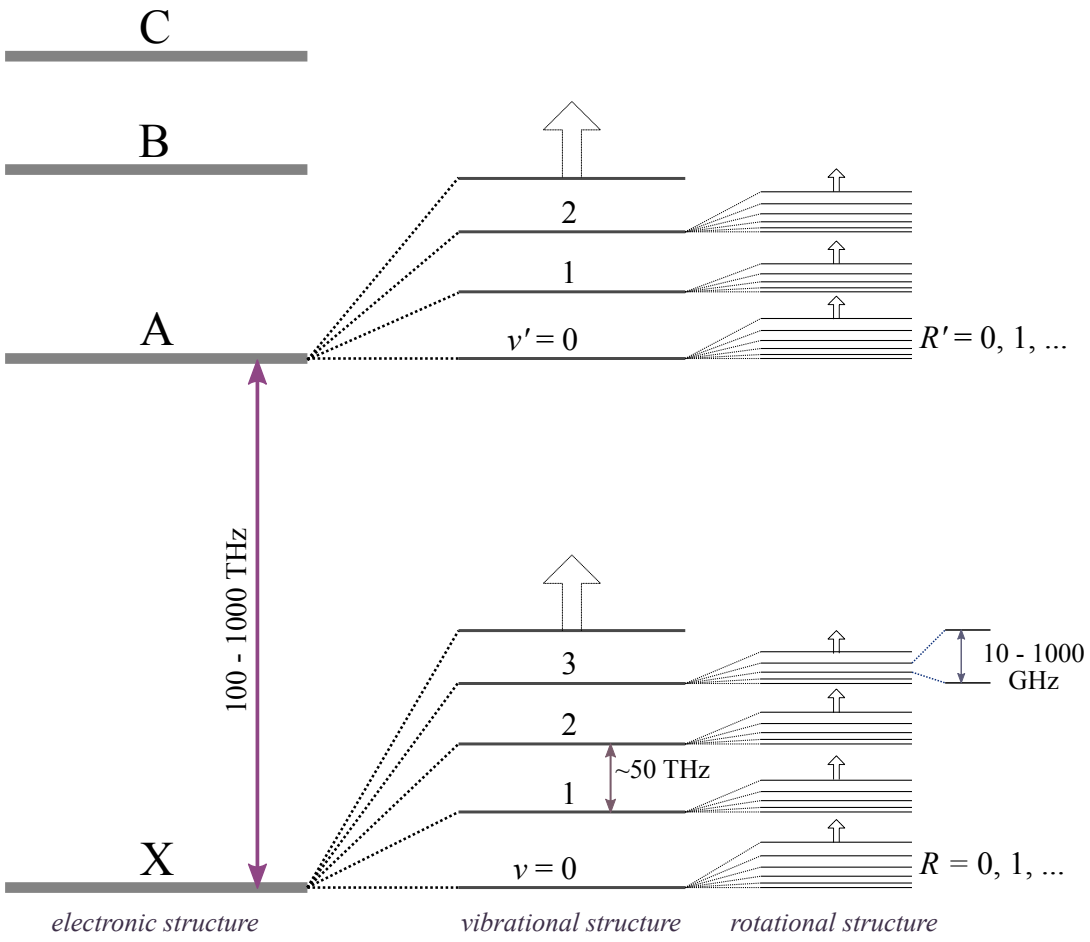

Figure 2.1: Schematic of the typical energy level structure for a diatomic molecule.

metric about the nucleus, however the addition of a second nuclei in a diatomic molecule makes this no longer the case. The force is instead cylindrically symmetric about the molecule's internuclear axis. We can define the $\boldsymbol{z}$ axis of our coordinate system to be along the internuclear axis and call the electronic orbital and spin angular momentum operators $\hat{\boldsymbol{L}}$ and $\hat{\boldsymbol{S}}$ as usual. However, $\hat{\boldsymbol{L}}$ does not commute with the electronic Hamiltonian of the molecule, meaning that L is not a good quantum number. Because of the cylindrical symmetry, the projections of $\hat{\boldsymbol{L}}$ along $\boldsymbol{z}$ does commute with the Hamiltonian. The quantum numbers for the projections in $\boldsymbol{z}$ are usually labelled Λ for $\hat{L}_z$ and Σ for $\hat{S}_z$ to make the distinction between the molecular and lab coordinates clear. The energies of terms with $|\Lambda| > 0$ will be split due to the spin-orbit interaction. Similarly, the quantum number for the projection of $\hat{\boldsymbol{J}}$ along $\boldsymbol{z}$ is labelled Ω, where $\Omega = \Lambda + \Sigma$. States $\pm\Lambda$ correspond to the direction of orbital angular momentum being either clockwise or anti-clockwise about $\boldsymbol{z}$, and the energies of these states are (to first order) equal. This is also the case for states with $\pm\Omega$, so states are labelled with the absolute value of these quantities, $|\Lambda|$ and $|\Omega|$. Analogously to atomic states $|\Lambda|$ is labelled using a Greek character in the molecular term symbol:

L or $\lvert\Lambda\rvert$ value	0	1	2	3	...
atomic state label	S	P	D	F	...
molecular state label	Σ	Π	Δ	Φ	...

For a given S there are $2S+1$ values of Σ. We can therefore write the molecular term symbol as:

$$^{2S+1}|\Lambda|^{(+/-)}_{|\Omega|}, \tag{2.2}$$

where the $+$ or $-$ sign is used to denote whether the state is symmetric or antisymmetric with respect to reflection in a plane containing $\boldsymbol{z}$. There are an infinite number of these planes; but for all $|\Lambda|$ there is a state which is symmetric and a state which is antisymmetric with respect to this reflection. For molecules with terms $\Lambda \neq 0$ these states are degenerate, and the $+/-$ label is omitted. However, the Σ^+ and Σ^- states are not degenerate and are therefore labelled.

2.1.2 Vibrational structure

The second largest molecular energy scale corresponds to the vibrational modes of the nuclei. Separations between vibrational states are in the order of 50 THz.

For small displacements about the equilibrium internuclear separation the potential is harmonic. The energy eigenstates of the potential are

$$E_v = \hbar\sqrt{k_{\text{nuc}}/m_r}\left(v+\tfrac{1}{2}\right), \tag{2.3}$$

where m_r is the reduced mass of the nuclei, k_{nuc} is a spring constant, and v is the vibrational quantum number. This is an accurate approximation for vibrational states with low v, but at increased displacement from equilibrium, the potential becomes anharmonic. The solutions may be given in general as a power series as in Eq. (6.188) of [116],

$$E_v = \omega_e\left(v+\tfrac{1}{2}\right) - \omega_e x_e\left(v+\tfrac{1}{2}\right)^2 + \omega_e y_e\left(v+\tfrac{1}{2}\right)^3 + ..., \tag{2.4}$$

where ω_e is the vibrational constant and x_e, y_e, ... are anharmonic constants, and $\omega_e \gg \omega_e x_e \gg \omega_e y_e$. The spacing between vibrational levels decreases with increasing v. Here I will label vibrational states with their quantum number v for those in the ground electronic state, and with v' for those within electronically excited states.

2.1.3 Rotational structure

Rotational structure is the smallest (diatomic) molecule-specific energy scale. These correspond to the rotation of the nuclei about their centre of inertia. Spacings between

rotational levels are of the order 10 - 100 GHz and so transitions between rotational states can usually be driven by commercially available microwave sources.

Energies of rotational states are well approximated by those of a rigid rotor,

$$E_{\text{rotation}} = BR(R+1), \tag{2.5}$$

where R is the rotational quantum number. B is the rotational constant,

$$B = \frac{\hbar^2}{2I}, \tag{2.6}$$

where I is the moment of inertia which will depend on the electronic and vibrational state. For high lying rotational states the molecule will stretch due to centrifugal forces. To include the effect of the increased moment of inertia, and of the energy change in vibrational states due to the increased internuclear separation, the rotational energy is often written as a power series as in Eq. (6.196) of [116],

$$E_{\text{rotation}} = B_v R(R+1) - D_v R^2(R+1)^2 + H_v R^3(R+1)^3 + ..., \tag{2.7}$$

where B_v is the rotational constant for vibrational level v, and terms D_v, H_v correct for centrifugal distortion.

2.1.4 Coupling of angular momenta

So far we have discussed; the electronic orbital angular momentum, the rotational angular momentum of the nuclei, and the electronic spin angular momentum, $\hat{\boldsymbol{L}}$, $\hat{\boldsymbol{R}}$ and $\hat{\boldsymbol{S}}$ respectively. These can all couple with each other. Hund's cases are idealised situations of ways in which these can couple which can help with our understanding of molecular structure. There are five Hund's cases, the most common of which are labelled (a) and (b). These are the most relevant to this thesis. Here, $\hat{\boldsymbol{J}}$ is the total angular momentum, and $\hat{\boldsymbol{N}}$ is the total angular momentum excluding the electron spin, so $\hat{\boldsymbol{N}} = \hat{\boldsymbol{J}} - \hat{\boldsymbol{S}}$, and $\hat{\boldsymbol{R}} = \hat{\boldsymbol{N}} - \hat{\boldsymbol{L}}$. Fig. 2.2 illustrates these schemes.

Hund's case (a)

In this case, the interaction between the nuclear rotation and the electronic motion is weak. $\hat{\boldsymbol{L}}$ and $\hat{\boldsymbol{S}}$ are strongly coupled to one-another, and also to the internuclear axis, $\boldsymbol{z}$. The axial components of $\hat{\boldsymbol{L}}$ and $\hat{\boldsymbol{S}}$, Λ and Σ are well defined, as is Ω. The precession of $\hat{\boldsymbol{L}}$ and $\hat{\boldsymbol{S}}$ about $\boldsymbol{z}$ is presumed to be much faster than the rotation of $\hat{\boldsymbol{R}}$ about $\hat{\boldsymbol{J}}$.

The good quantum numbers for this case are Λ, S, Σ, J and Ω. This condition applies when $A\Lambda \gg BJ$, where A is the spin-orbit coupling constant.

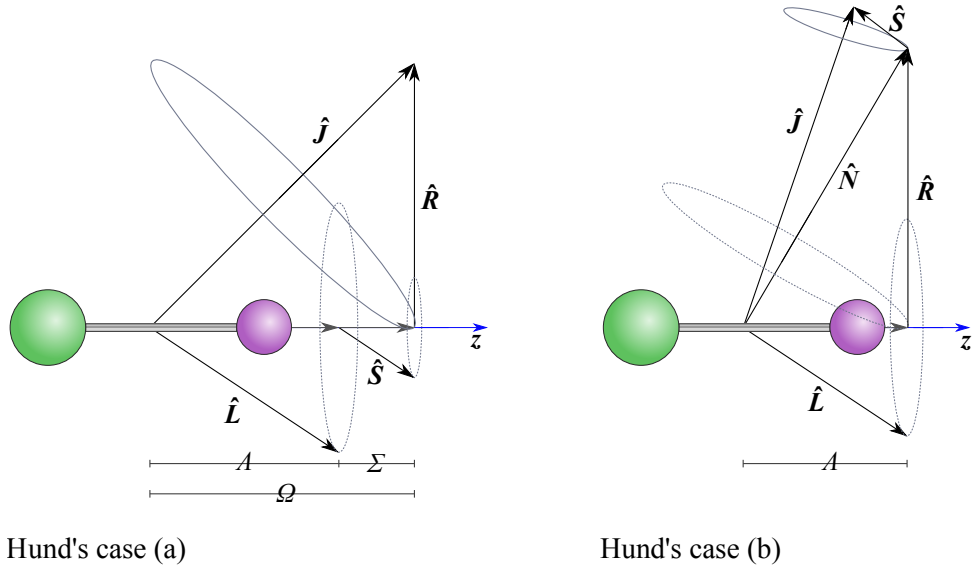

Figure 2.2: Diagram of Hund's angular momentum coupling cases (a) and (b) based on that in [116].

The precession of $\hat{\boldsymbol{L}}$ and $\hat{\boldsymbol{S}}$ about the internuclear axis can be clockwise or anti-clockwise. These states have equal energy, and have projections $\pm\Lambda$ and $\pm\Sigma$. Consequently, Ω is doubly degenerate also. The degeneracy in Λ is called Λ-doubling, and the degeneracy in Ω is called Ω-doubling. This degeneracy can be lifted by the rotation of the molecule, or by interaction with neighbouring electronic states which have different λ.

Hund's case (b)

If the rotational energy of the molecule is much larger than the spin-orbit coupling (or $\Lambda = 0$), then case (b) is a better description of the molecule. Here, $\hat{\boldsymbol{L}}$ precesses rapidly about $\boldsymbol{z}$, with a well defined Λ. $\hat{\boldsymbol{R}}$ is coupled to $\hat{\boldsymbol{L}}$ to form $\hat{\boldsymbol{N}}$, which is coupled to $\hat{\boldsymbol{S}}$ to form $\hat{\boldsymbol{J}}$. The projection of $\hat{\boldsymbol{N}}$ in $\boldsymbol{z}$ is Λ.

The good quantum numbers are Λ, N, S, J. This condition applies when $A\Lambda \ll BJ$.

2.1.5 Transitions

For electric dipole transitions in molecules the selection rules are given in the table below. Derivations of these can be found in Sec. 6.11.3 of [116].

Rotational transitions	$\Delta J = 0, \pm 1,\ \Delta m_J = 0, \pm 1$
Vibrational transitions	$\Delta v = \pm 1$
	$\Delta J = 0, \pm 1,\ \Delta m_J = 0, \pm 1$
Electronic transitions	Δv - no selection rules
	$\Delta J = 0, \pm 1,\ \Delta m_J = 0, \pm 1$

Here, m_J is the magnetic quantum number, which takes $2J+1$ values, $m_J = -J, 1-J, ..., J$. The selection rule in m_J is due to the choice of laser polarisation used to drive the transition. As for all electric dipole transitions, the parity of the initial and final state must be opposite, $\Delta P = \pm 1$.

The transition strengths for vibrational state change within an electronic transition are called the Franck-Condon factors (FCFs). They are the square of the overlap integral of the two vibrational states,

$$f_{v',v} = |\langle \psi_{v'} | \psi_v \rangle|^2 \tag{2.8}$$

where $\psi_{v'}$ and ψ_v are the vibrational eigenfunctions of the upper and lower electronic states. For an excited state where the excitation of an electron has little effect on the vibrational potential, state decays $v' \to v$ where $v' = v$ will be very highly likely. It is said that this transition has a 'highly diagonal Frank-Condon matrix'. In this situation $f_{0,0} \gg f_{0,1} \gg f_{0,2} \gg ...$ which is important for laser cooling. Generally, this is not the case, and the excited state of a molecule will decay to a large number of ground vibrational states.

2.1.6 Hyperfine structure

In molecules where one of the constituent nuclei has nuclear spin, $\hat{\boldsymbol{I}}$, then the total angular momentum is labelled $\hat{\boldsymbol{F}} = \hat{\boldsymbol{J}} + \hat{\boldsymbol{I}}$, and $\hat{\boldsymbol{J}}$ is the total angular momentum excluding the nuclear spin. For each value of J quantum number F takes values $F = J+I, J+I-1, ..., |J-I|$. As usual, each quantum state F has $2F+1$ magnetic hyperfine states labelled m_F.

The selection rules for electronic electric dipole transitions for molecules with hyperfine structure are $\Delta F = 0, \pm 1$ and $\Delta m_F = 0, \pm 1$, but there is no $m'_F = 0 \to m_F = 0$ transition when $\Delta F = 0$. The change in m_F depends upon the polarisation of the electromagnetic wave.

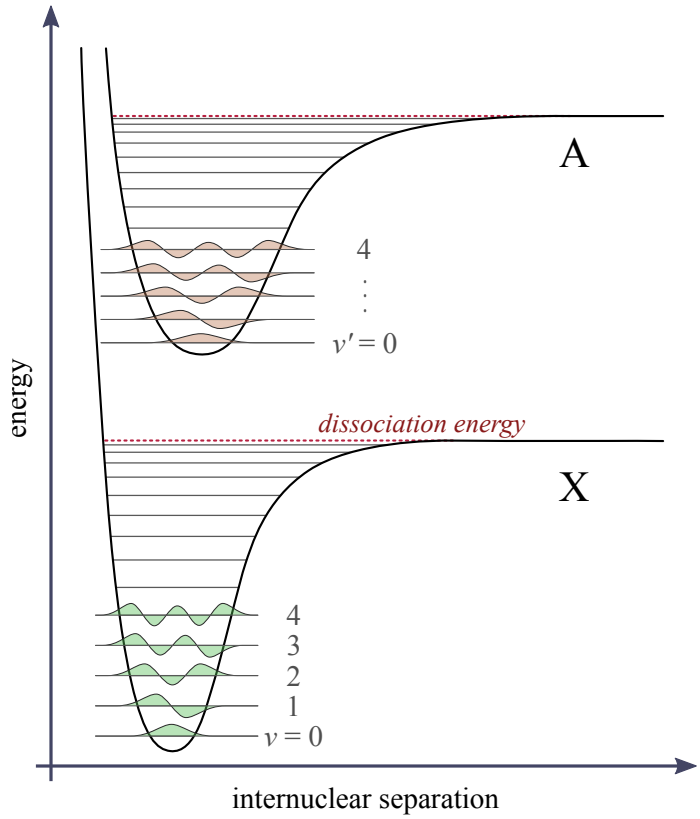

Figure 2.3: A sketch of potential energy curves for the ground and excited states of a molecule, with the first four vibrational wavefunctions. The potential is harmonic close to the bottom of the well and therefore the spacing between energy levels is equal. At higher energy the separation between eigenstates becomes smaller.

2.2 YbF details and structure

The YbF molecule consists of ytterbium which exists in nature as seven stable isotopes, and fluorine which exists as ^{19}F. In the experiments in this thesis we are most interested in YbF composed of the most abundant ^{174}Yb isotope, however our molecular source produces YbF molecules composed of all seven isotopes of Yb. The even isotopes have the helpful quality of not having nuclear spin, so, not causing additional hyperfine interaction in the molecule to that of the spin 1/2 ^{19}F, nucleus.

The Yb-F bond is very ionic; Yb($[\mathrm{Xe}]4f^{14}6s^2$) transfers a $6s$ electron to F($[\mathrm{He}]2s^22p^5$) to produce F^- and Yb^+ which have all of their atomic orbitals filled except for the unpaired $6s$ electron orbiting a Yb^{2+} core [117]. It is the unpaired $6s$ electron whose spin precession is measured in the eEDM experiment of our group [90].

YbF has a $\mathrm{X}^2\Sigma^+$ ground state which is best described by Hund's case (b). YbF's first excited state is $\mathrm{A}^2\Pi_{1/2}$ which is best described by Hund's case (a). Fig. 2.4 illustrates the rotational and fine structure of these states. In the A state for each value of J', there are two states with opposite parities, as a result of the Ω-doubling. In Fig. 2.4, the

allowed transitions are labelled using spectroscopic notation; for simplicity, I will refer to the $P_1(N)$ and $Q_{12}(N)$ lines together as $P(N)$ lines, and the $Q_1(N)$ and $R_{12}(N)$ lines as the $Q(N)$ lines, where N is the X-state quantum number.

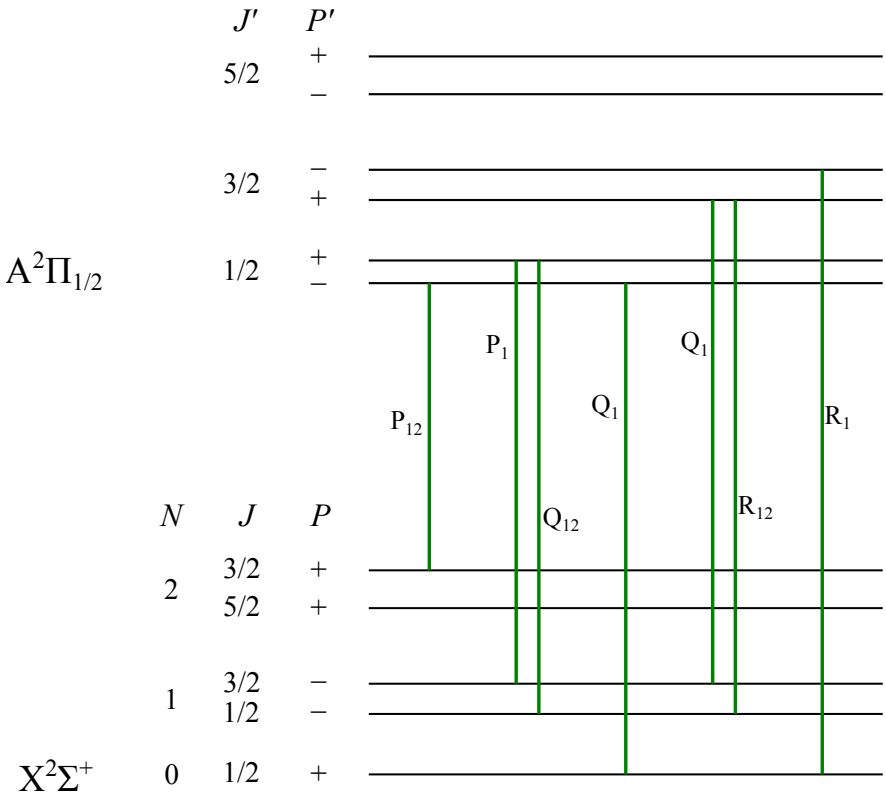

Figure 2.4: The rotational and fine structure of the $X^2\Sigma^+$ and $A^2\Pi_{1/2}$ states. The six types of allowed $X^2\Sigma^+ \rightarrow A^2\Pi_{1/2}$ transitions. In the X-state, J is only an approximately good quantum number. Transitions are labelled as in Fig. 123 of [118].

2.2.1 X state structure

Fig. 2.5 shows the substructure of the $X^2\Sigma^+$ $N = 1$ ground state levels relevant to this thesis. As the ^{19}F nucleus has nuclear spin $I = 1/2$ there is an additional hyperfine splitting. In the ground state, the size of this hyperfine interaction is comparable to spin-rotation interaction, meaning that J is not a good quantum number. The sub-levels of the $N = 1$ states are labelled with F the total angular momentum quantum number. The two states with $F = 1$ for each $N = 1$ state are labelled with a superscript $+/-$ to denote the higher/lower energy state. These $F = 1$ states are mixtures of $J = 1 \pm \frac{1}{2}$, the mixing coefficients are given in [119].

The parity, P, of X state levels depends upon N, where $P = (-1)^N$. For brevity, I will label the groups of $N = 1$ hyperfine states for each $v = 0, 1, 2...$ state as the X(0), X(1), X(2)... states in this thesis.

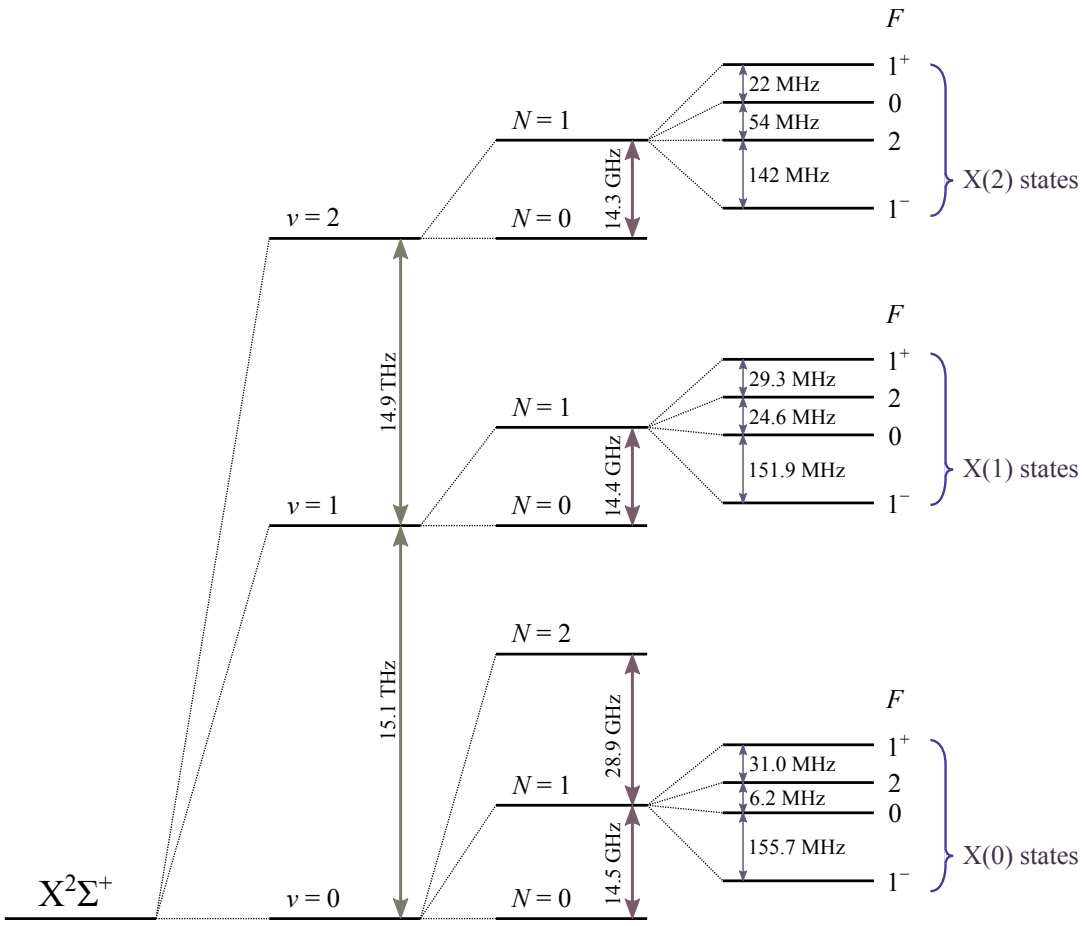

Figure 2.5: The structure of the $X^2\Sigma^+$ state of YbF. The hyperfine components of the $N = 1$ levels are shown in full as these are the relevant ground states for laser cooling. The energy separations are calculated from molecular parameters in [120, 119]. The hyperfine structure of the $(v = 2, N = 1)$ state was determined from work done in this thesis.

2.2.2 A state structure

The $A^2\Pi_{1/2}$ state has a $Yb^+([Xe]4f^{14}6p^1)F^-$ configuration. It has an energy of 542.8 THz relative to the ground state. Fig. 2.6 shows the splitting of the Ω-doublet and hyperfine splitting in the $v' = 0$ A-state. The Ω-doublet correspond to the symmetric and anti-symmetric combinations of the $\Omega' = \pm 1/2$ wavefunctions. These opposite parity combinations have different energies in YbF because they mix differently with neighbouring electronic levels [121].

The hyperfine interaction causes a smaller splitting in the A-state than in the X-state, because the outer electron is on average further from the molecule's nuclei in a p-state than in an s-state. The hyperfine components in the excited state are labelled with total angular momentum quantum number F'. The excited states used for laser cooling are the hyperfine components of the positive parity excited state to which we can drive transitions from the negative parity $N = 1$ ground state.

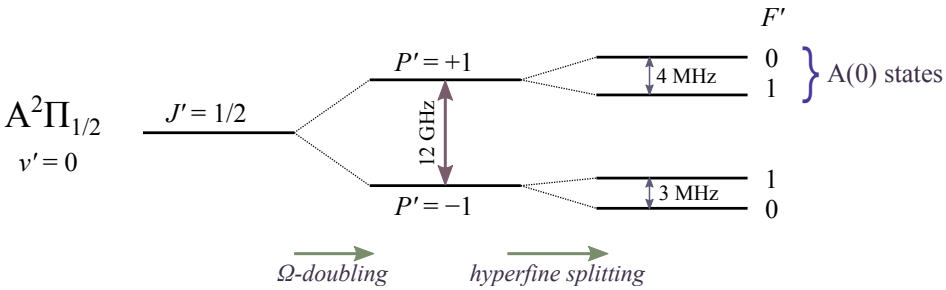

Figure 2.6: The substructure of the $A^2\Pi_{1/2}(v' = 0, J' = 1/2)$ state of YbF. Energy seperations were measured in [120, 121]

2.2.3 Hybrid structure of the excited state

The vibrational states of $A^2\Pi_{1/2}$ where $v' > 0$ are strongly perturbed by a second state found by Dunfield *et al.* which they called [18.6]0.5. It was given this name as it has a separation of $18,600\ \text{cm}^{-1}$ from the ground state, and because $\Omega = 0.5$ for this state [120]. In this and further work by Sauer *et al.* [121], it was found that the $A^2\Pi_{1/2}(v' = 1)$ state is strongly mixed with the $[18.6]0.5(v' = 0)$ state and $A^2\Pi_{1/2}(v' = 2)$ is strongly mixed with $[18.6]0.5(v' = 1)$ forming pairs of hybrid states. The character of the [18.6]0.5 state is not known, however it is expected to have electronic configuration derived from the atomic configuration $[Xe]4f^{13}6s^2$. The relevant hybrid levels in this thesis are the ones resulting from the mixing of the $A^2\Pi_{1/2}(v' = 1)$ and $[18.6]0.5(v' = 0)$. These states will be labelled [557] and [561], where the numbers in brackets are the energy separation of the states in THz relative to $X^2\Sigma^+(v = 0)$. I will label the $J' = 1/2, P' = +1$ states of the [557] and [561] state A(1) and A(2) respectively.

2.3 Laser cooling YbF

To laser cool a molecular species, we would like to exert a large radiation pressure on the molecules so that they are slowed in a short length of time. Driving vibrational or rotational transitions would not be very useful, since radiation pressure relies on spontaneous emission, and the lifetime of vibrational and rotational states is long. Additionally, the momentum change supplied by a rotational or vibrational state changing photon is small. Instead, we would like to drive an electronic transition to a state with a short excited state lifetime.

Ideally, this excited state would decay only to the same ground state from which the molecule was excited such that the molecule could continue scattering photons of only a single laser frequency. However, due to the lack of vibrational selection rules in electronic transitions, this will not be possible. After only a few photon scatters, molecules will be pumped into a large number of ground vibrational levels. In 2004, Di Rosa pointed out that there were a group of molecules that have A-X transitions with highly diagonal Franck-Condon matrices, which could be suitable for laser cooling [122]. YbF is one such molecule, and this section details the laser transitions we use to drive a cycling transition YbF. We would like to minimise the number of laser frequencies required such that the experiment does not become too costly and complicated, but maximise the photon scattering rate, and number of molecules that remain in 'bright' states - i.e. a state which is coupled to one of the lasers.

In the article in which Di Rosa suggested that certain molecules could be laser cooled, he gave three helpful criteria for choosing a molecular species and transition for laser cooling, these are:

1. There should be a large oscillator strength between ground and excited states to ensure high photon scattering rates.
2. The transition should have a highly diagonal Franck-Condon matrix.
3. There should be no intervening electronic states to which the upper state can radiate.

2.3.1 Choosing an electronic transition

The electronic transition we use to laser cool YbF is the $X^2\Sigma^+ \rightarrow A^2\Pi_{1/2}$ transition, which has a natural width of 5.7 MHz. For YbF, $A^2\Pi_{1/2}$ is the first excited state with the same multiplicity as the ground state. There are intermediate electronic states which correspond to the excitation of a $4f$ electron [123], however decays from the A-state to these should be very unlikely.

It is possible to use transitions to higher excited states for laser cooling as is done in this group using the CaF molecule [42]. In this experiment, the $X^2\Sigma^+ \rightarrow B^2\Sigma^+$ transition

is used because $B^2\Sigma^+ \rightarrow X^2\Sigma^+$ has more favourable FCFs than $A^2\Pi_{1/2} \rightarrow X^2\Sigma^+$ in CaF, and the branching from $B^2\Sigma^+$ to $A^2\Pi_{1/2}$ is very small. This is important because decays to the ground state via an intermediate state increase rotational branching.

YbF has an $A^2\Pi_{3/2}$ state with an energy of 584 THz relative to the X state, and a $B^2\Sigma^+$ state with an energy of 632 THz [124]. It is not possible to drive a rotationally closed transition to the $A^2\Pi_{3/2}$ state as its lowest angular momentum state has $J' = 3/2$. The FCFs for the $B^2\Sigma^+$ state are not known, nor are those for the higher lying electronic states of YbF which have been found [125]. It would be interesting to determine whether any of these high-lying states offers some advantages for laser cooling over $A^2\Pi_{1/2}$.

2.3.2 Addressing vibrational structure

YbF has relatively good FCFs for laser cooling, where decays from the $A^2\Pi_{1/2}(J' = 1/2, v' = 0)$ state return population to $X^2\Sigma^+(N = 1, v = 0)$ with a probability of $f_{0,0} = 93.3\,\%$ [126]. The average number of photons that a molecule will scatter before being pumped into a higher vibrational state is given by the geometric series

$$\gamma = 1 + p + p^2 + p^3 + ... = \frac{1}{1-p}, \tag{2.9}$$

where p is the probability of decay to a state that is bright. To find the average number of photon scatters on the A-X transition, $p = f_{0,0}$, so $\gamma = 15$. The recoil velocity for a photon scattered on this transition is 3.7 mm s^{-1}, so, to slow molecules by 10 m s^{-1} they must scatter at least 3,000 photons with a low probability of being pumped to a vibrational dark state. To scatter this number of photons, the probability of decay to a dark vibrational state must be $< 0.03\%$. We can achieve this by repumping the first four vibrational states, because the decay probability to all higher lying vibrational states than $v = 3$ should be smaller than the FCF for $f_{0,3} = 0.03\%$.

The laser cooling scheme we use to do this is shown in Fig. 2.7. The FCFs for the transitions are given in Tab. 2.1. So far, we have built and bought the laser systems required to drive transitions from X(0), X(1) and X(2) but have not set up a laser to address the X(3) state.

	$v=0$	$v=1$	$v=2$	$v=3$	$v=4$
$v'=0$	93.3(3)	6.6(3)	0.30(5)	0.03	-
[557]	13.2(5)	70.7(6)	13.9(2)	1.9(2)	<0.2
[561]	2.8(3)	89(1)	7.8(2)	<0.2	-
[574]	<1	8.1(6)	75(2)	15(2)	1.9(8)
[578]	<1	13.3(6)	82.5(7)	4.1(6)	<1

Table 2.1: The FCFs for decays from electronically excited states to the $X^2\Sigma^+(v)$ states. Decays from $A^2\Pi_{1/2}(v'=0)$ were measured in [126], decays from [557], [561], [574] and [578] were measured in [127].

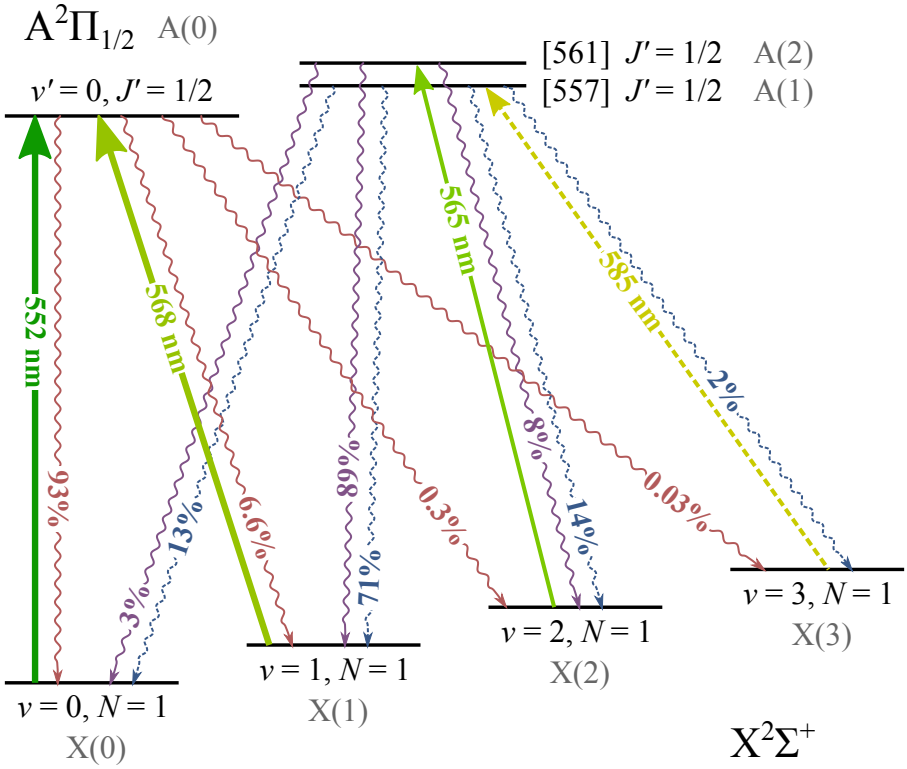

Figure 2.7: The laser cooling scheme we use for YbF. The wavelengths of the required lasers are given in nanometres and FCFs are given as percentages. Currently we do not use the 585 nm transition. The laser power requirements for the A(0)-X(0) and A(0)-X(1) transitions are greater than for the A(2)-X(2) and A(1)-X(3) transitions as discussed in section 2.5.2.

2.3.3 Driving a closed rotational transition

Next, we consider the rotational states; we would like to drive a transition between a single ground and excited state only, such that additional lasers are not required to repump additional ground states. Considering only the selection rule $\Delta J = 0, \pm 1$ it seems as though multiple rotational ground states will be populated from spontaneous emission from the excited state. However, it was pointed out by Stuhl *et al.* that rotational branching can be avoided by driving transitions where $R = 1 \rightarrow R' = 0$ [31].

We can laser cool on an $R = 1 \rightarrow R' = 0$ transition in YbF by exciting, from the odd parity $X^2\Sigma^+(N = 1)$ state to the even parity $A^2\Pi_{1/2}(J' = 1/2)$ state, by driving the P(1) transitions. There should not be decays to other rotational states due to the selection rules $\Delta F = 0, \pm 1$ and $\Delta P = \pm 1$. Decays to $X^2\Sigma^+(N = 3, F = 2)$ are not forbidden, but because J is an 'approximately good quantum number' for $X^2\Sigma^+$ states, these decays should be very highly suppressed since $J = 5/2$ for this state.

2.3.4 Addressing hyperfine structure

The separation between the ground hyperfine states, Fig. 2.5, is large compared to the 5.7 MHz linewidth of the transition, however, the separation between the $F' = 0$ and $F' = 1$ excited state components is unresolved. Exciting on a transition from only one of the hyperfine ground states would optically pump molecules into the other hyperfine states until optical cycling ceased. To continuously cycle photons, additional laser frequency components, which we call RF-sidebands, may be used to excite all four hyperfine levels simultaneously, as illustrated in Fig. 2.8.

2.3.5 Destabilising dark states

Driving an $R = 1 \rightarrow R' = 0$ transition means that there will be a larger number of angular momentum eigenstates in the ground state than in the excited state, some of which will not be able to couple to the polarisation of the laser, and will be stationary dark states. There may also be coherent dark states where the dark state is a coherent superposition of angular momentum eigenstates. These dark states may be stationary or non-stationary. Molecules will be optically pumped into these stationary dark states, and cease to scatter photons. This can be solved by destabilising the dark states using a magnetic field or by modulating the polarisation of the laser [128]. More complicated schemes are also possible, such as the use of microwaves to drive transitions between adjacent rotational states as explained in [129].

As shown in Fig. 2.8, for linear polarised excitation there are two $m_F = \pm 2$ magnetic sub-levels that do not couple to the excited state. We use a static magnetic field, B,

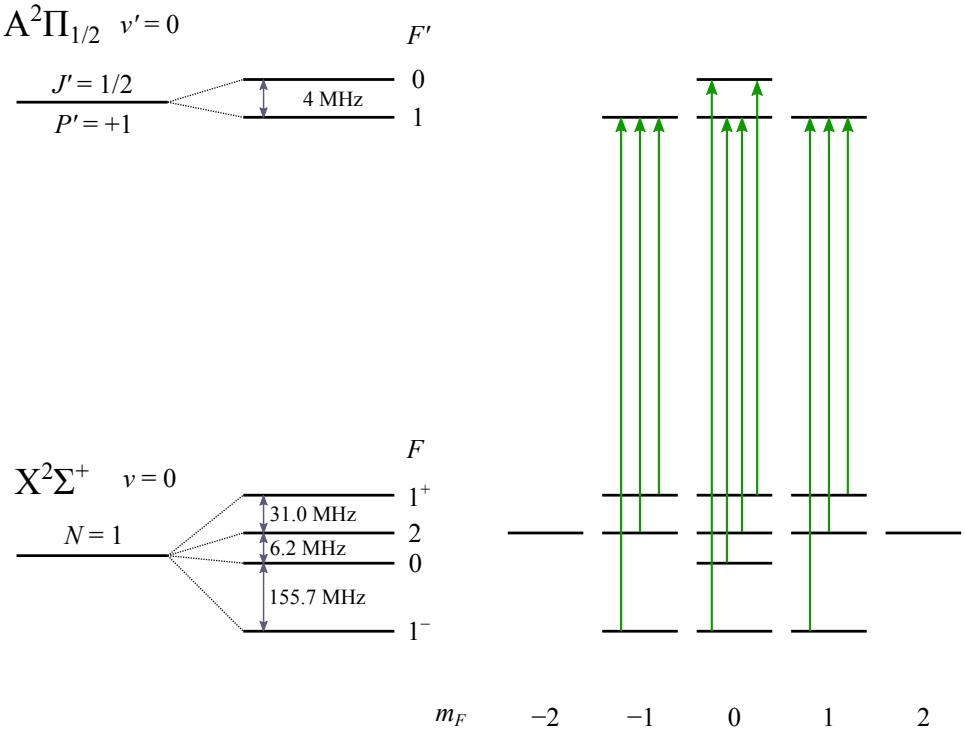

Figure 2.8: A(0)-X(0) transitions between the m_F states for π-polarised light.

of a few Gauss at an angle to the laser polarisation of $\sim 45\,^\circ$, as demonstrated in [130]. The applied field mixes the m_F states at the rate of the Larmor precession frequency, $\omega_B = g\mu_B B/\hbar$, where g is the Landé-g factor of the state, and μ_B is the Bohr magneton. I will call the use of a magnetic field to destabilise the dark states, 'remixing'. The rate of remixing should be similar to the scattering rate such that accumulation of population in dark states is not rate limiting. Typical scattering rates in the experiment are of the order $2\pi \times 1$ MHz. A magnetic field that is too large will Zeeman-shift m_F states out of resonance with the laser. I will call this effect 'magnetic field broadening'.

2.4 Multilevel rate equation model for the scattering rate

The most accurate way in which we could model laser cooling would be to solve the optical Bloch equations (OBEs) for the multilevel system interacting with the laser frequencies and magnetic field for dark state remixing. For our system there would be 28 levels as the simultaneous A(0)-X(0) and A(0)-X(1) transitions would need to be modelled. There are 12 m_F eigenstates per X-state and four in A(0), I will therefore call this laser cooling scheme a $12 + 12 + 4$ level system. The other transitions may be modelled separately without much loss of accuracy as they are not strongly coupled.

The OBEs may be solved numerically for some given set of parameters as has been done by the DeMille group for their $12 + 12 + 4$ level system for laser cooling SrF [129].

However, using these solutions it is difficult to arrive at an optimum set of parameters because of the high computational cost of the calculation.

To give us some physical insight into the system we can treat the problem using a multi-level rate equation (MLRE) model. In a rate equation model, coherent effects are not considered and magnetic remixing cannot be modelled accurately, however the results should not be so dissimilar from reality. Here, we find steady state solutions to rate equations for the system to make some simple predictions. For simplicity, the effects of finite laser linewidths, excitation by off resonance laser frequencies, and magnetic field broadening are neglected.

2.4.1 Single excited state

As in [72], for a molecule with a single excited state, s_e, coupled to N_g ground states, $s_{\mathrm{g},j}$, by laser light, we can write the occupation probabilities of the ground states, $n_{\mathrm{g},j}$, and excited state, n_e, as a set of coupled rate equations,

$$\frac{\mathrm{d}n_{\mathrm{g},j}}{\mathrm{d}t} = A_j n_\mathrm{e} - R_j(n_{\mathrm{g},j} - n_\mathrm{e}), \tag{2.10a}$$

$$\frac{\mathrm{d}n_\mathrm{e}}{\mathrm{d}t} = -\Gamma n_\mathrm{e} + \sum_{j=1}^{N_\mathrm{g}} R_j(n_{\mathrm{g},j} - n_\mathrm{e}), \tag{2.10b}$$

where A_j is the partial spontaneous decay rate for $s_\mathrm{e} \to s_{\mathrm{g},j}$, and R_j are the excitation rates for that transition. $\Gamma = \sum_{j=1}^{N_\mathrm{g}} A_j$, the total spontaneous emission rate for s_e. Solving the ground state equations in the steady state, where $\partial n_{\mathrm{g},j}/\partial t = 0$, with normalisation condition

$$n_\mathrm{e} + \sum_{j=1}^{N_\mathrm{g}} n_{\mathrm{g},j} = 1, \tag{2.10c}$$

gives an excitation probability,

$$n_\mathrm{e} = \frac{1}{(N_\mathrm{g}+1) + \sum_{j=1}^{N_\mathrm{g}} A_j/R_j}. \tag{2.11}$$

A_j/R_j may be written as $2I_{\mathrm{sat},j}/I_j$, where I_j is the intensity of light resonant with the $g_j \to e$ transition of wavelength λ_j, and $I_{\mathrm{sat},j} = \pi hc\Gamma/(3\lambda_j^3)$ is the saturation intensity for that transition,

$$n_\mathrm{e} = \frac{1}{(N_\mathrm{g}+1) + 2\sum_{j=1}^{N_\mathrm{g}} I_{\mathrm{sat},j}/I_j}. \tag{2.12}$$

To maximise the scattering rate $R_\gamma = \Gamma n_\mathrm{e}$, we should make n_e as large as possible. Increasing n_e can be achieved by increasing I_j for any transition. Since the wavelengths used for our laser cooling do not vary significantly across vibrational states, we can approximate

$I_{\mathrm{sat},j}$ as a constant, I_{sat}, which can be brought outside the sum,

$$n_{\mathrm{e}} \simeq \frac{1}{(N_{\mathrm{g}}+1) + 2I_{\mathrm{sat}} \sum_{j=1}^{N_{\mathrm{g}}} 1/I_j}. \tag{2.13}$$

As can be seen from equation (2.12), an increase in laser intensity on any one transition, I_j, has approximately the same effect on increasing n_{e}, regardless of the transition strength. At first sight, it is perhaps surprising that this is the case since far fewer photons are scattered via weaker transitions. However, since both the rate of pumping and spontaneous decay are proportional to the same branching ratio, an increase of $I_j/I_{\mathrm{sat},j}$ on any transition yields the same depletion of ground state $s_{\mathrm{g},j}$, and therefore increase in n_{e}.

If we have a fixed total laser intensity this is best divided up equally across all transitions to maximise n_{e}, since this makes the sum, $\sum_{j=1}^{N_g} 1/I_j$, smallest. Therefore, in an experiment, we should choose for the laser power addressing all molecular transitions to be similar (but not reduce laser power where extra is available). If we choose all I_j to equal intensity I, we are left with the simple equation,

$$n_{\mathrm{e}} \simeq \frac{1}{(N_{\mathrm{g}}+1) + 2N_{\mathrm{g}} I_{\mathrm{sat}}/I}. \tag{2.14}$$

2.4.2 Multiple excited states

In the more complicated case, where there are a number of excited states, N_{e}, and ground states, N_{g}, we can write a set of rate equations for the total population of the ground and excited states, as done in [96]. Here, we assume that the populations of all ground states, n_{g} are always equal to one another, as are the populations of the excited states, n_{e}. Where each ground state is coupled to all excited states, the rate equations for the total ground and excited state populations (and normalisation condition) are,

$$N_{\mathrm{g}}\dot{n}_{\mathrm{g}} = \Gamma N_{\mathrm{e}} n_{\mathrm{e}} - R_a N_{\mathrm{e}} N_{\mathrm{g}} (n_{\mathrm{g}} - n_{\mathrm{e}}), \tag{2.15a}$$

$$N_{\mathrm{e}}\dot{n}_{\mathrm{e}} = -\Gamma N_{\mathrm{e}} n_{\mathrm{e}} + R_a N_{\mathrm{e}} N_{\mathrm{g}} (n_{\mathrm{g}} - n_{\mathrm{e}}), \tag{2.15b}$$

$$1 = N_{\mathrm{e}} n_{\mathrm{e}} + N_{\mathrm{g}} n_{\mathrm{g}}, \tag{2.15c}$$

where R_a is the average excitation rate for all the transitions. $R_a N_{\mathrm{e}} N_{\mathrm{g}}$ is the total excitation rate from the ground to excited state because there are $N_{\mathrm{e}} N_{\mathrm{g}}$ possible transitions between them. Solving for the total steady-state excited state population, we obtain,

$$N_{\mathrm{e}} n_{\mathrm{e}} = \frac{N_{\mathrm{e}}}{N_{\mathrm{tot}} + N_{\mathrm{g}} A_a / R_a}, \tag{2.16}$$

where $N_{\mathrm{tot}} = N_{\mathrm{e}} + N_{\mathrm{g}}$, and $A_a = \Gamma/N_{\mathrm{g}}$ is the average partial spontaneous decay rate on each transition. We can substitute $A_a/R_a = 2I_{\mathrm{sat}}/I$ as in the case with the single excited state, to get,

$$N_{\mathrm{e}} n_{\mathrm{e}} = \frac{N_{\mathrm{e}}}{N_{\mathrm{tot}} + 2N_{\mathrm{g}} I_{\mathrm{sat}}/I}. \tag{2.17}$$

Eq. (2.17) assumes that all ground states are coupled to all excited states by laser transitions, however, in real atomic and molecular systems, some transitions are forbidden by angular momentum selection rules, and transitions are often driven with a single polarisation of light. The allowed transitions between the pairs of ground and excited states for excitation by π-polarised light and spontaneous decay are shown in Fig. 2.9. For any pair of hyperfine states, there are three times the number of routes for spontaneous decay between them as there are for stimulated processes due to a single laser polarisation. We can therefore re-write Eqs. (2.15a, 2.15b) as;

$$N_{\mathrm{g}} \dot{n}_{\mathrm{g}} = \Gamma N_{\mathrm{e}} n_{\mathrm{e}} - R_a \tfrac{N_{\mathrm{e}} N_{\mathrm{g}}}{3} (n_{\mathrm{g}} - n_{\mathrm{e}}), \tag{2.18a}$$

$$N_{\mathrm{e}} \dot{n}_{\mathrm{e}} = -\Gamma N_{\mathrm{e}} n_{\mathrm{e}} + R_a \tfrac{N_{\mathrm{e}} N_{\mathrm{g}}}{3} (n_{\mathrm{g}} - n_{\mathrm{e}}), \tag{2.18b}$$

where the number of possible excitation routes is $N_{\mathrm{e}} N_{\mathrm{g}}/3$ rather than $N_{\mathrm{e}} N_{\mathrm{g}}$. With this reduced net pumping rate Eq. (2.17) becomes

$$N_{\mathrm{e}} n_{\mathrm{e}} = \frac{N_{\mathrm{e}}}{N_{\mathrm{tot}} + 6N_{\mathrm{g}} I_{\mathrm{sat}}/I}. \tag{2.19}$$

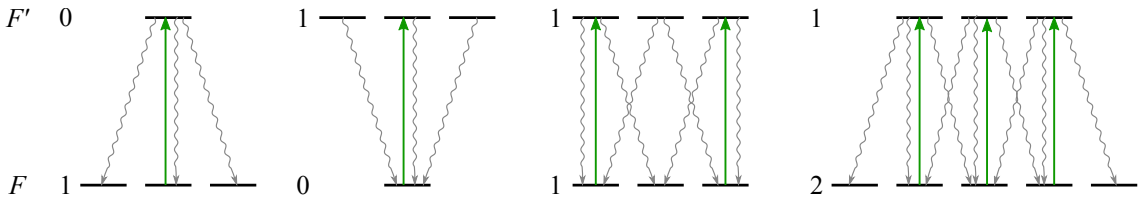

Figure 2.9: Transitions between (F, m_F) states relevant for YbF laser cooling, showing excitation with π-polarised light and spontaneous decay. There are three times more routes down than up. For σ^+- and σ^--polarised light there is the same ratio (and number of stationary dark states). The sum of the branching ratios to all ground states is the same for each excited state, due to the isotropy of space.

From Eq. (2.19), we find that in the limiting case when I is high, the population is distributed equally over all levels, and $N_{\mathrm{e}} n_{\mathrm{e}}$ tends to $N_{\mathrm{e}}/N_{\mathrm{tot}}$.

2.4.3 Multiple excited states and mixed dark states

In the case where there is a number, N_d, of ground state that are dark, which are mixed[1] with a number, N_m, of bright ground states, and there are also a number, N_g, ground states that are not mixed with these dark states, we can write the set of rate equations,

$$N_\mathrm{g}\dot{n}_\mathrm{g} = A_a N_\mathrm{g} N_\mathrm{e} n_\mathrm{e} - R_a \tfrac{N_\mathrm{e}N_\mathrm{g}}{3}(n_\mathrm{g} - n_\mathrm{e}), \tag{2.20a}$$

$$N_\mathrm{m}\dot{n}_\mathrm{m} = A_a N_\mathrm{m} N_\mathrm{e} n_\mathrm{e} - R_a \tfrac{N_\mathrm{e}N_\mathrm{m}}{3}(n_\mathrm{m} - n_\mathrm{e}) + M N_\mathrm{d} N_\mathrm{m}(n_\mathrm{d} - n_\mathrm{m}), \tag{2.20b}$$

$$N_\mathrm{d}\dot{n}_\mathrm{d} = A_a N_\mathrm{d} N_\mathrm{e} n_\mathrm{e} - M N_\mathrm{d} N_\mathrm{m}(n_\mathrm{d} - n_\mathrm{m}), \tag{2.20c}$$

$$N_\mathrm{e}\dot{n}_\mathrm{e} = -\Gamma N_\mathrm{e} n_\mathrm{e} + R_a \tfrac{N_\mathrm{e}N_\mathrm{g}}{3}(n_\mathrm{g} - n_\mathrm{e}) + R_a \tfrac{N_\mathrm{e}N_\mathrm{m}}{3}(n_\mathrm{m} - n_\mathrm{e}), \tag{2.20d}$$

$$1 = N_\mathrm{e} n_\mathrm{e} + N_\mathrm{g} n_\mathrm{g} + N_\mathrm{m} n_\mathrm{m} + N_\mathrm{d} n_\mathrm{d}. \tag{2.20e}$$

Here, $n_{\mathrm{g,m,d,e}}$ are the populations of each type of state. M is the rate of mixing between pairs of bright mixed states and dark mixed states, and we are assuming that all pairs of N_d and N_m states are mixed. In this case $\Gamma = A_a(N_\mathrm{g} + N_\mathrm{m} + N_\mathrm{d})$, and we are making the assumption that the total rate of spontaneous emission into all three types of ground states is equal (which will not necessarily be the case). Solving these equations for the total excited state population in the steady state, with the substitution $A_a/R_a = 2I_\mathrm{sat}/I$, we obtain,

$$N_\mathrm{e} n_\mathrm{e} = \frac{N_\mathrm{e}}{N_\mathrm{tot} + 6N_\text{g-eff} I_\mathrm{sat}/I}. \tag{2.21a}$$

where $N_\text{g-eff}$ is an effective number of ground states. In the case of fast mixing, $M \to \infty$,

$$N_\text{g-eff} = N_\mathrm{g} + \frac{(N_\mathrm{d} + N_\mathrm{m})^2}{N_\mathrm{m}}. \tag{2.21b}$$

and when the mixing rate equals the pumping rate, $M = R_a$,

$$N_\text{g-eff} = N_\mathrm{g} + \frac{(N_\mathrm{d} + N_\mathrm{m})^2 + \frac{1}{3}N_\mathrm{e}N_\mathrm{d}}{N_\mathrm{m}}. \tag{2.21c}$$

For high laser intensities and large rates of mixing, population is again distributed equally over all states.

2.4.4 Repumping

The repump transitions do not share the same excited state as the main cooling cycle, CC, transitions. I will use CC as a label for the A(0), X(0) and X(1) states together. The rate of decay into any higher lying vibrational state is small compared to decay to ground states of CC. The transitions may therefore be modelled separately. The system that is

[1] For example, by a magnetic field.

modelled is illustrated in Fig. 2.10.

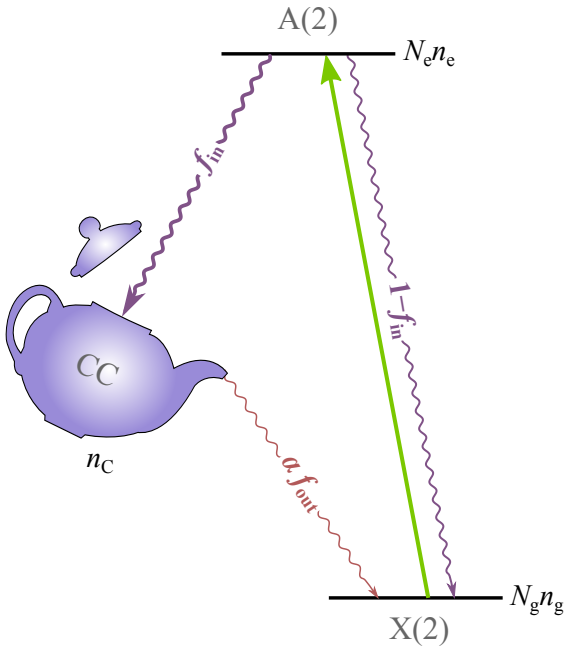

Figure 2.10: A schematic of the model for A(2)-X(2) repumping. The states of the cooling cycle are represented by the teapot.

The dark states in the repump transition are not considered. In this case, the labels $N_{e,g}$ and $n_{e,g}$ represent the number of states and population per state for the excited and ground states involved in the repump transition, and not those of CC. A single extra state is introduced, which represents all of the CC states which has population n_C. The probability of decay from the excited state of the repump transition, A(2), being into any of the ground states of the cooling cycle is f_{in}. We assume that decays to higher vibrational ground states are very small, and the probability of decay from A(2) to X(2), is $1 - f_{in}$. The rate of decay out of the cooling cycle into X(2) is $f_{out}\alpha\Gamma$, where f_{out} is the FCF for the transition A(0)-X(2), and α is the fraction of molecules in CC that are in an excited state.

The probability of decay to any ground state is equal, for both decays from CC and A(2). The spontaneous decay rates of A(0) and A(2) should be very similar, so we set both to Γ. This gives the following set of rate equations and normalisation condition,

$$N_g \dot{n}_g = A_a N_g N_e n_e + \alpha A_a \frac{f_{out}}{1-f_{in}} N_g n_C - R_a \frac{N_e N_g}{3}(n_g - n_e), \tag{2.22a}$$

$$N_e \dot{n}_e = -\Gamma N_e n_e + R_a \frac{N_e N_g}{3}(n_g - n_e), \tag{2.22b}$$

$$\dot{n}_C = -\alpha\Gamma f_{out} n_C + \Gamma f_{in} N_e n_e, \tag{2.22c}$$

$$1 = n_C + N_e n_e + N_g n_g. \tag{2.22d}$$

Here, $A_a = \Gamma(1 - f_{in})/N_g$ is the rate of spontaneous decay from a sublevel of A(2) to a

sublevel of X(2). The steady state solution for the number of molecules in CC is,

$$n_{\mathrm{C}} = \frac{1}{1 + \frac{\alpha}{N_{\mathrm{e}}} \frac{f_{\mathrm{out}}}{f_{\mathrm{in}}} \left(\frac{6N_{\mathrm{g}}}{1-f_{\mathrm{in}}} I_{\mathrm{sat}}/I + N_{\mathrm{tot}} \right)}, \tag{2.23}$$

where I is the intensity of light resonant with each repump transition, and I_{sat} is for the wavelength of the repump light.

2.4.5 Effect of the complicated structure on the scattering rate

Using the steady state solutions to the MLREs derived above, we can make some guesses about the effect of the complicated level structure on the scattering rate, R_γ, in a real experiment to laser cool molecules.

For the main cooling cycle

For the main cooling cycle, we consider here only those transitions that are driven to the same set of excited states. These are the simultaneous A(0)-X(0) and A(0)-X(1) transitions shown in Fig. 2.7, which I will call A(0)-X(0,1).

We see from Eq. (2.13) that to maximise the scattering rate, we should divide up laser power evenly into the frequency components required for addressing transitions of similar wavelength, regardless of the transition strength. This was calculated for the situation where all ground states are coupled to a single excited state, however this should be our first guess at the optimum laser power distribution.

The scattering rate for a two level system is given by

$$R_\gamma = \frac{\Gamma}{2} \frac{I/I_{\mathrm{sat}}}{1 + I/I_{\mathrm{sat}} + 4(\delta/\Gamma)^2}, \tag{2.24}$$

where δ is the detuning from resonance. In the same form, we can write a scattering rate for the multilevel system on resonance by rearranging Eq. (2.21a) and multiplying by Γ,

$$R_\gamma = \frac{\Gamma}{N_{\mathrm{tot}}/N_{\mathrm{e}}} \frac{\frac{N_{\mathrm{tot}}}{6N_{\text{g-eff}}} I/I_{\mathrm{sat}}}{1 + \frac{N_{\mathrm{tot}}}{6N_{\text{g-eff}}} I/I_{\mathrm{sat}}}. \tag{2.25}$$

where we can consider $s_{\mathrm{eff}} = \frac{N_{\mathrm{tot}}}{6N_{\text{g-eff}}} I/I_{\mathrm{sat}}$ to be the effective saturation parameter for the system.

From Eq. (2.25) we can see that $R_\gamma \propto N_{\mathrm{e}}/N_{\mathrm{tot}}$, and in the high intensity limit, $R_\gamma^{\max} = \Gamma N_{\mathrm{e}}/N_{\mathrm{tot}}$. To maximise R_γ therefore, we should maximise the ratio between the number of excited and ground states. This means, when designing a laser cooling scheme for molecules it is better to avoid using the same excited state for repumping multiple ground states. Fig. 2.11 shows two possible schemes for laser cooling of YbF. In scheme 1, only

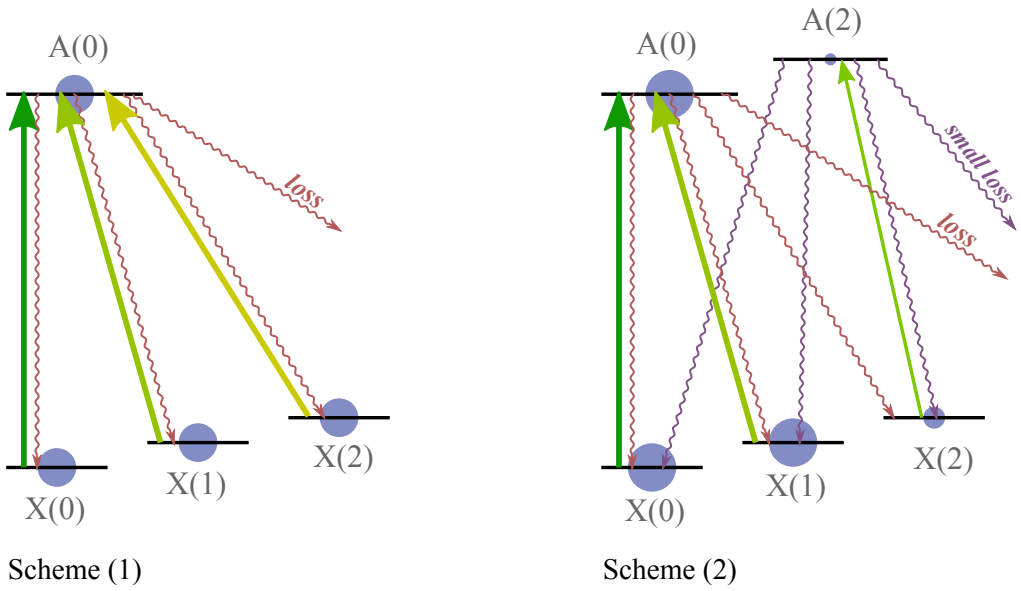

Figure 2.11: A comparison of two laser schemes for laser cooling YbF with strong pumping. The circles represent the population (number of molecules) per m_F sub-level in each state. In scheme (1) in the steady state, the population is distributed evenly over sub-levels in all four states, X(0,1,2) and A(0). In Scheme (2), population is distributed equally over sub-levels in states X(0,1) and A(0), but there are only a small number of molecules in X(2) and an even smaller number in A(2). This is because there is no laser driving stimulated emission on the A(0)-X(2) transition, so this level is populated only due to spontaneous emission.

the A(0) state is used and $N_e/N_{tot} = 4/40$. Scheme 2 makes use of the hybrid state [561], labelled here as A(2). In this scheme, $N_e/N_{tot} = 4/28$, and so the scattering rate should be 40% higher.

It is possible to think up more complicated schemes where transitions address the second (or higher) electronically excited states in order to increase the ratio N_e/N_{tot}. Two such schemes are shown in Fig. 2.12. These schemes rely on all electronic transitions having diagonal FC matrices, and the probability of spontaneous decay to intermediate excited states being very small. At present, not enough is known about the branching ratios from the B and C states of YbF to evaluate whether these alternative schemes are worth exploring.

Under the MLRE assumptions, the effect of the dark states is to increase the intensity required to pump with the same saturation by the ratio $N_{g\text{-eff}}/N_g$. For our system, X(0)-A(0)-X(1), we have $N_e = 4$, $N_d = 4$ as there are two dark $F = 2$ sub levels per ground state, $N_m = 6$ as there are three $F = 2$ levels per X-state that are mixed with the dark states, leaving $N_g = 14$. In the limit of fast remixing, the required intensity increase is $\sim 30\%$.

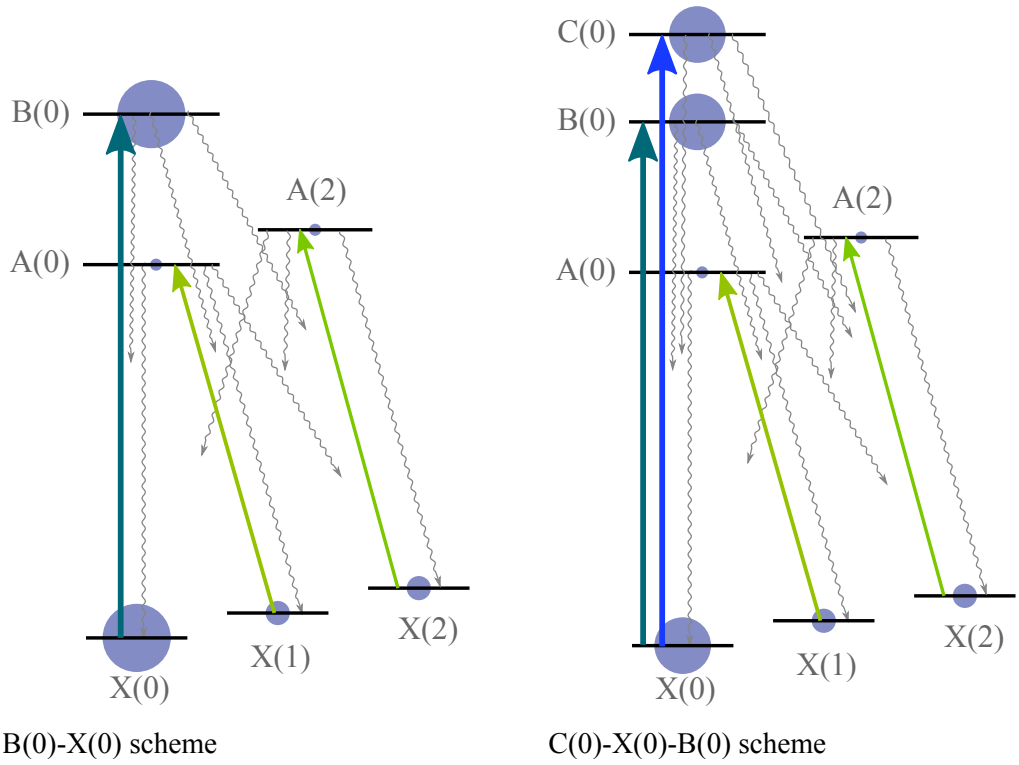

Figure 2.12: Schemes for laser cooling which improve the ratio N_e/N_{tot} compared to scheme (2) in Fig. 2.11. The blue circles represent the population per m_F sub level of each state. The B(0)-X(0) type scheme has been used to laser cool CaF [42]. If these schemes were suitable for optical cycling in YbF, one would obtain $R_\gamma \propto \Gamma/4$ for the B(0)-X(0) scheme, and $R_\gamma \propto 2\Gamma/5$ for the C(0)-X(0)-B(0) scheme (under the rate equation assumptions). In the C(0)-X(0)-B(0) scheme, the C(0)-X(0) and B(0)-X(0) transitions could be driven using orthogonal laser polarisations to eliminate stationary dark states.

For the repump transitions

Because the repump transitions are coupled to excited states that are different from the cooling cycle excited state, the power requirements for these transitions can be made much smaller than those of the cooling cycle by choosing a repump transition where, $f_{\text{in}} \gg f_{\text{out}}$. For the maximum possible scattering rate in the YbF cooling cycle, the rate of decay into the X(2) state is , $f_{\text{out}}\alpha\Gamma = f_{0,2}\frac{1}{7}\Gamma$. $\alpha = \frac{1}{7}$ because that is the maximum possible occupation fraction in A(0). In the limit of strong repumping, Eq. (2.23) becomes,

$$n_{\text{C}} = \frac{1}{1 + \alpha\frac{f_{\text{out}}}{f_{\text{in}}}\frac{N_{\text{tot-r}}}{N_{\text{e-r}}}}, \tag{2.26}$$

where I have re-labelled N_{tot} to $N_{\text{tot-r}}$, and N_{e} to $N_{\text{e-r}}$ to show that these are the numbers of states involved in the repump transition only. Eq. (2.26) indicates that even at very high saturation, not all of the population ends up in the cooling cycle. However, because $f_{\text{out}}/f_{\text{in}}$ should be very small, $n_{\text{C}} \approx 1$.

The effect of slow repumping will be to slow down the total scattering rate. The scattering rate on the repump transition will be negligible compared to that of the cooling cycle. We can therefore, approximate the total scattering rate including one repump by taking the product $\Gamma N_{\text{e}} n_{\text{e}} n_{\text{C}}$, where $N_{\text{e}} n_{\text{e}}$ is the excited state fraction given by Eq. (2.21a) and n_{C} is the fraction in the cooling cycle given by Eq. (2.23).

2.4.6 Estimate of the laser cooling force

The frequency dependence of the scattering rate is given by the extension of Eq. (2.25) to the case of non-zero detuning,

$$R_\gamma = \frac{\Gamma}{N_{\text{tot}}/N_{\text{e}}}\,\frac{s_{\text{eff}}}{1 + s_{\text{eff}} + 4(\delta/\Gamma)^2}, \tag{2.27}$$

where each laser component is detuned by the same amount, δ. The force experienced by a molecule travelling with velocity, v, along the laser propagation axis is then,

$$F_\pm = \pm\frac{\hbar k\Gamma}{N_{\text{tot}}/N_{\text{e}}}\,\frac{s_{\text{eff}}}{1 + s_{\text{eff}} + 4(\delta \mp vk)^2/\Gamma^2}, \tag{2.28}$$

where $k = 2\pi/\lambda$. F_+ (F_-) corresponds to a laser beam propagating in the positive (negative) direction along the axis. As in the low-intensity theory for optical molasses in one dimension (1D) [7], we can sum the $F_\pm$ force components to find the optical molasses force on molecules. The acceleration on a YbF molecule as a result of this force is plotted

in Fig. 2.13. For small v, the optical molasses force is $F_{\mathrm{M}} = -\beta v$, where

$$\beta = \frac{2}{N_{\mathrm{tot}}/N_{\mathrm{e}}} \frac{8\hbar k^2 \delta s_{\mathrm{eff}}}{\Gamma(1 + s_{\mathrm{eff}} + 4(\delta/\Gamma)^2)^2}. \tag{2.29}$$

The approximation of summing the forces due to the two counterpropagating beams is only really valid for small saturation intensities, where the force from one beam is not influenced by saturation of the scattering rate by the other beam, and where absorption from one beam followed by stimulated emission into the other is rare.

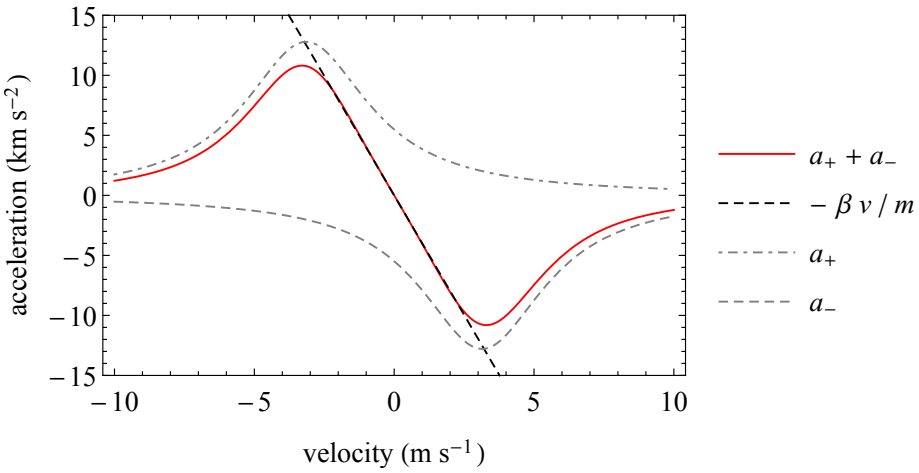

Figure 2.13: An estimate of the acceleration of a YbF molecule in 1D optical molasses using Eq. (2.29), where $s_{\mathrm{eff}} = 2$ and $\delta = -\Gamma$. Accelerations, $a_\pm = F_\pm/m$, where m is the mass of a YbF molecule.

2.5 Experimental requirements for laser cooling

So far, we have discussed the required wavelengths for the lasers, and some general principles for maximising the scattering rate in the multilevel system, but need to know how much laser power is needed for a laser cooling experiment. Having more laser power available is always better, but this comes at increased cost and technical difficulty. Here I will use the solutions to the MLREs found in the previous section, to estimate the required laser intensities to drive the laser cooling transitions with high saturation.

2.5.1 Expected laser power requirements for the cooling cycle transitions

For the X(0)-A(0)-X(1) transitions, in the limit of fast remixing, $s_{\mathrm{eff}} = \frac{7}{46} I/I_{\mathrm{sat}}$. To slow molecules in a short length of time we would like the scattering rate to be as high as possible. The maximum possible scattering rate is $R_{\gamma\text{-max}} = \Gamma/7$. To reach $\frac{2}{3} R_{\gamma\text{-max}}$

(where $s_{\text{eff}} = 2$), $I = 13I_{\text{sat}}$. For A(0)-X(0), $I_{\text{sat}} = 4.4\,\text{mW}\,\text{cm}^{-2}$, and for A(0)-X(1), $I_{\text{sat}} = 4.1\,\text{mW}\,\text{cm}^{-2}$.

To evaluate the power requirement, let us consider the specific laser cooling set-up envisaged for an eEDM experiment. We aim to apply transverse laser cooling to the molecular beam using 3 lasers to address the A(0)-X(0), A(0)-X(1) and A(2)-X(2) transitions. The lasers will pass multiple times through the vacuum chamber in order to give the desired interaction time with the molecules. The transverse size scale for the molecular beam is set by the gap between the electric field plates of the eEDM experiment, which is typically $\sim 1\,\text{cm}$. Therefore, we would like to have transverse laser cooling beams with this characteristic size. The intensity should be chosen to give $s_{\text{eff}} \sim 2$ to ensure a high scattering rate. Choosing a $1/\text{e}^2$ laser beam radius of 5 mm, we find that each laser frequency component should have a power of $\sim 30\,\text{mW}$.

In each of the X(0) and X(1) states there are four sets of F states which should be addressed with frequency components. We therefore require ~ 120 mW of light at 552 nm and at 568 nm. In order to make sidebands with this total power, and deliver the light to the experiment, we would like to have between two and four times this laser power initially, to allow for losses when generating the sidebands and losses in delivery. For the A(0)-X(0) transition the ground $F = 0$ and $F = 2$ states are separated in frequency by $\sim \Gamma$ (see Fig. 2.5), the transitions from these states can therefore be driven with one sideband with double the power of the others.

2.5.2 Expected laser power requirements for the repump transitions

To estimate the required repump power we can use Eq. (2.23). For the A(2)-X(2) transition, $f_{\text{in}} = f_{2,0} + f_{2,1} = 92\%$ and $f_{\text{out}} = f_{0,2} = 0.3\%$. For the A(1)-X(3) transition, $f_{\text{in}} = f_{1,0} + f_{1,1} + f_{1,2} = 98\%$ and $f_{\text{out}} = f_{0,3} = 0.03\%$. For both cases $N_{\text{g-eff}} = \frac{61}{3}$, in the limit of fast remixing. For the situation described in the previous section where the scattering rate in the X(0)-A(0)-X(1) system is $\frac{2}{3}R_{\gamma\text{-max}}$, $\alpha = \frac{2}{3} \cdot \frac{1}{7}$. For both repump transitions we can plot the dependence of the number of molecules in CC, on the repump intensity, Fig. 2.14.

For the A(2)-X(2) transition, to have 90% of the molecules to remain in CC when A(1)-X(3) is very strongly saturated, $I_{\text{r}} \approx 1.1I_{\text{sat}}(565\text{ nm}) = 4.5\,\text{mW}\,\text{cm}^{-2}$. For A(1)-X(3), to have 90% of the molecules to remain in CC when A(2)-X(2) is very strongly saturated, $I_{\text{r}} \approx 0.4I_{\text{sat}}(585\text{ nm}) = 1.5\,\text{mW}\,\text{cm}^{-2}$. If the transitions were both driven with this intensity, in the steady state there would be $\sim (90\%)^2 \approx 80\%$ of the molecules in CC.

For each repump transition, we must address each of the four F components of X(2) and X(3), so for the 5 mm $1/\text{e}^2$ radius beam, we need $\sim 3\,\text{mW}$ of 565 nm light, and $\sim 1\,\text{mW}$ of 585 nm light addressing each transition.

This assumes we are addressing these transitions on resonance. Because the repump transitions have small branching ratios, and are addressed with low intensities, they will not be significantly power broadened. If the Doppler width corresponding to the velocity range of molecules exceeds the natural width of the transition, more power would be needed.

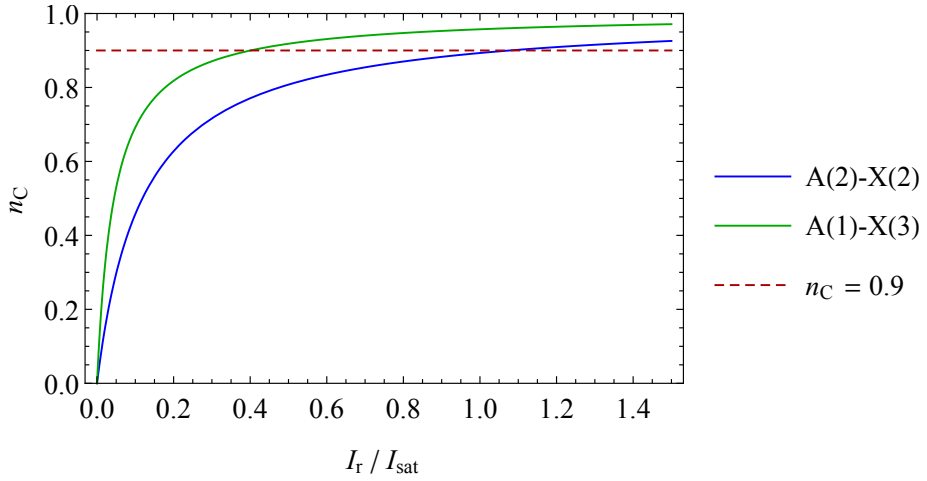

Figure 2.14: The probability of molecules in the CC, n_C as a function of repump intensity. For the A(2)-X(2) curve – A(1)-X(3) is strongly saturated, and for the A(1)-X(3) curve – A(2)-X(2) is strongly saturated.

Chapter 3

Experimental hardware I: Buffer gas source

3.1 Buffer gas cooling and molecular beams

In the work presented in this thesis, three molecular sources have been used. A supersonic source was used to acquire spectra of the $X^2\Sigma^+(v = 1) \rightarrow A^2\Pi_{1/2}(v' = 0)$ transition, described in Sec. 5.1.2. Both single-stage and double-stage helium buffer gas sources were used to obtain preliminary spectroscopy and optical cycling data. These sources are described in [131]. An additional (very similar) buffer gas source was used for the majority of the work described in this thesis. It is based on the design in Sec. 6.2 of Ref. [132], with some modifications, and is the source that is described in this chapter.

3.1.1 Velocity distributions from molecular sources

In making an eEDM measurement with a laser cooled molecular beam, it is beneficial to use a molecular source which produces a high flux, low temperature, and low forward speed. Fig. 3.1 shows a qualitative comparison of the velocity distributions from three molecular sources. Compared with other options for producing molecular beams, the buffer gas method offers key advantages. Buffer gas beams can be much slower than room temperature supersonic sources, and in some cases have a significantly higher flux [133]. Similarly narrow velocity distributions can be obtained with both techniques. Room temperature effusive sources produce molecular beams with a low population per rotational state, because the population is thermally distributed, and the spacing between low-lying rotational states is of order 1 K. For reactive species (such as YbF) effusive sources have a low extraction efficiency,[1] because molecules which collide with the wall of the cell are

[1] Extraction efficiency: The ratio of the number molecules that leave the cell to the number that were initially produced inside the cell. In an effusive source, the extraction efficiency is proportional to the ratio of the aperture size to the surface area of the inside of the cell.

lost. For certain applications, the presence of a slow tail in the velocity distribution of an effusive source may be an advantage.

We use a buffer gas source to produce a molecular beam slow enough, $\sim 180\,\mathrm{m\,s^{-1}}$, such that the molecules have adequate interaction time with the cooling laser, and to obtain a relatively high molecular flux, $2 \times 10^{10}\,\mathrm{sr^{-1}}$ per pulse in X(0). Further details about supersonic source design for YbF can be found in [134, 135]. Further details about YbF buffer gas source design can be found in [131, 136].

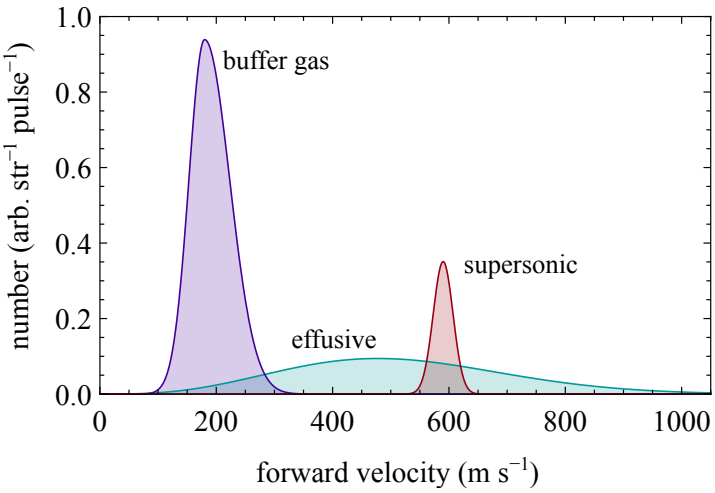

Figure 3.1: Comparison between types of molecular sources. The buffer gas distribution is representative of the velocity distribution of YbF molecules produced by the source described in this thesis. The supersonic distribution is representative of the YbF source that is used in our group in the current eEDM experiment which uses room temperature argon as the carrier gas. The relative amplitudes of the buffer gas and supersonic distributions are intended to be representative of the total number of molecules in both $N = 0, 1$ ground states for each. However, the time-averaged flux from the supersonic source is higher than the buffer gas source as it can currently run at $\sim 10\times$ the repetition rate. The buffer gas source produces the greatest flux when run at $\sim 2\,\mathrm{Hz}$. The effusive distribution shown is for a 1500 K YbF source, as used in the first generation YbF eEDM experiment [88]. The amplitude of the effusive distribution is greatly exaggerated to make it visible in the figure.

3.1.2 Buffer gas sources

In a buffer gas source molecules (or atoms) of interest are cooled by elastic collisions with a cold (buffer) gas inside a cold cell. As well as translational motion, these collisions can cool rotational and, to a lesser extent, vibrational degrees of freedom. After thermalisation, molecules leave the cell through an aperture, forming a beam. The technique is general, and can be applied to any species which can be loaded into a cryogenic cell, and does not react with the buffer gas species. Beam temperatures produced are typically a few kelvin, limited by the temperature of the buffer gas, which in turn is limited by the need

to have sufficient vapour pressure of the buffer gas for efficient cooling. For these reasons, the majority of experiments use helium as a buffer gas, but neon has also been found to have some advantages [137]. The technique was first used by the De Lucia group [138], and was later developed by the Doyle group [139].

Here, I will briefly discuss the theory of buffer gas beams. Further details and considerations can be found in [133] and [27].

Cooling via collisions

The number of collisions required to cool a species may be estimated using a hard sphere model as in [140]. Here, the translational temperature following N collisions of a molecule with buffer gas atoms is determined to be

$$T_N \approx (T_0 - T_\mathrm{b})\mathrm{e}^{-N/\kappa} + T_\mathrm{b}, \tag{3.1}$$

where T_b is the temperature of the buffer gas, T_0 is the initial temperature of the molecular species, and $\kappa = (m+m_\mathrm{b})^2/(2m_\mathrm{b}m)$, where m is the molecular mass and m_b is the mass of a buffer gas atom. We produce YbF inside the cell by laser ablation followed by a chemical reaction. We do not know the initial temperature of the YbF molecules. In [134] it was observed that the temperature of Yb atoms after laser ablation at room temperature was $\sim 2 \times 10^4\,\mathrm{K}$. If we assume that the YbF molecules have this temperature, and the helium buffer gas has a temperature of $\sim 4.5\,\mathrm{K}$, it will require ~ 250 collisions to cool YbF to within 20 % of the buffer gas temperature.

The molecular rotations and particularly vibrations are not cooled as rapidly. This is due to the energy spacing between rotational and vibrational states being too large and the time for which the system is perturbed by a collision being too short for effective transfer. This is explained in [28] in the context of supersonic beams. From rotational spectroscopy measurements, we find that the rotational temperature is approximately the same as the temperature of the buffer gas.

After N collisions, molecules will have travelled some distance, d_N inside the cell, which must be between the distance for a diffusive random walk and a directed expansion [141],

$$\sqrt{N}\lambda < d_N < N\lambda, \tag{3.2}$$

where $\lambda = 1/(\sqrt{2}n_\mathrm{b}\sigma)$ is the mean free path, σ is the YbF-He collision cross section, and n_b is the buffer gas number density. The buffer gas density inside the cell will be [142],

$$n_\mathrm{b} \approx \frac{4\phi_\mathrm{b}}{A_\mathrm{ap}}\sqrt{\frac{m_\mathrm{b}}{3k_\mathrm{B}T_\mathrm{b}}} \tag{3.3}$$

where A_{ap} is the area of the output aperture, and ϕ_{b} is the flow rate into the cell.

Using a helium flow rate of 1 SCCM, which is 4.5×10^{17} atoms s^{-1}, a circular aperture with diameter $d_{\mathrm{ap}} = 3\,\mathrm{mm}$, and a cell temperature of 4.5 K gives $n_{\mathrm{b}} = 1.5 \times 10^{21}\,\mathrm{m}^{-3}$. We can estimate that $\sigma \approx 10^{-18}\,\mathrm{m}^2$ from the measured diffusion cross section in [136]. This means $7.5\,\mathrm{mm} < d_N < 120\,\mathrm{mm}$. The diameter of the inside bore of the cylindrical cell is $d_{\mathrm{cell}} = 10\,\mathrm{mm}$ therefore a large fraction of molecules will be lost in collisions with the walls of the cell before thermalising. Running our cell with a higher flow does increase the extraction efficiency, but also increases our vacuum chamber pressure, which can be problematic.

Flow regime

The regime of operation of a buffer gas source can be roughly categorised by the Reynolds number, Re, at the exit aperture of the cell. As explained in [133], Re can be expressed as,

$$\mathrm{Re} \approx 2\frac{d_{\mathrm{ap}}}{\lambda_{\mathrm{b}}}, \tag{3.4}$$

where λ_{b} is the mean free path for the buffer gas atoms in the approximate region within distance d_{ap} of the aperture. In the effusive regime, there are no collisions near the aperture and $\mathrm{Re} \lesssim 1$. The output molecular beam is therefore a sampling of the thermal distribution in the cell. In the intermediate regime, $1 \lesssim \mathrm{Re} \lesssim 100$, the collisions at the aperture change the velocity distribution from that inside the cell. The distribution is typically boosted to a higher forward velocity because collisions are preferentially in the forward direction near the aperture. This is the regime in which buffer gas beams usually operate. In the supersonic regime, $\mathrm{Re} \gtrsim 100$, the gas behaves more like a fluid and there is significant cooling in the expansion outside the cell aperture. The forward velocity in the supersonic regime is the same as that of a cold supersonic source $\sim 1.4\bar{v}_0$, where $\bar{v}_0$ is the mean thermal speed of molecules inside the cell, $\bar{v}_0 = \sqrt{3k_{\mathrm{B}}T/m}$.

We run our source in the intermediate regime. We can tell this from the output velocity distribution, which is not narrow about the supersonic speed,[2] nor do we see a cold effusive distribution.[3]

For an effusive beam, the FWHM divergence solid angle is π. As Re increases, the divergence becomes smaller because collisions at the aperture boost the forward velocity of the beam but do little to increase the transverse velocity of the molecules. The result is that the beam divergence approaches $\pi m_{\mathrm{b}}/m$.

[2] Supersonic speed: $235\,\mathrm{m\,s}^{-1}$ for He at 4.5 K

[3] Effusive distribution: ${}^{32v^3}/_{\pi^2\bar{v}_0^4} \exp\left({}^{-4v^2}/_{\pi\bar{v}_0^2}\right)$

Extraction efficiency

YbF molecules which collide with the walls of the cell will react or freeze. For efficient extraction, the rate at which molecules in the cell are pumped out of the aperture should be large compared to the rate at which they stick to the walls. Two time constants can be derived for these processes [133], the diffusion timescale and the pump-out time. These are,

$$\tau_{\text{diff}} = \frac{14}{9\pi}\frac{{d_{\text{cell}}}^2 n_{\text{b}}\sigma}{\bar{v}_0} \tag{3.5}$$

$$\tau_{\text{pump}} = \frac{4V_{\text{cell}}}{A_{\text{ap}}\bar{v}_0}, \tag{3.6}$$

where V_{cell} is the cell volume which is $2.4\,\text{cm}^3$, and d_{cell} is a characteristic length before molecules collide with a cell wall, which I have taken to be the diameter of the cell, 1 cm. We therefore get $\tau_{\text{diff}} = 0.4\,\text{ms}$ and $\tau_{\text{pump}} = 8\,\text{ms}$. This indicates that the extraction of thermal molecules in the cell is most likely not very efficient. This could perhaps be improved by increasing the diameter of the cell and reducing its length, or increasing the size of the aperture. The equation for τ_{pump} does not take into account of there being a direction of net flow through the cell.

3.2 Buffer gas source hardware

This section describes the buffer gas source that was used in transverse laser cooling experiments described in this thesis.

3.2.1 Buffer gas cell

The buffer gas cell (BGC) is illustrated in Figs. 3.2, 3.3. The cell and the majority of components are made from oxygen free copper for high thermal conductivity. The parts are machined in-house. The baseplate of the cell is fastened to the cold plate of a cryocooler, Fig. 3.4, using brass screws. These are used as brass has a slightly larger thermal expansion coefficient than copper, therefore components should not loosen when the assembly is cooled. The temperature of the cell is ~ 4.5 K.

YbF is a radical that cannot be stored and must be produced on demand in the experiment. We produce it by ablating a Yb rod in the presence of SF_6 gas inside the BGC. The resulting molecules are then entrained in a flow of helium that is pre-cooled to 4 K. The flows of both helium and SF_6 are continuous. We use flow rates of $0.3 \rightarrow 2.0$ SCCM for helium, and $0.01 \rightarrow 0.1$ SCCM for SF_6. Gas flow is controlled using mass flow controllers (Alicat Scientific, range $0.005 \rightarrow 5.0$ SCCM for SF_6, MKS Instruments, GE50A for He). Before entering the cell, helium is cooled upon passing through $1/8''$ copper tube, which

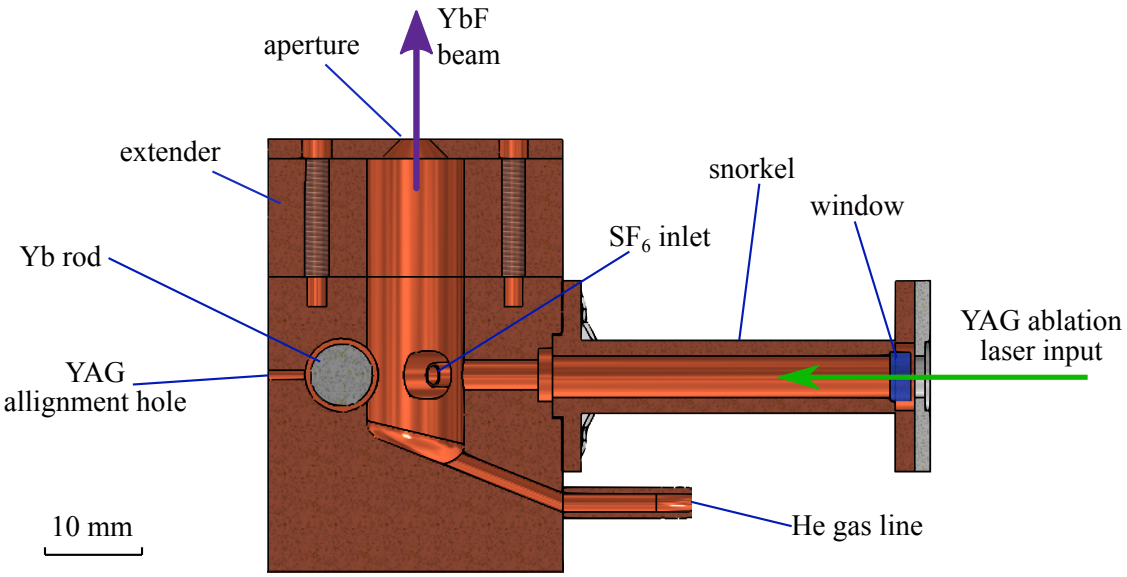

Figure 3.2: A cross section of the BGC to scale, The diameter of the bore of the cell is 10 mm, the aperture is 3 mm in diameter. The length of the extender we use is 10 mm in length rather than 15 mm as shown here.

is wound around and soldered to a bobbin, illustrated in Fig. 3.3. The bobbin is attached to the cryocooler cold plate. SF_6 enters the cell through a warm gas line to prevent it from freezing to the walls of the tube before entering the cell. The temperature of the end of the SF_6 line is approximately 220 K. A 3D-printed plastic holder is used to attach the tube to the cell. The holder is designed such that it has minimal contact with both the tube and the cell, in order to minimize the thermal conductivity between the two.

For the laser ablation, a pulsed Nd:YAG laser (Continuum, Minilite II) is used to ablate the surface of a Yb metal rod. We use a repetition rate of 2 Hz; the pulses are of 10 ns duration, and $\sim$ 10 mJ energy. The spot size on the Yb rod is about 1 mm in diameter. YbF molecules are produced by a chemical reaction that takes place between Yb in the ablation plume and SF_6. Several other molecular species will also be produced in the ablation process such as the chemically stable YbF_2 and YbF_3. The YAG beam enters the cell through a tube which we call a 'snorkel'. The snorkel is there to increase the distance between the point of ablation and the window through which the laser enters the cell. This reduces the rate at which the window is coated with Yb and other ablation products, meaning that we can run the experiment for many weeks without having to break vacuum and warm the cold plate to replace the window.

The Yb rod is cast and has 1/4″ diameter (Goodfellow, YB007910). It is attached to the threaded copper rod turner, so that the rod can be rotated using a rotational vacuum feed-through. The surface of the rod is damaged by the ablation; after one spot on the rod has been ablated $\sim$ 5000 times, damage causes the molecular yield to drop by $\sim$ 1/2. Turning the rod enables fresh surface to be exposed and advances the position of the rod

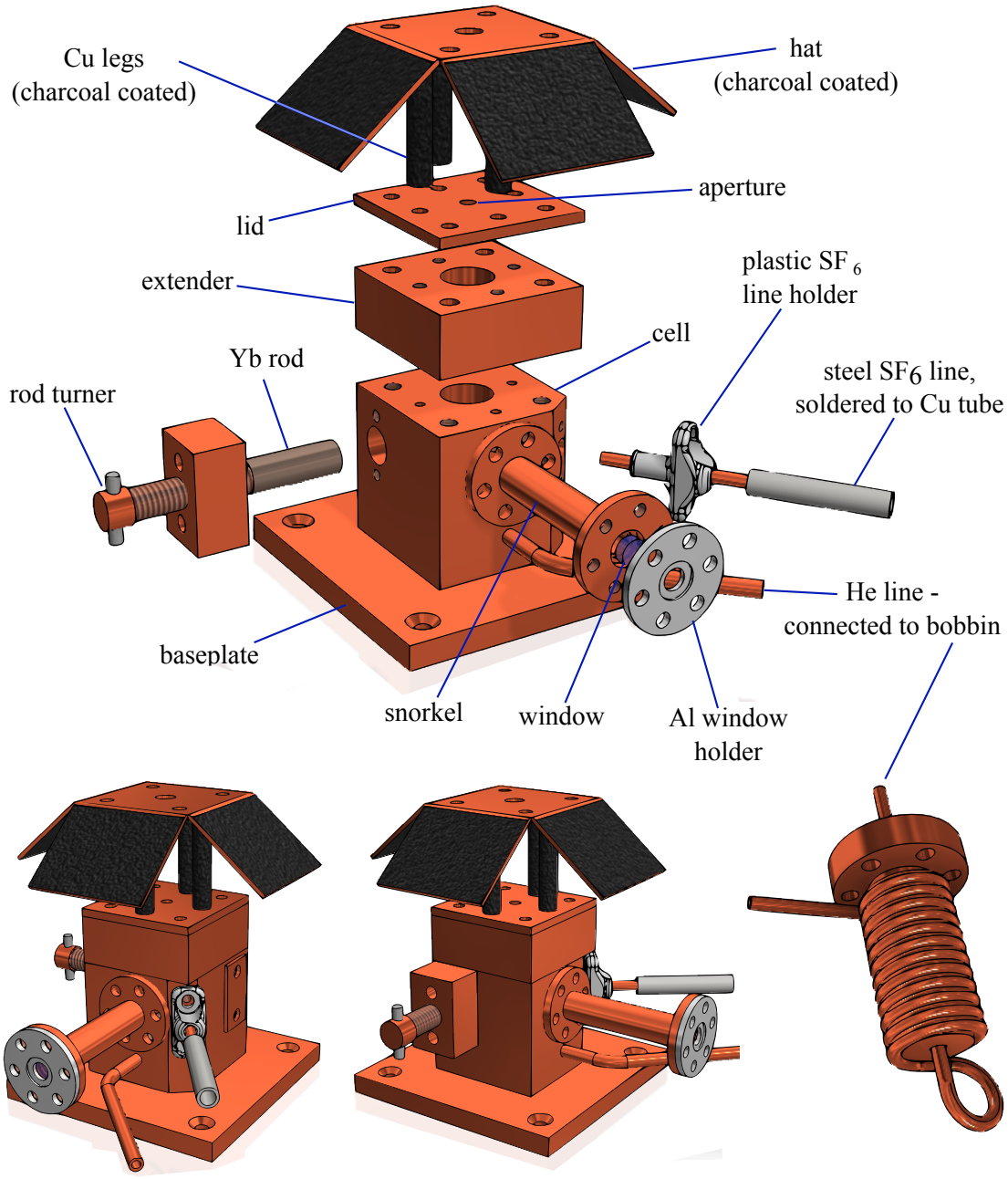

Figure 3.3: An exploded view of the parts of the BGC, above, and the cell as seen from two different angles, below. The molecular beam is emitted from the aperture in the top of the cell. In the bottom right a bobbin is illustrated. All components which are not labelled otherwise are machined from oxygen-free high thermal conductivity copper. All components are connected using brass screws, except for the SF_6 line holder which is attached to the cell using nylon screws.

into the cell, such that a large area of the rod surface is accessible for ablation. It is important for the Yb rod to make adequate thermal contact with the turner and cell so that its temperature does not increase significantly under continuous ablation. This would cause the buffer gas and therefore molecular beam to increase in temperature. The rod is attached to the end of the rod turner using a grub screw and a Stycast epoxy.

The hot YbF molecules thermalise with the helium and leave the cell through the aperture in the lid of the cell, with a forward velocity distribution similar to that of the helium. The extender was added to the cell after we found that the time of flight (ToF) profile of the beam to be strongly dependent upon the position of the YAG ablation spot on the Yb rod. Adding the extender significantly reduced this dependence. The 'hat' on the cell acts as a kind of skimmer, to reduce the helium pressure in the vacuum chamber. The underside of the hat is coated in charcoal which absorbs helium at low temperature, as described in the following section.

3.2.2 Cryogenic and vacuum apparatus

Fig. 3.4 illustrates the vacuum and cryogenic assembly. We use a closed-cycle cryocooler (Sumitomo Heavy Industries, RDK-415D), which delivers 1.5 W of cooling power to the second stage cold plate at 4 K. It also has a first cooling stage which is cooled to ~ 40 K. To the first stage we attach cylindrical aluminium radiation shields. Their job is to prevent room temperature radiation impinging directly upon the charcoal shields, lid and the bottom of the second stage cold plate. The charcoal shields are two half copper cylinders which are attached to the second stage cold plate; the charcoal lid rests on top. All fastenings are brass screws.

The inside of the shields and lid are coated in grains of coconut charcoal which is glued to the surfaces using Stycast epoxy, (Henkel Loctite, Stycast 1266, we have previously used Stycast 2850FT), the charcoal acts as a sorbtion pump. The charcoal shields have an inner diameter of 118 mm, and a height of 120 mm. Coconut charcoal is used because it has been found to be a very good absorber of helium at cryogenic temperatures, with a pumping speed of 6.7 l s^{-1} cm^{-2} at 4 K, when fresh [143]. The optimum grain size for the charcoal is $\sim$ 1 mm [144]. Stycast is used as it has a relatively good thermal conductivity, for an adhesive, at low temperature [145]. Helium is pumped predominantly by the charcoal because the helium source is within the charcoal shields, additionally, the pumping speed for turbo pumps is low for helium. The charcoal must be replaced after several months of use as its pumping efficiency decreases.

We use two turbo pumps. The pump attached to the lower vacuum can has a pumping speed of 1200 l s^{-1} for He (Leybold, Turbovac 400110V0051), however there is a low conductance to this pump as it is attached via an ISO 100 adaptor. This pump replaced

a smaller one (Leybold, Turbovac 361, He pumping speed 340 l s^{-1}) during the transverse laser cooling experiment, Sec. 6. For the transverse laser cooling experiment, a second pump (Leybold, Turbovac 361) was attached to the vacuum can, at the top of the experiment (not shown in Fig. 3.4).

The cryocooler base makes a seal with the lower vacuum can with an O-ring. Other vacuum seals are also made using O-rings. The vacuum cans are ISO-K 250 (Kurt J. Lesker, with modifications made in-house), they have ports with ISO or KF (QF) flanges.

The gas lines are connected using Swagelok fittings. The helium and SF_6 gas lines enter the chamber through a feed-through. The helium first passes through a 0.5 m long coiled steel tube, before going through a copper wound bobbin, Fig. 3.3, attached to the first cooling stage cold plate. It then passes through a thin walled steel tube before arriving at the copper bobbin attached to the second cooling stage. Steel is a poor thermal conductor compared to copper, and the steel sections and first bobbin are present to reduce the heat load due to conduction on the second stage cold plate. The SF_6 gas line goes directly from the feed-through into the cell along a ~ 0.5 m long, 3/16″ steel tube, where it is soldered to a 5 mm diameter copper tube before entering the cell.

The largest gas load is due to the continuous flow of helium from the cell. When running at 0.3 SCCM the pressure reading on our penning gauge (Leybold, Penningvac PTR225) is 2×10^{-7} mbar. We must divide by the gas correction factor for helium, 0.18 (as it is more difficult to ionise than N_2), to get the actual helium pressure of 10^{-6} mbar. When helium is not flowing, the chamber pressure reaches 9×10^{-8} mbar. The cold surfaces inside the chamber are sorbs for N_2 and O_2. Before the cryocooler is switched on the chamber pressure reaches 2×10^{-7} mbar.

The turnaround time when making a change to the set-up is at least a day, as it takes ~ 4 hours for the cold plate to reach room temperature and ~ 8 hours to cool down. The chamber cannot be opened when the cold plates are much below room temperature, as water vapour in the air will condense (or freeze) onto the cold surfaces. In order to speed up the warming time to 4 hrs, we have installed aluminium housed power resistors on the cold plates which act as heaters. We use these to heat both the first and second stage cold plates using 20 W of power for each.

We monitor the temperature of the cell and cold plates using cryogenic thermistors (Lake Shore, Cernox CX-SD). We purchased one calibrated thermistor, and calibrated several others from this one. The thermistors are attached to bobbins, along with ~ 0.25 m of ~ 0.3 mm diameter enamelled, copper magnet wire which is connected to their terminals. The wire is wound around the bobbin and glued using Stycast. This is to eliminate the effect of heat conducted along the wires heating the thermistor, and resulting in inaccurate temperature readings.

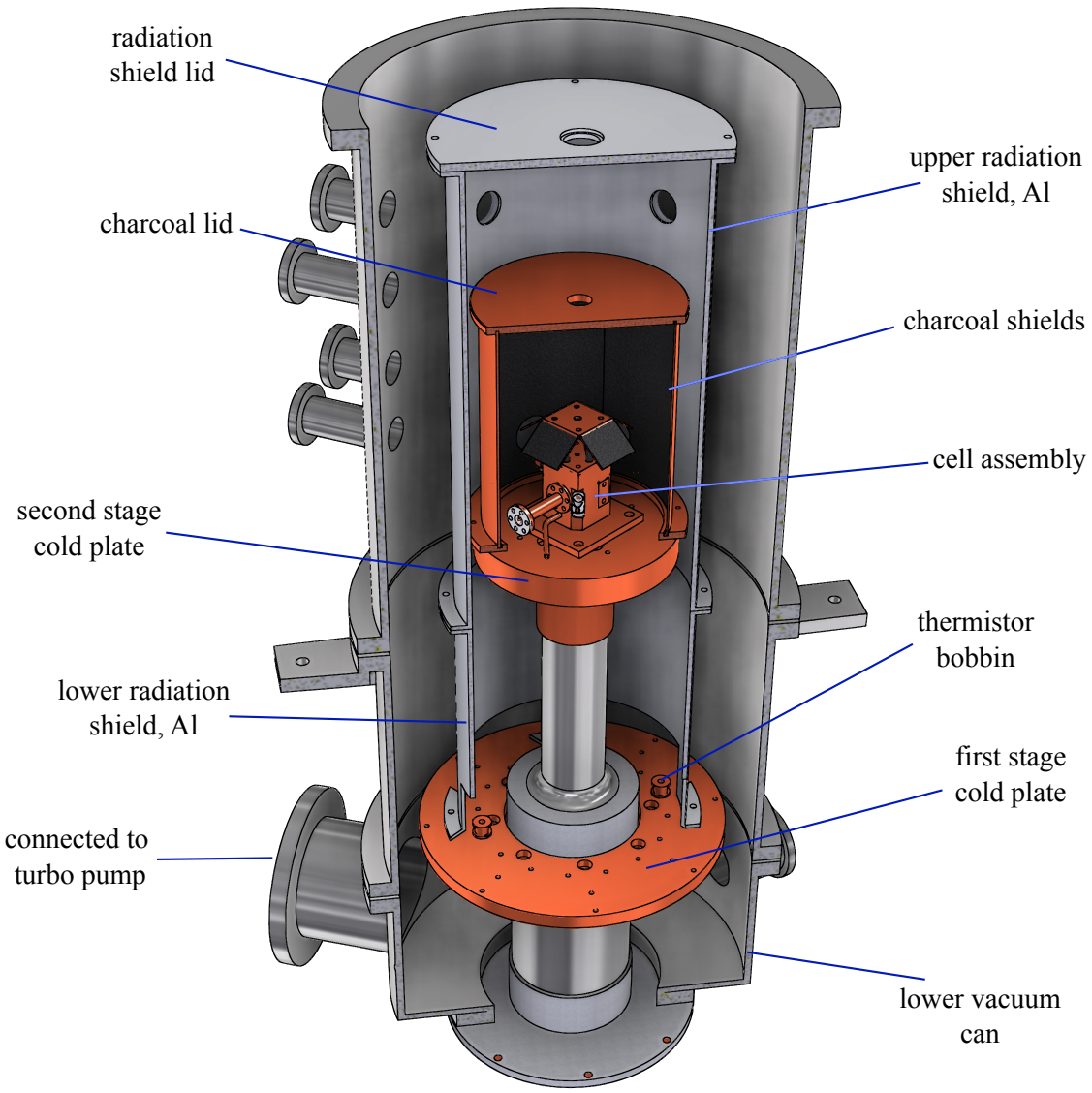

Figure 3.4: A drawing of the cryogenic and vacuum assembly of our source chamber. The gas lines and electrical connections are not shown.

3.2.3 Source stability and maintenance

The molecular flux from the cell can vary significantly for a number of different reasons. Here I will discuss some of the problems we encountered and solutions we found. We have spent considerable time investigating many of these effects, but have not been successful in understanding the cause of some problems. This is largely because there is a large number of hypotheses that one could come up with to explain a particular problem, and there is a long turnaround time required to make changes to the set-up in order to test each. When discussing the flux of molecules from the source, I mean the number of molecules per steradian per shot in the $X^2\Sigma^+(v = 0, N = 1)$ states, which I am calling X(0). If the molecular beam is hotter, molecules will be emitted with a rotational distribution that is skewed towards higher N. We typically get a flux of $\sim 2 \times 10^{10}\,\mathrm{sr}^{-1}$ per shot in X(0), where a shot is one pulse of the YAG laser.

After having run the source for a few days and the flux has decreased, an improved flux may be recovered by warming the cold plate to room temperature and then cooling is down again (but vacuum not breaking vacuum). The improvement may be as large as 10×. Warming the cell to room temperature will remove frozen SF_6 (and any N_2 and O_2 from the air) from the inside surfaces, which could improve the thermalisation of helium with the walls of the cell. Another possibility could be that the end of the SF_6 gas line becomes cold, and SF_6 is freezing in the tube and not reaching the cell. To test for this we installed a thermistor on the SF_6 copper tube close to the cell, and some heating resistors on the steel tube. When the signal has dropped, and become independent on the flow rate of SF_6, we have switched on the heaters to heat the gas line to greater than the sublimation temperature of SF_6, but have found that a high molecular signal does not return.

We use the heaters on the cold plates to bake them to around 50 °C whilst the chamber is under vacuum, before cooling down, this improves the performance of the charcoal sorbs, perhaps by removing adsorbed water vapour from the charcoal.

Some signal gain can be achieved by switching the cryocooler off for 5 min (after switching it back on it takes 10 min to return to 4.5 K), this is accompanied by a large increase in pressure as the helium is desorbed from the charcoal shields at temperatures $\gtrsim 10\,\mathrm{K}$. Afterwards, the running pressure is improved.

The inside surfaces of the cell become coated with a flaky deposit of ablation products after many thousands of shots. After cleaning the inside of the cell, the flux usually increased, again this increase can be 10×. Sometimes we find that the signal from the source has dropped by a large amount overnight, or the shot-to-shot stability has become poor (we consider a good shot-to-shot stability to be $\sim 10\%$), this can often be improved by warming up and cooling down again without breaking vacuum.

The surface of the Yb rod becomes pitted due to laser ablation, and this affects the shot-to-shot stability of the flux. When we break vacuum, we re-surface the rod using sandpaper, and eventually replace the rod when it is considerably damaged. It seems best to use a shiny surface, that is free of pollutants.

When the ablation laser begins firing (on a fresh, or previously used ablation spot), the molecular signal starts off very low, it quickly becomes large over the course of ~ 5 shots, and the time-of-flight profile and flux fluctuate enormously. After ~ 100 shots, the signal becomes stable, and from then, slowly decreases. We find that if the rod is rotated by an angle $\gtrsim 20^\circ$ between YAG shots, whilst it fires continuously, the signal of the next shot is very low, it increases and is unstable for the next few shots. The stability requires a few 10s of shots to recover. If the rod is rotated only a small amount between each shot $\lesssim 5^\circ$, then the molecular flux can be increased $\sim 2\times$, at the cost of some shot-to-shot flux stability. Possible explanations for these observations are that the ablation process creates reactive species on the surface of the rod close to the ablation spot following one ablation pulse, which react to produce YbF upon the next pulse, or that there is an optimum surface temperature of the ablation spot, and it must first warm up. The decrease in flux over longer time-scales could somehow be due to damage to the surface of the rod, which is discussed in chapter 4 of [131]. We have tried to take advantage of the signal increase for small rotations of rod between shots using a stepper motor system designed by N. Fitch, however the decreased stability is detrimental to experiments.

We have tried to increase the repetition rate of the ablation laser so that the number of molecules per second is increased, enabling faster data collection.[4] However, increasing the YAG repetition rate to 5 or 10 Hz decreases the time averaged flux. We have attempted to investigate the cause of this decrease to improve flux. The Yb rod will be hotter at higher repetition rates which should result in the molecules being more likely to be in rotational states where $N > 1$, but we have not done the spectroscopy to test for this.

We have changed the ablation target for a thin 0.5 mm walled cylindrical Yb sleeve[5] which surrounded a copper rod (instead of using the bulk Yb rod), to test whether improved heat conduction away from the ablation spot increased the molecular yield at higher repetition rates. The sleeve fitted snugly to the copper rod and was fixed using a thin layer of Stycast. This layer does not limit the heat transfer to the copper since the thermal conductivity of Stycast is similar to that of Yb at low temperatures [146]. We expected this design to improve the heat conduction away from the ablation spot since the thermal conductivity of copper is about 1000 times greater than Yb. However, the performance of the Yb sleeve was not obviously better than the bulk Yb rod.

To improve the signal from the buffer gas source it would be worthwhile checking

[4] There is no increase in gas load when running at a higher rep-rate as the helium flow is continuous.
[5] To make the Yb sleeve, the center of a Yb rod was machined out using wire erosion.

whether using a fluorine containing gas other than SF_6 gives a higher molecular yield. We have briefly tested running the source using CH_2FCF_3.[6] Comparing running the flux from the source with 0.01 SCCM flow rate of each fluorine containing gas; CH_2FCF_3 produced $\sim 80\%$ of the signal compared to using SF_6.

3.3 Characterising the source

In this section I will give the results of some measurements that were made on the properties of the buffer gas beam. These were made when the cell was at a slightly higher temperature than 4.5 K.[7] The current forward velocity distribution from the cell should therefore have a slower mean velocity.

3.3.1 Velocity distribution

Using the experimental set-up illustrated in Fig. 3.5 we made a measurement of the forward velocity of the molecular beam. This was done recording fluorescence spectra taken using two laser beams, one perpendicular, and one at 60°, to the beam propagation direction. The relative frequency shift between the resulting spectra, caused by the Doppler effect, could then be extracted. At the time this measurement was made, the BGC temperature was (6.5 ± 0.2) K, the helium flow rate was 2.0 SCCM and the SF_6 flow rate was 0.01 SCCM.

To determine the velocity distribution, the following procedure was used. The voltage sent to the piezoelectric actuator of laser(0,0) (described in Sec. 4.1.1) was adjusted to scan the laser frequency over $\sim$ 800 MHz across a set of spectral features.[8] For each voltage, a time-of-flight (ToF) profile was recorded, Fig. 3.6(a), for the 90° and 60° probe beams. Some of the light from the laser was sent to a fixed length confocal reference cavity with a 150 MHz free spectral range. The transmission of this cavity was recorded in order to convert the piezo voltage into a relative frequency using the method described in Sec. 5.1.2. Plotting the fluorescence signal (integrated over each ToF) as a function of frequency yields a Doppler-free reference spectrum for excitation by the 90° beam, and a Doppler shifted and broadened spectrum for the 90° beam, Fig. 3.6(b).

The ToF data for the Doppler-shifted spectrum were then binned into 24 contiguous time bins each of 140 µs width, and were used to generate Doppler shifted spectra for each time bin. A model consisting of a sum of four pseudo-Voigt profiles was fitted to the reference spectrum. Let the result of this fit be called $f(\nu)$ where ν is the frequency. To

[6] We had this available in the lab as it is the gas used in many compressed 'air' dusters.

[7] The measurements were made when the cryocooler cooling power was diminished, as it was in need of servicing.

[8] This was the A(0)-X(0) transition of the ^{172}YbF isotopologue, which was used because it is more isolated from other spectral features than the ^{174}YbF A(0)-X(0)transition.

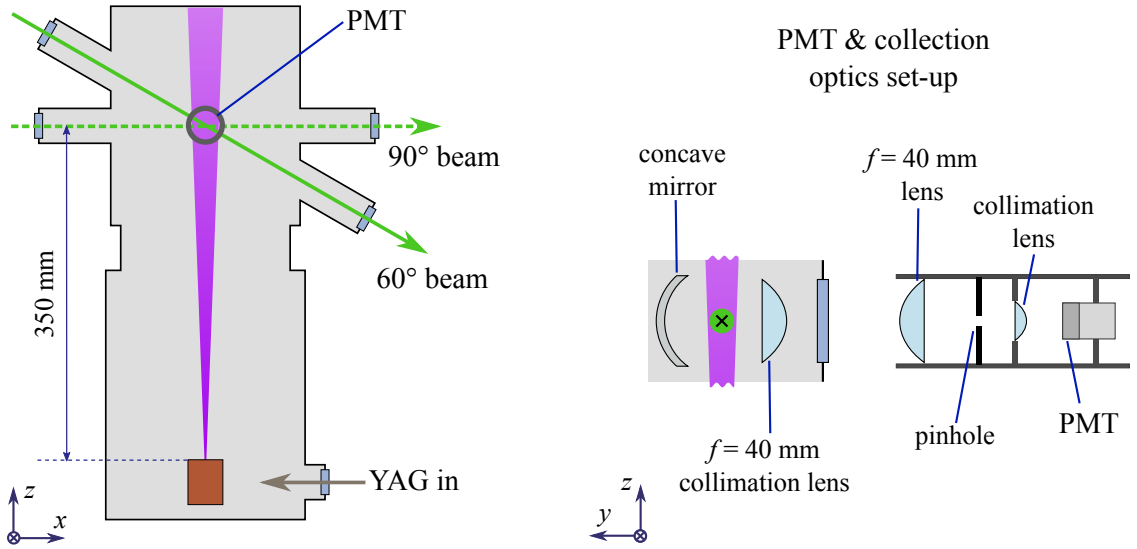

Figure 3.5: Set-up for measuring the buffer gas beam velocity. The 60° and 90° beam were alternately chopped on and off between shots. On the right, the optical set-up for detection is illustrated. We use a collimation lens and parabolic back-reflector inside the vacuum chamber to maximise the solid angle for light collection. By adjusting the size of the pinhole we can adjust the size of the imaging region in the yz-plane. We have used this type of set-up for the PMT collection optics in all experiments.

each of the Doppler shifted spectra we then fit the model $Af(\nu - \nu_D)$, where ν_D is the Dopppler shift between the shifted and reference spectra. Some of these fits are shown in Fig. 3.6(d). The fitted frequencies were used to calculate the mean velocities of molecules detected within each time bin. The detuning parameter was then converted into a velocity, $v = c(-\nu_D/\nu_0)\csc(\theta)$, where ν_0 is the laser frequency, and θ is the angle between the two laser beams which was measured to be $(26.6 \pm 0.1)°$.

The arrival time of molecules at the detector and their velocity are well correlated as shown in Fig. 3.6(c). Therefore, to obtain molecular distribution as a function of forward velocity v, we can use the method in [42]. This is done by binning the ToF profile into equal velocity width bins, each with center v_c. To convert between forward velocity and arrival time, we fit the function $t = \sum_{n=0}^{m} a_n/v^n$ to the data in Fig. 3.6, where a_n are free parameters and $m = 2$. The velocity bins used are contiguous, with width $4\,\mathrm{m\,s^{-1}}$. The ToF profile within each velocity bin is then integrated to yield the number of molecules within each bin v_c. The resulting distribution is shown in Fig. 3.6(e). Lower and upper bounds on the velocity distribution are calculated from the error on the fit of the arrival time as a function of velocity. The distribution has a mean of $(200 \pm 20)\,\mathrm{m\,s^{-1}}$ and FWHM $\sim 120\,\mathrm{m\,s^{-1}}$.

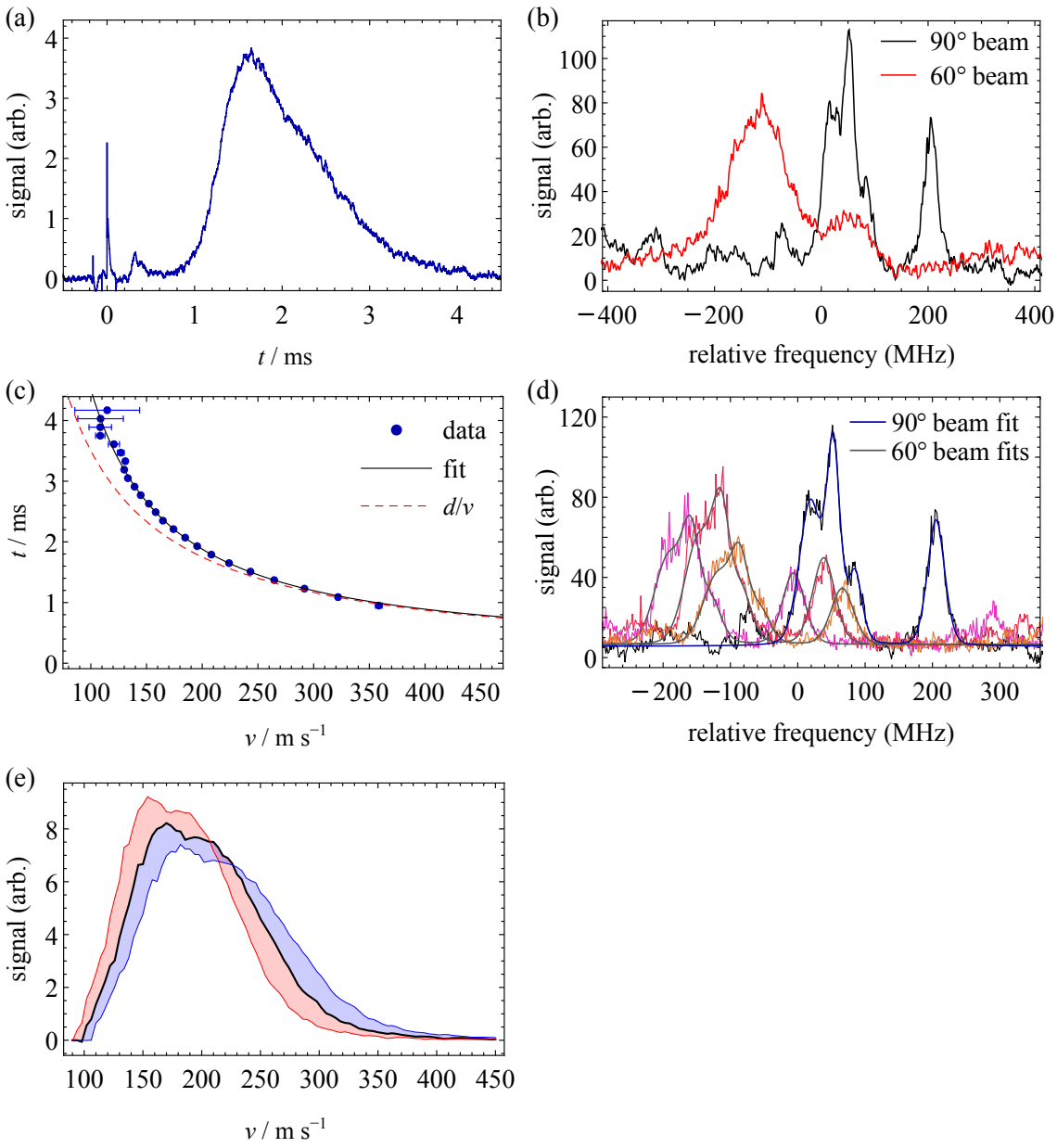

Figure 3.6: Results and analysis of the velocity measurement data. (a): The mean ToF profile for the reference spectrum. (b): The spectra recorded with the orthogonal and angled beams, obtained by integrating the whole ToF profile for each laser detuning. (c): The correlation between forward velocity and arrival time at the detector. The dashed curve is the earliest possible time molecules of a given velocity could arrive at the detector. (d): The fit to the reference spectrum, and three of the fits to 140 µs time-binned angled beam spectra. (e): The forward velocity distribution; the extent of the blue and red shaded regions are σ confidence intervals on the distribution from the standard error on the fit in plot (c).

3.3.2 Vibrational state populations

We made a rough measurement of the vibrational state populations of the molecules leaving the buffer gas cell, this was done by measuring the laser-induced fluorescence as a function of probe laser intensity for the ^{172}YbF A(0)-X(0), A(0)-X(1) and A(2)-X(2) transitions.[9] Transitions were driven from the $F = 1^-$ ground state each time which is furthest separated from the other hyperfine components. When making this measurement we used a helium flow rate of 2.0 SCCM and an SF_6 flow rate of 0.01 SCCM, the cell temperature was (5.8 ± 0.2) K.

Fig. 3.7 shows the results of the measurements of fluorescence as a function of laser power. The scatter in the data is mainly due to source flux decay; the order in which the data were collected was randomised in order to reduce systematic bias. We fit the model $f_\gamma = A\frac{P/P_{\text{sat}}}{1+P/P_{\text{sat}}}$ to the data, where P is the laser power and A, P_{sat} are free parameters. $P_{\text{sat}} \propto I_{\text{sat}}$ for the transition, and A is proportional to the number of molecules in a given state. We obtain relative vibrational state populations of approximately 1.0, 0.4 and 0.07 for X(0,1,2) respectively.

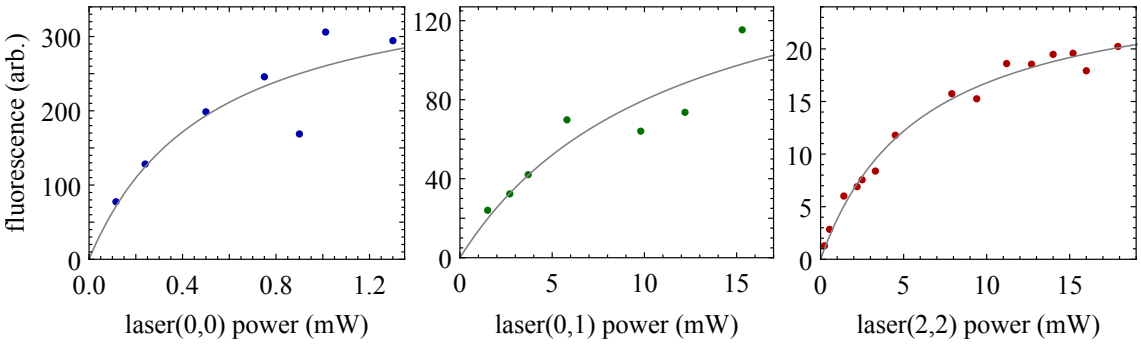

Figure 3.7: Points: Saturation measurements for the A(0)-X(0), A(0)-X(1) and A(2)-X(2) transitions. Curves: Fits to the data.

[9] Again, ^{172}YbF was used because the P(1) line is well isolated from other transitions.

Chapter 4

Experimental hardware II: Laser systems

4.1 Laser systems

As discussed in chapter 2, a number of different laser wavelengths are required for our laser cooling scheme. The lasers which we currently have drive the transitions shown in Fig. 4.1. I will name these lasers according to the transitions that they drive; laser(0,0) has wavelength 552 nm and drives the A(0)-X(0) transition, laser(0,1) drives the A(0)-X(1) transition and has wavelength 568 nm, and laser(2,2) drives the A(2)-X(2) transition and has wavelength 565 nm.

To generate each of these wavelengths, we use an infra-red (IR) external-cavity diode laser (ECDL) as the oscillator. The output of each ECDL is amplified using a solid state amplifier to increase the IR power from ~ 10 mW to ~ 5 W. The output of each amplifier is then frequency doubled, using a nonlinear optical crystal, to produce the wavelengths of light required for laser cooling.

In this section I will describe each of the laser systems.

4.1.1 552 nm laser(0,0)

(a) ECDL

For laser(0,0), shown in Fig. 4.2(a), a homebuilt ECDL is used which operates at 1104.6 nm. It has an anti-reflection (AR) coated laser diode (LD) (Eagleyard Photonics EYE-RWE-1120-090000-1300-SO), and a reflective holographic grating (Thorlabs GH13-12V)[1] in the Littrow configuration with a design based on that of [147]. Fig. 4.3 shows a sketch of the ECDL.

[1] We have also used Thorlabs grating G13-12U which gives $\sim 25\%$ less output power.

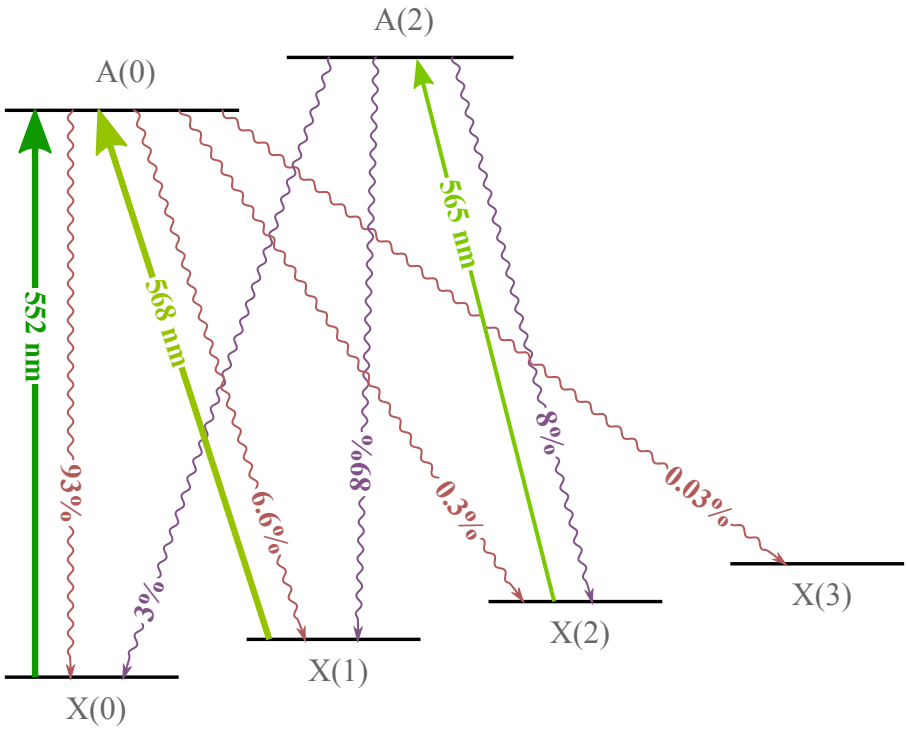

Figure 4.1: The laser cooling scheme we use for YbF, showing the three laser wavelengths which we currently use. The wavelengths of the required lasers are given in nanometres and FCFs are given as percentages.

To control the current to the LD, we use a commercial 250 mA current driver (an older model of Thorlabs LDR1255R). The piezo voltage is controlled by computer for scanning and locking the laser (see Sec. 4.3.2). The output from the computer is amplified using a homebuilt 1 kV piezo driver with circuit design as in [148].

The mirror mount of the ECDL is clamped to a Peltier device which maintains the temperature of the laser. We typically run the laser at temperatures between 19 °C and 22 °C. The temperature is controlled using a commercial proportional-integral controller (Wavelength Electronics MPT2500), the temperature sensor is a 10 kΩ thermistor. We have found that it is best to position the thermistor relatively close to the Peltier, in a hole drilled in the back plate of the mirror mount. It is better for the thermistor to be close to the Peltier rather than the diode as this reduces the time constant for feedback to the controller, resulting in smaller temperature oscillations. The heat sink for the Peltier is a ~ 2 kg aluminium block.

An upper limit to the RMS linewidth of the laser over 100 ms is (320 ± 20) kHz, which was measured by recording the noise in the transmission through an optical cavity, with the cavity length set so that the laser frequency was approximately half a cavity linewidth from resonance. The linewidth of the frequency doubled output of this laser system is therefore approximately double this value. The linewidth estimate for this laser is not

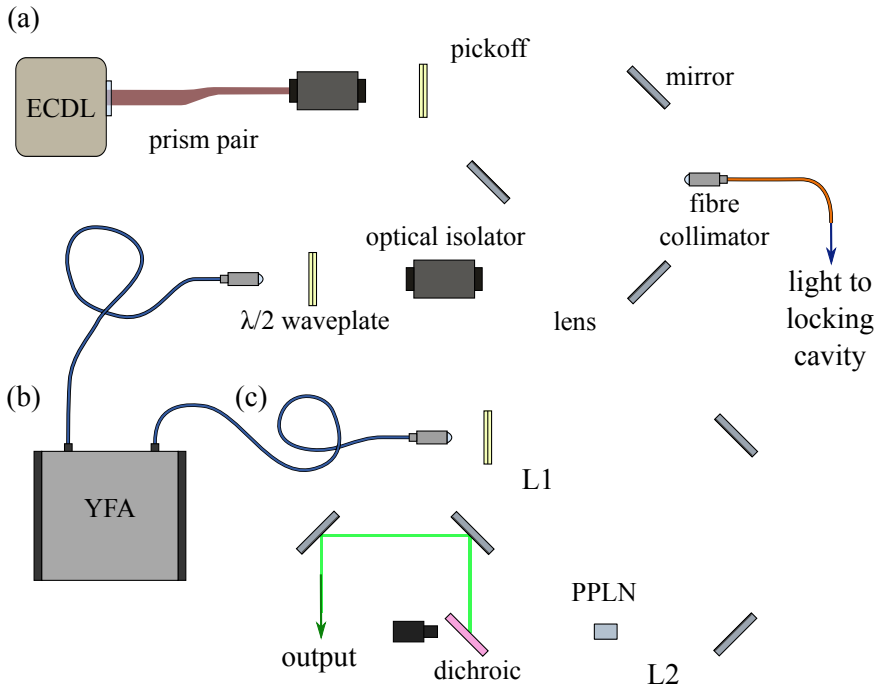

Figure 4.2: The laser(0,0) set-up. (a): The ECDL set-up. (b): The fibre amplifier. (c): The frequency doubling set-up.

especially narrow; this could be improved by isolating the ECDL from vibrations and increasing the mechanical stability of the mirror mount. Alternatively, a different design which is more resistant to mechanical vibrations could be used such as interference filter stabilised ECDL in a cateye configuration [149, 150]. However, because the natural width of the A-X YbF transitions are broad (5.7 MHz), the ECDL linewidth is adequate. The mode-hop-free tuning range (MHFTR) of the ECDL is ~ 3 GHz. If necessary, this could be improved by using a feed forward to the current of the LD. The output power is 42 mW for a 125 mA current to the LD.

(b) Yb fibre amplifier

The laser light is amplified using a Yb-doped fibre amplifier (YFA) that was custom built to operate at 1105 nm (Keopsys CYFA-PB-BW5-PM-37-NL1-OM1-B203-FA-C1). To verify the amplifier worked with our ECDL seed, we sent the ECDL set-up to Keopsys in Brittany, and I travelled there to align the seed and help test the system. The amplifier produces 5 W of laser light from a 5 mW input. Prior to purchasing the YFA from Keopsys, the ECDL seed was amplified using one of the two custom YFAs that were purchased by the CCM in 2009 (Nufern SUB-1151-55). These have similar specifications to the Keopsys YFA, however, we have had considerable problems with both of them.

Problems we have experienced with the Nufern YFAs include: a large fraction of

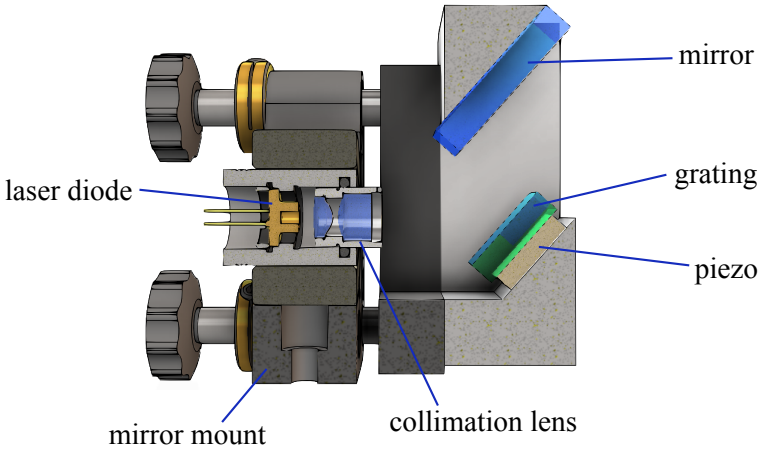

Figure 4.3: A sketch of the ECDL. In addition to the design in [147], there is a mirror mounted on the front plate of the mirror mount (Newport U100-P3K), parallel to the grating such that the beam pointing does not significantly change during coarse tuning of the grating angle.

the output power being composed of amplified spontaneous emission (ASE) instead of laser light, the amplifier frequently switching itself off due to internal faults, and large fluctuations in the output power.

Measuring the ASE produced by a laser amplifier is one of the less straightforward tests to do on our laser systems without the use of an optical spectrum analyser. We have therefore developed the following technique to measure it using an optical cavity. A small fraction of the output light of the amplifier is coupled into a confocal optical cavity. The cavity must have broadband dielectric mirrors which have similar reflectivities for the laser wavelength and the typical ASE wavelength range produced by the amplifier. The length of the cavity is scanned over a distance greater than $\lambda/2$, where λ is the wavelength of the seed laser, and the transmission of the cavity is recorded; this is the 'total signal' curve in Fig. 4.4. To ensure stray light does not affect the measurement, a background signal is measured when the light into the cavity is blocked; this is 'signal without laser' in Fig. 4.4. The ASE from the amplifier should be of a similar wavelength to the laser wavelength,[2] and it will be on a very similar beam path to the laser light as they were both emitted from the same optical fibre. Therefore, both laser and ASE should be similarly coupled into the cavity, and the cavity should have a similar finesse for ASE and laser wavelengths. The ratio of ASE to laser power in the output can therefore be found by determining the areas labelled 'laser' and 'ASE' in Fig. 4.4. As shown in Fig. 4.4, two adjacent cavity peaks should be used when making this measurement using a confocal cavity, because the amplitude of adjacent peaks may be different depending upon cavity alignment. This is because alternate confocal cavity peaks correspond to the transmission of different sets of

[2]The ASE is centred around $\sim 1070\,\text{nm}$ for YFAs

transverse cavity modes (this is discussed in Sec. 4.4). The total ASE and laser output of the amplifier may be measured using a thermal power meter.

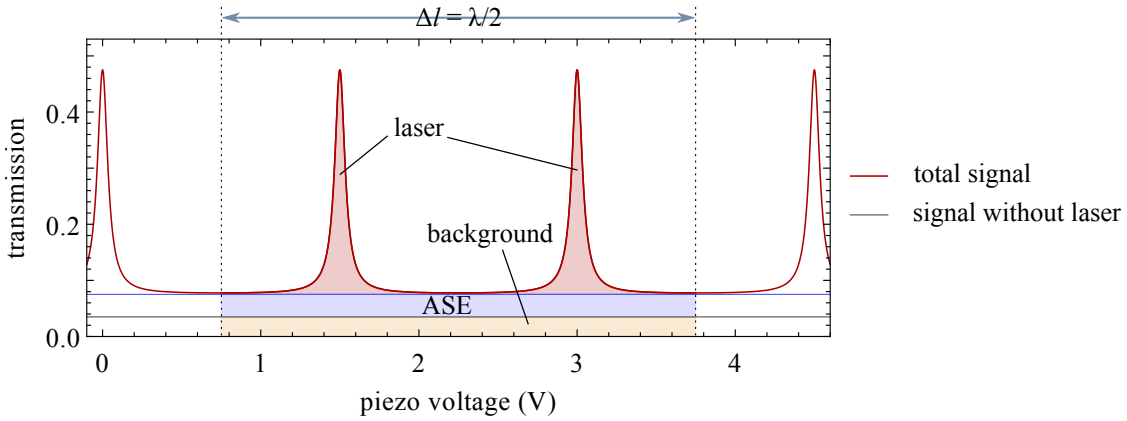

Figure 4.4: Measuring the fraction of ASE produced by a fibre amplifier. The relative areas of the red and blue shaded regions correspond to the relative power fractions emitted from the amplifier which are laser light and ASE. The size of the ASE and background regions are exaggerated here; for a properly working amplifier the ASE fraction should be $< 5\%$

Another possible problem when using fibre amplifiers is light that is back-reflected inside the amplifier being amplified. This back reflected light can destabilise the seed laser. To prevent destabilisation, we have found it necessary to have 60 dB isolation from back reflections, which we get using two 30 dB Faraday effect optical isolators, as shown in Fig. 4.2(a).

(c) Frequency doubling

We used a periodically poled lithium niobate (PPLN) crystal (Covesion MSFG1-0.5-20) for second harmonic generation (SHG). The crystal is 20 mm long and has several channels with different poling periods which are 0.5 mm high and 0.5 mm wide. The crystal is in a brass mount, which is clamped to the hotplate of a small oven. The oven is mounted on a pitch and yaw platform which can be translated in z (where z is the beam propagation direction). For alignment, lens L2 (50 mm focal length) in Fig. 4.2(c), is mounted on a xy-translation mount, and to adjust the beam size at the focus, lens L1 (250 mm focal length) can be moved in z. The temperature of the oven is set to $\sim 100\,^{\circ}\mathrm{C}$ and kept stable to within $\pm 0.1\,^{\circ}\mathrm{C}$ using a homebuilt temperature controller. The optimum temperature depends upon the beam pointing through the crystal. One method of achieving good alignment is by iteratively increasing the temperature (such that the doubled output power starts to decrease), then re-optimising the alignment. After several iterations, the new optimum temperature can be found for the improved beam pointing. Since the SHG efficiency is proportional to the square of the intensity, it is important to tune the focal spot size of the IR input to the crystal in order to obtain a tightly focussed beam with a high intensity

along the whole length of the crystal. The doubling efficiency is also dependent upon the position of the focus in z to a lesser degree.

We obtain maximum 552 nm output power of 750 mW, from 5.0 W of IR, which is a doubling efficiency of $0.03\,\mathrm{W}^{-1}$. This maximum is obtained when the beam waist at the focus, w_0, inside the crystal is $(31.3 \pm 0.7)\,\mu\mathrm{m}$, which was measured by profiling the beam using a CMOS camera after the doubling efficiency is optimised (with the crystal removed). To find the w_0, images are recorded at different positions along the beam propagation axis, z. Slices are taken from each profile in x and y through the centre of mass of the image, and the beam waist, w, at each position is determined by fitting a Gaussian to the intensity distribution in each slice. The function for the Gaussian beam waist,

$$w(z) = w_0 \sqrt{1 + \left(\frac{\lambda(z - z_0)}{\pi {w_0}^2} \right)^2}, \tag{4.1}$$

is then fit to the results for w, to determine the position of the focus, z_0, and w_0. These beam profile images were recorded using the light that leaked through the fibre amplifier from the seed ECDL when the amplifier was switched off.

We have had problems with the PPLN crystal becoming damaged when used with one of the Nufern YFAs. The amplifier was working incorrectly and produced short (<1 µs) high intensity pulses of laser light which are frequency doubled by the crystal. The high intensity of green light then produces a damage spot inside the crystal. The temporary solution to this was to reduce the power seeding the YFA such that the amplifier was not strongly saturated, since at low seed power it did not produce these pulses.

4.1.2 568 nm laser(0,1)

For laser(0,1), we use two commercial systems, an IR ECDL, and a Raman fibre amplifier (RFA) whose output is frequency doubled. The ECDL (Toptica Photonics DL 100 pro 17430) supplies 27 mW of 1136.2 nm fibre-coupled light to seed the RFA which is custom for our wavelength (MPB Communications VRFA-SF).

The amplifier works by stimulated Raman scattering, and is pumped by a high power Yb-doped fibre laser.[3] It amplifies the input to ~ 6 W. This light is then frequency doubled in a pre-aligned free-space doubling head (also supplied by MPB) containing a PPLN crystal to produce 1.1 W of 568 nm light. An upper limit to the RMS linewidth of the yellow/green output was measured to be (230 ± 20) kHz over 100 ms, measured in the same way as the laser(0,0) ECDL.

[3] In the Raman scattering (Stokes scattering) process, a longer wavelength beam (the seed) and a shorter wavelength beam (the pump) propagate through a non-linear medium. A pump photon produces an oscillating polarisation in the medium, exciting it to a virtual energy state, and the medium is de-excited by stimulated emission from the seed. The energy difference is lost to the medium as heat.

For the ECDL, we originally used a different LD (Toptica LD-1150-0100-AR-1) which initially produced 83 mW at 338 mA. This system had a mode-hop free tuning range of >20 GHz with feed forward from the piezo voltage to the current. This diode failed in normal operation, and there was no replacement of this model available, therefore a new diode was fitted (Toptica LD-1150-0100-AR-2). This initially produced 81 mW at 220 mA. The ECDL now has a MHFTR of $\gtrsim 5$ GHz, but requires a very large feed forward coefficient to scan this range.

4.1.3 565 nm laser(2,2)

For laser(2,2), we use a commercial IR ECDL, a tapered amplifier (TA) in a homebuilt mount, and a waveguide PPLN crystal for frequency doubling. The ECDL (Toptica DL 100 03098 with LD-1150-0100-AR-2) is used to seed the TA with 40 mW of 1129.6 nm light.

Before buying the Toptica system, we checked whether a spare LD of the same type as that used for the laser(0,0) system could be used to generate the 1130 nm light. In order to get the LD to run at 1130 nm it had to be heated to 44 °C. At this temperature, the maximum output power dropped by a factor of ~ 2 compared to room temperature operation. We decided it would be more convenient to purchase the complete Toptica system, rather than obtaining a different type of LD and building our own ECDL.

The TA chip (Toptica TA-1135-0500-1) produces 224 mW output from 40 mW input. In order to best mode match to the TA we rotate the mode of the laser beam from the ECDL by 90°. The TA output mode is reshaped using cylindrical lenses and passes through a 60 dB optical isolator, to prevent back reflected light from damaging the TA, it is then fibre coupled. The TA mount is based on that described in [151]. It is illustrated in Fig. 4.5. Each lens is aligned by temporarily attaching its holder to an arm connected to an xyz-translation stage.[4] Once alignment is achieved, the ceramic dowel pins are inserted and glued in place with an epoxy. Once the epoxy has hardened the arm can be detached, leaving the lens in place. To stabilise the temperature, a Peltier element is used which is driven by a 5 A temperature controller (Wavelength Electronics PTC5K-CH).

The fibre coupled output of the TA is frequency doubled using a waveguide PPLN crystal (NTT Electronics WH-0565-000-F-B-C). Due to the high intensity inside the crystal, this process is very efficient; from an IR input of 200 mW, 70 mW of visible light is produced.

[4] This can be done using either a clamp, a small amount of super-glue, or nail-varnish.

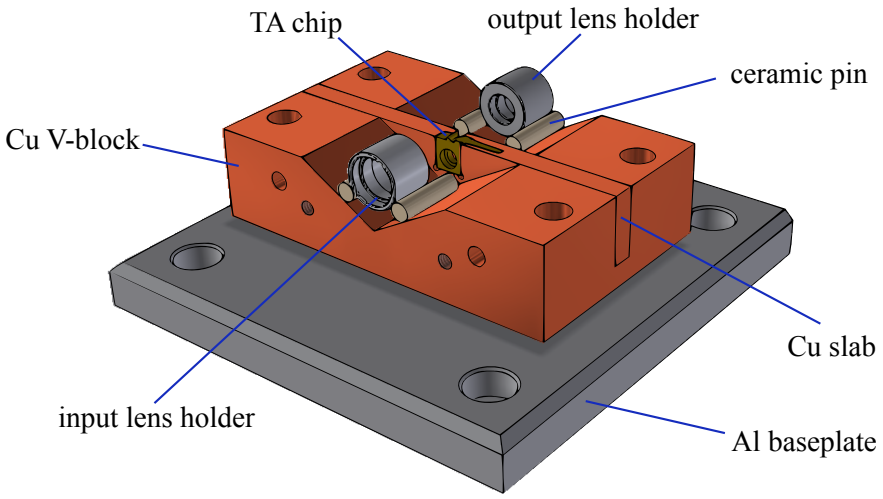

Figure 4.5: The TA mount. The copper V-block is 80 mm wide and V-angle is 120°. The focussing and collimation lenses are glued into aluminium holders using an epoxy. The brass C-mount of the TA is attached to the copper slab which is clamped inside a slot in the V-block. A Peltier element is clamped between the V-block and the baseplate, a 10 kΩ thermistor is positioned in a hole drilled in the V-block.

4.1.4 552 nm probe-laser(0,0)

In addition to laser(0,0), we have a second independent probe system at 552 nm which I will call probe-laser(0,0). We use this system for detection of molecules; it is beneficial to have an independent probe laser for detection so that we can change the detuning of the pump laser in laser cooling experiments without changing the detection frequency. For this system, we use a homebuilt IR ECDL, either a TA in a homebuilt mount or a Nufern YFA as an amplifier, and a free-space frequency doubling set-up.

The ECDL uses the same diode, and has a similar design to the laser(0,0) ECDL, with the difference that the mount housing the LD and grating is mounted at 90° to that of laser(0,0) ECDL, to assist with mode-matching into the TA. This ECDL uses similar electronics to those of laser(0,0).

The TA chip (Eagleyard photonics EYE-TPA-1060-00500-3006-CMT03) is salvaged from an older experiment, and mounted in the same way as that described for laser(2,2). Recently we have used one of the Nufern YFAs to amplify the light from the ECDL as it can produce more power than the TA.

The amplified output is frequency doubled using a similar set-up as in laser(0,0). Here we use a homebuilt PPLN crystal oven, Fig. 4.6, which is controlled by a commercial temperature controller (Thorlabs TC200-EC).

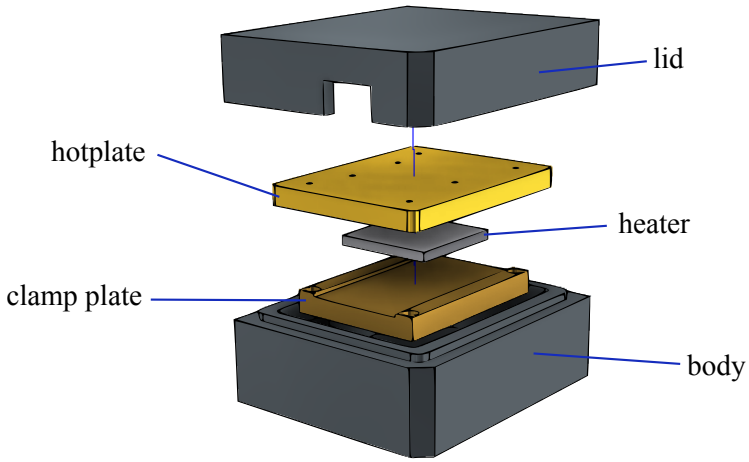

Figure 4.6: Exploded view of the PPLN oven. The hotplate is 45 mm wide. The lid and body are made of 25% carbon filled PTFE. The hotplate and clamp plate are made of brass. The metal-ceramic heater is clamped between these plates. A 10 kΩ thermistor is positioned inside a hole drilled in the underside of the hotplate. The crystal mount is clamped to the top of the hotplate; light passes through the notch cut into the lid.

4.2 Addressing the hyperfine structure

As discussed in Sec. 2.3.4, we require each laser to have multiple frequency components (sidebands) to address the hyperfine structure of the X-states. The energy separation between hyperfine states is in the radio frequency (RF) range. We produce the sidebands using electro-optic modulators (EOMs) and acousto-optic modulators (AOMs).

4.2.1 Addressing transitions using RF-modulators

Fig. 4.7 shows our optical set-up for adding sidebands to the lasers and combining the laser frequencies. We fibre couple all of the laser frequency components into the same fibre for convenience. This fibre takes the light to a different table where the vacuum chamber is situated. The energy separation between F states within X$(0, 1, 2...)$ is irregular, and differs for each state, so we use a different modulation scheme for each laser frequency. The relative frequencies and polarisations at the output of the sideband set-up are shown in Fig. 4.8.

To address the transitions from X(0), the light from laser(0,0) is split into three beams. We use the fundamental of laser(0,0) to drive transitions from X(0) $F = 1^-$, and so one beam is not frequency shifted. To address the other X(0) hyperfine states, light in the other two beams is shifted into the -1^{st} order using AOMs. The -192 MHz AOM is used to address the $F = 1^+$ state, and has a diffraction efficiency of 85%. The -159 MHz AOM is used to address both $F = 0, 2$ and has 76% efficiency at 159 MHz.

The fundamental of laser(0,1), drives transitions from X(1) $F = 2$ state. The 170 MHz

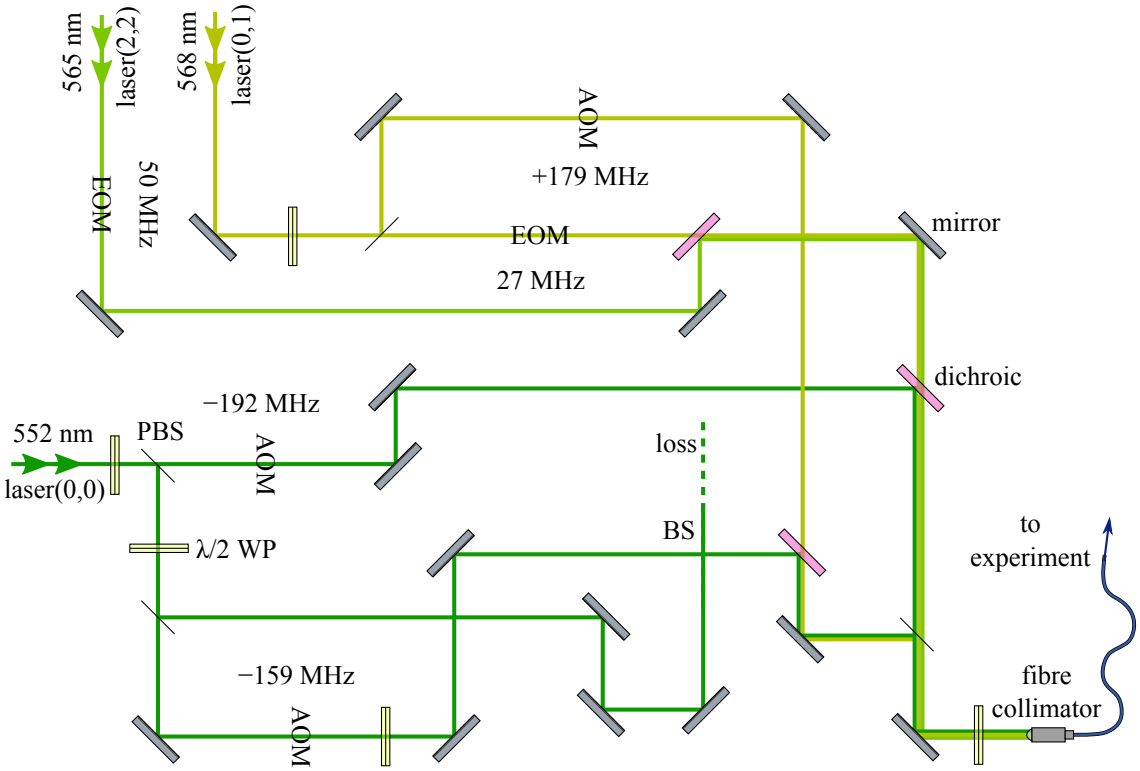

Figure 4.7: The optical set-up used to produce the sidebands to address the hyperfine structure of the X$(0, 1, 2)$ states, and combine the frequencies into an optical fibre. In the set-up, we use collimated beams with $1/e^2$ waist $\sim 0.75\,\text{mm}$.

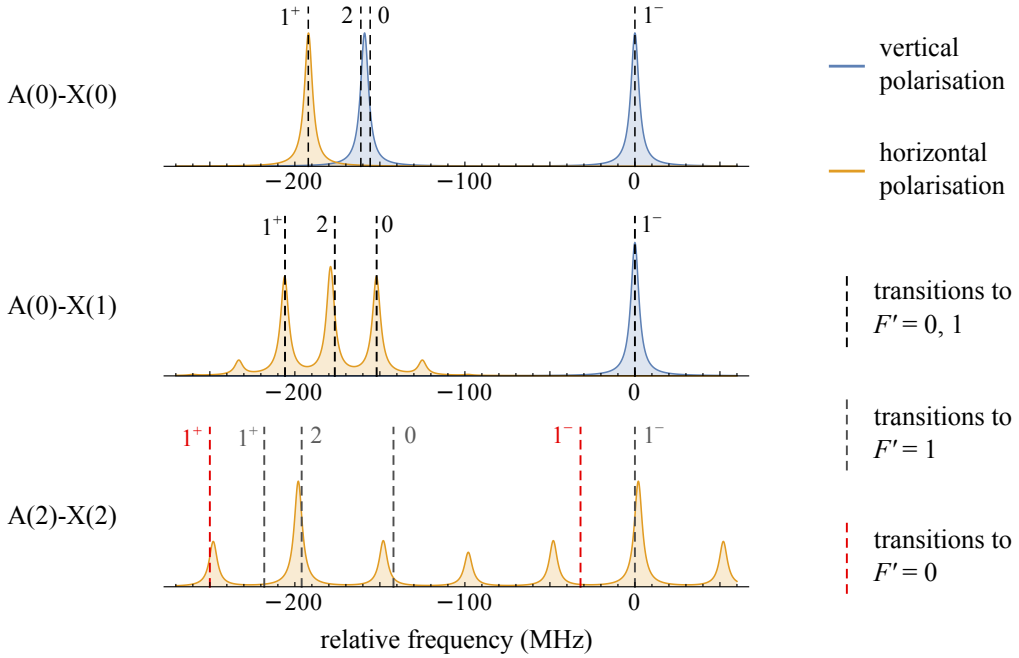

Figure 4.8: The frequency spectrum of laser sidebands produced by the modulator set-up (Fig. 4.7). Shaded curves represent the laser frequencies convolved with the natural linewidth for A-X transitions. The dotted lines are the transition frequencies which are labelled by the X-state F quantum number.

AOM shifts the light into the $+1^{\text{st}}$ order to address $F = 1^-$. The $F = 0, 1^+$ states are relatively evenly spaced from $F = 2$, therefore an EOM may be used to address both of them, by adding $\pm 27\,\text{MHz}$ frequency components to the fundamental.

For laser(2,2), it seems we can get away with using only one EOM at 50 MHz to generate all the sidebands required. We use the EOM to generate seven sidebands with appreciable amplitude of which four lie within $\sim \Gamma$ of a transition. In the A(2) state, we measured (Sec. 5.2.1) the hyperfine splitting to be 32 MHz, which is much larger than the unresolved splitting of A(0). This means there are six resolved A(2)-X(2) transitions, as shown in Fig. 4.8. To repump the X(2) state, we need only address four out of the six transitions, where the four transitions must be from each of the ground F states. Not addressing all six transitions on resonance will reduce the repumping rate from the estimation in Sec. 2.5.2. However, because we have a significantly larger amount of laser(2,2) power available than that calculated in the preliminary calculation, this can be compensated for by using increased power.

All of the beams containing different frequency components are combined and coupled into a single mode polarisation-maintaining optical fibre in the way shown in Fig. reffig:sidebandSetup. The fibre delivers light to the experiment.

In addition to the modulator set-up shown in Fig. 4.7 we also generate sidebands for probe-laser(0,0) using two AOMs in the same way as for laser(0,0). Sidebands are used for the probe laser such that the fluorescence signal can be increased when detecting molecules using optical cycling in the detection region.

All three of the AOMs we use (Gooch & Housego 3200-125) have large active areas of $2.5 \times 1.5\,\text{mm}$, and have acoustic resonances at 200 MHz. A high diffraction efficiency is obtained using collimated beams. In the modulator set-up, we aim for all the beams to have $1/e^2$ waists of $\sim 0.75\,\text{mm}$. The AOMs are all oriented such that the light is orthogonally polarised to the RF propagation direction which gives maximum diffraction efficiency.[5] The EOMs we use are homebuilt and their construction is detailed in the following section.

To generate the RF we use integrated voltage controlled oscillator (VCO) circuits (Mini-Circuits POS- series) which form part of homebuilt circuits used to adjust the RF amplitude and isolate the VCO from the load. To amplify the RF for the AOMs we use 1.6 W RF amplifiers (Motorola CA2832).

4.2.2 Homebuilt EOMs

At the CCM, we have built a large number of resonant EOMs. They are quite straightforward to build, and the only costly component required is the electro-optic crystal. Com-

[5] The −192 MHz and −159 MHz AOMs are mounted at 90° such that the RF propagates vertically.

pared to purchasing commercial EOMs, we have found it to be approximately a quarter of the cost per unit (for ordering a batch of 4-8 crystals). Typical EO crystals used for modulators are $KTiOPO_4$ (KTP) and $LiNbO_3$. In our modulators we use $LiNbO_3$, which is doped with 5% MgO in order to improve the resistance of the crystal to optical damage [152]. The design we use for resonant modulators is based on [153], and modulators built by the DeMille group [154]. A slightly different EOM design using a brewster cut crystal is shown in [155].

Basic EOM theory

An EO crystal is a non-linear crystal, whose refractive index is changed by applying an external electric field (E-field). In these birefringent crystals the effect of the E-field on the refractive index can be described by a third order tensor. However, if the laser polarisation and the applied E-field are both oriented along a principal axis of the crystal, the change in the refractive index, n, is

$$\Delta n = n_0^3 r \frac{E_\mathrm{m}}{2}, \tag{4.2}$$

where n_0 is the refractive index of the crystal in zero field, r is the element in the electro-optic tensor for the crystal axis, and E_m is the applied E-field. For $LiNbO_3$, the largest element in the EO tensor is r_{33} [156], which means that the largest change in the refractive index is along the extraordinary-axis, or z-axis, when an electric field is also applied along this axis. For some types of crystals, the E-field may produce a large change in the refractive index effect when applied orthogonally to the laser polarisation (for example, those using KD_2PO_4).

The E-field dependence on the phase shift that light of wavelength λ will experience when passing through a crystal of length l is therefore,

$$\phi = \frac{\pi n_0^3 r V_\mathrm{m}}{\lambda} \frac{l}{d}, \tag{4.3}$$

where V is the applied voltage, and $E_\mathrm{m} = V_\mathrm{m}/d$, where d is the separation between electric field plates. The voltage required to shift the phase by π is $V_\pi = \frac{\lambda}{n_0^3 r} \frac{d}{l}$.

The electric field of laser light with angular frequency ω can be written as $E(t) = E_0 \mathrm{e}^{\mathrm{i}\omega t}$. If the voltage across the crystal is varied sinusoidally, $V_\mathrm{m}(t) = V_{\mathrm{m}0} \sin(\omega_\mathrm{m} t)$, then the E-field of the light after passing through the crystal becomes

$$E(t) = E_0 \mathrm{e}^{\mathrm{i}\omega t + \mathrm{i}\phi_0 \sin(\omega_\mathrm{m} t)}, \tag{4.4}$$

where $\phi_0 = \frac{\pi {n_0}^3 r V_{\mathrm{m}0}}{\lambda} \frac{l}{d}$. This can be rewritten using the Jacobi-Anger expansion to give

$$E(t) = E_0 \mathrm{e}^{\mathrm{i}\omega t} \left(J_0(\phi_0) + \sum_{k=1}^{\infty} J_k(\phi_0) \mathrm{e}^{\mathrm{i}k\omega_{\mathrm{m}} t} + \sum_{k=1}^{\infty} (-1)^k J_k(\phi_0) \mathrm{e}^{-\mathrm{i}k\omega_{\mathrm{m}} t} \right), \tag{4.5}$$

where J_α are Bessel functions of the first kind of order α. From Eq. (4.5) we can see that the result of sinusoidal phase modulation will be a discrete set of laser frequency components with spacing ω_{m} and intensities proportional to $J_k(\phi_0)^2$. Since only the phase is being modulated, the output intensity is constant.

Instead of modulating the E-field sinusoidally, it can be modulated with an arbitrary waveform to generate different spectra. This is best done using a modulator where the EO crystal acts as a waveguide for the light. For these modulators V_π is small as $d \sim \lambda$, which simplifies the required electronics.

As well as modulating the frequency of laser light, an EO crystal can also be used as a variable waveplate (Pockels cell) to modulate laser polarisation. If the input polarisation of the laser is not aligned with a crystal axis, the output polarisation will be changed by an applied E-field. Because the crystal is birefringent, even in the absence of an E-field, it will act as a multi-order waveplate. This birefringence is changed with temperature, making the output polarisation temperature sensitive.

To modulate laser amplitude, a polarisation modulator can be positioned between two orthogonal polarising filters. Alternatively, a phase modulator can be placed in one arm of a Mach-Zender interferometer to adjust the relative phases between the arms on recombination. The interferometric method, however, requires the optical wavefront to undergo minimum distortion during transmission through the crystal.

Resonant EOM parts and construction

The $LiNbO_3$ crystals we have used are Y-cut with the Z-faces gold coated (or Cr+Au coated) to act as the electrodes. The ends should be AR coated for the laser wavelength. We have used $4 \times 4\,\mathrm{mm}$ cross section crystals with $l = 40\,\mathrm{mm}$ 5% MgO doped $LiNbO_3$ crystals (Supplied by Photonics Solutions and others).

The biggest problem that we have encountered is purchasing dodgy crystals. This has happened on a few occasions; in one purchase, the crystals we received had the incorrect faces gold coated, and in a different purchase, the crystal behaved as poor quality polarising filters.[6]

To make a sinusoidal phase modulator, the Au-coated crystal is used as the capacitor in a resonant LC-circuit as shown in Fig. 4.9(a). The resonant frequency of an LC circuit is

[6] Photonics Solutions did once supply us with crystals with the wrong faces Au-coated, but resolved this.

$\nu_{\text{res}} = \frac{1}{2\pi}\frac{1}{\sqrt{LC}}$. To estimate the capacitance of the crystal in the circuit, its DC-capacitance may be measured directly, or, we can assume the crystal to be a parallel plate capacitor with $C = \epsilon_0 \epsilon_r \frac{A}{d}$, where A is the area of one of the Au-coated surfaces, ϵ_0 is the vacuum permittivity, and ϵ_r is the dielectric constant. For lithium niobate, $\epsilon_{33} = 29$ [157], so, for our crystal $C \approx 10\,\text{pF}$. For the inductor, thin copper magnet wire is wound around a Teflon core.[7] For the 27 MHz EOM, a 3 mm diameter core was used with ~ 40 turns of 0.3 mm diameter magnet wire. To impedance match the 50 Ω transmission line input to the low impedance resonant circuit, a 1 : 16 RF-transformer (MiniRF XFA-0101-16UH) is used.

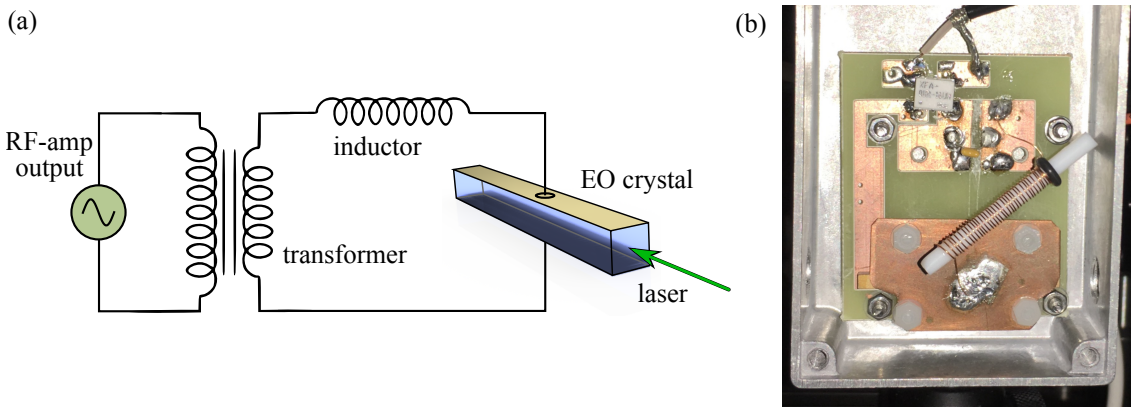

Figure 4.9: (a): The resonant EOM circuit. (b): A photograph of the modulator.

The crystal is mounted on top of a printed circuit board and clamped beneath a thin copper plate using nylon screws. A photograph of the mount is shown in Fig. 4.9(b). ν_{res} may be tuned by changing the number of turns on the inductor, or squashing or stretching the existing coil. We have used trimmer capacitors in series with the circuit to fine tune the ν_{res}, however, this tends to reduce the circuit quality factor.

Without the use of a network analyser, the resonant frequency can be tuned by connecting the circuit to the VCO through a pair of directional couplers to monitor the input and back-reflected RF simultaneously. This is done whilst scanning the VCO frequency to look for a phase shift between the input and back reflected signal. The RF is amplified using a $\sim 1\,\text{W}$ amplifier (Mini-Circuits ZHL-1A+). With maximum RF power, $\phi_0 \approx 5\,\text{rad}$ may be obtained, which is enough for our purposes.

We have not experienced any problems with this simple design. However, if the RF amplitude is to be changed during an experiment, beam pointing may change over $\sim 1\,\text{s}$ time-scales as the crystal heats and cools. This is discussed in [129], along with details for an improved mount design.

[7] Teflon is used as it has a small ϵ_r, so that the inductor is not lossy.

Polarisation switch

We have also attempted to build a fast $\sim 5\,\mathrm{MHz}$ square wave polarisation modulator for dark state remixing. However, results of optical Bloch equation simulations done by E. Hinds,[8] indicate that sinusoidal modulation can be just as effective. For the polarisation switch, the same $4 \times 4 \times 40\,\mathrm{mm}$ crystals as for the resonant EOM were used.[9]

To rotate the polarisation by 90°, the crystal's z-axis must be mounted at 45° to the laser polarisation. We can estimate the voltage required to do this from Eq. (4.3) by considering the effect of the electric field on the two refractive index components,

$$V_R = \frac{\lambda}{n_e^3 r_{33} - n_o^3 r_{13}} \frac{d}{l}. \tag{4.6}$$

For non-doped $LiNbO_3$ the refractive indices can be found from the Sellmeir equations in [158], for $\lambda = 552\,\mathrm{nm}$, $n_o = 2.32$ and $n_e = 2.23$. The EO tensor elements are $r_{13} = 8.6\,\mathrm{pm\,V^{-1}}$ and $r_{33} = 30.8\,\mathrm{pm\,V^{-1}}$ [156], which gives a calculated value for $V_R = 237\,\mathrm{V}$. The measured value for our crystal was 265 V. In preliminary testing, the crystal was clamped to an aluminium block oriented at 45° to the optics table using a springy clip. The block was temperature stabilised using a Peltier element with a 2.5 A commercial temperature controller. From the temperature, T, dependence of the Sellmeir equations in [158], we see that a ΔT of 0.5 K causes a $\sim \pi/2$ polarisation rotation.

A schematic of the circuit used for square wave modulation, designed by B. Sauer, is shown in Fig. 4.10. Using the circuit, the modulator could be driven at frequencies up to 1.3 MHz. The variable resistor in Fig. 4.10 was used to suppress ringing at the edges of the square waves; with this set to $130\,\Omega$, the rise time was $\sim 20\,\mathrm{ns}$. The high voltage, HV was set to $V_R = 265\,\mathrm{V}$. The output fraction of light in a given polarisation could be switched between $\sim 80\%$ and $\sim 20\%$. The fidelity of polarisation switching depended upon the width of the laser beam; with a smaller beam giving a higher switching fidelity. This indicates that either the crystal structure, or the electric field is not uniform across the laser beam inside the crystal. The electric field could be made to be more uniform across the width of the crystal by using crystals which are rectangular in cross section, with the same d but an increased width. This would reduce the effect of the fringe fields.

When the circuit was driven at frequencies approaching 1 MHz, there were additional higher harmonic frequency components to the polarisation modulation. It was determined that this was due to mechanical resonances driven by the piezoelectric effect in the crystal.

[8] The simulations were for a toy model (a Λ-system).

[9] We had intended to use smaller $2 \times 2 \times 40\,\mathrm{mm}$ Y-cut crystals, however these were Au-coated on the wrong faces. The smaller crystal will have approximately half the V_π, which reduces the demands on the electronics.

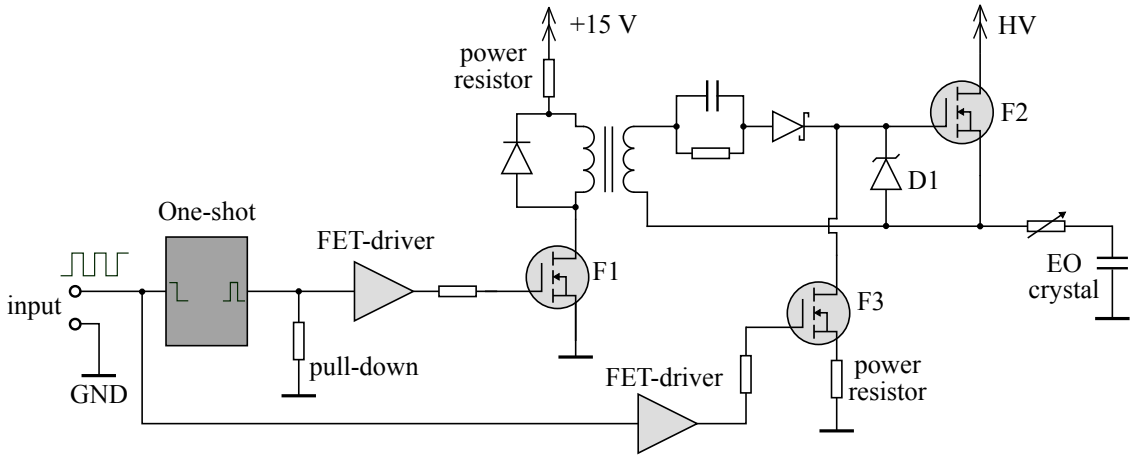

Figure 4.10: Circuit schematic for the fast polarisation switch. When driven with a square wave, the One-shot (Monostable Multivibrator) produces a short pulse on each falling edge. This opens the n-channel FET (field effect transistor) F1, allowing a current pulse through the transformer. The pulse opens F2 which supplies high voltage (HV), $\sim 200\,\mathrm{V}$ to the EO crystal's E-field plate. The Zener diode, D1, is used to maintain the gate-source voltage drop across F2 after the pulse. When the input square wave is high, F3 is open, this switches off F2 and discharges the EO crystal's E-field plate. The transformer is a few turns of magnet wire on a high permeability core.

This is a known problem in EO devices. In commercial designs, the crystal is usually clamped. The high frequency modulation in our device was prevented by clamping the crystal between lead plates and good contact was made between the electrodes using indium foil.

Typically, two crystals are used in series in commercial polarisation modulators, with their z-axes orthogonal to one another to passively compensate for temperature variation. This arrangement is shown in Fig. 4.11.[10]

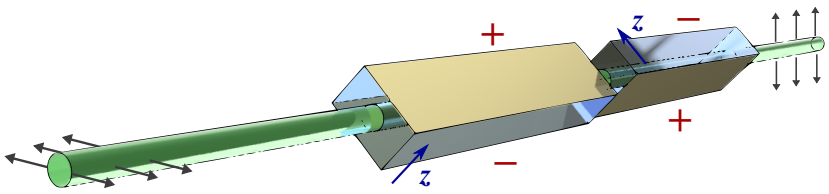

Figure 4.11: Illustration of a passively temperature stabilised polarisation modulator, z is the direction of the crystal's z-axis.

[10]This would be a change that I would make if building an improved design.

4.3 Experimental control

4.3.1 Computer control

The experiment is run using a computer using Scan Master software, which was originally written by J. Hudson [159]. This is used to control the timing of the YAG laser flash lamp and Q-switch, as well as the frequencies of the lasers. It is also used to read in the data from PMT and PD amplifiers. We also use this software to control any other devices required when collecting data, such as shutters or switching AOMs. Data is read into and transmitted from the computer using the analogue and digital inputs and outputs of several data acquisition (DAQ) cards (National Instruments).

4.3.2 Transfer cavity lock

The frequencies of the lasers can be locked with respect to a reference laser using a transfer cavity lock (TCL) based on that described in [160]. For the reference laser, we have used a stabilised 633 nm He-Ne laser, but have switched to using a 780 nm diode laser. This is stabilised to a sub-Doppler polarisation spectroscopy feature in ^{87}Rb. This system was built by T. Wall to a design based on [161], and is shared between a number of experiments. The reference is stable to < 0.5 MHz per hour and < 1.5 MHz per day, both of which are improvements over the He-Ne reference.

TCL operation

The TCL works by comparing relative frequencies of the laser to be stabilised (known as the 'slave') to the 780nm reference laser using a scanning cavity, and feeding back to the piezo of the slave ECDL to keep the relative frequency fixed.

In our system, photodiodes (PDs) are used to monitor the transmission of both slave and reference light through a confocal cavity with a fringe spacing of $\frac{c}{4L} = 750$ MHz, where the cavity length, L, is 100 mm. The cavity length is continuously scanned over approximately one fringe spacing using a piezo attached to one of the cavity mirrors. This is driven with a voltage ramp at ~ 12 Hz. The ramp and transmission signals are read into a computer using DAQ cards. For each ramp, the transmission signals for both reference and slave lasers are plotted as functions of cavity ramp voltage using a piece of software, that was originally written by S. Tokunaga [159]. The software fits a function to each transmission peak to find its voltage offset. The user chooses a relative voltage offset between slave and reference transmission peaks, and the software produces an error signal that is fed back to the piezo-driver of the slave ECDL in order to maintain the relative voltage offset. To scan the slave laser frequency, the lock point can be continuously adjusted.

For good operation, the cavity should have finesse $\gtrsim 100$, for both reference and slave laser wavelengths, and the reference and transmitted light from the two lasers must be separated and sent to separate PDs. This can be done using either dichroic or polarising beam-splitters.

TCL set-up

The experiment currently requires four lasers to be locked, laser(0,0), laser(0,1), laser(2,2) and probe-laser(0,0). We can lock these to the same reference laser without the need for a separate cavity for every slave laser, by combining and separating the light from different lasers using dichroic and polarising beam-splitters. For the four lasers we use two cavities, the optical set-up we use to do this is shown in Fig. 4.12.

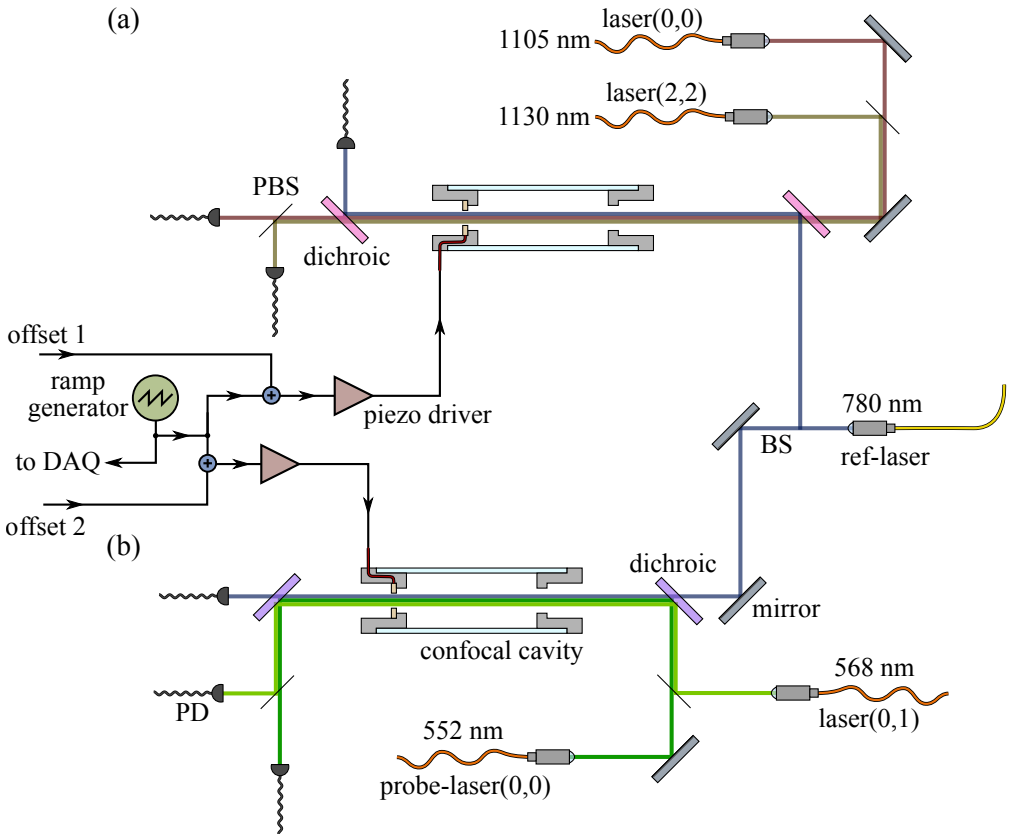

Figure 4.12: The TCL set-up. The cavity in (a) is used to lock laser(0,0) and laser(2,2) by using the IR light from the ECDLs. The cavity in (b) is used to lock laser(0,1) and probe-laser(0,0) using their frequency doubled output light. The output of the transimpedance amplifier of each PD is connected to DAQ card analogue inputs. The offset inputs are used to compensate for cavity drift, (for example, due to temperature changes) the computer feeds back to these to keep the reference laser peaks at fixed positions on the voltage ramps.

We do not mode match to the cavities; in fact some of the laser light is delivered to the set-up via multi mode optical fibres. In the symmetric confocal cavities used, resonances

for sets of even transverse electromagnetic modes, TEM_{mn} where $m+n$ is even, and resonances for sets of odd modes, where $m+n$ is odd, overlap with one another.

The transimpedence amplifiers for the PDs are homebuilt op-amp circuits. The cavities used are homebuilt to the design of J. Barry in [129]. They consist of a quartz tube spacer with steel end-caps which house the mirrors. The steel end caps hold the mirrors recessed in the quartz tube, which gives the cavity an athermal design; the temperature dependent cavity-lengthening expansion of the quartz tube is counteracted by the cavity-shortening expansion of the steel. The cavities are housed inside vacuum tight containers made from KF50 parts, but are not evacuated. This is to prevent drift due to changes in atmospheric pressure or humidity.

The cavity in 4.12(a) has broadband dielectric mirrors (Layertec 103282), which have reflectivity $(97 \pm 1)\,\%$ over the range $630 \rightarrow 1120\,\mathrm{nm}$ and are specified as output couplers.[11] The cavity in 4.12(b) has high reflectivity broadband dielectric mirrors (Layertec 105740), which have $> 99.9\%$ reflectivity over the range $500 \rightarrow 760\,\mathrm{nm}$.

Neither of these mirror sets is ideal for the locking cavity set-up: The IR mirrors give the cavity a high transmission, but a low finesse, reducing the accuracy of the software fit to find the peak centre. The visible mirrors give the cavity a high finesse, but a very low transmission of $\sim 0.1\%$ on resonance, indicating that there is significant absorption in the mirror substrates. Both cavities are adequate for our purposes, but could be improved by using a better choice of mirrors. A good compromise are mirrors which are $\sim 99\%$ reflective over the required range which are specified for use as output couplers, and so are AR-coated on the reverse. The piezo drivers used are homebuilt, and the voltage required for the piezo (Noliac NAC2123) to scan a fringe spacing is $\sim 35\,\mathrm{V}$ at $780\,\mathrm{nm}$.

Piezo linearity

Unfortunately, the extension of the piezos, $\frac{\mathrm{d}L}{\mathrm{d}V}$, is non-linear over the scan range, and also depends upon the ramp offset. Over an FSR for 780 nm light, $\frac{\mathrm{d}L}{\mathrm{d}V}$ can decrease (monotonically), with increasing V, by up to $\sim 17\,\%$. We have compared the piezo scan linearity with and without a resisting force on the piezo. This resisting force was due to the piezo pressing against a rubber O-ring as in the design in [129]. Without a resisting force, the voltage required to scan an FSR dropped to $\sim 25\,\mathrm{V}$, compared to $\sim 35\,\mathrm{V}$, however the scan linearity was not significantly changed. The $\frac{\mathrm{d}L(V)}{\mathrm{d}V}$ curve is not strongly dependent upon the scan ramp frequency; the linearity when the cavity is scanned with 10 Hz and a 30 Hz ramp is similar.

The linearity may be improved by replacing the single piezo element for a low voltage piezo stack. This may provide improved scan linearity as the extension of each piezo ele-

[11] We have previously used $> 99.9\%$ high reflective mirrors (Layertec 103950), but these made a cavity with a very low transmission.

ment in the stack is small, and the piezoelectric effect should be linear for small displacements. Piezo stacks are often used in commercial optical-cavity inteferometers, however a stack cannot be easily incorporated into the cavity design that we have used.

4.4 Combining laser beams using optical resonators

In order to address the hyperfine structure of the laser cooling ground states, a set of three or more laser frequencies are used which have irregular frequency separations of the order of 10 MHz, as discussed in Sec. 4.2.1. Currently, we combine these laser frequencies using either polarising or non-polarising beam splitters. When more than two of these frequencies are combined, a significant fraction of laser power is lost. For example, the first two laser beams may be combined on a polarising beam splitter in orthogonal polarisations (low loss), but then there is not an obvious way to combine a third beam without the loss of some large power fraction of both of the first two.

Therefore, as a kind of puzzle, I have tried to think of ways in which multiple laser beams with similar frequencies could be combined with low loss. This section discusses a method of doing this which I have tested.

4.4.1 Introduction

There are numerous applications that require the combination of multiple laser beams. The approaches that can be used to do this fall into two categories; coherent beam combining and spectral beam combining. Coherent beam combining requires pairs of beams to have the same frequency and relative phase stability. Beams are combined on a beam splitter, and the relative phases are set such that the fields are out of phase at one output, and in phase at the desired output. Spectral beam combining can be used to combine beams which have different wavelengths by use of a wavelength sensitive element such as a prism, a dichroic mirror, a diffraction grating, or a volume Bragg grating.

To combine two beams with very similar λ we must engineer some sort of wavelength sensitive optical element which has a substantially different effect on the two frequencies. Current methods of spectral beam combining require the frequencies of the beams used to differ by ~ 100 GHz [162], however we are interested in combining frequencies separated by ~ 10 MHz.

One possible method is to engineer an optical component which rotates the laser polarisation of the two frequency components differently. A possible method of doing this is shown in Fig. 4.13(a). First, the two frequencies are combined in orthogonal polarisations, then a wavelength dependent birefringent element (for example a polarisation maintaining fibre) is used to change the polarisations relative to one another such that

they arrive at the output in the same polarisation. Where frequencies of light are similar, the relative retardance will be small, and therefore the path length inside the birefringent material should be very long. Due to the long length, the loss during transmission through the birefringent element will most likely be high. Additionally, stabilising the output polarisation of such a device would also be challenging, and the technique is not easily scalable.

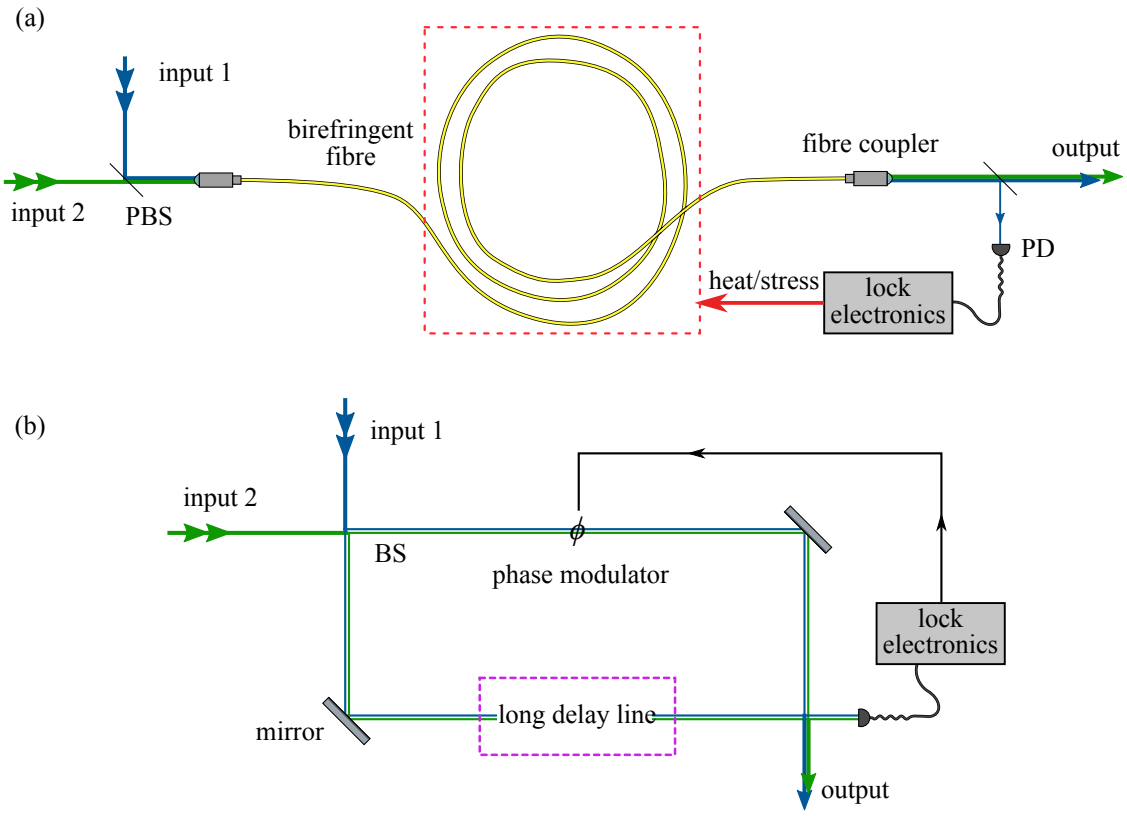

Figure 4.13: Possible methods of combining laser beams which have similar frequency. In (a), a polarisation maintaining fibre is used where light is coupled into the fibre at 45° to the optical axes. In (b), it is assumed that the phase modulator has approximately the same effect on both input beams, although their wavelengths are slightly different.

Fig. 4.13(b) illustrates an interferometric method, which is slightly more practical than Fig. 4.13(a). A Mach-Zehnder interferometer is used where the path length difference in the arms of the interferometer differs by a multiple of $\lambda/2$ for the two frequencies used.[12] For two frequencies of light with $\lambda = 500\,\text{nm}$ that differ in frequency by 10 MHz, the path length difference between the arms of the interferometer should be 15.5 m, which is a little impractical. It could be possible to scale this technique, with the condition that the difference in wavelength between all pairs of beams is $n\lambda_d$, where λ_d is common, and n is an integer.

[12] Remembering to account of the π difference in phase shift when light is reflected from the front versus the reverse of a beam-splitter.

A third option is to use an optical cavity as a dichroic element. Depending upon the cavity's FSR and finesse, $\mathcal{F}$, it may transmit one wavelength, and reflect a second, which can be very similar to the first. The technique is scalable to an extent, allowing perhaps tens of beams to be combined. To combine N laser frequencies, $N-1$ optical cavities are required. The relative frequencies of the input beams used should be fixed. The technique may be of use in atomic and molecular laser cooling or magneto-optical trapping experiments where several re-pump laser frequencies are required, but laser power is limited. Other applications could include very dense wavelength-division multiplexing in optical fibres, and power-scaling of laser systems.

I will discuss two such methods; the first uses a Fabry Pérot cavity, the second, a ring cavity. Results of experimental tests of the Fabry Pérot method are presented.

4.4.2 Fabry Pérot cavity combiner method

The optical set-up used to combine two beams using a Fabry Pérot (FP) cavity is illustrated in Fig. 4.14. The two laser beams used are labelled $b_{1,2}$, and have frequencies $\nu_{1,2}$, where $\nu_2 - \nu_1 = 180\,\mathrm{MHz}$. ν_1 is resonant with the cavity, therefore b_1 is transmitted. ν_2 is far from resonance, therefore b_2 is reflected. In order to overlap the beams, two $\lambda/4$ waveplates (WPs) and two polarising beam splitters (PBSs) are used as shown.

Beam b_1 arrives at PBS1 s-polarised, and is right-handed circularly polarised (r-polarised) by WP1. After being transmitted by the cavity WP2 returns it to s-polarisation, it is then reflected by PBS2. Beam b_2 is transmitted by PBS2 in p-polarisation. After WP2 it is left-handed circularly polarised (l-polarised), upon reflection from the cavity it becomes r-polarised. It is then made s-polarised by WP2, and reflected from PBS2.

Aligning the set-up so that the beams are overlapped is equivalent to mode matching both beams to the cavity. Lenses L1 and L2 are identical and are equidistant from the centre of the cavity. They are used to match both beam waists to that of the lowest order transverse electromagnetic mode of the cavity, TEM_{00}.

The cavity is locked to resonance with ν_1 using a Pound-Drever-Hall type technique [163]. Rather than locking the frequency of the laser to the cavity, the cavity is locked to resonance with the laser by adjusting its length, L, using a piezo attached to one of its mirrors. In order to generate an error signal, L is dithered over the transmission peak by sending a voltage ramp to the piezo. The back reflected power of b_1 is monitored on a PD. This signal is sent to a lock-in amplifier (EG&G Brookdeal 9503) which produces an error signal proportional to the phase of the oscillating PD signal with respect to the ramp. The back reflection from the cavity is minimised by feeding back the error signal to the piezo driver (homebuilt). The ramp frequency used was $\sim 200\,\mathrm{Hz}$.

The cavity used was confocal with $l = 100\,\mathrm{mm}$. It was homebuilt to the design in

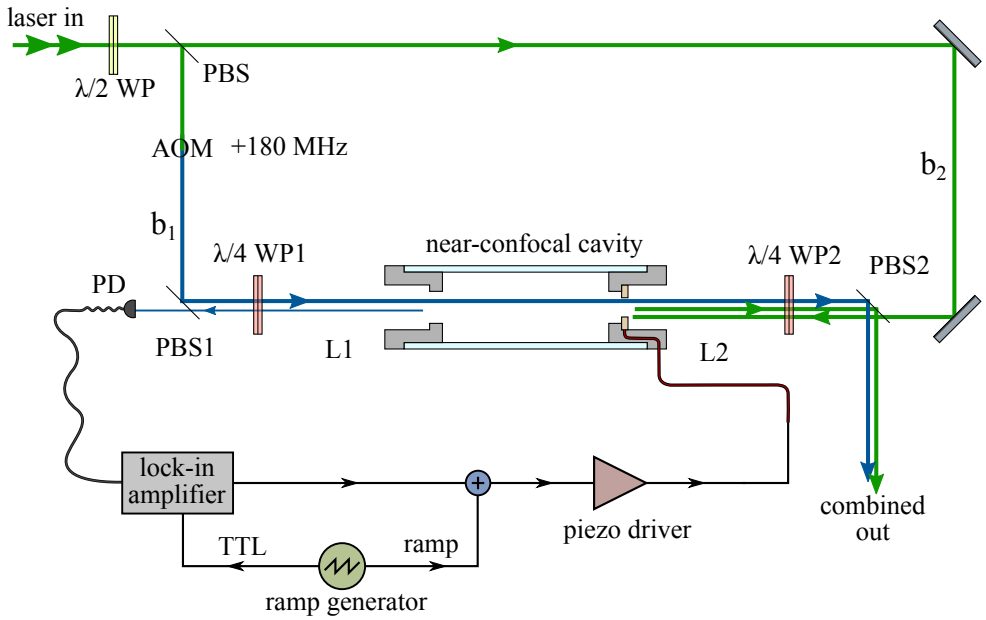

Figure 4.14: Schematic of the set-up used to combine laser beams using a Fabry Pérot cavity.

[129]. The mirrors were specified for use as output couplers, and had nominal radii of curvature 100 mm, reflectivities of (99.0 ± 0.5) %, and were AR-coated on the reverse (Layertec 103265).

The lenses were plano-convex spherical singlets with 250 mm focal length, and were chosen to mode match the input collimated beams with $1/e^2$ radii of 750 µm to the beam waist at the focus of the cavity, $w_0 = 95$ µm (accounting for the cavity mirrors, which are diverging lenses). The laser light was from laser(0,1), of wavelength 568 nm.

Alignment

The coarse mirror separation of the cavity may be adjusted. For alignment, the cavity length was initially set to the confocal configuration. With L1 and L2 removed the alignment of both beams to the cavity was optimised. This was done by scanning the cavity continuously over a few FSRs by driving the piezo with a voltage ramp. In a symmetric confocal cavity, all even Hermite-Gaussian TEM_{nm} modes ($n + m$ even) are resonant at cavity lengths $L = \lambda(p + 1/2)/2$, where p is an integer, odd $n+m$ modes are resonant when $L = \lambda p/2$ [164]. To optimise coupling into TEM_{00}, the beam pointing should therefore be adjusted to optimise the coupling into the even modes at the expense of the odd modes.

This may be done by overlapping the incoming path with the back reflected beam for each laser beam separately, by adjusting a mirror far from the cavity, then overlapping the two spots transmitted by the cavity by adjusting a mirror nearer to the cavity. This causes every alternate transmitted peak to increase in amplitude at the expense of their

neighbours, which can be viewed using a PD and oscilloscope. The input lens may then be replaced, and translated in x, y, z to further maximize the even mode signal.

The cavity length was then changed[13] to move the cavity away from the confocal configuration. This is so that the even modes no longer overlap. The TEM_{00} mode will have the largest amplitude, and the power in this mode can be further maximised by adjusting the beam pointing and lens positions for each beam in turn. The relative positions and profiles of TEM_{mn} modes are shown in Fig. 4.15. The cavity could then be locked to resonance with b_1, to combine the beams at the output. If desired, the output and PD position can be reversed to combine the beams such that b_2 is transmitted and b_1 is reflected.

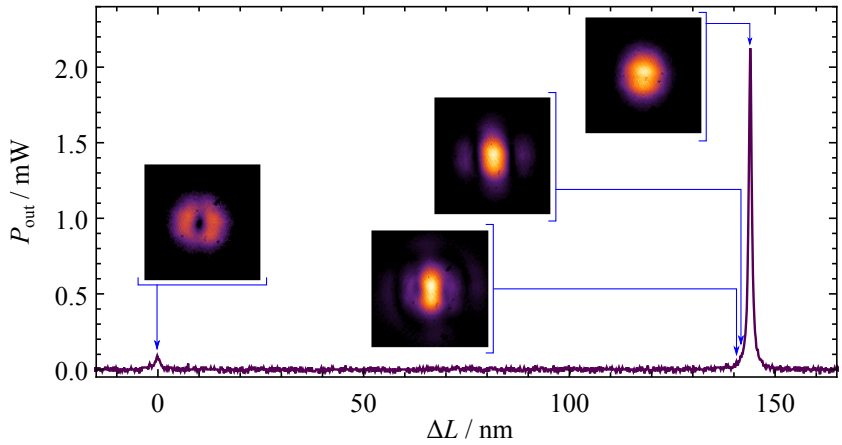

Figure 4.15: Transmitted power as a function of cavity length. The inset images show the profile of the transmitted modes at the positions indicated by the arrows. An odd mode can be seen at $\Delta L \approx 0\,\mathrm{nm}$, even modes are shown at $\Delta L \approx 145\,\mathrm{nm}$. For the even modes, the TEM_{mn}, $m + n \neq 0$ modes are unresolved from TEM_{00}.

4.4.3 Fabry Pérot cavity combiner results

The key parameters which specify the efficacy of the beam combiner are its efficiency, and the output beam quality. The efficiency is $P_{\mathrm{out}}/P_{\mathrm{in}}$, where P_{in} is the input power in $\mathrm{b}_{1,2}$, and P_{out} are their powers at the output. The beam quality can be quantified using the M^2 parameter [165]. This is a parameter which modifies the divergence angle, θ, of a laser beam in a given radial direction from that of a diffraction-limited Gaussian beam, for which $M^2 = 1$,

$$\theta = M^2 \frac{\lambda}{\pi w_0}, \tag{4.7}$$

where w_0 is the beam waist in that axis at the focus.

Fig. 4.16(a) is a plot of the output power of the cavity combiner as a function of the cavity's resonant frequency. Fig. 4.16(b,c) are plots of $P_{\mathrm{out}}/P_{\mathrm{in}}$ for b_1 and b_2 respectively.

[13] This was done by unscrewing the movable mirror holder in our cavity to increase the length by $\sim 0.5\,\mathrm{mm}$

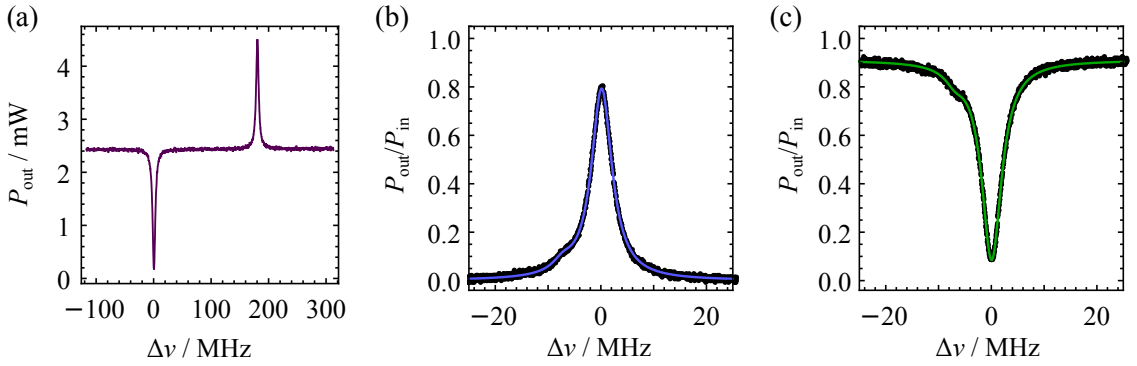

Figure 4.16: (a): The output power of the beam combiner as a function of the resonant frequency of the cavity. At $\Delta\nu = 0\,\text{MHz}$, b_2 is transmitted by the cavity, and at $\Delta\nu = 180\,\text{MHz}$, the beams are combined at the output. (b): The power fraction of b_1 transmitted by the cavity. (c): The power fraction of b_2 reflected by the cavity. In (b) and (c), black points are measured data and coloured lines are Airy model fits to the data. The asymmetry of the resonance features is primarily due to coupling into $m + n = 2$ modes.

To measure the efficiency with which b_1 was combined, P_{in} was measured after the AOM, and P_{out} was measured at the output for the cavity resonant with ν_1. For b_1, $P_{\text{out}}/P_{\text{in}} = (79 \pm 2)\,\%$. For b_2, P_{in} was measured before PBS2, and P_{out} was measured when the cavity was off resonance for this beam. For b_2 $P_{\text{out}}/P_{\text{in}} = (91.1 \pm 0.1)\,\%$.

The power loss of b_1 due to reflection from PBS1 and transmission through WP1 and L1 was $(4.4 \pm 0.1)\,\%$. The power loss of b_2 in transmission through PBS2, WP2, and L2 was $(4.98 \pm 0.05)\,\%$. The beam combiner power loss for b_2 is therefore predominantly due to back reflections from the optics.

As well as the $\sim 10\%$ loss in transmission and reflection due to the lenses and polarising optics, for b_1 there is an additional loss. The majority of this loss can be attributed to imperfect mode matching to the cavity. The power fraction of the input transmitted in the $m + n = 1$ modes is $\sim 4\%$, and that of the $m + n = 2$ modes is $(4.7 \pm 0.4)\,\%$. To find the power in the modes where $m + n = 2$, the function,

$$\frac{P_{\text{out}}}{P_{\text{in}}} = \frac{A_0}{1 + \left(\frac{2\mathcal{F}}{\pi} \sin \frac{\pi(\Delta\nu - \delta_0)}{\nu_{\text{FSR}}}\right)^2} + \frac{A_2}{1 + \left(\frac{2\mathcal{F}}{\pi} \sin \frac{\pi(\Delta\nu - \delta_2)}{\nu_{\text{FSR}}}\right)^2}, \tag{4.8}$$

was fit to the transmission signal. This is the sum of two Airy functions; A_0 is the power fraction of b_1 transmitted when the cavity is on resonance with the TEM_{00} mode, and A_2 is that transmitted at resonance with the $m+n = 2$ modes. $\delta_{0,2}$ are resonance frequencies for the modes. $\mathcal{F}$ is the finesse of the cavity. For equal reflectivity mirrors, of reflectivity $R \approx 1$, $\mathcal{F} = \pi\sqrt{R}/(1 - R)$. From fitted values of $\mathcal{F}$, we find that $R = (99.02 \pm 0.04)\,\%$.

To determine the M^2 parameters for the output beam, the transmitted and reflected outputs of the beam combiner were focussed, and the beam profiles were recorded using

a CMOS camera at positions along the beam propagation direction, z. The beam waist, w, in the x and y directions were found by fitting the function,

$$I = I_0 \exp\left(\frac{-2r^2}{w^2}\right) \tag{4.9}$$

to horizontal, $r = x$, and vertical, $r = y$, slices through each profile. To find M^2, the function

$$w = w_0\sqrt{1 + \left(M^2\frac{z - z_0}{\pi w_0^2}\lambda\right)^2}, \tag{4.10}$$

was fit to the data for w, which is the function for a Gaussian beam waist with its diffraction limited divergence angle modified by M^2. Here, w_0 is the beam waist in a given axis at the focus, and z_0 is the position of the focus in that axis. The data and fits are shown in Fig. 4.17.

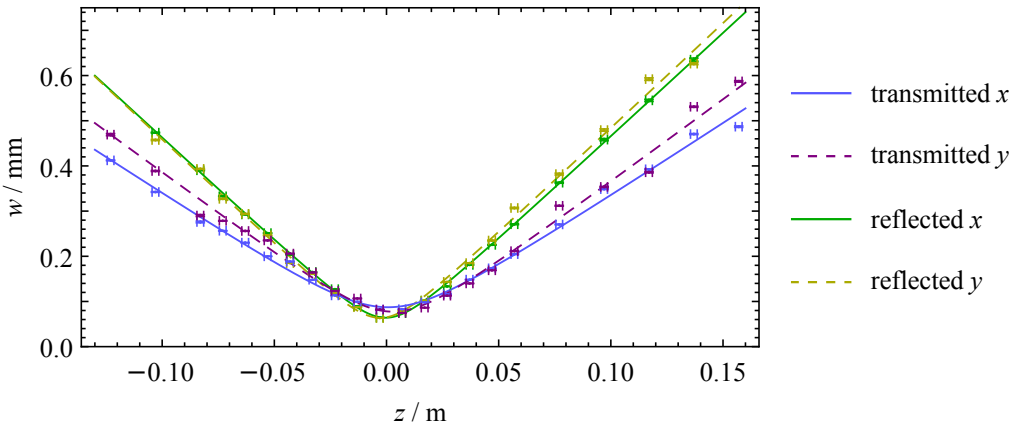

Figure 4.17: Measurements of the beam waists of transmitted and reflected beams, b_1 and b_2 respectively. Points are measured values and curves are fits to these data.

The fitted parameters for the beams are given in the following table.

		z_0/mm	w_0/µm	M^2
b_1	x	0.7(9)	87(5)	1.58(8)
	y	3(1)	77(8)	1.6(2)
b_2	x	−0.3(2)	64(2)	1.63(5)
	y	−2.7(8)	64(8)	1.6(2)

As can be seen from the w_0 parameters, the transmitted and reflected beams have different waist sizes. From z_0 it is determined that the beam transmitted by the cavity is slightly astigmatic. The transmitted mode of the cavity is slightly elliptical in the far field, with major axes which lie approximately along x and y. This indicates that the mirrors of the cavity are misaligned with respect to the optical axis. The M^2 parameters

of both the reflected and transmitted beams differ significantly from $M^2 = 1$ for an ideal Gaussian TEM_{00} beam.

Therefore, to improve the efficiency and the output beam quality, the alignment of the cavity mirrors could be improved by using tighter tolerances in its manufacture. Additionally, the spherical singlet lenses (L1 and L2) could be replaced with either aspheric or 'best form' lenses to improve beam quality. The input mode quality could also be improved. As well as power loss due to imperfect mode matching, there is a $\sim 10\,\%$ loss due to the other optics. This could be improved by using AR-coatings and polarising optics designed for high performance at single wavelengths, rather than those used which were designed for broadband performance. Nevertheless, this first test set-up already demonstrates that two nearby frequencies with the same polarisation can be combined into a single beam with an efficiency of 85 %.

This set-up could be used to combine beams with a frequency separation as small as 20 MHz with a similar efficiency as for the 180 MHz separated beams combined here. Combining beams with smaller frequency separations could be done using this method, but would require a cavity with higher finesse, low loss optics and the consideration of impedence matching. This technique could be used to combine laser beams with much higher power. In high finesse cavities with high input powers, the mirrors are susceptible to damage due to high intracavity intensity, however, dielctric mirrors with high reflectivity and low loss are available [166], and the beam waist at the mirrors can be chosen to be large, by using a different cavity geometry.

4.4.4 Ring cavity combiner

Beams may also be combined using a ring cavity. This scheme has some advantages over the FP-scheme. A scheme for doing this is shown in Fig. 4.18.

One advantage of the ring cavity is that polarising optics are not required to overlap the beams, because light is not reflected from the output coupler (M3) at normal incidence. This means that the power loss of the reflected beam may be significantly reduced from the FP arrangement as the reflected beam does not make two passes through a WP and PBS.

In Fig. 4.18, the simplest possible triangular cavity is shown, however other geometries (for example the bow-tie configuration) could be used. The beam waist is between mirrors M2 and M3. Because light is incident on M1 at a small angle, the cavity TEM_{00} mode will be astigmatic, but this astigmatism can be made to be small by minimising this incidence angle.

Another advantage is that a locking scheme may be used which does not require the cavity length to be dithered. In Fig. 4.18, a Hänsch-Couillaud type locking scheme is used

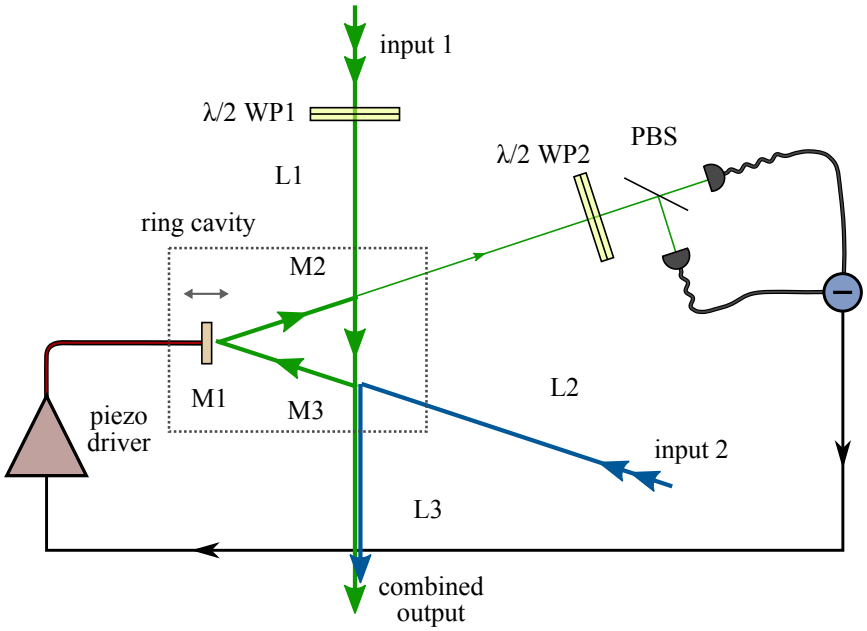

Figure 4.18: Schematic of a set-up which may be used to combine laser beams using a ring cavity.

[167, 168, 169]. In this scheme, rather than the cavity containing a separate polarising element, the dielectric mirrors act as birefringent elements for light that is reflected at non-normal incidence angles. The cavity may therefore be locked as follows; b_1 is either s- or p-polarised at the input with respect to the cavity. WP1 is used to rotate the polarisation by a small angle; this means that the back reflected light will acquire a new polarisation which is dependent upon the cavity length with respect to the length at resonance. The polarisation may be analysed using the PBS and two PDs, the difference signal from the detectors is an error signal to which the cavity may be locked. To lock the cavity to resonance, the angles of WP1 and WP2 are tuned.

This variant of the cavity combiner has not yet been tested. It would be interesting to test it and compare its efficiency relative to the Fabry-Pérot cavity design. The cavity combiner has the potential to be an efficient and robust way of combining multiple frequencies in order to deliver more power to the laser cooling experiment.

Chapter 5

Results I: Spectroscopy and optical cycling

In this chapter I will explain how we have identified the A(0)-X(1) and A(2)-X(2) transitions, and discuss our results in driving the quasi-closed cycling transitions necessary for laser cooling.

5.1 Addressing the A(0)-X(0) and A(0)-X(1) transitions

5.1.1 Optical cycling on the A(0)-X(0) transition

The first step towards laser cooling is to drive the rotationally closed A(0)-X(0) transition. To verify that this can be done using the three sidebands of laser(0,0) we made measurements of the increase in fluorescence when all X(0) F-states are driven simultaneously, compared to when they are not.

As described in Sec. 2.3, for single frequency excitation, only some of the X(0) F-states are coupled strongly to the excited state, therefore population is rapidly optically pumped out of these states and into the other F-states, and also to X($v > 0$). The molecule therefore only scatters a small number of photons, γ, within the interaction time, τ. When transitions from all X(0) F-states are driven simultaneously, γ will be larger, and now be limited by decay to dark m_F-states and X($v > 0$) states. The dark m_F-states may be destabilised by the application of a magnetic field (B-field) which is neither perpendicular nor parallel the laser polarisation. The application of a magnetic field should therefore increase γ further.

To measure the relative fluorescence for these cases, first, transitions were driven using a single laser frequency, and then with the sidebands added. The effect of the B-field was also investigated. These experiments were done using molecules produced from the double stage buffer gas source described in [131] in collaboration with J. Bumby. The

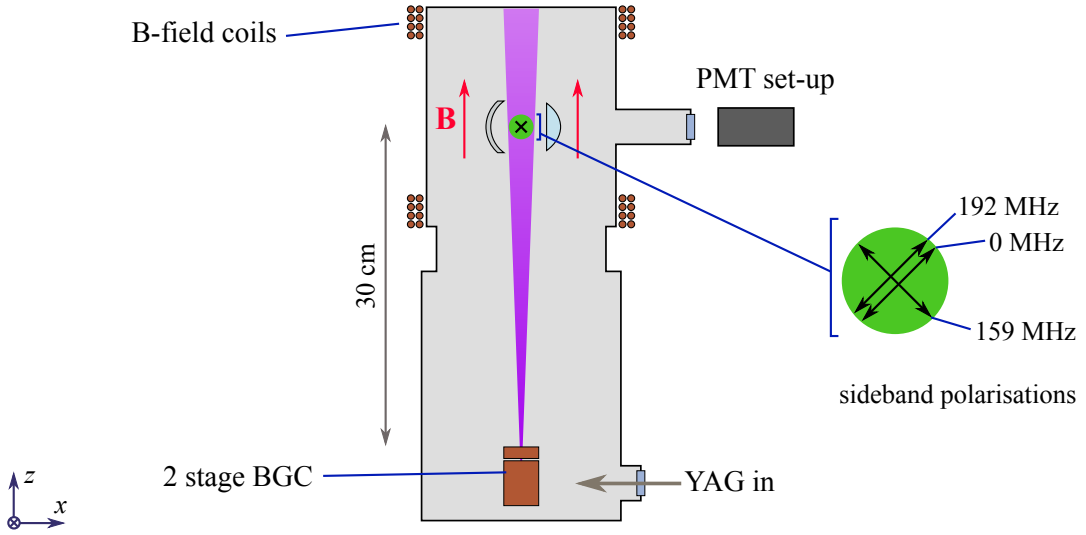

Figure 5.1: Set-up used for observing optical cycling on the A(0)-X(0) transition. The magnetic field is 45° to all laser polarisations. The PMT and collection optics set-up is the same as that illustrated in Fig. 3.5. The laser beam used had a $1/e^2$ diameter of $\sim 10\,\text{mm}$.

experimental set-up used is illustrated in Fig.5.1.

Optical cycling

The spectrum obtained using single frequency excitation with no applied B-field is shown in Fig. 5.2(a). This spectrum is overlapped with a line spectrum which was calculated from the molecular parameters in [120, 170].[1] The ^{174}YbF A(0)-X(0) transitions are the P(1) lines[2] centred around 542 807.9 GHz. The spectrum at the band head is quite complicated and some spectral lines overlap. The line spectrum contains all transitions of the ^{172,174,176}YbF isotopomers.[3]

The spectrum obtained when scanning each of the three laser components separately across the P-branch band head, and then summing the result is shown in Fig. 5.2(b), labelled 'separate sidebands'. The spectrum obtained by scanning all sidebands simultaneously is labelled 'simultaneous sidebands', and this is measured with and without a 0.25 mT B-field. As well as the applied B-field, dark states will be mixed by the Earth's magnetic field, $\sim 50\,\mu\text{T}$, and local magnetic fields in the lab. These were not compensated for in the experiment. The laser beam had a $1/e^2$ diameter of $\sim 10\,\text{mm}$, and the power in each sideband component was 4.6 mW.

From Fig. 5.2(b), we can see that γ is increased when the sidebands are used simultan-

[1] These two sets of parameters yield slightly different results for the spectrum close to the P-branch band head – neither of which quite matches the measured spectrum. The parameters from [120, 170] were averaged, and the $A^2\Pi$ T_v parameter for ^{172}YbF was adjusted to get the overlap in Fig. 5.2(a)

[2] By which I mean both the $P_1(1)$ and $Q_{12}(1)$ lines

[3] Probably, there will also be transitions in the other ^{170,171,173}YbF isotopomers in the range shown in Fig. 5.2(a), which are not labelled here.

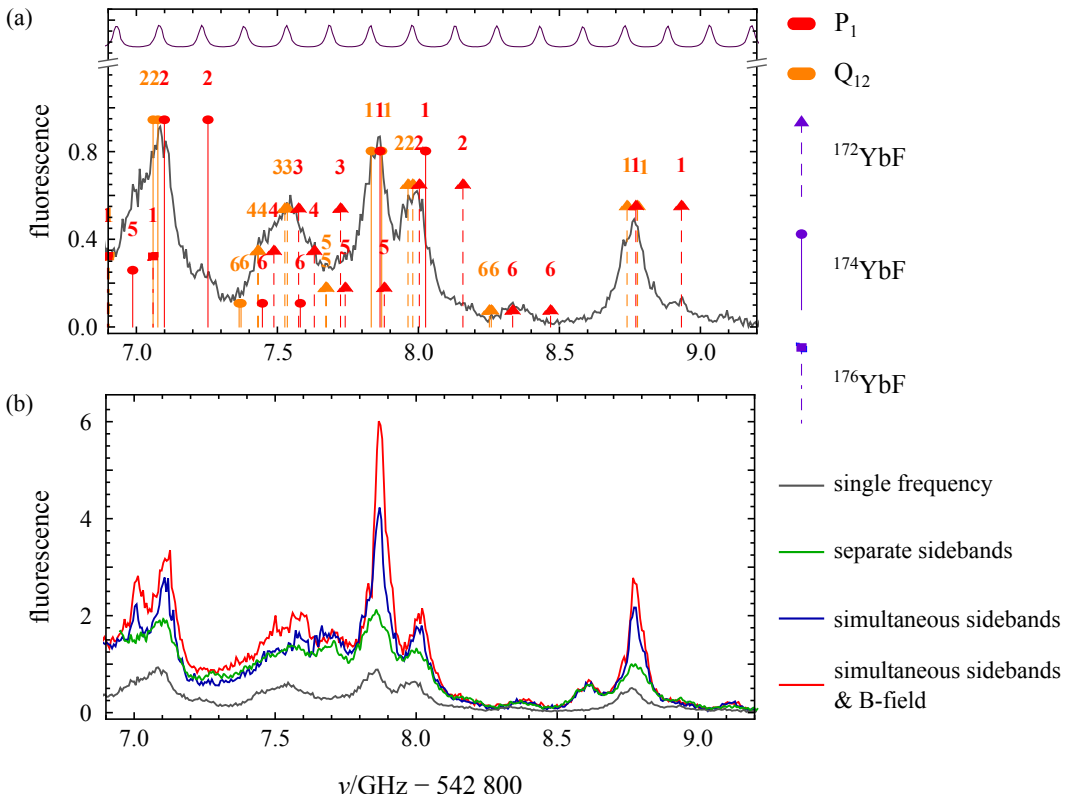

Figure 5.2: (a): The spectrum of part of the $A^2\Pi_{1/2}(v' = 0) - X^2\Sigma^+(v = 0)$ P-branch band head overlaid with a line spectrum of the P_1 and Q_{12} transitions, some lines overlap and cannot be seen. The lines are labelled with a coloured number, which is the ground state quantum number, N, of the state involved in the transition. Line lengths are weighted by the relative isotopic abundance, and N-state populations at 4 K. The spectrum exhibits significant power, and Doppler broadening. (b): Spectra for excitation with multiple frequencies. The single frequency spectrum in (a) is repeated for reference. The single frequency spectrum was recorded using the middle 159 MHz sideband. The spectra were linearised using the method described in Sec. 5.1.2.

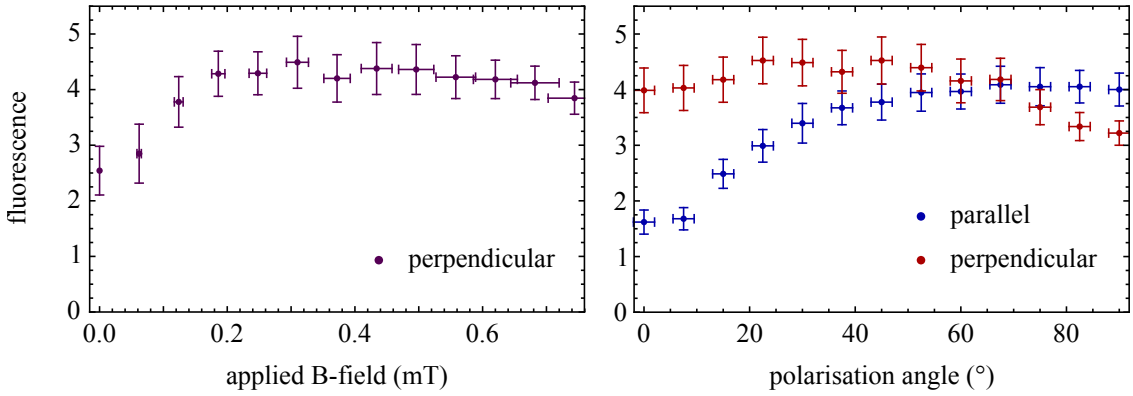

Figure 5.3: Fluorescence for optical cycling on the ^{172}YbF transition. Left: Polarisations are at 45° to the B-field. Each sideband has a power of 4.7 mW. Right: The effect of the angle between the magnetic field and laser polarisation on the rate of optical cycling for two relative polarisation orientations of the sidebands. Each sideband has a power of 3.7 mW and the B-field strength is 0.37 mT. The angle for the perpendicular polarisations is that of the 0 MHz and 192 MHz frequency components.

eously to drive the ^{174}YbF or ^{172}YbF A(0)-X(0) transition from the peaks at 542 807.9 GHz and 542 808.8 GHz. This shows that optical cycling is taking place. The application of a magnetic field further increases γ by mixing the X(0) $m_F = \pm 2$ dark states. We also see a small amount of cycling when the sidebands are resonant with the ^{174}YbF P(2) lines at 542 807.1 GHz, and the ^{172}YbF P(2) lines at 542 808.0 GHz. The $X^2\Sigma^+(N = 2)$ state has similar hyperfine intervals to $X^2\Sigma^+(N = 1)$, and there should be some increase in optical cycling when $N = 2$, F-states are addressed simultaneously even though the P(2) transition is not rotationally closed.

Effect of the magnetic field

To determine the effect of the magnetic field on the rate of optical cycling the laser was locked such that the sidebands were resonant with the ^{172}YbF P(1) transition. This was used rather than ^{174}YbF, because it is more isolated from other spectral features. The B-field strength and the angle of the laser polarisation with respect to the field were each varied.

Two relative orientations of the laser polarisation were used, the orientation labelled 'perpendicular' is that shown in Fig. 5.1 where the polarisation of the 159 MHz sideband is orthogonal to the other two. The orientation labelled 'parallel' is where all laser sidebands have parallel polarisations. The results of these measurements are shown in Fig. 5.3.

For the interaction time, τ, and the laser intensity used, we find the optimum field is ~ 0.3 mT for the perpendicular laser polarisations. For the parallel polarisations, the polarisation angle has a significant effect on fluorescence, with angles of $\sim 60°$ producing the most fluorescence. For the perpendicular polarisation, there is no strong dependence

but angles close to 90° are best avoided. At 90° the polarisation of the 159 MHz sideband which drives transitions from the $F = 2$ state is parallel with the B-field, meaning that the $m_F = \pm 2$ states will be dark to this sideband.

Comparison with model

Using the rate equation model that will be discussed in Sec. 6.2, the multi-frequency excitation spectra were simulated for the experimental parameters used. Fig. 5.4, shows a comparison between the model and experiment of the ^{172}YbF P(1) lines. In the model, all molecules traverse the laser beam at $150\,\mathrm{m\,s^{-1}}$, the Gaussian intensity distribution, and Doppler broadening effects are considered, but the forward velocity distribution is not, and all molecules traverse the laser beam at $150\,\mathrm{m\,s^{-1}}$. Modelling an ensemble of molecules with a forward velocity distribution more representative of that produced by the source (for example, a Gaussian distribution centred at $150\,\mathrm{m\,s^{-1}}$ with a $1/e^2$ full width of $100\,\mathrm{m\,s^{-1}}$) would not significantly alter the result. From the model, we can obtain a predicted average number of photons a molecule scatters whilst traversing the laser beam. In order to overlap the data with the model, the fluorescence axis for the data has been rescaled.

The FWHM of the measured resonance is 67 MHz whereas the modelled resonance is 21 MHz wide, and the increase in fluorescence for optical cycling with a remixing field is approximately half of the modelled value. There are a number of possible reasons for these discrepancies: Molecules in the beam could have a much higher mean forward speed than $150\,\mathrm{m\,s^{-1}}$, or there could have been a high frequency of molecule-helium collisions in the interaction region. It is likely that there are underlying transitions for the ^{170,171,173}YbF isotopomers. It is also possible that the magnetic field is not well modelled, or that there are significant coherent effects that the rate equation model does not capture.

To determine whether more power was required to saturate the cycling transition, saturation curves were recorded for the two sets of sideband polarisations. The angle of all polarisations was $\sim 45°$ to the B-field. The saturation curve is shown overlapped with the modelled curve, where the data has been rescaled to overlap with the model. In the model, there is no distinction between the two polarisation cases. The comparison indicates that the saturation intensity for the cycling transition is similar to the expected value. In the limit of high power, the number of photons scattered per molecule in the model is 14.3, which is $1/(1 - f_{0,0})$. This indicates that the transition was strongly saturated using 4.6 mW per sideband in a 10 mm diameter beam.

In conclusion, we find that the transition can be driven with strong saturation with laser intensities similar to those predicted by the model, and the modelled saturation curve, Fig. 5.4(b), is consistent with the experimental results. The model fails to explain

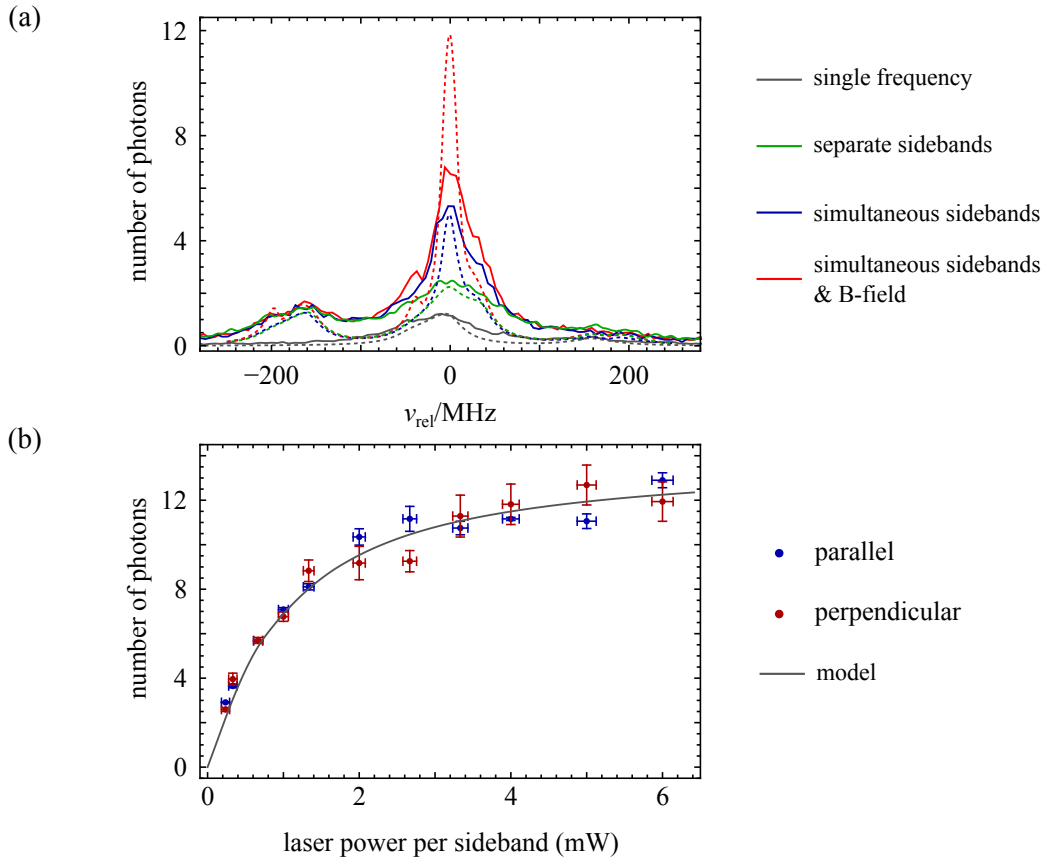

Figure 5.4: (a): Comparison of modelled multi-frequency fluorescence spectra with experimental results. The model results are the dashed curves. (b): Comparison between saturation curves for different sets of laser polarisation, and a modelled curve.

the relative amplitudes and linewidths of the resonant features in Fig. 5.4(a). This could be due to an estimate of the detection volume that is too small, or the molecules having a significantly faster mean velocity than expected. Molecule-helium collisions may also have played a role in pressure broadening the experimentally observed resonances. The model may not capture the effect of the magnetic field well, as it is incorporated in a phenomenological manner (see Sec. 6.2.1). This may cause the large difference between the relative amplitudes of the experimental and modelled 'simultaneous sidebands' plots in Fig. 5.4(a) when comparing those with and without an applied magnetic field.

5.1.2 Spectroscopy of the $A^2\Pi_{1/2}(v' = 0) - X^2\Sigma^+(v = 1)$ transition

We have measured a fluorescence spectrum spanning 30 GHz over the $A^2\Pi_{1/2}(v' = 0) - X^2\Sigma^+(v = 1)$ transition which includes the A(0)-X(1) laser cooling repump transition. This was done to identify the A(0)-X(1) transition and identify the surrounding spectral features.

The molecular source used was a pulsed supersonic beam made via the method described in [134], using the same molecular beam apparatus used in [171], with the calcium ablation-target swapped for ytterbium. In this method, YbF molecules are formed by ablating a Yb metal target, using a pulsed Nd:YAG laser ($\sim$ 10 ns pulse duration), into a gas pulse of sulphur hexafluoride (2%) and argon (98%). In the ablation plume, a chemical reaction takes place producing YbF radicals. The YbF radicals then become entrained in the supersonic expansion jet.

In the set-up, there was a skimmer 70 mm downstream from the pulsed valve with a 2 mm aperture. The interaction region was approximately 300 mm from the skimmer. Light from laser(0,1) was used to interrogate the molecular pulses, perpendicular to their direction of travel. Photons emitted in the direction orthogonal to both the laser propogation direction and the molecular beam were focused onto a PMT using the collection optics described in [172].

A set of 13 spectra were recorded, each $\sim$ 4 GHz in length. To produce the spectra, the frequency of laser(0,1) was scanned by changing the voltage, V, sent to the piezo of the ECDL linearly. The relative frequency of the laser, ν_{rel}, is not linearly proportional to V. So that V could be converted to ν_{rel}, a fraction of the laser light was coupled into a low finesse confocal Fabry-Pérot cavity with an FSR of $\nu_{\mathrm{FSR}} = 375$ MHz, whose transmittance was recorded during the scan.

To determine the relation between ν_{rel} and V, an Airy function is fit to the transmit-

tance signal, T_e, where ν_{rel} has polynomial dependence upon V,

$$T_e = \frac{A}{1 + F \sin^2(\pi\nu_{\mathrm{rel}}/\nu_{\mathrm{FSR}} - \phi)}, \tag{5.1a}$$

$$\nu_{\mathrm{rel}} = \sum_{n=1}^{m} a_n (V - V_0)^n, \tag{5.1b}$$

where $m = 3$ and a_n, F, A, and ϕ are free parameters. V_0 is the center voltage of each scan range. The 13 linearised spectra were then combined manually by overlapping the cavity fringes and fluorescence peaks. The resulting spectrum is shown in Fig. 5.5.

The spectrum is overlaid with a line spectrum of the calculated transition frequencies determined from the molecular constants measured in [120], which were determined by measuring the spectrum of the high lying rotational states. The absolute frequency of some transitions was coarsely measured using a wavemeter (HighFinesse MC8). In order to overlap the spectra, a global frequency offset of 1.5 GHz was added to the freqency of the measured spectra. Additionally, the frequency axis of the measured spectra is stretched by a factor 1.013 to improve the overlap with the calculated spectrum. This factor could possibly be attributed to the homebuilt reference cavity having an FSR of 380 MHz rather than the expected 375 MHz.[4] We also found that the molecular constant T_v in [120], for the ^{176}YbF isotopologue, must be adjusted to 501.895 cm^{-1} to fit our data, which is within the error in the reference value. The spectrum enabled us to identify the A(0)-X(1) transition for ^{174}YbF, which are the $P_1(1)$ and $Q_{12}(1)$ lines at $\sim$ 527 754.5 GHz in Fig. 5.5.

[4] A different, more relaible, $\nu_{\mathrm{FSR}} = 150$ MHz reference cavity was used when aquiring other spectra in this thesis.

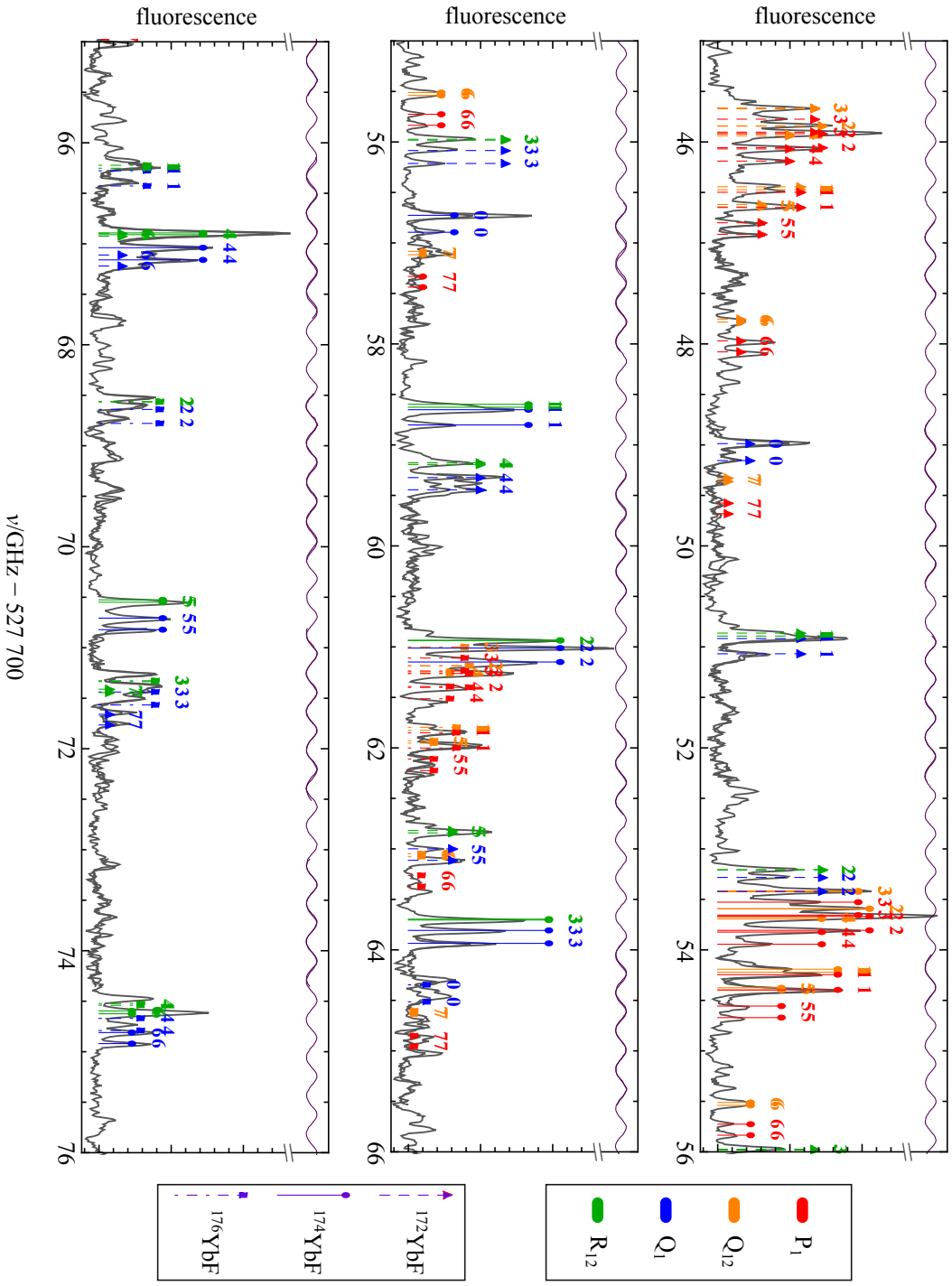

Figure 5.5: Fluorescence spectrum of the $A^2\Pi_{1/2}(v' = 0) - X^2\Sigma^+(v = 1)$ transition. Overlaid is a line spectrum for the ^{172}YbF, ^{174}YbF, and ^{176}YbF isotopologues calculated from the molecular constants in [120], and hyperfine parameters for ^{174}YbF from [119], which are assumed to be the same for ^{172}YbF and ^{176}YbF. The line colour represents the type of transition. The line style represents the isotopologue. Coloured numbers are the N quantum number for the ground state of the transition. The line length is weighted by the Boltzmann distribution for X-state rotational populations at 5 K, and relative isotopic abundance (rotational branching ratios are not considered). The sinusoidal lines are cavity fringes of each scan.

5.1.3 Optical cycling on the A(0)-X(0,1) transitions

Pumping into X(1)

After finding the A(0)-X(1) transition, we verified that the optical pumping was working as expected by doing a pump-probe experiment. In the experiment, laser(0,0) drives the A(0)-X(0) transition with sidebands with an applied remixing field of 0.4 mT. This has the effect of optically pumping population from X(0) into X(1). The population in X(1) is then probed using laser(0,1) to drive A(0)-X(1). This was done using a similar experimental set-up to Fig. 5.1 with an additional interaction and detection region for the probe laser $\sim$ 10 cm above the pump. The frequency of laser(0,1) is scanned to record a spectrum with and without the pump laser. For both pump on/off scans the B-field is applied.

As can be seen in Fig. 5.6, the population in X(1) increases by $\sim 2.5\times$. Although we have not measured the vibrational state population from the molecular source used for this experiment, if it is similar to the 1.0 : 0.4 ratio measured in Sec. 3.3.2, one would expect an increase in population of $3.5\times$ if τ is long enough such that all the population is pumped out of X(1).

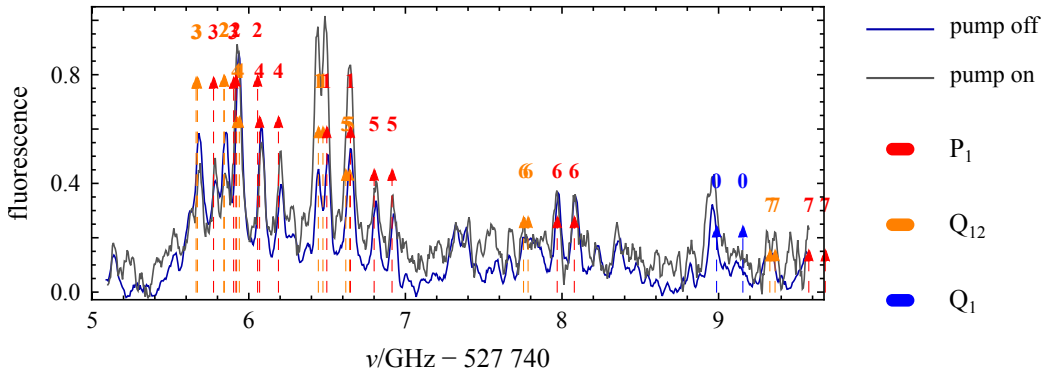

Figure 5.6: A spectrum showing optical pumping into the X(1) state of ^{172}YbF. The stick spectrum and associated labelling are the same as for Fig. 5.5.

In this experiment, the power per laser frequency component was 4.7 mW in a laser beam with $\sim$ 1 cm $1/e^2$ diameter. In Eq. 2.25 this gives $I/I_{\text{sat}} \approx 1$ and a scattering rate $R_\gamma \approx 1$ MHz. A molecule travelling at 150 m s^{-1} through the interaction region should therefore have time to scatter $\sim$ 65 photons, $\gamma = 65$. The probability of the molecule remaining in the X(0) states after this number of scattering events is $f_{0,0}^{\gamma} \approx 1\%$, suggesting τ is sufficient for optically pumping almost all of the population out of X(0). Therefore, when these data were taken, the optical pumping did not appear to be working as expected. One possible reason is that the pressure in the vacuum chamber was not low enough. If the pressure is too high, the number of collisions between YbF and helium may be high enough that there is a significant probability of a rotational or vibrational state-changing collision taking place. This has the effect of reducing the visibility of optical pumping in

an experiment. At the time when these data were recorded the vacuum chamber pressure was $\sim 10^{-5}$ mbar, as a relatively large 5 SCCM helium gas flow was used. It is therefore quite likely that the increase in population in the X(1) state was not as large as expected due to molecule-helium collisions distribution population from X(1) into other rotational states within the $v = 1$ manifold.

In conclusion, this experiment indicated that the laser sidebands used to address the A(0)-X(0) transition caused optical cycling and population was optically pumped into X(1) as was expected. The increase in population in X(1) was not as large as one would expect when considering the measured FCFs (Tab. 2.1), the estimated relative populations of the X(0) and X(1) states, and the expected scattering rate of molecules passing through the laser beam. This difference may have been caused by collisional redistribution of population amongst rotational states which occurred when molecules were travelling between the pump and probe region.

Optical cycling

The second step towards laser cooling is to drive the A(0)-X(0) and A(0)-X(1) transitions simultaneously. With all F-states addressed by the sidebands in Sec. 4.2.1 and a remixing field applied, the only loss of molecules should be to X($v > 1$).

To check that the optical cycling worked as expected we measured the increase in the number of scattered photons per molecule, γ, when driving A(0)-X(0,1) compared to A(0)-X(0) only. This was done using a similar set-up to that shown in Fig. 5.1 but with the single stage buffer gas source described in chapter 3, where molecules had a mean forward velocity of $\sim 200\,\mathrm{m\,s^{-1}}$. The laser beam had a $1/e^2$ diameter of 4.5 mm, laser(0,0) had a power of 14 mW per sideband, and laser(0,1) had a power of 30 mW per sideband. Results of the experiment are shown in Fig. 5.7.

The relative integrated amplitudes of the ToF profiles in Fig. 5.7 are 0.37 : 1.0 : 4.6. The large increase when laser(0,1) light is applied shows that molecules are being optically pumped from X(0) to X(1) and back. The spectrum shows that the resonance for the laser(0,1) sidebands is quite broad and has a FWHM of ~ 60 MHz. The non-zero fluorescence that can be seen in the 'spectrum' away from the resonances is due to the A(0)-X(0) optical cycling. The sharp dip in the centre of the peak appears to be a real feature, rather than noise, and is reproducible for a given B-field strength. This is probably due to the formation of a coherent dark state. Though interesting, we did not investigate this feature any further.

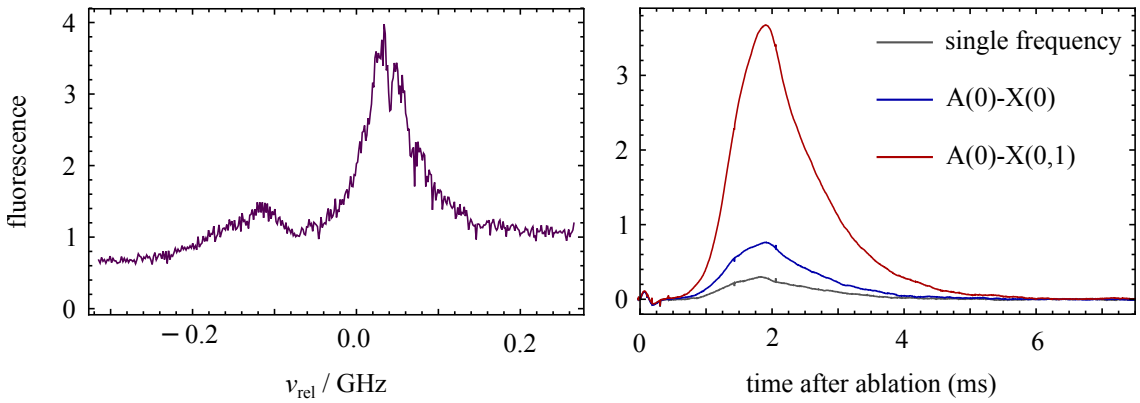

Figure 5.7: Optical cycling from driving A(0)-X(0,1). Left: Fluorescence as a function of the relative centre frequency of laser(0,1) as it is scanned over the A(0)-X(1) transition. For the duration of the scan, laser(0,0) is locked at resonance with the A(0)-X(0) transition. Both lasers have sidebands, as in Fig. 4.8. Right: ToF profiles with both laser(0,0) and laser(0,1), each with sidebands, locked at resonance with their respective transition. The curve for 'single frequency' excitation was measured at the frequency that produces maximum fluorescence for A(0)-X(0) excitation using a single frequency.

Comparison to model

Simulating the number of photons scattered by molecules travelling at $200\,\mathrm{m\,s^{-1}}$ through the laser beam using the model in Sec. 6.2, yields relative fluorescence signals with amplitude ratio 0.17 : 1.0 : 5.2, for the single frequency excitation, A(0)-X(0) excitation, and A(0)-X(0,1) excitation cases discussed in the previous section. The difference between single frequency and multi-frequency excitation on the A(0)-X(0) transition is significantly larger than the experimental measurement. However, the difference between addressing A(0)-X(0) and A(0)-X(0,1) is similar in the experiment and model.

The multi-frequency fluorescence spectrum in Fig. 5.7 was modelled, and is shown overlaid with the experimental data in Fig. 5.8. The fluorescence axis of the experimental data has been rescaled so that it is of comparable amplitude to the model. Although the model is quite simple, the shape of the modelled spectrum agrees remarkably well with the experimental data, showing that the model predicts the relative amplitude of the A(0)-X(1) peak compared to the A(0)-X(0) background correctly.

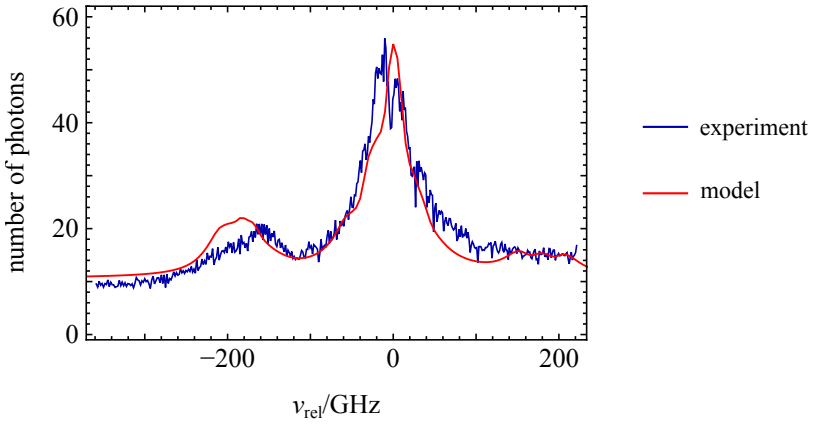

Figure 5.8: A comparison between experimental results and a model for A(0)-X(0,1) cycling. The vertical axis is the modelled number of photons scattered per molecule.

5.2 Addressing the A(2)-X(2) transition

By addressing A(0)-X(0,1) YbF molecules will scatter approximately 330 photons before being pumped into X($v > 1$). However, this is not enough to laser cool an appreciable number of molecules. More repump transitions must be driven. The next most important of which is A(2)-X(2). The spectrum of the $[561] - X^2\Sigma^+(v = 2)$ transition had not previously been measured, therefore we first had to find the frequency of the A(2)-X(2) transition, and then determine the hyperfine structure of the A(2) and X(2) states. This section explains how we did this.

5.2.1 Spectroscopy of the $[561] - X^2\Sigma^+(v = 2)$ transition

In order to find the A(2)-X(2) repump transition, we recorded the $[561] - X^2\Sigma^+(v = 2)$ fluorescence spectrum over a 100 GHz range so that we could assign the spectral lines. This was done using molecules produced from the single stage buffer gas cell described in chapter 3. The resulting spectrum is shown in Fig. 5.9. The spectrum is linearised using a fixed length, $\nu_{FSR} = 150$ MHz, reference cavity as described in Sec. 5.1.2.

The assignment of the spectral lines was not obvious; the spectrum did not match the lines calculated from previously measured molecular parameters [120]. Therefore, we did a pump-probe experiment to determine if any of the spectral lines we had measured belonged to transitions from the X(2) state. This was done by scanning laser(2,2) over each transition, every alternate shot, a pump beam composed of light from laser(0,0) and laser(0,1) was used which drove the A(0)-X(1,2) transitions before molecules reached the probe region. It was expected that when laser(2,2) was addressing either the P(1), Q(1) or R(1) transitions from the X(2) state, there would be an increase in probe fluorescence when the pump beam was on compared to when it was off, as the pump light would

optically pump molecules into X(2). In the experiment, the pump light counter-propagated with the molecular beam and was shuttered using an AOM. However, we found that the fluorescence from many of the bunches of spectral lines that we had found were enhanced by the pump. We found strong evidence that the reason for this was due to molecule-helium collisions causing rotational state change following optical pumping into X(2). These collisions resulted in increased populations in many of the rotational states within the $v = 2$ manifold. This evidence was found after the assignment of the transitions, by changing the delay between YAG ablation and the switch on time for the pump light, $t_{\rm on}$, whilst keeping the length of time for which the pump light was on fixed. The result was that for larger $t_{\rm on}$, the population increase in $N = 1, v = 2$ compared to $N \neq 1, v = 2$ increased. An explanation for this is that the pressure is highest within the charcoal and radiation shields near to the source. The higher pressure means more collisions, and therefore larger population in $N \neq 1$ states for smaller values of $t_{\rm on}$. These collisions would significantly reduce the effectiveness of laser cooling, therefore, we took measures (resulting in the set-up described in Sec. 3.2) to reduce the chamber pressure to the level where we no longer observe their effects. These measures included replacing the charcoal on the charcoal shields, and adding more charcoal sorbs to the cold plate (strips of copper coated in charcoal), and reducing the flow rate of helium through the buffer gas cell.

We were able to make the theoretical spectrum match with the measured result by adjusting the Λ-doubling coefficients, $p + 2q$, from those obtained through measurement in [120]. Values for the $p + 2q$ parameters for the ^{172,174,176}YbF isotopologues that fitted our measured data can be obtained by multiplying those in [120] by $\sim 4/3$.[5] This factor changes the structure of the calculated spectrum significantly. It is not clear why this parameter differs so substantially compared to the measurements and confidences quoted in [120], however the parameter has a larger effect on the position of rotational lines with small N, as measured in this experiment, than those with larger N, as measured in [120].

Our assignment of the spectral lines is shown in Fig. 5.9. To check that the assignment was correct, we compared sets of P(1) lines for ^{172}YbF and ^{174}YbF, and observed the effect of $t_{\rm on}$ on optical pumping as previously described.

[5] It is possible to adjust a number of parameters to make the calculated spectrum similar to that measured, but assignment in Fig. 5.9 requires the adjustment of the fewest, and gives a good match.

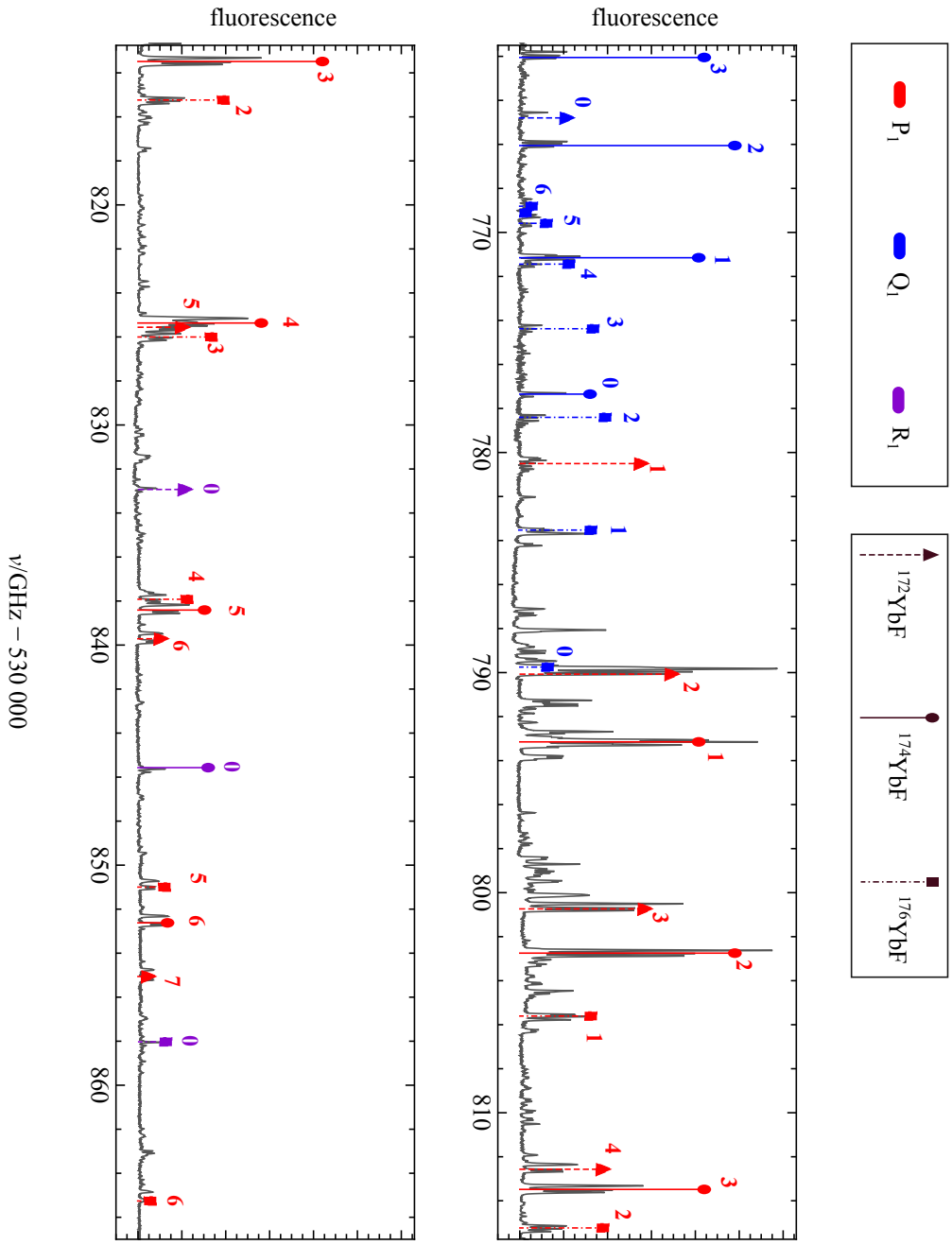

Figure 5.9: Fluorescence spectrum of the $[561] - X^2\Sigma^+(v = 2)$ transition. Overlaid is a line spectrum for ^{172}YbF, ^{174}YbF, and ^{176}YbF calculated as described in the text. The line colour represents the type of transition. The line style represents the isotopologue. Coloured numbers are the N quantum number for the ground state of the transition. The line length is weighted by the Boltzmann distribution for X-state rotational populations at 8 K, and relative isotopic abundance (rotational branching ratios are not considered). The spin-rotation and hyperfine structure is not calculated; the majority of the measured peaks within ~ 200 MHz of the calculated transition frequencies are due to this structure. Other unassigned peaks are most likely due to transitions in isotopologues other than ^{172,174,176}YbF.

5.2.2 Determining hyperfine structure of A(2) and X(2)

We then determined the hyperfine structure of the X(2) and A(2) states in order to decide upon a set of laser sidebands to generate for repumping X(2). To do this we looked at the fine structure of the P(1) and Q(1) transitions. The spectra were obtained using optical pumping, to obtain a large fluorescence signal, and the results are shown in Fig. 5.10.

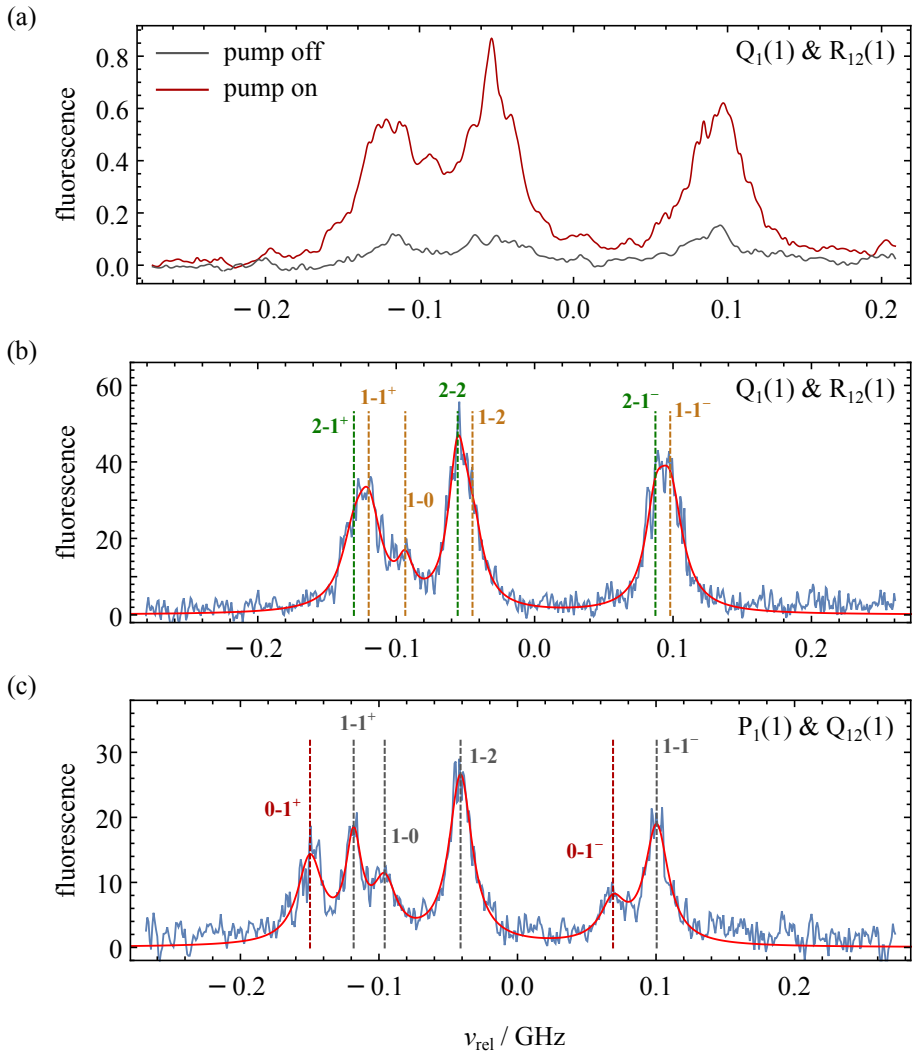

Figure 5.10: Hyperfine structure of the A(2)-X(2) P(1) and Q(1) transitions. (a): Fluorescence enhancement in the Q(1) transition with the counterpropagating pump beam. (b): Q(1) spectral line assignment, dashed lines are the estimated frequencies of the transitions obtained by fitting peaks to the data. Transitions are labelled F'-F. (c): P(1) spectral line assignment. Transitions are labelled as in (b).

There are six allowed P(1) transitions which may have distinct frequencies, depending upon the size of the hyperfine splittings, and whether transition frequencies happen to overlap. For Q(1), there are seven. Both P(1) and Q(1) share the $N = 1$ ground state, therefore the separations between some pairs of lines should be the same in both. Additionally P(1) transitions from the same F but to different F' will be separated by the

hyperfine splitting in the J' states. We also guessed which peak corresponded to transitions from $F = 2$ by applying a large magnetic field, and measuring the change in the width of the lines. This is because the transitions from $F = 2$ are broadened the most by the Zeeman interaction.[6]

Using this information, we can obtain the assignment for the spectral peaks shown in Fig. 5.10, and the state structure given in Fig. 5.11. The hyperfine splitting in $J' = 3/2$ is unresolved, therefore an accurate value for the Q(1) transition frequencies was not obtained. The P(1) transitions are well enough resolved for frequencies to be accurate to within ± 1.5 MHz. With the hyperfine structure of the X(2) state determined, we were able to design the optical system to apply the correct sidebands to the $v = 2$ repump laser. This set-up is shown in Fig. 4.7.

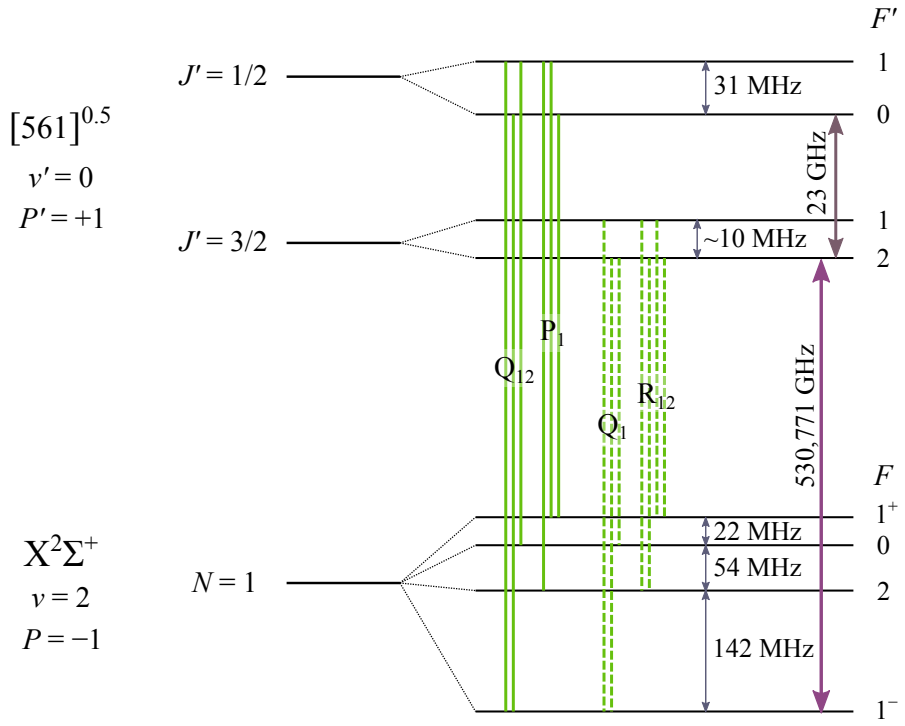

Figure 5.11: Deduced hyperfine structure of X(2) and A(2) states.

[6]The g-factor for $F = 2$ is $1/2$. We do not know its exact value for the X(2) $F = 1^-, 1^+$ states, but it must be $-1/2 > g > 1$ for each.

Chapter 6

Results II: Laser cooling YbF

This chapter discusses our progress in cooling a YbF molecular beam in one dimension. Doppler and sub-Doppler cooling is discussed, and Doppler cooling in the experiment is modelled.

6.1 Experimental set-up

6.1.1 Overview

For the transverse laser cooling experiments, the set-up shown in Fig. 6.1 was used. Molecules travel a distance l_1 from the aperture of the BCG to the start of the laser cooling region. Molecules then interact with the laser cooling light over a distance l_c. The laser cooling light consists of all of the sidebands to address the A(0)-X(0), A(0)-X(1) and A(2)-X(1) transitions (shown in Fig. 4.7). All of the laser frequencies that make up the cooling light are emitted from a single mode, PM fibre. The cooling beam passes multiple times through the vacuum chamber intersecting the molecular beam ~ 40 times, and making a small angle θ, with $\boldsymbol{x}$. In these experiments we have used a 5.5 mm $1/e^2$ diameter laser cooling beam. The lasers are polarised in the yz-plane with some frequencies polarised along $y = z$ and others along $y = -z$.[1] A magnetic field, $B\boldsymbol{z}$, is applied, where $\boldsymbol{z}$ is a unit vector in the z-axis. The molecules then travel through a 'clean-up' region where they interact with a laser beam containing all of the frequencies to address the A(0)-X(1) and A(2)-X(2) transitions, and a remixing B-field. This is to optically pump population from X(1,2) into X(0) after cooling.

The molecules are detected at either the lower or upper detectors which are at distances l_2 and $l_2 + l_3$ from the end of the cooling region. In the experiments described in this chapter, different values for l_1, l_c, and l_2, have been used, as the set-up has been modified between experiments. The detection is done by driving the A(0)-X(0) transition in the

[1] Neglecting the small polarisation component in $\boldsymbol{x}$ due to the beam propagating with angle θ to $\boldsymbol{x}$.

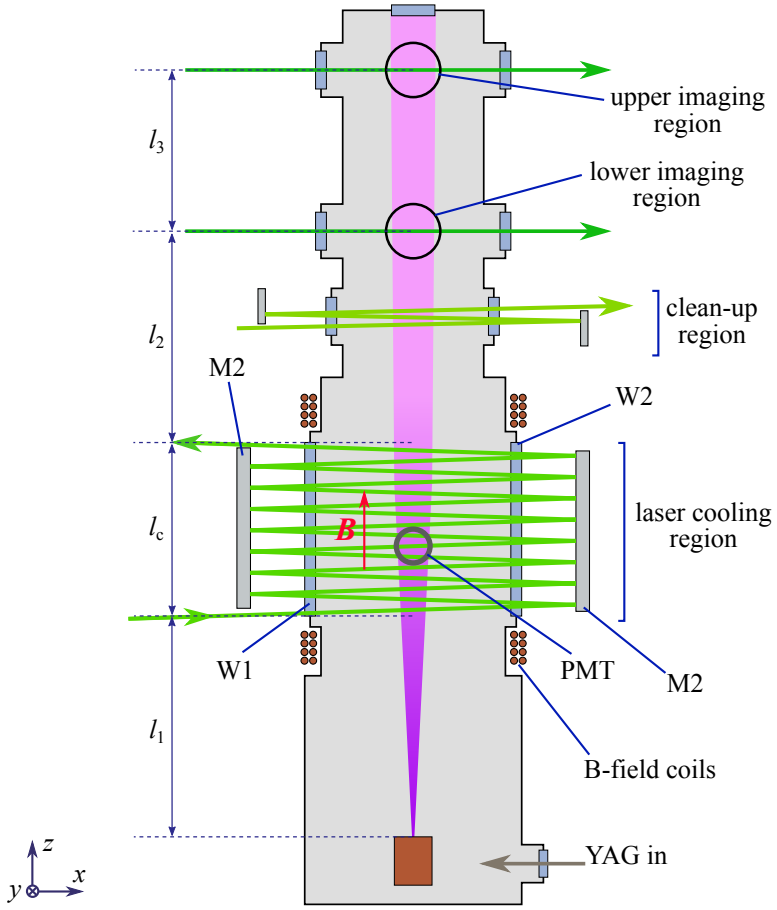

Figure 6.1: The experimental set-up used for transverse laser cooling.

presence of a remixing B-field and imaging the resulting fluorescence onto a CCD camera. Optical cycling is used in the detection region to increase the fluorescence signal so that the ratio of signal to noise in the image is improved.

In future, images will be recorded at both detection regions simultaneously (or on alternate shots) so that we can measure the expansion of the molecular beam between detectors. This will provide a better measure of the transverse temperature after cooling, but has not yet been implemented, and therefore l_3 is not used.

Both the windows (W1 and W2) and mirrors (M1 and M2) used in the laser cooling region are custom built (CVI Laser Optics). The windows are AR-coated for $< 0.3\,\%$ reflectivity per surface for the wavelengths of the lasers. The mirrors are broadband dielectric and have 99 % reflectivity for the laser wavelengths. We measure the loss to be $\sim 1\,\%$ per pass through the cooling region (i.e. for transmission through two windows and one mirror bounce). The length of the open aperture of the laser cooling windows is 200 mm in z, which is the maximum interaction distance, l_c. We estimate that the mean speed of our molecular beam is $180\,\mathrm{m\,s^{-1}}$, therefore the average time spent in the cooling region is ~ 1.1 ms. The spacing between the mirror surfaces in x is 400 mm.

Experimental considerations

In order to produce a collimated beam with a narrow position distribution, it is best to begin laser cooling as close to the molecular source as possible so that the beam will not have diverged far before laser cooling begins. However, we have previously found that there can be a high rate of molecule-helium collisions close to the source. These collisions can change the rotational states of molecules (see Sec. 5.2.1). We therefore leave a gap, l_1, between the source and cooling region. Our first transverse cooling experiments had $l_1 = 430$ mm. We later realised that this was too large and so we adapted the vacuum chamber such that $l_1 = 215$ mm.[2] With the gas flow rates (0.3 SCCM He, 0.01 SCCM SF_6) and values of l_1 used in experiments detailed in this section, we have not been able to observe effects due to collisions, so it is likely that reducing l_c further would be beneficial. We check for collisions by pumping molecules out of X(0), at the bottom of the laser cooling region and detecting if population has retuned to X(0) at the lower imaging region.

In order to see the greatest effect of the laser cooling it is best to detect far from the laser cooling region, as the contrast between cooled and non-cooled molecular beams increases with propagation distance. For the same reason, if two detection points are used, the spacing between the detectors should be large. Currently, we are limited by the height of the roof of our laboratory, however, a horizontal beam line is planned.

All optics are mounted on a second aluminium frame which surrounds the frame which

[2] The larger value of l_1 used was due to mechanical constraints at that time.

supports the vacuum chamber assembly. The additional frame is required because the vibrations produced by the cryocooler pump cause the vacuum chamber and its support frame to vibrate. Initially, the optics were mounted to the same frame as the vacuum chamber, and we were unable to damp the vibrations such that the pointing of the laser cooling beam (after multiple passes) was not affected.[3]

It is worth considering the best configuration for multi-passing the cooling light. Some possible options are shown in Fig. 6.2. We have used configurations (a) and (b), however other configurations may offer an advantage. For configurations (a,b,d), the faces M1 and M2 should both be parallel with $\boldsymbol{z}$. If they are parallel to one another, but at angle θ to $\boldsymbol{z}$ then molecules will be cooled towards a non-zero transverse velocity, $v_x = v_z \tan\theta$, where v_z is the forward velocity of the molecules. Configuration (c) was used for Sisyphus cooling in the first demonstration of laser cooling a diatomic molecule [23]. This arrangement was chosen because it produces standing waves at the top of the cooling region which are necessary for Sisyphus processes.

6.1.2 Photographing molecules

Molecules are imaged using a CCD camera (Hamamatsu ORCA-R2 C10600-10B). The camera was chosen for its low readout noise, which we measure to be ~ 6 electrons per bin. The CCD has 1344×1024 pixels which may be binned individually or in larger sizes on-chip (into bins of up to 8×8 pixels) to improve the signal to readout noise ratio at the expense of resolution. In our experiments, readout is the dominant source of noise and therefore we use bin sizes of 8×8 pixels. The CCD has a total area of $8.67\,\text{mm} \times 6.60\,\text{mm}$.

The lens arrangement used for imaging is shown in Fig. 6.3(a). We chose to use this two lens arrangement, rather than position the camera closer to the chamber and use only the camera lens, because we had originally wanted to be able to quickly swap between arrangement (a) and (c) to change the demagnification without moving the position of the camera (by removing the $f = 200\,\text{mm}$ lens and adjusting the position of the camera lens).

The 200 mm lens is a spherical singlet with 75 mm diameter. The camera lens assembly has an effective focal length of 35 mm, and an f-number of 1.4 (Thorlabs MVL35M1). This arrangement gives a measured demagnification of 5.46 ± 0.02, and therefore a field of view of length 47 mm in x. The lenses are mounted as shown in Fig. 6.3(d), where the alignment plate is used only to position the camera, not support it. For the optics arrangement used, and for the two others shown in Fig. 6.3, the field of view, and collection efficiency as a function of transverse position are shown in Fig. 6.3(e). This was measured by imaging a uniformly illuminated white piece of paper and ruler. We chose to use arrangement (a)

[3] We had originally intended to install a mirror rather than one of the windows on to the vacuum chamber in order to reduce the laser power loss per pass through the cooling region, however the vibrations caused by the cryocooler prevented this from being viable.

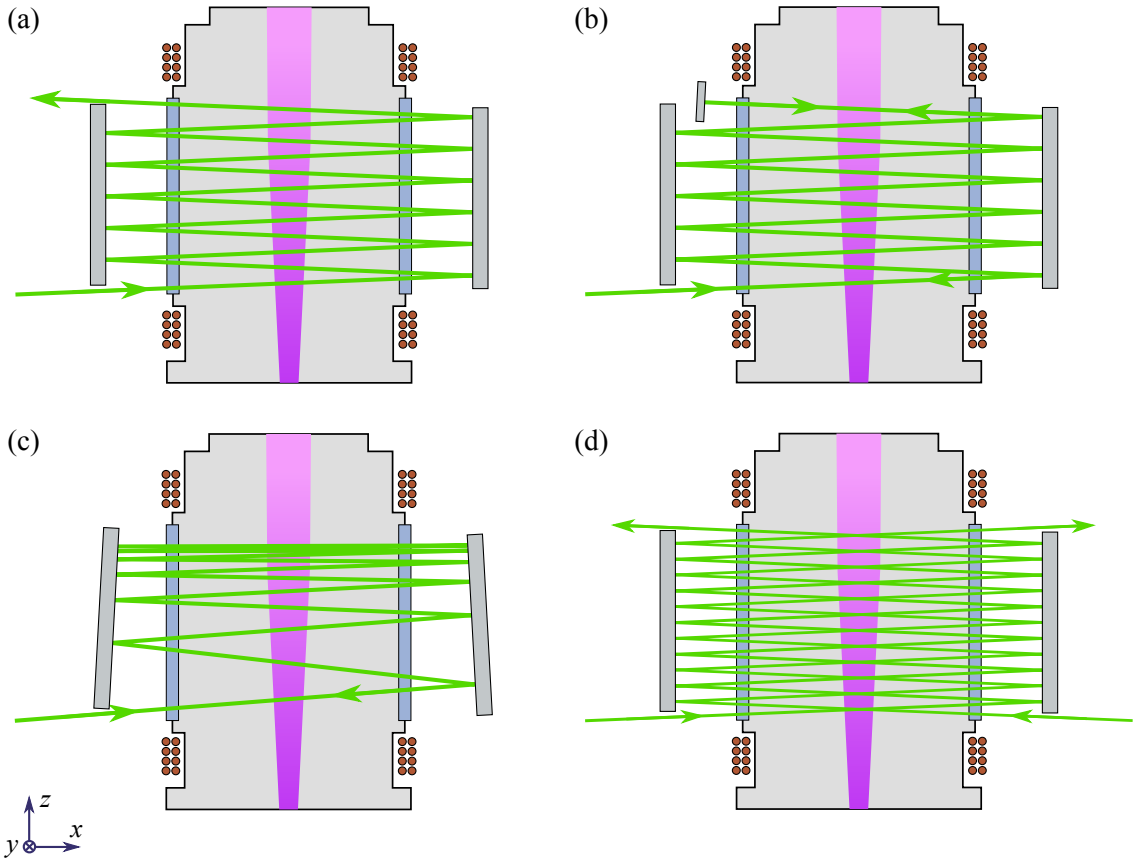

Figure 6.2: Some possible configurations of the multi-pass set-up in the laser cooling region. (a): Light enters the cooling region at the bottom, and leaves at the top. The spacings between mirror bounces in z are equal. (b): As in (a), but the light is retro-reflected at the top, to follow the same beam-path in reverse down the cooling region. (c): The mirrors are angled such that light travels up the cooling region, and then back down. At the top of the cooling region the propagation direction is orthogonal to z. (d): Two beams, each containing all frequency components are used. On each pass through the cooling region, they intersect at the centre of the molecular beam in x.

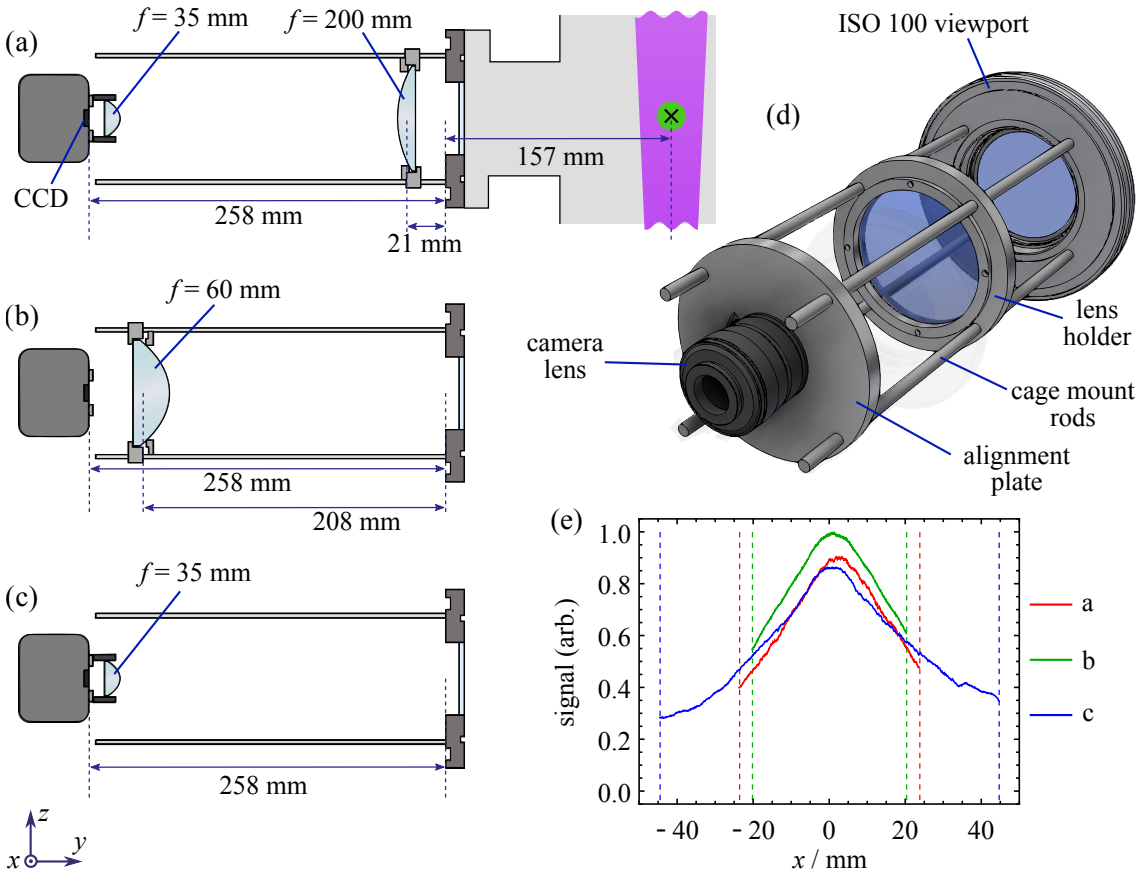

Figure 6.3: (a,b,c): A set of different arrangements of imaging optics. Arrangement (a) was used for laser cooling experiments. Arrangement (b) gave a similar collection efficiency to (a), however resolution was poor, perhaps because the lens had poor surface smoothness. Arrangement (c) provides a wider field of view, however, due to this the collection efficiency per unit area is decreased. (d): A drawing of the imaging optics. (e): The collection efficiencies and fields of view, dotted lines, for arrangements (a,b,c).

over (b) as the resolution of the images produced using only the $f = 60\,\text{mm}$ asphere was very poor. Although arrangement (a) and (c) appear to have a similar collection efficiency in Fig. 6.3(e), the area imaged by each pixel for arrangement (c) is 3.46 times larger than that for (a).

Because the ISO viewport is clamped against an O-ring, the alignment of the optics can change due to the force exerted by each clamp. The use of CF flanges would offer greater reproducibility. A larger source of misalignment is the lack of sturdiness of the cage mount assembly. Therefore, a more robust design should be used for future experiments.

6.2 Modelling laser cooling

Before starting the transverse laser cooling experiment, we modelled it, in order to design an experiment with good parameters. This was done using a rate equation model, which can model Doppler, but not sub-Doppler, forces.

6.2.1 Model

Rather than using the solutions to the rate equations derived in Sec. 2.4, here we use a more realistic rate equation model to capture the effect of molecules interacting with multiple laser beams, frequencies and polarisations simultaneously, and to include the transition strengths for each $|F', m'_F\rangle$-$|F, m_F\rangle$ transition. These effects are not included in the steady-state analytical solutions in Sec. 2.4. The approach used follows that used in [38], to model magneto-optical trapping in systems with complicated level structures. In the model, excitation rates are calculated for every pair of ground and excited states, and for every laser component (direction, intensity, polarisation and frequency), and the rate equations for the populations of all internal states and the acceleration are solved numerically.

The molecule, has a set of ground states, g, and excited states, e, with populations n_g and n_e, interacting with a laser field with components, ρ. Each laser component has angular frequency ω_ρ and propagates in the direction of unit vector $\boldsymbol{k}_\rho$. Laser frequencies are similar, and a single wavelength is used to calculate the recoil velocity for all components, $\lambda \approx 2\pi c/\omega_\rho = 552\,\text{nm}$. There is a uniform magnetic field, $B\boldsymbol{z}$. All excited states have a common decay rate, Γ. The position and velocity of the molecule are $\boldsymbol{r}$ and $\boldsymbol{v}$. The rate

equations for the system, and the number of scattered photons, γ, are,

$$\dot{\boldsymbol{r}} = \boldsymbol{v}, \tag{6.1a}$$

$$\dot{\boldsymbol{v}} = \frac{h}{m\lambda} \sum_{\mathrm{e,g},\rho} \boldsymbol{k}_\rho R_{\mathrm{e,g},\rho}(n_\mathrm{g} - n_\mathrm{e}), \tag{6.1b}$$

$$\dot{n_\mathrm{g}} = \Gamma \sum_\mathrm{e} f_{\mathrm{e,g}} n_\mathrm{e} - \sum_{\mathrm{e},\rho} R_{\mathrm{e,g},\rho}(n_\mathrm{g} - n_\mathrm{e}) - B \sum_{\mathrm{g}'} \chi_{\mathrm{g,g}'}(n_\mathrm{g} - n_{\mathrm{g}'}), \tag{6.1c}$$

$$\dot{n_\mathrm{e}} = -\Gamma n_\mathrm{e} + \sum_{\mathrm{g},\rho} R_{\mathrm{e,g},\rho}(n_\mathrm{g} - n_\mathrm{e}), \tag{6.1d}$$

$$\dot{\gamma} = \Gamma \sum_\mathrm{e} n_\mathrm{e}. \tag{6.1e}$$

Here, m is the mass of the molecule, and $f_{\mathrm{e,g}}$ is the branching ratio for spontaneous decay for e-g transition. $R_{\mathrm{e,g},\rho}$ is the excitation rate for the e-g transition driven by laser component ρ, which is,

$$R_{\mathrm{e,g},\rho} = \frac{\Gamma}{2} \frac{q_{\mathrm{e,g},\rho} s_\rho}{1 + 4(\delta_{\mathrm{e,g},\rho} - 2\pi \boldsymbol{k}_\rho \cdot \boldsymbol{v}/\lambda - \Delta\omega_{\mathrm{e,g}})^2/\Gamma^2}, \tag{6.2}$$

where $q_{\mathrm{e,g},\rho}$ is the fractional transition strength, s_ρ is the saturation parameter, $\delta_{\mathrm{e,g},\rho}$ is the detuning from the resonance angular frequency for a stationary particle at zero field, and $\Delta\omega_{\mathrm{e,g}}$ is the Zeeman shift of the transition. The saturation parameter is $s_\rho = I_\rho / I_\mathrm{sat}$, where I_ρ is the intensity of laser component ρ, and I_sat is the saturation intensity for a two level atom. The transition strength is,

$$q_{\mathrm{e,g},\rho} = \frac{\left| \langle \mathrm{g} | \hat{\boldsymbol{d}} \cdot \boldsymbol{\epsilon}_\rho | \mathrm{e} \rangle \right|^2}{\sum_{\mathrm{g}'} \left| \langle \mathrm{g}' | \hat{\boldsymbol{d}} | \mathrm{e} \rangle \right|^2} \tag{6.3}$$

where $\hat{\boldsymbol{d}}$ is the dipole moment operator, and $\boldsymbol{\epsilon}_\rho$ is the laser polarisation. From these definitions, $q_{\mathrm{e,g},\rho} s_\rho = 2\Omega_{\mathrm{e,g}}^2 / \Gamma^2$, where $\Omega_{\mathrm{e,g}}$ is the Rabi frequency at which transition e-g is driven. The phenomenological magnetic remixing rate for ground states is, $\chi_{\mathrm{g,g}'} = g_\mathrm{g} B \mu_B / \hbar$ for pairs of ground states which have the same F, but differ in m_F by 1, where g_g is the Landé g-factor for state g. The remixing rate is zero for all other combinations of ground states.

6.2.2 Parameters for the model

We model the scattering rate for a molecule interacting with a laser field whose polarisation is at 45° to an applied magnetic field. The laser polarisation is resolved into $(\sigma^-, \pi, \sigma^+)$, components in the molecule's local coordinates, with relative amplitudes $\left(\frac{1}{2}, \frac{1}{\sqrt{2}}, \frac{1}{2}\right)$. Although in reality there would be ground states which are dark to the laser polarisation,

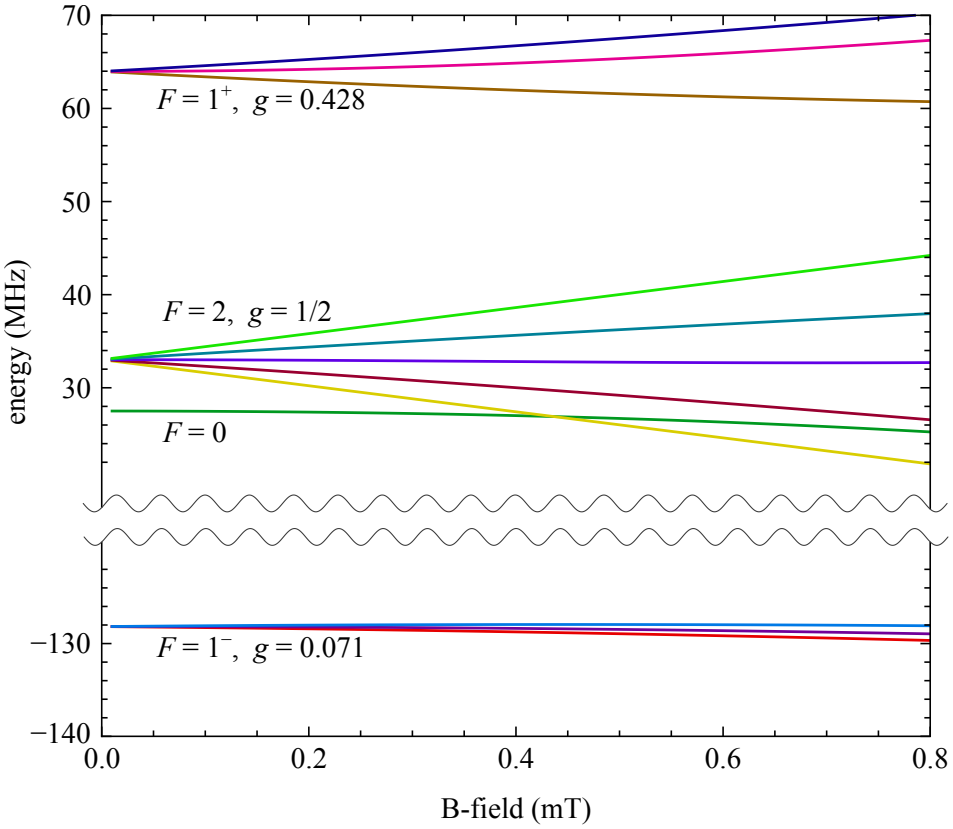

Figure 6.4: The Zeeman effect in the X(0) state, calculated by M. Tarbutt. The $F = 1^+$ and $F = 1^-$ states are of mixed $J = 1/2$, $J = 3/2$ character, which cause their g-factors to differ from the un-mixed values, which are $-1/3$ and $5/6$. The g-factors for the X(1) states are $0.17, 0, 1/2, 0.33$ for $F = 1^-, 0, 2, 1^+$ respectively.

this is not properly accounted for by the model. The solutions to (6.1) should not differ too much from reality in cases where dark states are mixed at a sufficiently high rate. Empirically we find the magnetic field which maximises the scattering rate to be $\sim 0.4\,\mathrm{mT}$, therefore this value is used for B. The remixing term $\chi_{\mathrm{g,g'}}$ in (6.1c) has the effect of distributing the population across m_F states more evenly, which increases the scattering rate.

The magnetic field also shifts transition frequencies via the Zeeman interaction; Figs. 6.4 and 6.5 give the g-factors and energy shifts for the X(0) and A(0) states.

The transition strengths, and branching ratios for $|F', m'_F\rangle$-$|F, m_F\rangle$ transitions in A(0)-X(0) are determined from the projection factors in Sec. B.2 of [96]. The same $q_{\mathrm{e,g},\rho}$ and $f_{\mathrm{e,g}}$ were used for corresponding pairs of angular momentum eigenstates for the A(0)-X(1) transition, as they do not differ significantly between vibrational levels.

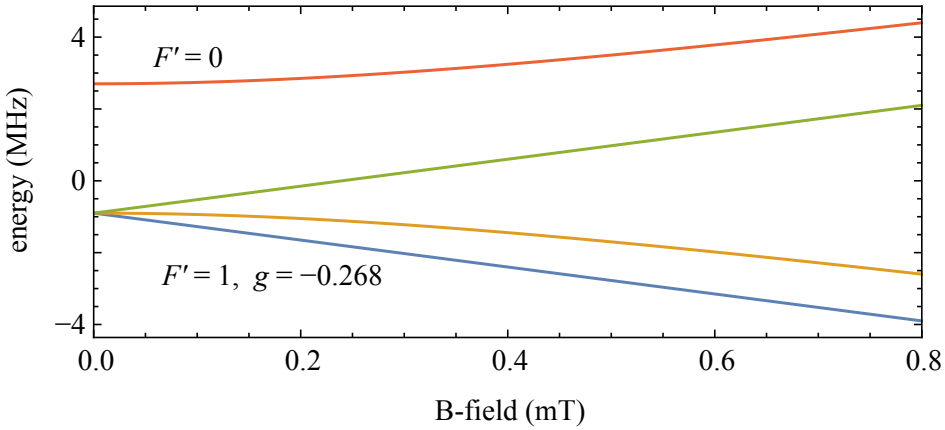

Figure 6.5: An estimate of the Zeeman effect in the A(0) state. The effective g-factor is calculated in [38]. The hyperfine splitting is -3.6 ± 0.9 MHz, which was determined in [121].

6.2.3 Cooling forces

First we compare the results for the scattering rate, $R_\gamma = \dot{\gamma}$, obtained from, Eq. 2.27, which we call the simplified rate equation model, sREM, with numerical solutions of Eqs. (6.1) which we call the full rate equation model, fREM. The laser frequencies used to drive the transitions have relative intensities I_ρ/I and relative frequency shifts $\Delta\nu$. These are given in Tab. 6.1. Here, I is one quarter of the total laser intensity of each laser. These are set to match the sideband frequencies used in the experiment, discussed in Sec. 4.2. The decay probability to higher vibrational states, X($v > 1$), is set to zero.

F	X(0)	X(1)
1^+	192.1	205.8
2	161.2	176.5
0	155.7	151.9
1^-	0.0	0.0

laser(0,0)		laser(0,1)	
I_ρ/I	$\Delta\nu$	I_ρ/I	$\Delta\nu$
1	−192.1	1	−206.0
2	−158.5	1	−179.0
1	0.0	1	−152.0
		1	0.0

Table 6.1: Left: The energy splitting, in MHz, of the hyperfine structure of X(0) and X(1) relative to the lowest frequency F state of each. Right: The laser frequencies, $\Delta\nu$ and their intensity ratios, I_ρ/I, used in this subsection. $\Delta\nu$ are relative to the highest frequency component of each laser.

Fig. 6.6 is a plot of the scattering rate for the two models as a function of the global detuning parameter, δ, which is a simultaneous detuning of all laser sideband components from the 'resonant' laser frequencies given in Tab. 6.1. The scattering rate given by fREM at $\delta = 0$ is $\sim 90\%$ of that of that of sREM, and the linewidth of the resonance feature is doubled. The dominant causes of these differences are that in fREM: there is magnetic

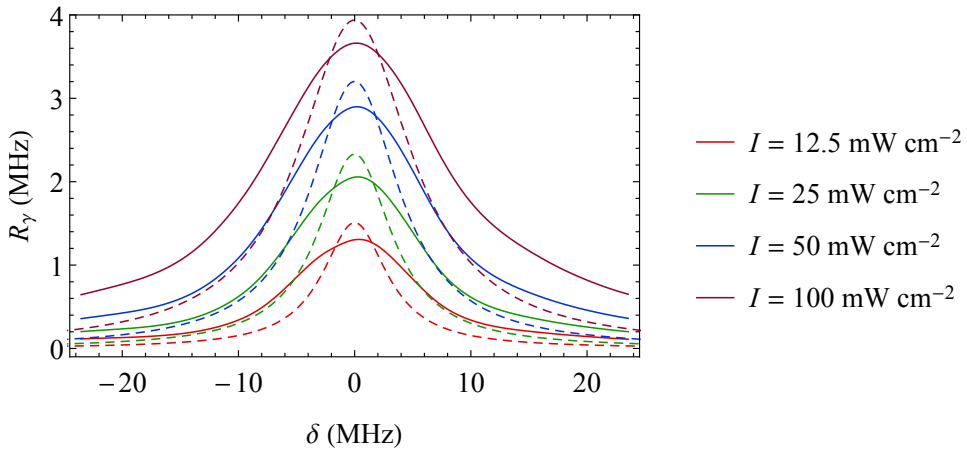

Figure 6.6: The scattering rate as a function of global detuning, δ, for different laser intensities. Continuous lines are the fREM solutions, dashed lines are for the sREM with $M = R_a$.

field broadening,[4] the hyperfine splitting in the excited state is considered, and there can be excitation by off resonant sidebands. The main effect of these inclusions is to broaden the multi-level resonance, as can be seen in Fig. 6.6. The slight reduction in the scattering rate 'at resonance' for the fREM when compared to the sREM could be attributable to the sidebands used to address the transitions not all being simultaneously at resonance with the transition they are intended to address at $\delta = 0\,\text{MHz}$ (see Tab. 6.1 for comparison).

By solving the fREM for molecules interacting with counter-propagating lasers, the acceleration and scattering rate for a 1D optical molasses can be calculated. Fig. 6.7 shows the acceleration in an optical molasses for different laser intensities, it can be seen that for the intensity range shown, higher laser intensities produce steeper slopes around $v_x = 0$, and therefore stronger cooling forces.

Fig. 6.8 compares the effect of detuning all laser frequency components simultaneously, or detuning only laser(0,0) and keeping laser(0,1) on resonance, $\delta_{(0,0)}$, or vice-versa, $\delta_{(0,1)}$. Detuning the lasers individually broadens the resonance and reduces maximum acceleration. However, the difference between the curves for δ and $\delta_{(0,0)}$ is small for small v_x. A negligible cooling force is obtained by detuning only laser(0,1). The largest damping force occurs when $\delta \approx -\Gamma$, for the largest capture velocity, a larger detuning such as $\delta \approx -2\Gamma$ is better.

In Fig. 6.9, the velocity dependent acceleration and scattering rate is plotted for a set of laser detunings. Since the laser cooling scheme currently has a significant leak to the X(3) state, it is useful to calculate $R_\gamma = \dot{\gamma}$ to calculate the number of photons scattered, γ, so that the number of molecules which will be lost to X(3) in an experiment can be estimated. Fig. 6.9 also compares a_x and R_γ obtained by solving the fREM for interaction with

[4] Magnetic field broadening = splitting of m_F components within an F state via the Zeeman interaction.

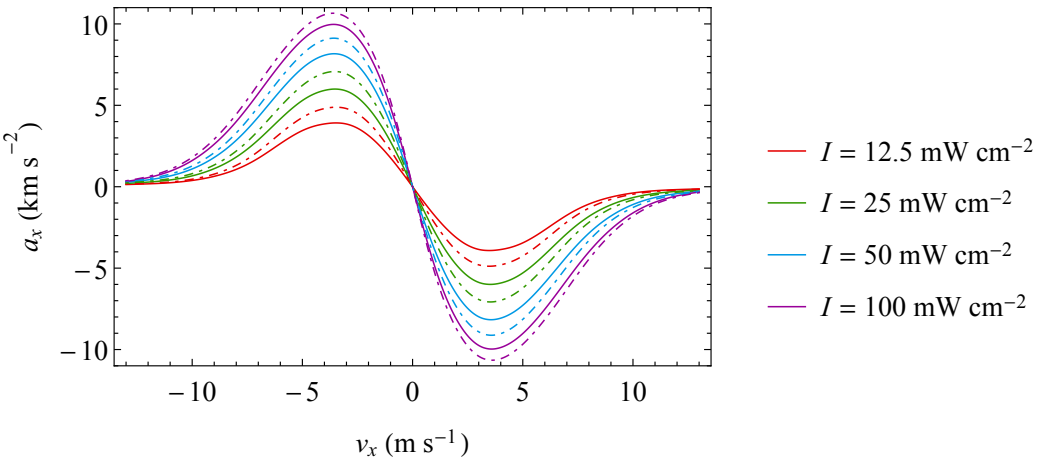

Figure 6.7: The optical molasses acceleration calculated using fREM for $\delta = -\Gamma$ for different laser intensities. The results for the laser intensity ratios in Tab. 6.1 are continuous lines. Dashed lines are for the situation where laser(0,0) sidebands have the intensity ratios given in Tab. 6.1, but the total laser intensity of laser(0,1) is double that of laser(0,0).

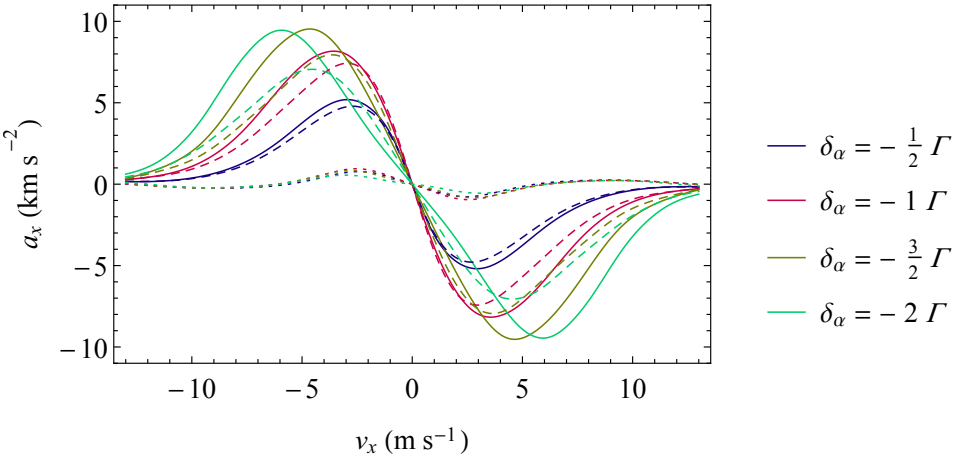

Figure 6.8: The optical molasses acceleration for $I = 50\,\mathrm{mW\,cm^{-2}}$, for $\delta_\alpha = \delta$, continuous lines, and $\delta_\alpha = \delta_{(0,0)}$, dashed lines, and $\delta_\alpha = \delta_{(0,1)}$, dotted lines.

both sets of counterpropogating laser frequencies, or simply calculating these functions for molecules interacting with a beam travelling in one direction and summing the forces and scattering rates for beams travelling in both $\pm\boldsymbol{x}$ directions. As one would expect, the approximation of summing R_γ for the two counterpropagating beams is not valid when the scattering rate is strongly saturated by both beams. Comparing the 'simultaneously solved' and 'left-right summed' accelerations in Fig. 6.9 gives an idea of the difference on the time averaged force on the molecules would be if they travelled through a laser cooling region where left and right propagating beams are either overlapped or interleaved. There is no significant difference between the two cases, however for molecules with $|v_x| < 5\,\mathrm{m\,s^{-1}}$ there is a slight advantage to having sets of overlapped left and right propagating pairs of beams.

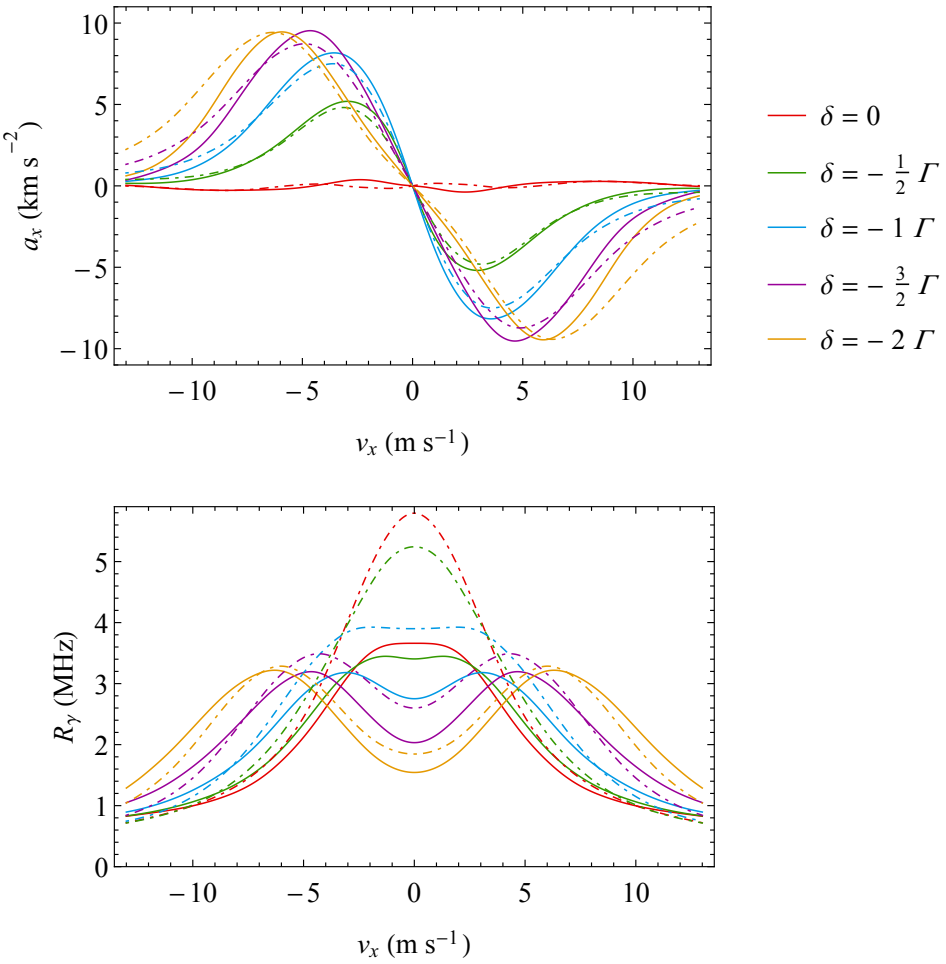

Figure 6.9: The optical molasses acceleration for $I = 50\,\mathrm{mW\,cm^{-2}}$. Top: The acceleration for different values of δ. The solid curves are the same as those in Fig. 6.8, shown again for comparison. Dashed curves are approximations obtained by summing the force or scattering rate due to right and left propagating beams calculated separately. Bottom: The corresponding scattering rates for the force curves in the Top figure.

6.2.4 Trajectory simulations

To model a transverse cooling experiment, trajectory simulations can be run. This was done by solving the rate equations, Eq. (6.1) for the position and velocity as well as the internal states. The laser parameters used in this section are given in Tab. 6.2.

laser(0,0)		laser(0,1)	
I_ρ/I	$\Delta\nu$	I_ρ/I	$\Delta\nu$
1.0	−192.1	1.8	−206.0
2.0	−158.5	1.8	−179.0
1.0	0.0	1.8	−152.0
		1.8	0.0

Table 6.2: Laser parameters used in trajectory simulations in this section.

The increase in relative intensity of the laser(0,1) sidebands to those of laser(0,0). This reflects the power ratio which we can produce with our laser systems, as the maximum output power of laser(0,1) is higher than laser(0,0), and less power is lost in sideband generation. We use the maximum power for laser(0,1) as increasing the intensity driving the A(0)-X(1) transition increases the laser cooling force, as can be seen in Fig. 6.7.

To model our experimental set up, Fig. 6.1, we use Gaussian laser beams with $1/e^2$ diameter 10 mm, and peak intensity, $I = 50\,\mathrm{mW\,cm^{-2}}$. This beam size is much larger than that used in the experimental results in this section.[5] The beams propagate in $\pm\boldsymbol{x}$, and there are 20 interleaved passes in each direction which are evenly spaced in the 20 cm interaction length. There is a power loss per pass through the interaction region of 1%. This is to model the type of multi-pass configuration shown in Fig. 6.2(a), however the beams do not propagate at an angle to $\boldsymbol{x}$.

A set of trajectories are shown in Fig. 6.10. The small oscillations in v_x are due to the interleaved beams propagating in $\pm\boldsymbol{x}$. The initial and final v_x of molecules for different δ are compared in Fig. 6.11. From the simulations it appears that the optimum δ should be $\sim -\Gamma$, as this produces the largest number of molecules with low transverse velocity, $|v_x| < 0.5\,\mathrm{m\,s^{-1}}$. Fig. 6.11 also gives the total number of scattered photons for various trajectories through the laser cooling region.

Modelling an experiment

To reduce the time required to simulate each trajectory, an acceleration map was first generated by using the rate equation model to calculate the steady state acceleration on

[5] According to the model, this larger beam size is better for Doppler cooling, and larger beam sizes should be tested in the experiment. The effect of the beam size is discussed later in this chapter.

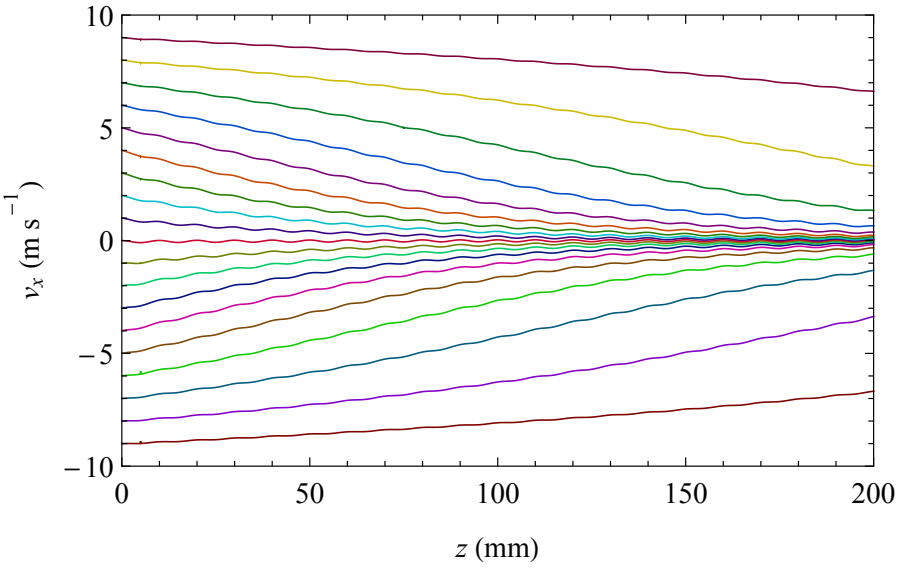

Figure 6.10: Plots of transverse velocity, v_x as a function of distance through the cooling region for molecules with $v_z = 180\,\mathrm{m\,s^{-1}}$ and a range of initial v_x, with $y = 0$ and $v_y = 0$. In these simulations, $\delta = -\Gamma$.

a molecule for a set of left/right laser intensity combinations, values of δ, and transverse velocity, v_x. It was verified that trajectories calculated using this map gives the same result as for simultaneously solving the rate equations and the equations of motion for each individual molecule. In the simulations, the intensity rations in the laser beams are the same as in Tab. 6.2.

In calculating the acceleration map, the ground states with $v > 1$, are not included. Instead, we account for the presence of X(2), and its interaction with laser(2,2) in a simple way. The intensity per sideband of repump laser(2,2) is $\sim I/10$. For the intensity range in which we are interested, $0 < I <\sim 100\,\mathrm{mW\,cm^{-2}}$, we find that molecules spend $\sim 90\%$ of their time in the cooling cycle using Eq. (2.23). To take this into account in the trajectory simulations, the acceleration and scattering rates are reduced by 10%.

The input distribution to the simulation was chosen to represent the output of the buffer gas cell (see Sec. 3.3). The input position distribution is a uniform disc in the xy-plane of radius 1.5 mm, with a distance in z of d_1 from the start of the laser cooling region. This is chosen because in the experiment, molecules leave the buffer gas cell through a 3 mm diameter aperture. The v_z distribution is a Gaussian with mean $180\,\mathrm{m\,s^{-1}}$ and $1/\mathrm{e}^2$ full width of $100\,\mathrm{m\,s^{-1}}$, the distribution in x, y is uniform over the velocity range in which we are interested $|v_{x,y}| < 10\,\mathrm{m\,s^{-1}}$. The modelled initial positions and velocities are uncorrelated.

The distance between the source and the start of the laser cooling region is $d_1 = 215\,\mathrm{mm}$, the length of the cooling region is $d_c = 200\,\mathrm{mm}$, and the free flight distance between the end of the cooling region and detection is $d_2 = 730\,\mathrm{mm}$. These distances were

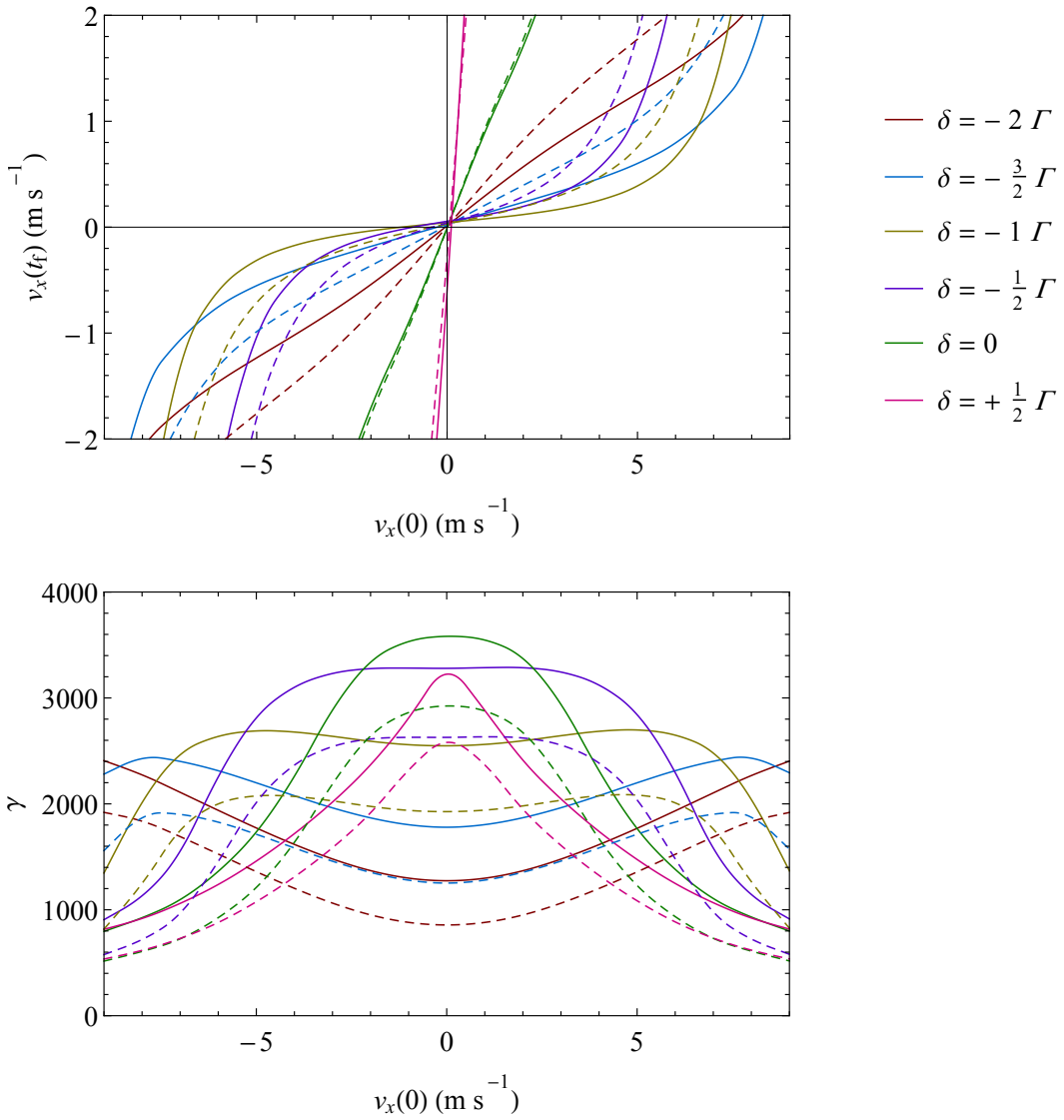

Figure 6.11: Top: The final transverse velocity $v_x(t_\mathrm{f})$ as a function of initial transverse velocity, $v_x(0)$ for a range of laser detunings. Bottom: The total number of photons scattered for the corresponding trajectory in the Top figure. All molecules have $v_z = 180\,\mathrm{m\,s^{-1}}$. For all plots $v_y = 0$; continuous lines are for molecules travelling in the $y = 0$ plane, through the maxima of the laser beams, dashed lines are for molecules travelling in the $y = 2.5\,\mathrm{mm}$ plane.

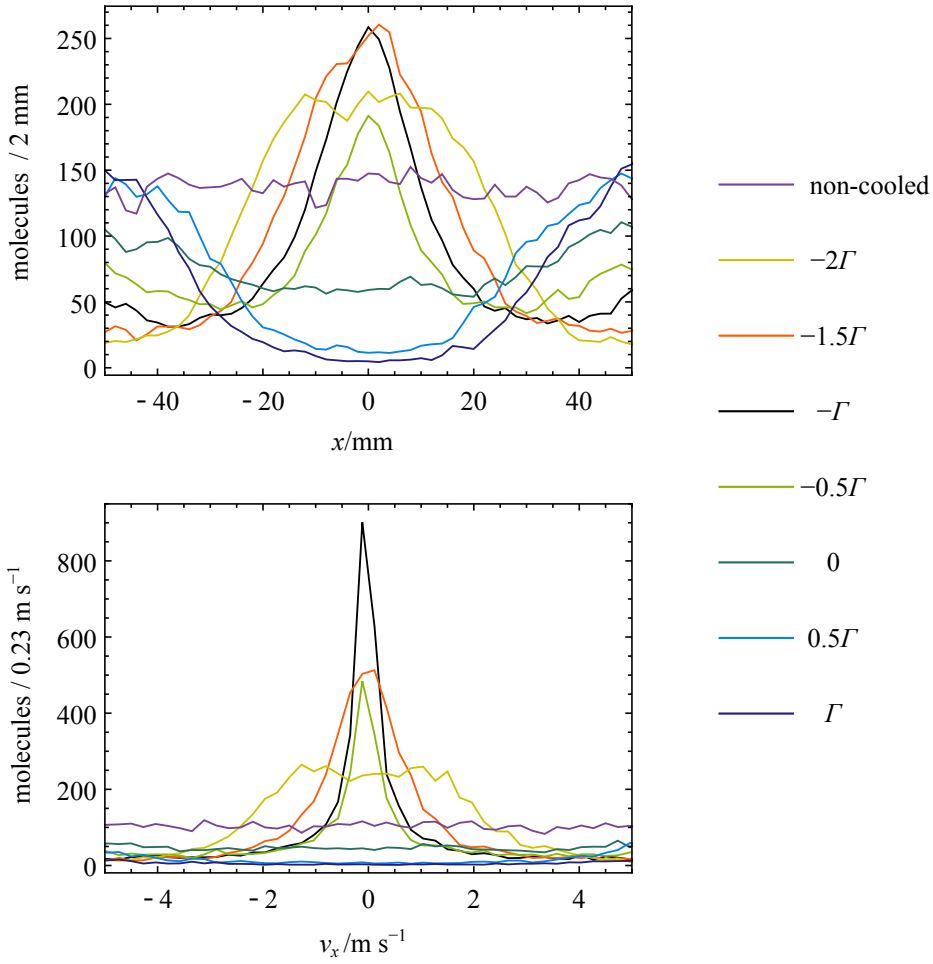

Figure 6.12: Histograms showing the modelled position and velocity distributions of laser cooled molecules for a range of detunings.

chosen to resemble a possible configuration for our experiment.

To find the final position and velocity distributions of the molecules in bright states, which is what we measure on the camera, the probability of each molecule having been lost to a dark state must be found. The loss probability per scatter is $\sim f_{0,3} = 3 \times 10^{-4}$, the FCF for A(0)-X(3), therefore the probability that a molecule is still in a bright state, is $(1 - f_{0,3})^{\gamma}$.

The final molecular distributions are calculated by determining the probability of each molecule being in a bright state, and then summing these probabilities over all molecules within a bin. The distributions at the detector are shown in Fig. 6.12. In the figure, the width of each position bin is $\Delta x = 2\,\mathrm{mm}$, and velocity bin is $\Delta v_x = 3/13\,\mathrm{m\,s^{-1}}$. Only molecules which arrive within a detection width of $|y| < 5\,\mathrm{mm}$ are counted.

The simulations show that when the cooling is applied the width of the distribution at the camera should be reduced. There should also be an increase in the number of molecules at the centre of the image, though this increase is limited to a maximum of about 1.7× compared to a non-cooled distribution, because of the loss of molecules to

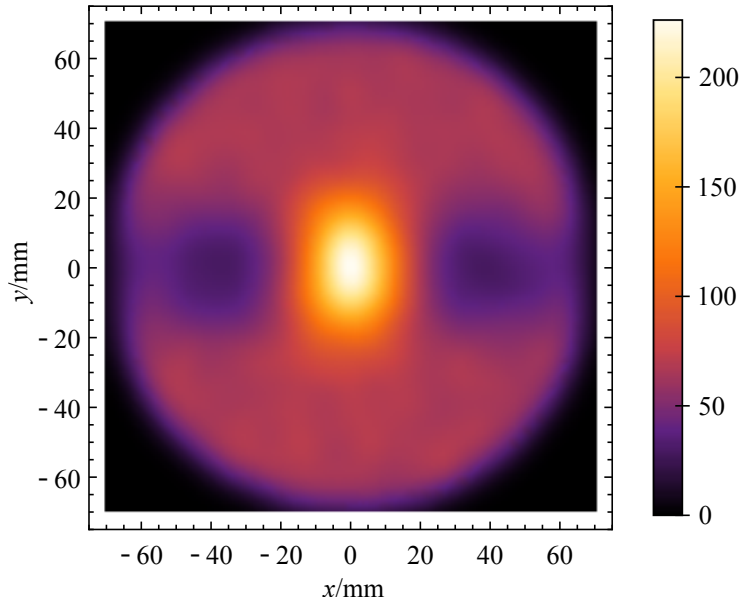

Figure 6.13: A density plot showing the position of molecules at the detection point with laser cooling applied. This includes molecules optically pumped into X($v > 2$) dark states. In comparison, the non-cooled xy-distribution is uniform over $\sqrt{x^2 + y^2} < 55\,\text{mm}$. It can be seen that molecules that would have appeared in the regions ($x = \pm 40\,\text{mm}, y = 0\,\text{mm}$) in the absence of laser cooling have been collimated, enhancing the density at the centre of the distribution.

X(3). These changes in the spatial distribution reflect the very large reduction in the width of the velocity distribution, as seen in the lower part of the figure. The detuning which produces the narrowest velocity distribution is $\delta = -\Gamma$. The position distribution in the xy-plane for the $\delta = -\Gamma$ trajectory simulation is shown in Fig. 6.13.

These simulations do not model the experimental results presented here. In the experiments, a smaller laser beam size has been used, and molecules were detected closer to the end of the laser cooling region. Our experimental results are presented and modelled in the following section.

6.3 Results I: Doppler Cooling

6.3.1 Experiment 1

In this experiment, the cooling beam size was 5.5 mm $1/e^2$ diameter. The beam made 40 passes through the cooling region in the manner of Fig. 6.2(a). The separation of the cooling mirrors, M1 and M2 in Fig. 6.1, was 400 mm, and therefore the Doppler shift due to the laser beam not being perpendicular to the molecular beam is -4.1 MHz for $180\,\text{m}\,\text{s}^{-1}$ molecules. In this experiment, $B = 0.12\,\text{mT}$, $l_1 = 430\,\text{mm}$, $l_c = 190\,\text{mm}$ and $l_2 = 255\,\text{mm}$. The clean-up region was immediately after the cooling region, and the

clean-up light passed through W1 and W2.

The powers used in the cooling beam were approximately 20 mW per sideband for laser(0,0), 35 mW per sideband for laser(0,1), and 10 mW in total for laser(2,2).

To tune the lasers to resonance, a PMT was used, see Fig. 6.1. First, the PMT is positioned at the bottom of the cooling region, the fluorescence is maximised by tuning the frequency of laser(0,0) with the other lasers blocked. The frequency of laser(0,0) is locked at the maximum. The PMT is then moved further up the cooling region and laser(0,1) is unblocked. Its frequency is tuned for maximum fluorescence and locked. Finally with the PMT positioned at the top of the cooling region, the tuning is repeated for laser(2,2). This procedure of translating the PMT in z for tuning each laser is used so that we observe the biggest effect of tuning the laser frequency for each of the cooling lasers. If the PMT is at the top of the cooling region when tuning laser(0,0), molecules are optically pumped into X($v > 0$) before being detected. If the PMT is at the bottom of the cooling region when tuning laser(2,2), few molecules are pumped into X(2) in the short interaction time, and so the laser(2,2) frequency has little effect on the observed fluorescence.

To observe the effect of the cooling lasers, all lasers were first red-detuned by ~ 10 MHz, then set to resonance, then blue detuned by ~ 10 MHz. For each detuning, a 'non-cooled' distribution was recorded, where the light to the cooling region was blocked. Fig. 6.14 shows the results of these experiments. Each plot in Fig. 6.14(a,b,c) is produced from 200 shots of the experiment. For each shot, an image is recorded, and between every shot, a background image is recorded. In the background image, the probe light is on but there is no molecular pulse. The mean background image is then subtracted from the mean image. To obtain the plots, the values of the pixels are summed along z, over a $\Delta z = 5.5$ mm region containing the probe beam.

In the following discussion, I will call the distribution obtained 'cooled' if the laser cooling light interacts with it (regardless of whether the width of the velocity distribution is increased or decreased), and 'non-cooled' if the cooling light is not present.

The distribution obtained red-detuning, shown in (a), there is a clear increase in the number of molecules in the centre of the distribution relative to the wings compared to the non-cooled case. For the blue-detuned distribution shown in (c), there is a decrease in the number of molecules at the centre relative to the wings, when compared with the non-cooled case. For zero detuning there is no obvious difference between the cooled and non-cooled profile. This is what is expected for Doppler cooling. The presence of the cooling light results in a loss of molecules irrespective of detuning, because there is optical pumping into the X(3) state.

The experiment was done without the independent probe laser, instead, the probe beam contained the 0 MHz and 159 MHz sidebands of laser(0,0). The optical cycling

rate in the detection region was not high enough to pump all of the molecules from X(0), therefore, the shape of the non-cooled distribution changes with detuning because molecules with different v_x scatter at different rates, and x and v_x are well correlated.

By dividing each cooled distribution by its corresponding non-cooled distribution, the effect of the cooling light becomes more clear, this is shown in Fig. 6.14(d). It can be clearly seen that there is a peak in the distribution for red detuning, a dip for blue detuning, and something in between for no detuning, as one would expect. The peak of the red-detuned distribution is smaller than 1.0 because molecules are optically pumped into X(3). Another apparent source of loss is underlying transitions with similar frequencies to the P(1) transitions. In our data, this appears as a $\sim 15\,\%$ loss of molecules because these states are pumped out before detection when the cooling light is applied, but not for the non-cooled measurements.

Although the peak of the cooled distribution in 6.14(d) is less than one, it is most likely that these results show laser cooling rather than some kind of velocity dependent optical pumping of fast molecules. This is because optical pumping would produce a similar shaped distribution for both blue and red detuning.

Comparison to model

Using the fREM, the experiment was simulated in the same manner as described in Sec. 6.2.4 using a similar molecular distribution. The simulation parameters were chosen to match those of the experiment, however the laser beam propagation direction was $\pm\boldsymbol{x}$ rather than $\pm\boldsymbol{x}\cos\theta + \boldsymbol{z}\sin\theta$, where $\theta = 12.5\,\mathrm{mrad}$. The effect of this difference in angle on the simulation results is very small. The modelled transverse position distribution and velocity distributions of molecules in bright states at the detector is shown in Fig. 6.15(a,b). Here, molecules arriving at the detection region within a range of $|y| < 2.5\,\mathrm{mm}$ are counted. The noise in the simulated distribution is counting noise from the initial random phase space distribution.

In Fig. 6.15(c) the experimental data is overlaid with the modelled distribution. The amplitude of the modelled data in (a) is multiplied by $1/190$ to arrive at the distribution shown in (c). There is a remarkably good agreement between the results of the experiment and the model. This agreement gives confidence that the results are indeed due to Doppler cooling of the beam. Since the agreement is good for the spatial distribution that we measure, it is reasonable to assume that the corresponding velocity distribution is the one predicted in the model, and to extract a temperature from that modelled velocity distribution. Fig. 6.15(d) shows a Gaussian fit to the modelled data. This yields a temperature of $(72 \pm 2)\,\mathrm{mK}$.

In order to extract velocity distributions directly from the experimental data, two

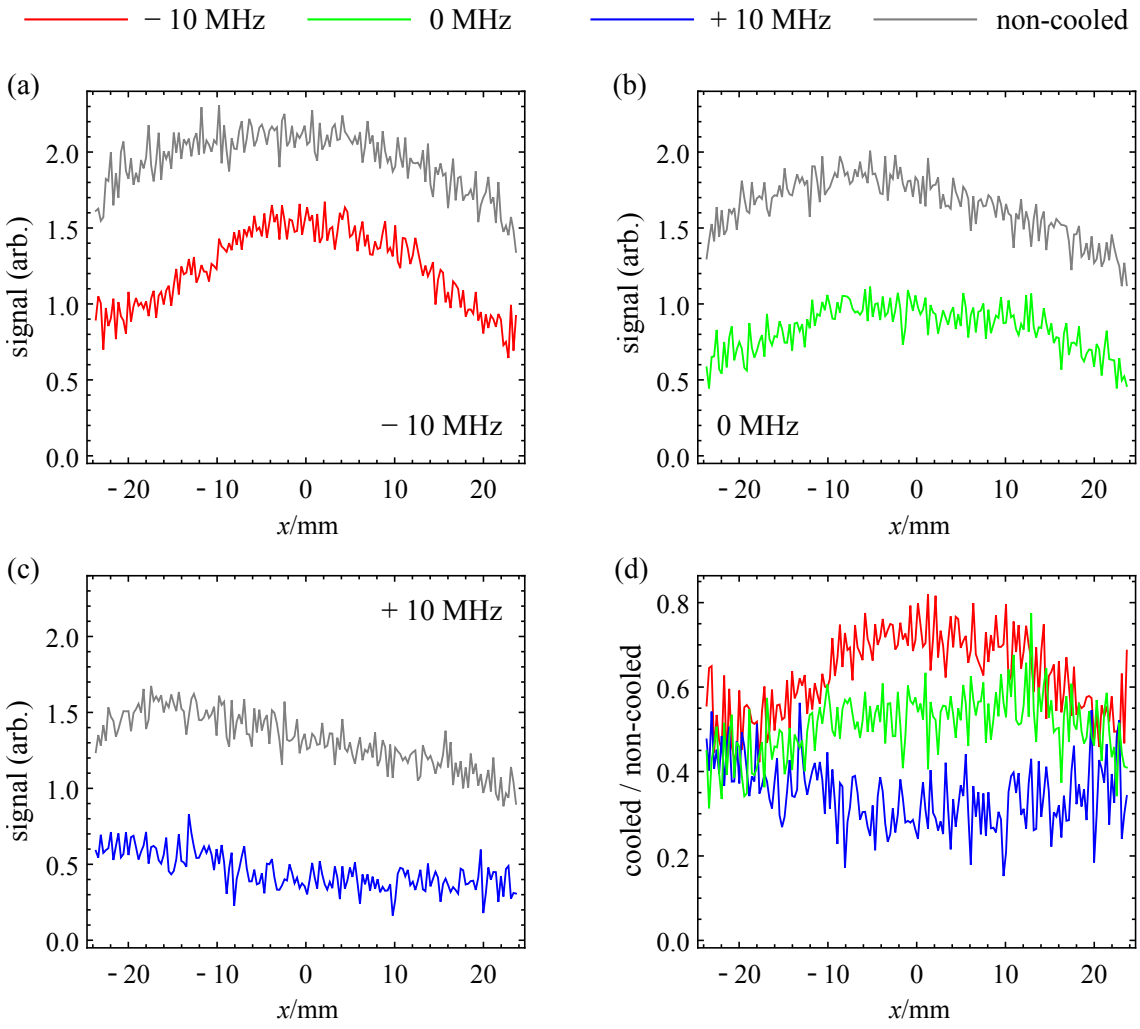

Figure 6.14: Plots of the Doppler cooling results. (a,b,c): The raw data for each detuning. The 'non-cooled' data is where the light to the laser cooling region was blocked. Each curve is produced using 200 images of molecules, and 200 background images. (d): The cooled distributions divided by the non-cooled distributions.

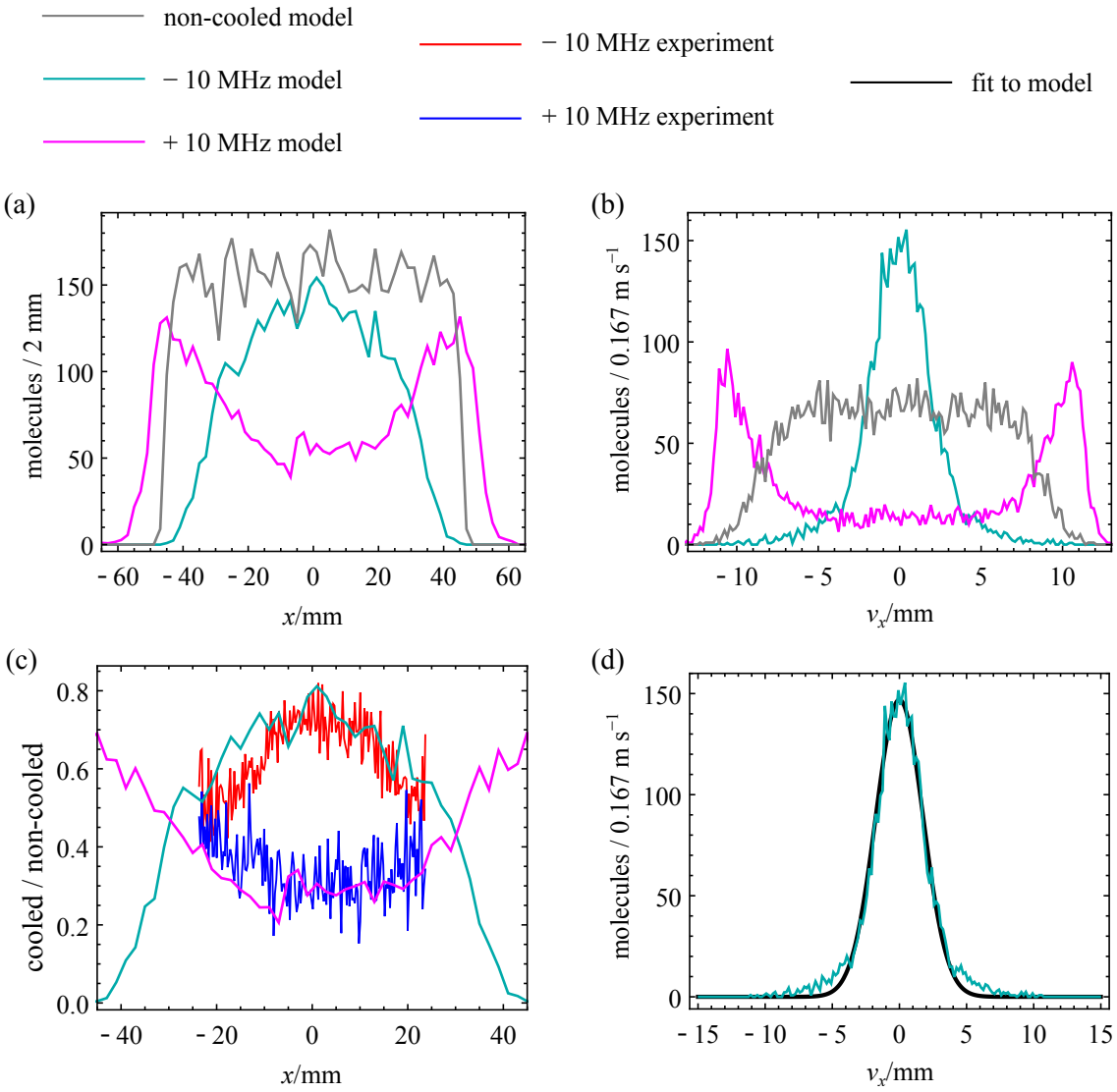

Figure 6.15: Modelled laser cooling results using fREM. (a): The position distribution at the detector of molecules in bright states. (b): The velocity distribution for molecules which arrive at the detector. (c): A comparison between the experimental results and the model. (c): A Gaussian fit to the laser cooled velocity distribution predicted by the simulation.

imaging regions will be used in future, to measure the change in the distribution between detectors. Additionally a larger detection area will be used so that the distribution over a larger range in x can be recorded. The acquisition of more Doppler cooling data for different detunings will enable better comparison with the model.

According to the trajectory simulations, smaller transverse temperatures may be produced by Doppler cooling for the same set-up and laser power by using a larger cooling beam size, $\sim 10\,\mathrm{mm}$ $1/\mathrm{e}^2$ diameter and laser detunings closer to $-\Gamma$. This is because the scattering rate is strongly saturated at the high intensity regions of the $\sim 5.5\,\mathrm{mm}$ $1/\mathrm{e}^2$ beam, but there are large spaces between beams where the intensity is low. Continuous interaction with lower intensity light therefore yields a better result. For a $\sim 10\,\mathrm{mm}$ $1/\mathrm{e}^2$ beam and $\delta = -10\,\mathrm{MHz}$, the model gives a distribution with temperature $(35.5 \pm 0.7)\,\mathrm{mK}$ and amplitude 222 ± 2 for molecules within the same range of $|y| < 2.5\,\mathrm{mm}$ at the detector. The larger beam also has the advantage of interacting with a greater width of the molecular distribution in the y-direction.

6.3.2 Experiment 2

This experiment was intended to be a repeat of Experiment 1, with some improved experimental parameters, for example, the distance between the source and laser cooling region was reduced to $l_1 = 215\,\mathrm{mm}$. Other length parameters were $l_c = 200\,\mathrm{mm}$ and $l_2 = 405\,\mathrm{mm}$. For detection, probe-laser(0,0) was used such that the shape of the non-cooled fluorescence distribution would not change as the frequency of laser(0,0) was scanned. To produce the most fluorescence in the detection region, the probe laser has sidebands identical to laser(0,0) and a remixing field was applied in the detection region. The frequency of the probe laser was locked at the frequency which produced the most fluorescence for the non-cooled molecular beam for the duration of the experiment. Here we also try to investigate the effect of the remixing magnetic field. In this experiment, the multi-pass configuration (b) in Fig. 6.2 was also used, instead of configuration (a).

The laser powers and beam-size were the same as in the previous experiment, however the cooling beam was retro-reflected at the top of the cooling region such that it followed the same beam path in reverse down the cooling region. At the top of the cooling region, after 40 passes the power had diminished to $\sim 65\,\%$ of the input.

The frequencies of the lasers were tuned as explained in the previous section, but with the retro-reflected cooling light present. To find the 'resonant' frequency for each, Gaussians were fit to frequency scans over the transitions. This yields a centre frequency accurate to $\sim \pm 1.5\,\mathrm{MHz}$ for the A(0)-X(0) and A(0)-X(1) transitions. A series of data sets were recorded for a range of values of detuning of laser(0,0) only, with the other lasers remaining locked at resonance. This was done for two magnetic fields, $B = 275\,\mu\mathrm{T}$ and

$B = 36\,\mu\mathrm{T}$. Bias coils were also used to cancel external B-fields. The data collection and processing is identical to the previous section.

Fig. 6.16 shows the resulting position distributions. From the data, it can be seen that the peaks of the distributions with negative detuning do not lie in the centre of the imaging region, instead they are at $x \approx -12\,\mathrm{mm}$. This is most likely due to the imaging optics being knocked, but could also result from the faces of the mirrors not being parallel to $\boldsymbol{z}$. Assuming the offset of the peak is due to misalignment of the imaging optics, it can be seen that negative detunings produce cooling, and positive detunings, heating for both B-field regimes. From the data in Fig. 6.16, the effect of the magnetic field is not clear. One would expect R_γ to be low at low B, and therefore the peaks in the position distribution to be less prominent. We might also expect to see a peak for blue detuning due to Sisyphus cooling, which will be discussed in Sec. 6.4. There is a small peak in the $B = 36\,\mu\mathrm{T}$, $\delta_{(0,0)}$ distribution where the detuning is 15 MHz.

The analysis of these data is complicated by the retro-reflection of the cooling beam. Because the beam is retro-reflected, in addition to the velocity dependent detuning, molecules see a different laser detunings of the cooling beam travelling up or down the cooling region compared to when it travels down. This is due to the Doppler shift due to the component of the laser $\boldsymbol{k}$-vector in the z-direction. This Doppler shift is large compared to Γ, and δ. For $180\,\mathrm{m\,s^{-1}}$ molecules it is $\mp 4.1\,\mathrm{MHz}$ for a beam travelling up or down the cooling region respectively.

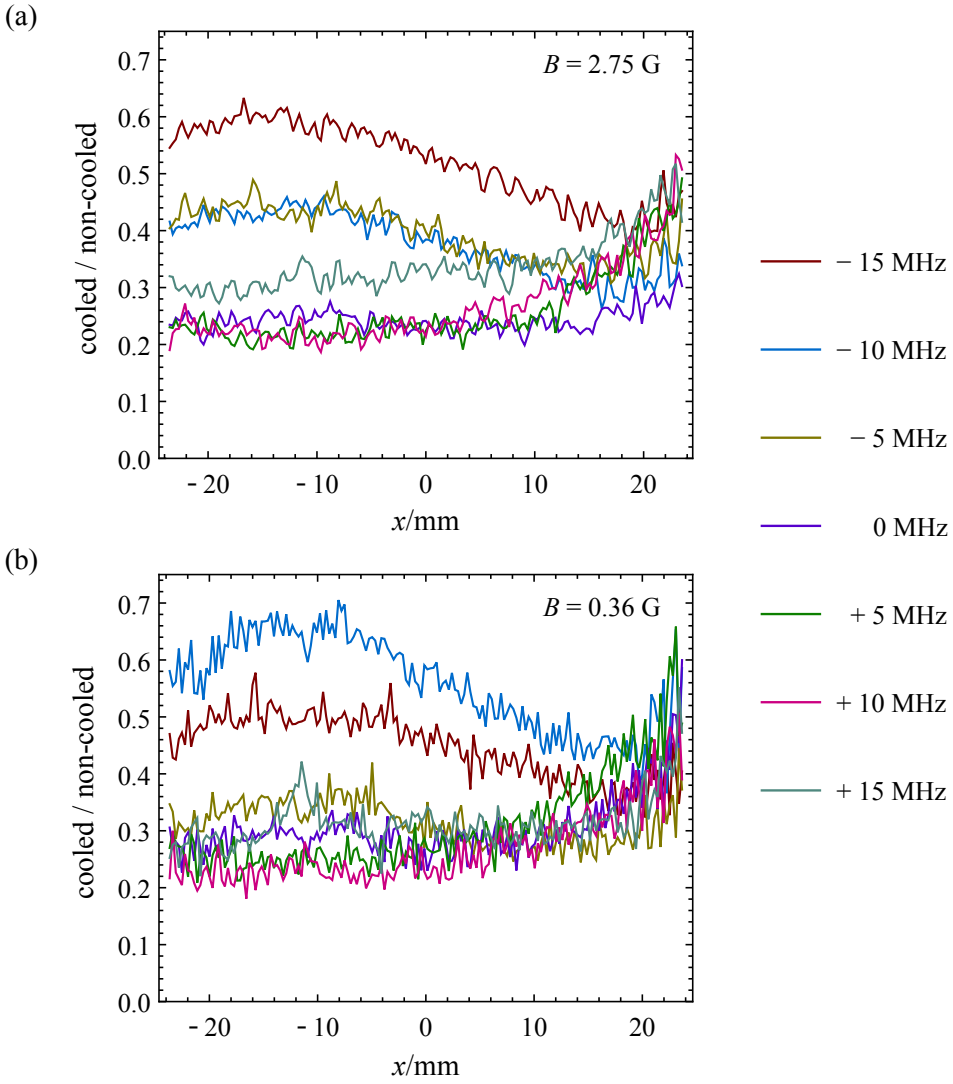

Figure 6.16: Doppler cooling results for a variety of laser detunings, $\delta_{(0,0)}$, and two values of B. (a): $B = 275\,\mu\mathrm{T}$ (b): $B = 36\,\mu\mathrm{T}$

6.4 Results II: Sisyphus cooling

In addition to the Doppler cooling which has so far been discussed, there may be significant sub-Doppler processes which can heat or cool the molecular beam and are dominant for molecules with low transverse velocity. One of these processes, which has previously been observed in 1D molecular laser cooling experiments [23, 44], is the magnetically assisted Sisyphus effect. This is discussed in the context of cooling atoms on type-I transition in Sec. 1.1.3. In our experiment we have observed what appears to be laser cooling via this effect.

6.4.1 Features and regime of the Sisyphus cooling mechanism

Compared to the atomic system discussed in Sec. 1.1.3, in the YbF cooling system there are many ground states which experience different AC Stark shifts depending upon the transition strength, laser power, and laser detuning. However, as in [23], we can estimate the velocity ranges and magnetic fields for which the Sisyphus force is dominant.

We expect the force to be maximum for molecules which travel a distance of $\lambda/4$ within the optical pumping time, τ_p, which is the time it takes for molecules to be optically pumped into dark angular momentum eigenstates. In the YbF system, the $F = 2$, $m_F = \pm 2$ states are dark. The maximum scattering rate is $R_\gamma^\mathrm{max} = \Gamma N_\mathrm{e}/N_\mathrm{tot}$, and the mean branching from all excited states to the $m_F = \pm 2$ states is $1/12$, therefore, $\tau_\mathrm{p} \sim 12/R_\gamma^\mathrm{max} = 84/\Gamma$. The force should therefore be maximum for molecules with velocity, $v_\mathrm{Sis} \sim \frac{\lambda}{4}\frac{1}{\tau_\mathrm{p}} = 0.06\,\mathrm{m\,s^{-1}}$.

The B-field should cause the molecules to precess out of the dark states in the time it takes them to travel a distance in x of $\lambda/4$. The Larmor precession frequency is $\omega_\mathrm{B} \sim B\mu_\mathrm{B}g/\hbar$, and for the $F = 2$ states, $g = 1/2$. The required B-field is therefore $B_\mathrm{Sis} \sim \frac{1}{\tau_\mathrm{p}}\frac{\hbar}{g\mu_\mathrm{B}} = \frac{\hbar\Gamma}{42\mu_\mathrm{B}} = 10\,\mu\mathrm{T}$. A sketch of the shape of the expected force curve for Sisyphus cooling in molecular systems is shown in Fig. 6.17.

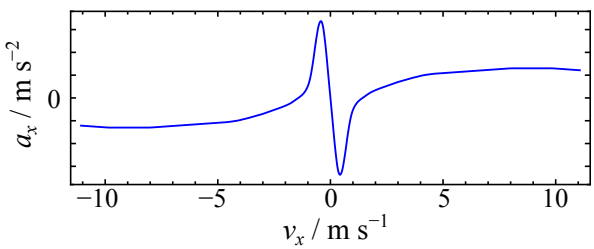

Figure 6.17: A sketch of the shape of the force curve that is expected for blue detuning and low B-field. We expect to see Sisyphus cooling for low $|v_x|$, and Doppler heating for larger $|v_x|$.

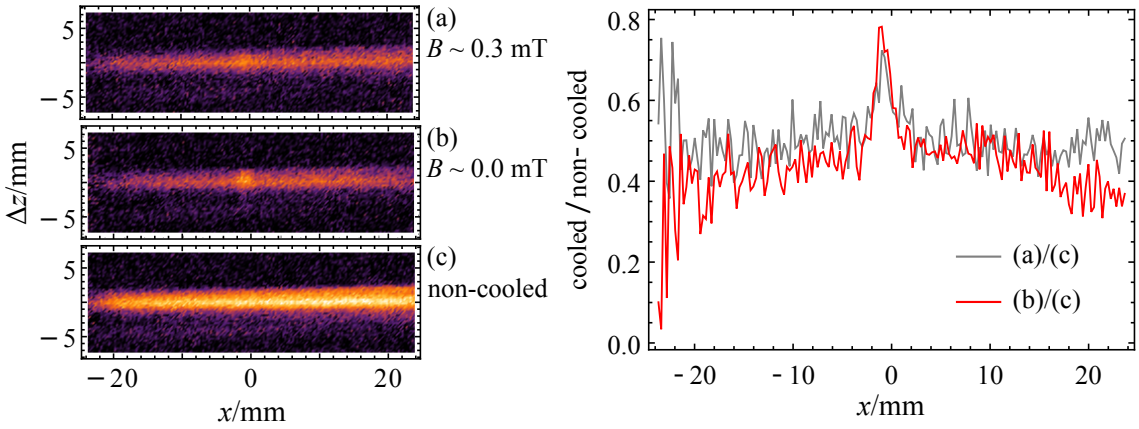

Figure 6.18: (a,b,c): Images of the molecules. Right: Position distributions as a fraction of the non cooled distribution.

6.4.2 Sisyphus cooling results

In the first laser cooling data we recorded, we observed a laser cooled distribution which could be attributed to be Sisyphus cooling. When the data were recorded, the experimental set-up was the same as that for the experiment described in Sec. 6.3.1. However, at this time, M1 and M2 were attached to the same aluminium support frame as the cryocooler and vacuum chamber, and were therefore vibrating due to the pumping of the cryocooler.

The mean images of the molecules after background subtraction are shown in Fig. 6.18(a,b,c). Here the non-cooled image was recorded with two passes of the cooling light through the detection region. The two passes were used for the non-cooled data in order to pump out states which have transition frequencies similar to P(1). Plots of the cooled signal as a fraction of the non-cooled signal are shown in the plot in Fig. 6.18. A sharp peak can be seen at the centre of the distributions. This is larger for the case where the applied magnetic field is switched off.[6]

A possible explanation for this peak is that it is due to Sisyphus cooling for molecules with low v_x, combined with Doppler heating for those with higher v_x, and a loss in the number of molecules of all velocities due to optical pumping into X($v \geq 2$). Another possible explanation is that molecules with low velocity become trapped in a coherent dark state and are not pumped into X($v \geq 2$) within the cooling region, whereas molecules with higher velocities are pumped out of X(0,1). For either of these explanations, it is surprising that the sharp peak should be obtained with and without an applied B-field. The Sisyphus effect should be weak for large B as found in [23], and one would expect a coherent dark state to be destabilised by the application of the B-field. Additionally, the laser beams propagating in $+\boldsymbol{x}\cos\theta + \boldsymbol{z}\sin\theta$ did not have a large overlap with those propagating in $-\boldsymbol{x}\cos\theta + \boldsymbol{z}\sin\theta$, as the centres of adjacent beam pairs were separated by

[6] In this experiment, there was no bias coils to cancel external B-fields.

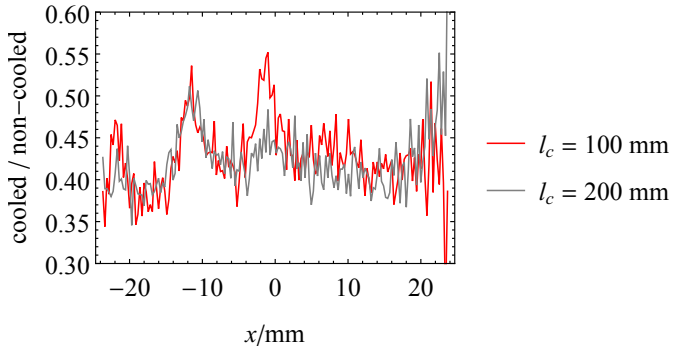

Figure 6.19: Three peaked distribution for low $B = 26\,\mu\text{T}$ and $\delta_{(0,0)} = 15\,\text{MHz}$.

5 mm at $x = 0$ but the beam size was 5.5 mm $1/e^2$ diameter.

In a more recent setup we have not been able to reproduce this result so far, which is most likely due to a change in alignment, although a similar feature is probably present in the $\delta = 15\,\text{MHz}$ data shown in Fig. 6.16(b). Further experimental work is required to confirm the feature and measure the temperature of the distribution using two detection regions. It would also be interesting to model the cooling system in more detail, for example, by solving the OBEs for the system, to determine the experimental conditions required for Sisyphus cooling or coherent population trapping.

6.4.3 Other observations

Using the same experimental configuration as in Sec. 6.3.2, we have observed a laser cooled position distribution which contains three small peaks, using a low remixing field of $B = 26\,\mu\text{T}$. In the experiment, $l_1 = 215\,\text{mm}$, $l_c = 100\,\text{mm}$ and $l_2 = 505\,\text{mm}$, and the multi-pass configuration of Fig. 6.2(b) was used. Here, with the retro-reflection mirror was moved half way down the cooling region, and the number of passes reduced to 20. At the time when the data was taken it is likely that the imaging optics were misaligned (as in Sec. 6.3.2), and therefore the centre of the distribution is at $x \approx -12\,\text{mm}$. The distribution is shown in Fig. 6.19, along with a distribution for the same parameters but with $l_c = 200\,\text{mm}$ and $l_2 = 405\,\text{mm}$.

A possible explanation for this strange distribution is Sisyphus cooling towards two different non-zero velocities. For the multi-pass configuration used, there are two distinct sets of regions of standing waves; the regions formed by pairs of beams propagating in directions $\pm(\boldsymbol{x}\cos\theta + \boldsymbol{z}\sin\theta)$ and those formed by beams propagating in $\pm(\boldsymbol{x}\cos\theta - \boldsymbol{z}\sin\theta)$. Due to the Doppler shift experienced by molecules because of their large v_z, each of these regions cools molecules towards a different, non-zero v_x; $v_{x,0} \approx \pm v_z \sin\theta$. For a molecular beam with $v_z = 180\,\text{m}\,\text{s}^{-1}$ and $\theta = \frac{5\,\text{mm}}{400\,\text{mm}}$, $v_{x,0} \approx \pm 2.25\,\text{m}\,\text{s}^{-1}$. In the time it takes the molecular beam to travel from source to the imaging region, molecules

with $v_x = \pm 2.25\,\mathrm{m\,s^{-1}}$ travel $\pm 10\,\mathrm{mm}$ in x. This can explain the two outermost peaks, separated from the center peak by $\sim 10\,\mathrm{mm}$. The central peak is explained by considering the shape of the time averaged force curve. This would look like the sum of two of the curves shown in Fig. 6.17 offset by $\pm 2.25\,\mathrm{m\,s^{-1}}$, making a third zero crossing at $v_x = 0$ with a negative gradient due to the Doppler cooling (in addition to the other two crossings at $\pm 2.25\,\mathrm{m\,s^{-1}}$).

Further investigation is required to verify these suggestions, however, it would appear that the multi-pass arrangement shown in Fig. 6.2(b) may be a poor choice for Sisyphus cooling. Instead the arrangements shown in Fig. 6.2(c,d) should be tested. There are flaws with these configurations too. In (c) the angle of the beam changes along z, and standing waves parallel with $\boldsymbol{x}$ are only formed in the last section of the cooling region. In (d), there are standing waves with amplitude modulation in both $\boldsymbol{x}$ and $\boldsymbol{z}$ due to the beams crossing with angle 2θ. The modulation of the AC Stark shift due to motion in z could reduce the cooling force in x.

Chapter 7

Outlook

7.1 Future improvements to the laser cooling experiment

This section will discuss some improvements to the transverse laser cooling experiment such that a large flux of slow, collimated molecules can be delivered to an eEDM experiment.

7.1.1 The X(3) repump laser

In the current experiment, a large source of loss of molecules is due to decays to the X(3) state, which is currently not repumped. From the fREM in Sec. 6.2, we can estimate the number of photons scattered by molecules in our transverse cooling experiments. From Fig. 6.11, we can see that this is around $\gamma = 300$. This means we expect to lose $1-(1-f_{0,3})^{\gamma} = 60\,\%$ of molecules to X(3), which is similar to the loss we observe in experiments. To improve the efficiency of the laser cooling, this state must also be repumped. As shown in Fig. 2.7, we will do this by driving the A(1)-X(3) transition.

First, the frequency of this transition must be found by spectroscopy. This has been done by J. Lim in collaboration with the group of T. Steimle [173]. Second, parts for a laser set-up to drive this transition must be purchased, and the set-up constructed. This set-up has been identified, and we are waiting for equipment to arrive. In Sec. 2.5.2, it was determined that for effective repumping, $\sim 1\,\mathrm{mW}$ of light is required to address each hyperfine ground state in the A(1)-X(3) transition. The laser system should produce $\gtrsim 40\,\mathrm{mW}$ of 585 nm light, and therefore, we can address the ground state hyperfine structure by broadening the laser frequency using an overdriven $\sim 20\,\mathrm{MHz}$ EOM.

With the addition of the A(1)-X(3) repump, the available number of cooled molecules will be more than doubled compared to the current experimental configuration. This will also make the effect of laser cooling much more clear, as the change in position distribution at the detector will be almost entirely due to radiation pressure, rather than

optical pumping of molecules into non-addressed states.

7.1.2 Experimental parameter optimisation

Optimised experimental parameters for the Doppler and Sisyphus cooling regimes should be determined. This includes the multi-pass configuration for the laser cooling beam (examples of which are given in Fig. 6.2), the laser beam size, the detunings and powers of the laser frequency components, and the magnetic field strength. By detecting the molecular beam at two locations after laser cooling, and extracting the divergence, the effect of adjusting these parameters should become clear.

7.1.3 Laser cooling in 2D

Laser cooling will be done in 2D, using a second cooling beam, which traverses the molecules in the orthogonal direction. This will reduce the divergence of the beam in both transverse directions. This can be done very quickly, as the large windows and mirrors are ready to be installed in the vacuum chamber. It can also be done without significant loss in laser power propagating in each cooling dimension. This is because a significant amount of laser power of laser(0,0) is lost in the current beam combining set-up, see Fig. 4.7, which could be used for a cooling beam propagating in y. Alternatively, the cavity combiner could be used to improve the beam combining efficiency, and after light has travelled through the multi-pass set-up in x, it could be re-cycled to do the same in y.[1]

However, the presence of the orthogonal beams propagating in y will decrease the cooling rate in x. Currently, the cooling transition is strongly saturated, therefore the additional light will compete to drive the transitions. For Doppler cooling, this may mean that the interaction length should be approximately doubled.

We would also like the laser cooled position distribution of the beam to be smaller. Currently, the cooled position distribution has a FWHM of $\sim 50\,\mathrm{mm}$ at the end of the cooling region. This is not through inefficiency of the laser cooling; it is as a result of the $\sim \pm 5\,\mathrm{m\,s^{-1}}$ transverse velocity range over which laser cooling has a large effect, together with the time taken for the molecules to reach the laser cooling region. However, it is difficult to laser cool such a large molecular beam in 2D, as very large laser beam sizes are required. This presents problems for multi-passing the cooling light, and achieving a high laser intensity. A significant reduction of the position spread could be obtained by starting the laser cooling very close to the molecular source. This would require an investigation into the He-YbF collision rate. Other methods of reducing the cooled beam size are discussed in Sec. 7.2.4.

[1] Additionally, the $\sim 40\,\%$ loss in fibre coupling could be addressed, by improving the mode matching of every laser frequency component to the fibre.

Compressing a position distribution can also be done by implementing a 2D MOT, This may reduce the velocity-dependent force somewhat, and it is currently unclear whether that is a price worth paying for the compression

7.1.4 Improvements to the buffer gas source

As is desired in most experiments, our experiment would benefit from a molecular source with higher flux, and lower forward velocity. It should be possible to improve the flux of the source through some optimisation, and reduce the forward velocity using a different cell design. The process by which molecules are produced, and the dynamics of their extraction from the buffer gas cell, are complicated, and the source is therefore difficult to model. Instead, we resort to trial and improvement.

Other members of the group are testing new buffer gas cell geometries, as well as a source which uses neon as the buffer gas rather than helium. The use of neon requires the buffer gas cell (BGC) to be at $\sim 20\,\mathrm{K}$ rather than $\sim 4\,\mathrm{K}$ such that the neon does not freeze. The thermal velocity of neon at $20\,\mathrm{K}$ is similar to that of helium at $4\,\mathrm{K}$ and so the forward speeds of both beams are similar. The higher temperature of the BGC can lead to a higher rotational temperature of the YbF molecules, meaning there are less in $N = 1$. However higher flow rates of neon can be used to achieve rotational cooling in the expansion after the aperture of the cell [137]. Significant rotational cooling in a YbF, neon buffer gas source has recently been observed in this group. It is possible to use higher flow rates of neon compared to helium, because neon is easier to pump. This is because it freezes to cold ($\lesssim 15\,\mathrm{K}$) surfaces inside the vacuum chamber, and Turbo pumps also have higher pumping speeds for neon compared to helium. In the neon buffer gas experiment at the CCM, the buffer gas cell is attached to the cold plate of a cryocooler, which is at $\sim 4\,\mathrm{K}$, via a small thermal link. The cell is then heated to $\sim 20\,\mathrm{K}$. The charcoal shields remain at $\sim 4\,\mathrm{K}$, and adsorb neon efficiently. It will be interesting to see if the neon buffer gas source can produce an improved molecular flux.

Additionally, there is the question of the method used to produce YbF. Instead of SF_6, a wide variety of fluorine containing gasses could be tested to find if a different gas would increase the molecular yield. It would also be interesting to collaborate with chemists, to determine whether a chemical process could be used to generate YbF efficiently.

J. Lim has considered producing YbF using femtosecond ablation, rather than using an Nd:YAG laser with a nanosecond pulse length. The argument for doing this is as follows. For nanosecond ablation, a significant proportion of the energy of the laser pulse goes into heating the ytterbium rod, and melting its surface, rather than forming an ablation plasma. This is because the pulse length is longer than the time it takes for electrons to conduct heat away from the surface, which is the order of $10\,\mathrm{ps}$ [174]. Using an ablation

pulse of picosecond or femtosecond duration can mean that the pulse length is shorter than the conduction time, and nearly all of the energy is used to vaporise ytterbium. So far, experimental results for picosecond ablation for a single pulse of comparable energy have not shown a clear advantage. There may be an advantage if shorter pulses are used. Using shorter pulses may also enable the source to produce a higher flux when it is run at higher repetition rates.[2]

Instead of using an ablation laser, YbF could be produced inside the cell in an electrical discharge, this idea is being considered by N. Fitch.

7.2 Guiding and collimating molecules

In addition to laser cooling, there are other methods by which a molecular beam may be collimated, such as the use of a magnetic or electrostatic lens. Such devices create a conservative potential, meaning that they cannot be used to increase the phase space density (Liouville's theorem).

During the course of this project, we have tested a magnetic guide, which had a collimation effect on our molecular beam. The entrance of the guide was close to the molecular source, and its exit was at the start of the laser cooling region. This was so that molecules were delivered to the centre of the cooling region, with a narrower transverse position distribution, because otherwise, there was a large gap between the molecular source and laser cooling region (for $l_1 = 410\,\mathrm{mm}$ in Fig. 6.1). However, the correlation between the position and velocity distributions of molecules leaving the guide is more complicated than of a molecular beam diverging from a small aperture. This results in the effect of laser cooling becoming less clear, and so the guide was not used in the laser cooling experiments presented in this thesis.

Here I will briefly discuss magnetic guiding, and compare results of trajectory simulations to experimental measurements of the transverse position distribution emitted from the guide. I will also suggest a simple approach, that could be used to produce a molecular beam with low transverse temperature, and a narrow transverse position distribution using both a magnetic lens and laser cooling.

7.2.1 Multipole magnetic guides

The equation for an ideal multipole field can be written as [175],

$$B_y + \mathrm{i}B_x = C_n(x + \mathrm{i}y)^{n-1}, \tag{7.1}$$

[2] For nanosecond ablation the time-averaged flux decreases for repetition rates significantly higher than 2 Hz.

where $B_{x,y}$ are the magnetic field components in the x and y directions, $B_z = 0$, and C_n is a complex number whose modulus determines the strength of the magnetic field and whose argument determines its orientation. The type of multipole field is determined by integer n. For a dipole, $n = 1$, a quadrupole $n = 2$, and a hexapole, $n = 3$. The magnitude of the magnetic field, $B = (B_x^2 + B_y^2)^{1/2}$, due to such a field is,

$$B = |C_n| r^{n-1}. \tag{7.2}$$

The force exerted on a particle with an effective magnetic dipole moment μ_{eff}, by magnetic field of magnitude B is,

$$\vec{F} = \mu_{\text{eff}} \vec{\nabla} B. \tag{7.3}$$

For a harmonic guide, $\vec{F} \propto -\hat{r}r$, where $\hat{r}$ is the radial unit vector. To obtain such a force, the field strength should increase quadratically with radial distance, so a hexapole field should be used. For the octopole guide, the restoring force $\vec{F} \propto -\hat{r}r^2$, and the oscillation frequency increases with the amplitude of oscillation. For a quadrupole guide, the restoring force is independent of r, and oscillation frequency decreases with amplitude.

The octopole guide was built for a previous experiment, and this configuration was chosen as the design offers the larger transverse phase space acceptance, TPSA, when built using permanent magnets with the same magnetic field strength. This is shown in the phase space plot in Fig. 7.1.

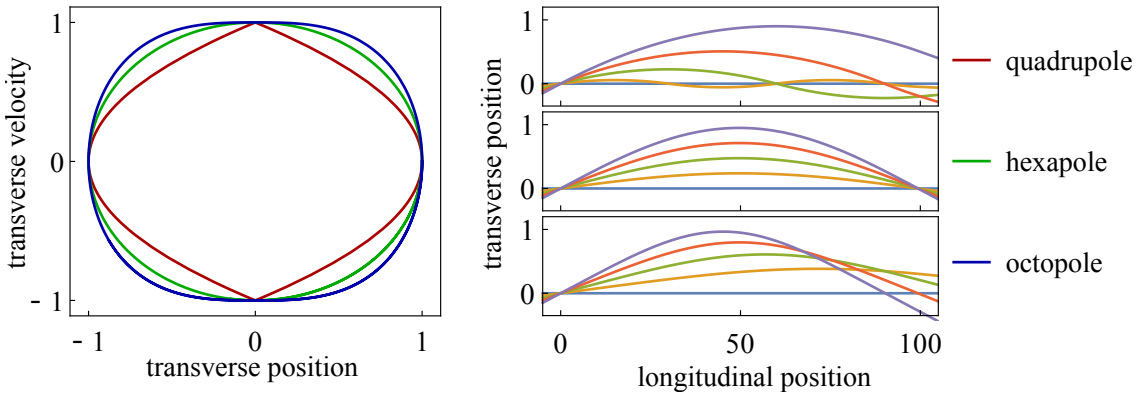

Figure 7.1: Left: The phase space acceptance of types of magnetic guide. Separatrices enclose the region of TPSAs for different types of guides with the same maximum magnetic field strength and inner radius (separation between opposing magnets). The difference in phase space acceptance between guide types is larger than the difference in area shown; it is proportional to phase space volume enclosed when separatrices are revolved about both the position and velocity axes. Right: Trajectories for particles travelling through the guides, which oscillate through the $r = 0$ axis, which all have the same longitudinal velocity. In the hexapole guide the oscillation period is independent of amplitude.

7.2.2 Octopole guide model

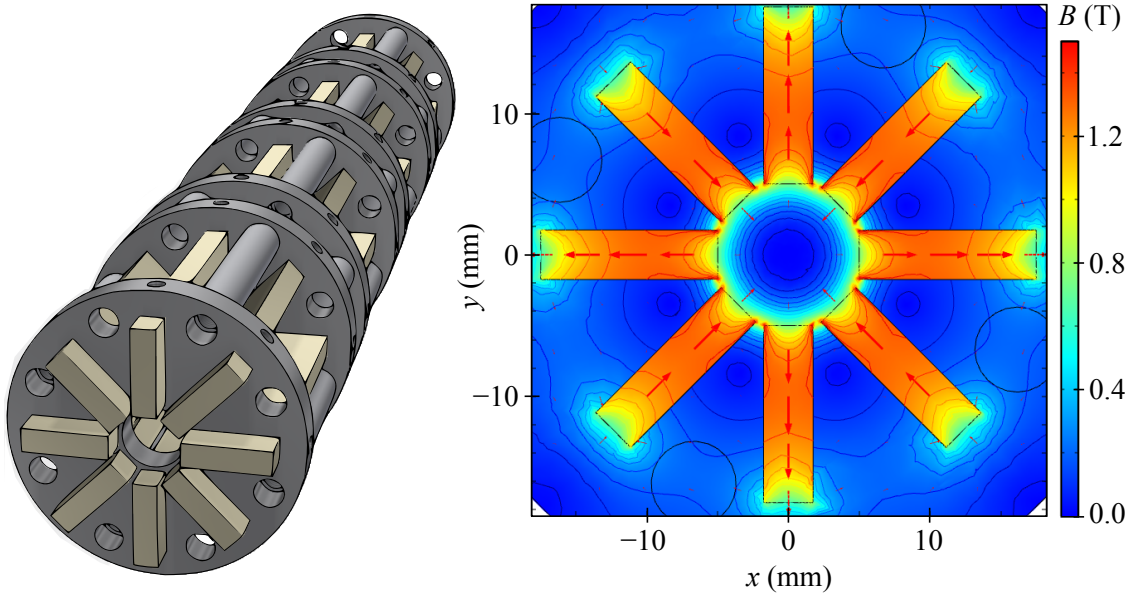

Figure 7.2: Left: A drawing of the magnetic guide, the inner diameter of the magnet holders is 9 mm and the spacing between magnets opposite one another is 10 mm. The guide is modular; here four modules are shown, each 56 mm long. Right: A cut-through of the magnetic field map.

The entrance of the guide was ~ 1 cm outside the charcoal shields which is 100 mm from the cell aperture. The length of the guide was 280 mm.

The magnetic field produced by two sections of guide was modelled using COMSOL Multiphysics by N. Fitch, to create a 3D magnetic field map, Fig 7.2. From the magnetic field map the expected transverse phase space acceptance of the guide can be calculated, this is shown in Fig 7.3. The magnetic guide was mounted from the lid of the radiation shields which is at around 70 K. According to manufacturers of neodymium magnets, the magnetization is reduced by around 15-20% at these temperatures. To account for this, all magnetic field strengths in the field map were scaled down by 20% (no scaling is applied in Fig. 7.2). This scaling factor was chosen to match the anticipated reduction in magnetization, and not selected to achieve a good match between experiment and model.

Fig. 7.3 suggests that molecules with transverse speeds of less than $5\,\mathrm{m\,s^{-1}}$ should be accepted by the guide. This is similar to the velocity range for which laser cooling will have a significant effect within the current interaction time of the experiment. In the 100 mm between the source and start of the magnetic guide, molecules with $v_r = 5\,\mathrm{m\,s^{-1}}$, $v_z = 180\,\mathrm{m\,s^{-1}}$, will have diverged by 2.8 mm. Additionally, the aperture of the source is 1.5 mm in radius. For these reasons, molecules do not enter the guide on axis. This should have the effect of reducing the maximum transverse velocity that may be guided compared to the velocity width of the separatrix.

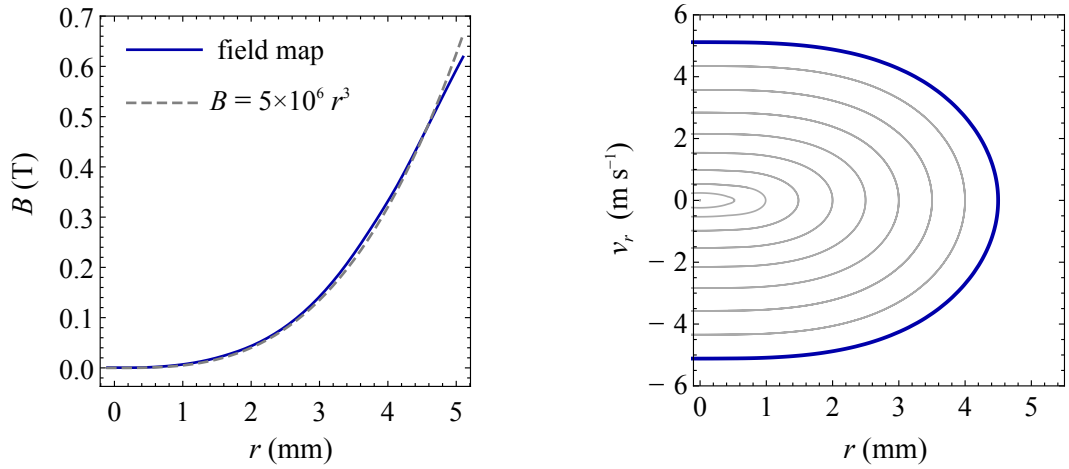

Figure 7.3: Left: A plot of the magnetic field distribution in the guide from the field map, with a 20% reduction in field strength. A curve where the field has r^3 dependence is plotted for comparison with the field distribution of an ideal octopole. Right: The phase space acceptance of the guide as determined from the field map, plotted in radial coordinates. The inner curves are trajectories for particles which travel through the $r = 0$ axis.

To model the effect of the guide on the molecular beam, taking into account the divergence before the guide, field inhomogeneities at the gaps between guide stages, and the orbital motion of molecules about the z axis, trajectory simulations were run for particles travelling through the magnetic guide, with the magnetic field determined by the field map.

The randomly chosen initial distribution for the simulation is the same distribution as that used in Sec. 6.2. The position distribution is a uniform disc in the xy-plane of radius 1.5 mm, 100 mm from the entrance of the guide in z. The speed distribution is Gaussian with mean 180 m s^{-1} and a 1/e^2 full width of 100 m s^{-1}, the distribution of the direction of travel is uniform. The modelled initial positions and velocities are not correlated.

Fig. 7.4 shows the Zeeman splitting of the $|F, m_F\rangle$ states in X(0). As can be seen from the figure, at field strengths greater than ~ 5 mT, the interaction with the magnetic field is larger than the spin-orbit interaction, and the molecules are in the Paschen-Back limit of the Zeeman interaction. In the magnetic guide, molecules will spend very little time in regions of magnetic fields < 5 mT, therefore we can make the approximation $\mu_{\text{eff}} = -\mu_{\text{B}}$ for the weak field seekers. Half of the ground m_F states are strong field seekers, therefore in the experiment half of the molecules are anti-guided and lost. To calculate the force on the molecules, Eq. (7.3) is used.

7.2.3 Octopole guide results

The results of the trajectory simulations for the transverse phase space are shown in Fig. 7.5. From Fig. 7.5 1.b and 1.c, we can see that molecules do approximately 1/4 of

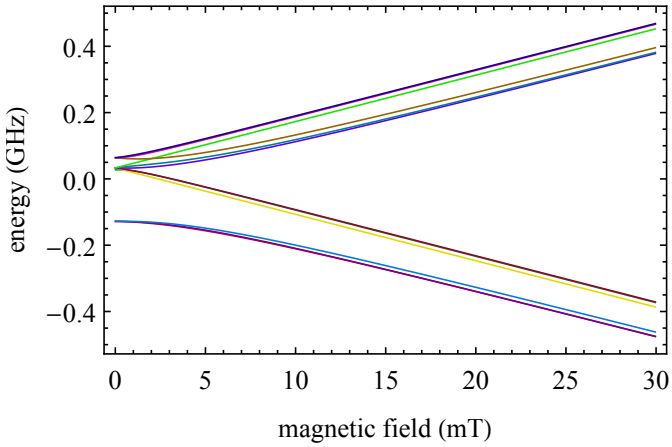

Figure 7.4: The Zeeman splitting in the X(0) state in a strong field. This was calculated using computer code of M. Tarbutt.

an oscillation inside the guide, which corresponds to a rotation of 90° in phase space. Molecules with low transverse velocities undergo slower rotations in phase space. Those with velocities $v_r \lesssim 2\,\mathrm{m\,s^{-1}}$ undergo close to 1/8 of an oscillation, which has the effect of collimating them, as can be seen by comparing Fig. 7.5 2.b and 2.c.

The molecular beam was imaged using the CCD camera and a similar imaging system to that described in Sec. 6.1.2 at two different distances in z after the guide. The imaging regions had a width of 44 mm in x. The probe beam propagated in y with a $1/e^2$ width of $\sim 5\,\mathrm{mm}$. To model the molecular distribution that we see on the CCD we plot a histogram of the x coordinates of particles in the simulation that have $-22\,\mathrm{mm} < x < 22\,\mathrm{mm}$ and $-2.5\,\mathrm{mm} < y < 2.5\,\mathrm{mm}$ at the z coordinate of the detector. The detection regions are 510 mm and 960 mm from the output end of the magnetic guide. Comparisons between the modelled distributions and experimental results are shown in Fig. 7.6.

The measured molecular distributions are good agreement with the simulation results. We do not have a direct comparison of the molecular flux with and without the guide, however the increase in observed signal was compatible with the simulation results. It can be seen from the increase in the number of molecules with transverse speed $\lesssim 2\,\mathrm{m\,s^{-1}}$ that the guide has the effect of collimating the molecular beam.

As well as the loss of the initial population of strong field seekers, other mechanisms of loss are Majorana transitions from weak field seeking states to strong field seeking states inside the guide, and state-changing molecule-helium collisions inside the guide which transfer population to strong field seeking states. Majorana losses in this guide were estimated by J. Bumby, [131] Sec. 6.4, and are negligibly small. The cross section for theses collisions was calculated in [176], and were found to be very small, and this should not be a significant effect inside the guide.

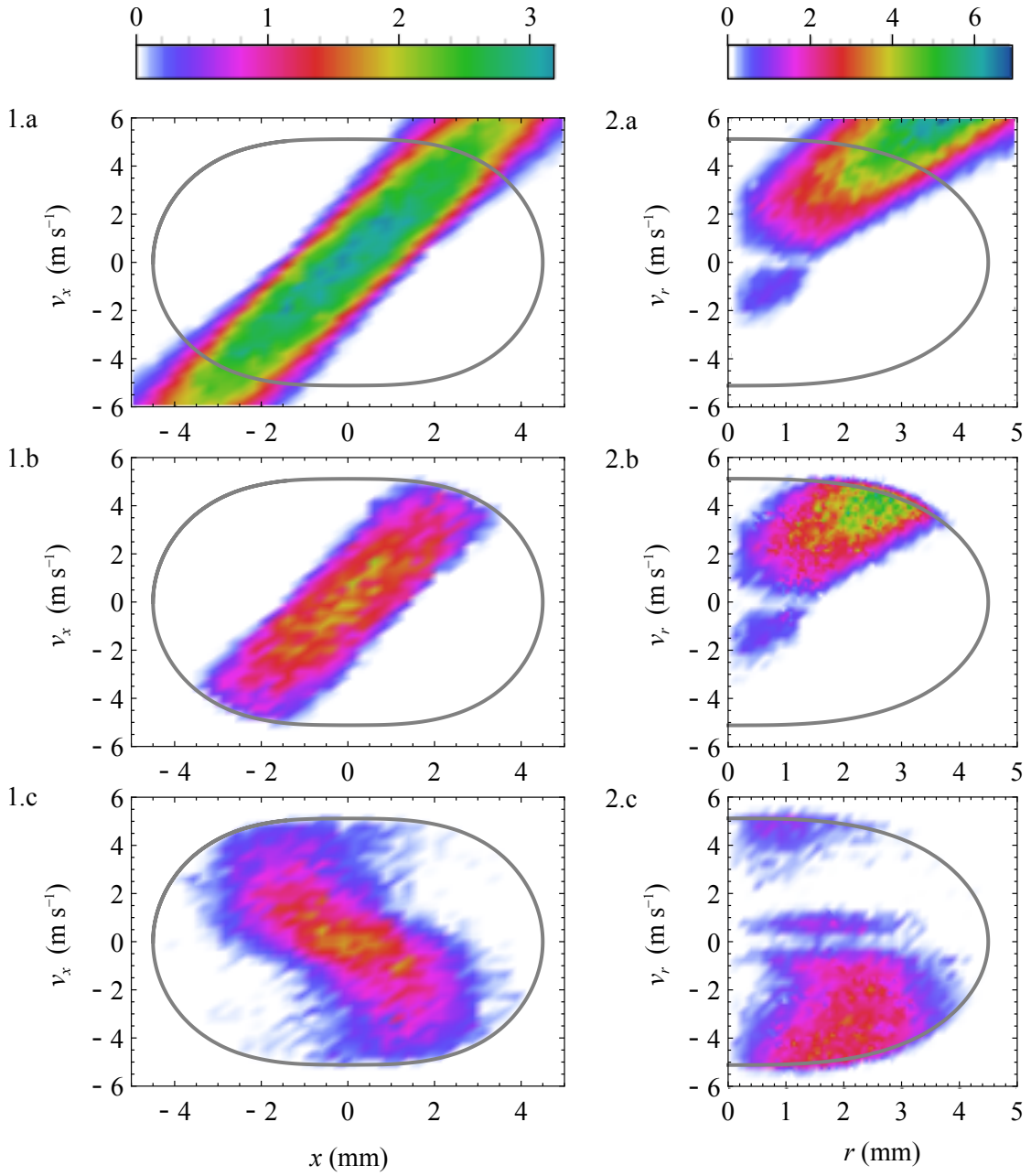

Figure 7.5: 1: The simulated phase space distribution in x, marginalizing over y. 2: The phase space distribution in r. a: The distributions at the guide entrance. b: The input distribution accepted by the guide. c: The distribution at the guide exit. Here, v_r is considered negative if molecules have a net motion towards the z-axis. In the initial distribution in 2.a, there is a small number of molecules which travel towards z because the molecular source is not a point source. The colour bars are proportional to the number of particles with a particular set of coordinates in (x, v_x) or (r, v_r).

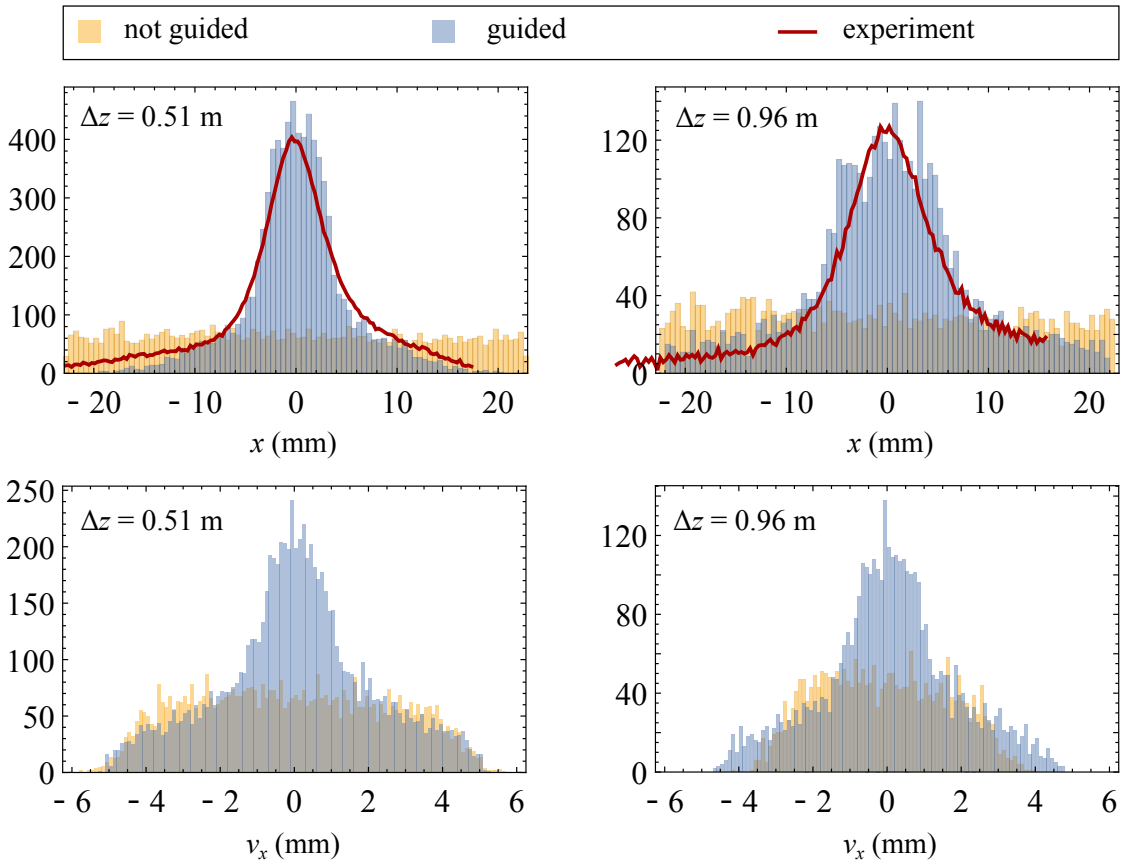

Figure 7.6: The histograms are the modelled position and velocity distributions in x at the two detection regions. The red lines are the measured position distributions. The comparison between guided and unguided molecules takes into account the factor of two loss of the number of guided molecules due to half being strong field seekers. The guide delivers an increase in signal of ~ 5.7 at the center of the lower imaging region, and ~ 4.8 at the upper imaging region.

7.2.4 Methods of increasing the laser cooled phase space density using a magnetic lens

Collimating and cooling

Instead of the octopole guide, a hexapole guide could be used as a magnetic lens, a hexapole of the correct length and built with magnets of the same field strength as used for the octopole, could collimate molecules with $v_r < 5\,\mathrm{m\,s^{-1}}$. Because molecules from the buffer gas source have different forward velocities, this collimation would not be perfect, however if the guide were designed to collimate molecules with $v_z = 180\,\mathrm{m\,s^{-1}}$, it would have a beneficial effect in reducing the transverse speed of all forward velocity classes.

Before the start of the guide, there should be a region of uniform field of around $\gtrsim 20\,\mathrm{mT}$ to Zeeman shift the strong and weak field seeking states to distinctly separate energies. In this region, the A(0)-X(0) transition is driven, where the light is resonant with

the strong field seekers in order to optically pump them into weak field seeking states.

The transverse position distribution at the exit of the guide will fill the area of the exit aperture. If the guide has a similar design to the octopole, this will be the area $r < 4\,\mathrm{mm}$. At the output of the guide the molecular beam may be transversely cooled in 2D to further reduce the transverse velocity spread. Depending on the capture velocity for Sisyphus cooling, this may be the most efficient method of doing this. Alternatively, a 2D MOT region could then be used to compress both the position and velocity distribution.

Focussing and cooling

A different approach, which may achieve a smaller phase space distribution is to use a hexapole as a focussing lens. Here the guide focusses molecules at some distance after the output where the position of the focus is inside the laser cooling region. With the correct choice of focal distance, molecules can approach zero transverse velocity as they approach $r = 0$. By this method, the transverse position distribution, for a certain range of v_z, can be made much smaller than by using laser cooling alone even if the cooling was to begin immediately in front of the aperture of the buffer gas source. Again, molecules can be optically pumped into weak field seeking states before entering the hexapole, such that half of them are not lost. Here, a simple model for this process is presented, and applied to the transverse cooling of YbF.

A molecule is emitted from a point source, and travels for a time t_f in free flight. It has initial transverse position $x(t = 0) = 0$, and initial transverse velocity $\dot{x}(t = 0) = v_0$. At t_f, it has position $v_0 t_\mathrm{f}$.

The molecule enters a hexapole magnetic guide. The change in longitudinal velocity of the molecule at the entrance to the guide is neglected, such that the molecule spends a time t_g in the magnetic guide, regardless of its transverse position on entry. In the guide, the molecule is subject to a harmonic acceleration

$$\mathrm{if}\,\{t_\mathrm{f} > t > (t_\mathrm{f} + t_\mathrm{g})\}: \quad \ddot{x}(t) = -\frac{k}{m}x(t), \tag{7.4}$$

its transverse position is given by,

$$x(t) = A\cos\left(\omega(t - t_\mathrm{f}) - \phi\right), \tag{7.5}$$

with,

$$\omega = \sqrt{\frac{k}{m}}, \tag{7.6}$$

$$A = \sqrt{\frac{v_0^2}{\omega^2} + v_0^2 t_\mathrm{f}^2}, \tag{7.7}$$

$$\phi = \arctan\left(\frac{1}{t_\mathrm{f}\omega}\right). \tag{7.8}$$

After leaving the guide it immediately enters a region of laser cooling. The acceleration on the molecule is,

$$\text{if}\,\{(t_\mathrm{f} + t_\mathrm{g}) < t < (t_\mathrm{f} + t_\mathrm{g} + t_\mathrm{c})\}: \quad \ddot{x}(t) = -\frac{\beta}{m}\dot{x}(t). \tag{7.9}$$

Solving for the position of the molecule, one obtains

$$x(t) = -\frac{\omega}{\alpha} A \sin(\omega t_\mathrm{g} - \phi)\left(1 - \mathrm{e}^{-\alpha(t - t_\mathrm{f} - t_\mathrm{g})}\right) + A\cos(\omega t_\mathrm{g} - \phi), \tag{7.10}$$

where $\alpha = \beta/m$. The molecule asymptotically approaches zero velocity. For the smallest transverse position at the lowest velocity, we should find the set of of experimental parameters t_f, t_g, ω and α which give $x(t \to \infty) = 0$. By solving Eq. (7.10) for this situation, one finds,

$$t_\mathrm{g} = \frac{1}{\omega}\left(\arctan\left(\frac{\alpha}{\omega}\right) + \arctan\left(\frac{1}{t_\mathrm{f}\omega}\right) + n\pi\right), \tag{7.11}$$

where n is an integer. The solution where the molecule spends the least time in the guide has, $n = 0$, and there is no advantage to choosing $n > 0$. This relation has no dependence upon v_0, therefore molecules with all initial transverse velocities will be collected towards $x = 0$ as $\dot{x} \to 0$. Example plots of molecular trajectories through such a set-up are shown in Fig. 7.7.

This position distribution cannot be narrower than the size of the aperture of the buffer gas source. It will also be broadened according to the forward velocity distribution of the molecules and the diffusion due to photon scattering. Both of these effects would also exist without the magnetic lens present. Because molecules do not enter the guide with position $x = 0$, there will be some change in their forward velocity upon entering the guide due to the field gradient in z. Molecules from the buffer gas source also have a large forward velocity spread. These differences in velocity reduce the effectiveness of the method, however with a careful choice of magnetic field strength and guide length and position, the method can increase molecular beam brightness for molecules over range of v_z compared with laser cooling without the magnetic lens.

For a hexapole guide which has a magnetic field of 1 T at the magnet surfaces, and the space between opposing magnets is 1 cm, $\omega \approx 1500\,\mathrm{rad\,s^{-1}}$ for YbF. From the laser cooling

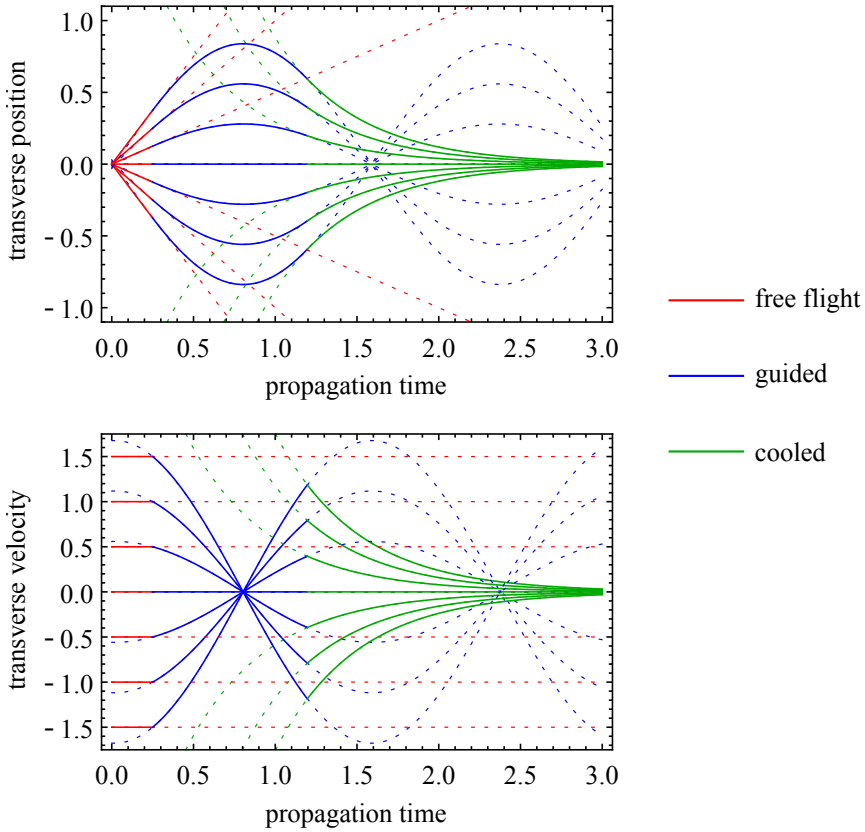

Figure 7.7: Plots of molecular trajectories through the lensing and cooling set-up described in the text. The choice of parameters fulfils Eq. 7.11. The parameters used are $t_\mathrm{f} = 1/4$, $\omega = 2$ and $\alpha = 2$, which sets $t_\mathrm{g} = 0.95$.

simulations in Sec. 6.2.3, we see that α may take a similar value. For a molecule travelling at $180\,\mathrm{m\,s^{-1}}$, which travels 10 cm in free flight before the guide, the guide should be 20 cm long for the molecules transverse position to approach zero as it is cooled. Additionally all molecules with forward velocities between $135\,\mathrm{m\,s^{-1}}$ and $275\,\mathrm{m\,s^{-1}}$ have smaller transverse displacements than they would have if they had been laser cooled as they emerged from the source. This method would also work well for smaller α, for the case of 2D cooling where the orthogonal beams compete.

7.3 Towards a fountain of YbF molecules

It had been anticipated that YbF molecules could be cooled in an optical molasses [72]. The plan was to use a two stage buffer gas source to produce the molecular beam. This source would produce a significant number of YbF molecules with forward velocities low enough to be brought to rest in an optical molasses or magneto-optical trap (without the need for any additional longitudinal slowing). In this reference the capture velocity of an optical molasses for YbF was estimated to be $\sim 10\,\mathrm{m\,s^{-1}}$. This would enable the eEDM experiment to be performed in a fountain geometry. A sketch of such an experiment is

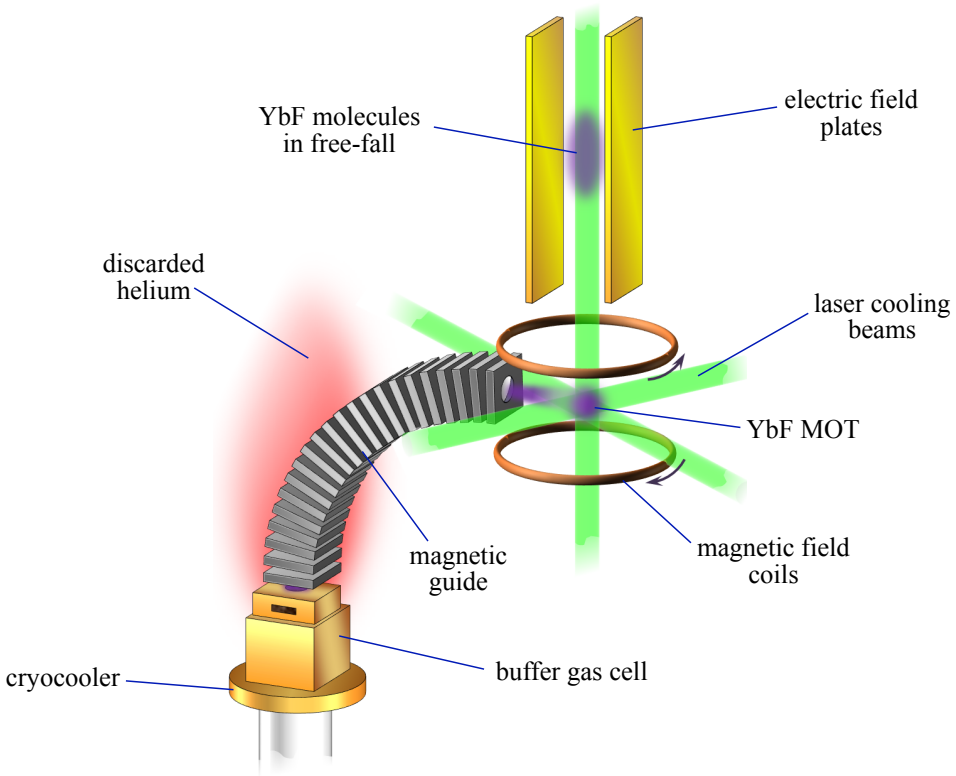

Figure 7.8: A schematic of the proposed eEDM experiment using a fountain of YbF molecules. First, molecules are produced from a two stage buffer gas cell. Slow molecules are guided around the bend of a curved magnetic guide. Helium atoms are diamagnetic, and are not guided. There is a differential pumping between the source and the output end of the magnetic guide, such that the pressure is low in the MOT region. Molecules are captured in a MOT, and cooled to $\sim 200\,\mu\mathrm{K}$. The MOT field is switched off, and molecules are launched vertically at $1.5\,\mathrm{m\,s^{-1}}$ by changing the relative detuning of the vertical laser beams. The eEDM interferometry experiment is then performed using the fountain of molecules. Molecules spend 250 ms in free-fall, and the interaction time with the electric field is increased by $\times 250$ compared to the current experiment, described in Sec. 1.3.4.

illustrated in Fig. 7.8.

In this section I will discuss methods that could be used to obtain molecules which are slow enough to be trapped in a magneto-optical trap. In the following section, simulation results for the forces in a magneto-optical trap for YbF molecules are presented.

7.3.1 A two stage buffer gas cell

The least technically challenging method of producing $< 10\,\mathrm{m\,s^{-1}}$ YbF molecules may be the use of a two stage buffer gas cell. The design and performance of a two stage buffer gas cell for molecules was first discussed in [177], where the CaH molecule was used.

In a single stage buffer gas cell, molecules leave the cell after thermalisation with the buffer gas species. However upon leaving the cell, the forward velocity of the molecules

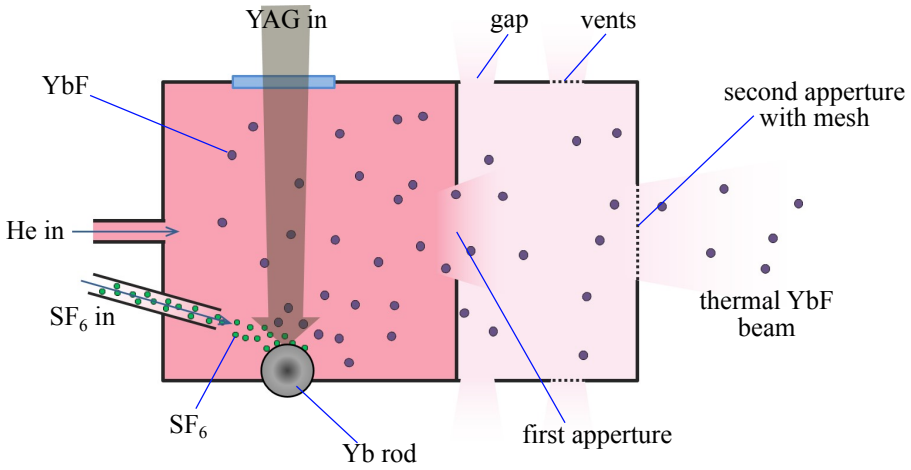

Figure 7.9: A schematic of the two stage buffer gas cell.

becomes similar to that of the buffer gas due to collisions in the forward direction. Because the buffer gas species is generally much lighter than the molecules, its thermal velocity is much higher. The result is that the forward velocities of the molecules are boosted to that of the atoms.

A schematic of a two stage buffer gas cell is shown in Fig. 7.9. In the two stage buffer gas cell, molecules enter a second cell after leaving the first. In the second cell the helium pressure is lower than the first. Over the aperture of the second cell, there is a mesh, whose purpose is to back scatter buffer gas atoms into the path of the molecular beam. This reduces the extraction efficiency of the cell, but also reduces the forward speed of the molecules as they leave the cell, and can result in a slow thermal tail to the velocity distribution.

A two stage buffer gas cell has been tested in our group by J. Bumby, and is discussed in [131]. The two stage cell had a slower velocity distribution than that of single stage designs, and had a peak velocity of $70\,\mathrm{m\,s^{-1}}$ and produced a flux of $\sim 2\times10^{9}\,\mathrm{sr^{-1}}$ per pulse in the $X^2\Sigma^+(v=0,N=0)$ state. This corresponds to a much higher flux of slow molecules with forward speeds $< 100\,\mathrm{m\,s^{-1}}$ in X(0) compared to a single stage design. However, it has not yet produced detectable molecules with forward velocities $< 10\,\mathrm{m\,s^{-1}}$. This method will be investigated further by this group in order to attempt to obtain YbF molecules with slow forward velocities. This will involve the trial of different cell geometries, and comparison of two stage source buffer gas beams where either helium or neon is used as the buffer gas.

7.3.2 Decelerating a YbF beam

Laser slowing

A different option is to use a single stage buffer gas source, and slow molecules in the beam to $\sim 10\,\mathrm{m\,s^{-1}}$ using radiation pressure. This has been done successfully for both SrF, [32], and CaF [42]. SrF has a mass of 107 u compared to that of YbF which is 193 u. Both have similar excited state lifetimes, which dictates the maximum scattering rate, and the momentum of a photon of the frequency of the A(0)-X(0) transition is similar for both. Therefore, it takes almost twice as long to slow YbF to rest compared to SrF, and during this time, molecules travel twice the distance. If we wished to slow YbF at $180\,\mathrm{m\,s^{-1}}$ to a similar final velocity, an interaction length of $\sim 4\,\mathrm{m}$ would be required.

A larger problem is that, the Franck-Condon factors (FCF) of YbF are less favourable than those of SrF (for example, $f_{0,0}^{\mathrm{SrF}} = 98\,\%$ compared with $f_{0,0}^{\mathrm{YbF}} = 93\,\%$) this means that more repump lasers are required such that molecules are not lost into non-addressed vibrational states. The recoil velocity per absorbed 552 nm photon for YbF is $3.7\,\mathrm{mm\,s^{-1}}$. To slow a YbF molecule from $180\,\mathrm{m\,s^{-1}}$ to rest, it must scatter at least 50 000 photons. Using the laser systems we have currently available, the X(3) state is not addressed, $f_{0,3} \sim 0.03\,\%$, and so the probability of a molecule remaining in a bright state after this number of photon scatters would be 3×10^{-7}, and we would detect no molecules.

We do not know the FCF for the A(0)-X$(4, 5, ...)$ transitions, but if the sum of these FCFs is $< 0.005\,\%$, 1/10 of the molecules would remain in bright states following the addition of the A(0)-X(3) repump laser, and this method may become viable. Assuming the off diagonal FCFs decrease geometrically, with the addition of a laser to repump X(4), this process could be an efficient method of decelerating molecules.

The use of a Zeeman-Sisyphus decelerator [51] (discussed in Sec. 1.2.3) to decelerate a buffer gas beam of YbF is also being considered. This would require fewer photons to be scattered for the same decrease in longitudinal velocity. However, Zeeman-Sisyphus deceleration for YbF would be complicated because Q(1) transitions would be Zeeman shifted into resonance with one of the optical pumping frequencies at low magnetic field.

Travelling wave decelerators

It should also be possible to decelerate molecules to rest using a Stark decelerator, [178], or Zeeman decelerator, [179]. In these techniques molecules are slowed through the force exerted by inhomogeneous electric or magnetic fields. The first versions of these methods could not perform well for decelerating particles to low velocity as they had a poor transverse phase stability. In improved versions of these designs, moving potential wells are formed, which confine atoms or molecules in 3D. The particles enter these wells at the

beginning of the decelerator, and the forward speed of the wells is decelerated in time, slowing the particles. These designs which offer 3D confinement are often called 'travelling wave decelerators' [180, 181], and have a much improved performance at low velocity.

Using a travelling wave Stark or Zeeman decelerator, it should be possible to decelerate YbF molecules in a buffer gas beam to MOT capture velocities. For SrF, this is being considered by the Hoekstra group, who have so far used a 4 m long travelling wave Stark decelerator, to slow molecules from a 290 m s^{-1} supersonic source to 120 m s^{-1}. They aim to increase the length of the decelerator such that it can operate at a larger phase space acceptance, and slow molecules to the capture velocity of a MOT.

7.4 Modelling a YbF MOT

7.4.1 Introduction

Molecular MOTs are more complicated to understand than their atomic counterparts due to the complexity of the cycling transition. There are many possible combinations of laser polarisations and frequency components from which one can choose to attempt to obtain an optimum trapping and cooling force. Here we will model some possible configurations to estimate the position and velocity dependent accelerations one would expect to find in a MOT for YbF.

In a MOT, where a transition is driven with a single frequency between a pair of angular momentum states j, j', the g-factor of j' is important in obtaining a trapping force [38]. For example, in the 1D case, where j' has no g-factor, there is no restoring force irrespective of the g-factor of j.[3] The choice of σ^+/σ^- polarisation of light that one should choose to obtain a restoring force for a j'-j transition depends upon the values of j and j', and the sign of the g-factor of j' [38]. For systems driven by multiple laser frequency components, magneto-optical trapping forces can also be generated when those frequency components have opposite polarisations and are blue/red detuned with respect to the transition frequency in zero field. This can produce a trapping force even when j has a small or zero g-factor [182].

For YbF, the $F' = 1$ A(0) state has a g-factor of intermediate size (-0.268) compared to those of the X(0) ground states (given in Fig. 6.4). Additionally, the transition must be driven with a set of frequency components to address the ground state hyperfine structure. The effects discussed above will therefore play a role in this system.

Here, to optimise the experimental parameters to achieve large damping and restoring forces, we will simply choose some sensible laser frequencies, and compare the MOT forces

[3] A restoring force can be recovered by using an RF-MOT also explained in [38] in the section entitled 'Rapid switching'.

for different combinations of laser polarisation of those frequency components. In future, it may be beneficial to use an algorithm to optimise the model parameters.

It should also be noted that once molecules reach low velocity in a MOT, there may be significant sub-Doppler effects. These effects have been modelled in [22] for more simple systems by solving the optical Bloch equations. These effects do not exist in the rate equation model used here.

7.4.2 Model

Using the same rate equation model as in [38, 182], (which was discussed in Sec. 6.2), we model a MOT for YbF in 3D. In the model, there are six orthogonal laser beams. Each beam contains n_f frequencies, and so there are $6n_f$ laser frequency components in total. The beams have $1/e^2$ diameters of 15 mm. There is a quadrupole magnetic field $\boldsymbol{B} = A(x\boldsymbol{x}, y\boldsymbol{y}, -2z\boldsymbol{z})$, where $\boldsymbol{x}, \boldsymbol{y}, \boldsymbol{z}$ are unit vectors in the x, y, z-axes, and $A = 150\,\mathrm{mT\,m^{-1}}$ is the field gradient in the xy-plane. The polarisations of the lasers is resolved into the local coordinates of the molecules, where the z-axis is determined by the magnetic field direction. The molecules are assumed to move slowly such that they adiabatically follow the field direction. In the MOT region there are no stationary dark states, as transitions from all ground states may be pumped by the orthogonal beams. In these simulations, no phenomenological magnetic field remixing term is used, i.e. $\chi_{g,g'} = 0$ in Eq. (6.1c).

The full non-linear Zeeman shifts of the X(0) states are used in the model, however the excited states and X(1) states have linear Zeeman shifts given by their g-factors.

7.4.3 Parameters for the model

There are a large number of laser parameters from which to choose. Here we will only focus on the choice of laser scheme used to drive the A(0)-X(0) transition which is the most important. In the rate equation model the choice of laser polarisation and frequency scheme for the A(0)-X(1) transition has only a small ($\sim 10\,\%$) impact on the performance of the MOT. The repump light must only be close to resonance, and have comparable intensity to the A(0)-X(0) light. This is because there is a low scattering rate from these beams.[4] We ignore repump transitions from X(> 1) by setting the branching to these states to zero. In reality, repumping the decays of these states would slow the scattering rate, and reduce the forces, by an amount proportional to the probability of occupancy of these states, which is $\sim 10\,\%$ for reasonable repumping rates.

In the simulations here, the A(0)-X(1) frequencies and polarisation are set such that there is the same total power in all of the frequency components addressing A(0)-X(1) as

[4] For repumping of X(> 1), the effect of the precise choice of laser scheme is negligible due to the tiny scattering rates.

there is in those addressing A(0)-X(0). All A(0)-X(1) beams are σ^+ polarised.

Fig. 7.10 illustrates two possible choices of laser frequency components which we investigate here. We choose to drive the A(0)-X(0) transition with either three or four laser frequency components. The relative frequencies of these components is given in Tab. 7.1, and there is a global detuning of δ for all of these frequencies. In the 3 frequency configuration, transitions from both the $F = 0, 2$ ground states are predominantly driven by a single laser frequency. For the 4 frequency option, the frequencies labelled f2a and f2b, both address the $F = 0$, and $F = 2$ states.

F	X(0)	X(1)
1^+	192.1	205.8
2	161.2	176.5
0	155.7	151.9
1^-	0.0	0.0

3 frequencies	
f	$\Delta\nu$
f1	-192.1
f2	-158.5
f3	0.0

4 frequencies	
f	$\Delta\nu$
f1	-192.1
f2a	-161.2
f2b	-155.7
f3	0.0

Table 7.1: Left: The energy splitting, in MHz, of the hyperfine structure of X(0) and X(1) relative to the lowest frequency F state of each. Centre: The laser frequencies, of each frequency component in the 3 frequency scheme. Right: The laser frequencies of each frequency component in the 4 frequency scheme.

7.4.4 Results

From the model, we obtain steady state solutions for the acceleration of stationary molecules for a range of positions along the x-axis of the MOT. Steady state solutions for the acceleration for a range of velocities in $\boldsymbol{x}$ for a molecule at the origin are also obtained, so that we may investigate the damping force. For the 3 frequency case and 4 frequency case, these accelerations are plotted in Fig. 7.11 and Fig. 7.12 respectively. If all sets of polarisations are reversed, the position dependent acceleration changes sign. We denote the polarisation of the frequency components as $(++-)$, for the case where the f1, f2, f3 components have polarisation σ^+, σ^+, σ^- respectively.

From Figs. 7.11,7.12, we can see that the polarisations which can produce the largest restoring force are $(-++)$ for the 3 frequency case, or either of $(-+++)$ or $(--++)$ for the four frequency case. However, although $(-+++)$ produces a large restoring force at long range, it produces a repulsive force at the MOT centre. The $(-++)$ scheme has virtually no restoring force at the centre. The capture velocity of the MOT will mainly be dictated by the frictional force, and the cooled cloud size will be determined by the restoring force close to the centre. Therefore, out of the three options we should choose $(--++)$, because the frictional forces are similar for all three, but $(--++)$ will produce

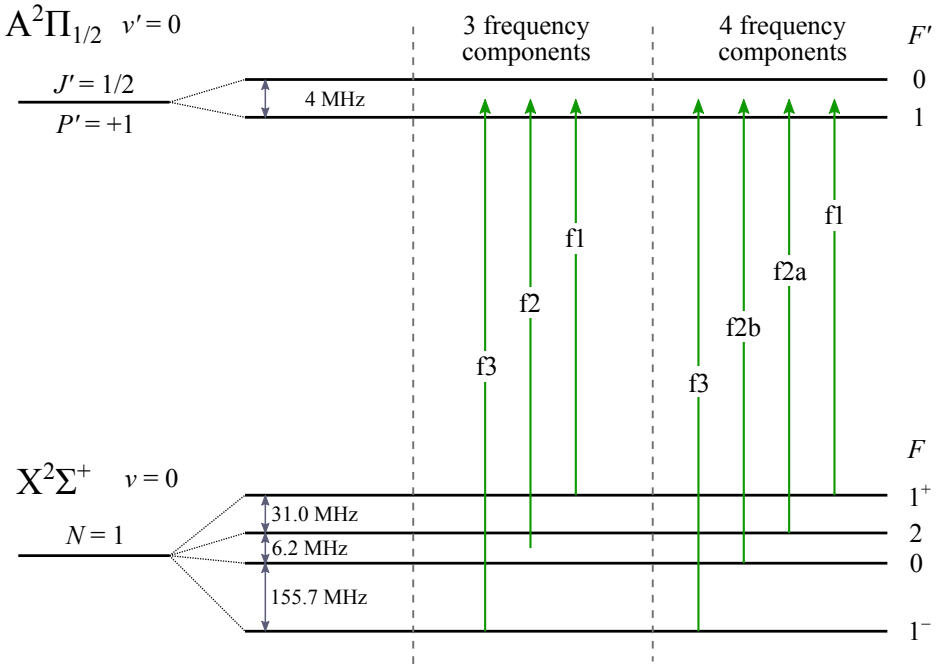

Figure 7.10: Schemes for driving the A(0)-X(0) transition in a YbF MOT.

a smaller molecular cloud than the others.

Now, we compare the difference between $(-+++)$ and $(--++)$ as a function of a global detuning, δ, to check whether a different detuning changes our decision on the choice of polarisation. The acceleration curves for the position and velocity dependent forces as a function of detuning are shown in Fig. 7.13. Here we see that the maximum damping force increases, and shifts towards higher velocity with increasing red detuning. This effect is similar for both polarisation cases, which is as one would expect for Doppler cooling. Interestingly, a restoring force is obtained for both red and blue detuning at displacements $\gtrsim 3\,\mathrm{mm}$. From these curves, it is not clear which set of polarisations is the better choice, as both can produce repulsive regions at the centre of the MOT for certain red detunings. It appears that $(--++)$ is better, because the slope of the restoring force can be made steeper than that of $(-+++)$. In Fig. 7.14, the effect of the laser power on the $(--++)$ scheme is shown. From this we can see that the restoring force is not strongly saturated, even at high laser power, but the damping force does saturate.

Finally, we determine the maximum capture velocity for some MOT configurations. We chose the $(--++)$ scheme, for its beneficial properties discussed previously, the power is set to 80 mW per frequency component per beam. Molecules are launched with direction of travel $\frac{1}{\sqrt{2}}(\boldsymbol{x}+\boldsymbol{y})$, with a range of speeds into the centre of the MOT. Their trajectories are shown in Fig. 7.15 for two detunings, $\delta = -\Gamma$, and $\delta = -2\Gamma$. It can be seen that for the case $\delta = -\Gamma$ molecules up to $(11 \pm 1)\,\mathrm{m\,s^{-1}}$ are captured by the MOT, and for $\delta = -2\Gamma$, molecules with speeds of up to $(12 \pm 1)\,\mathrm{m\,s^{-1}}$ are captured. The position

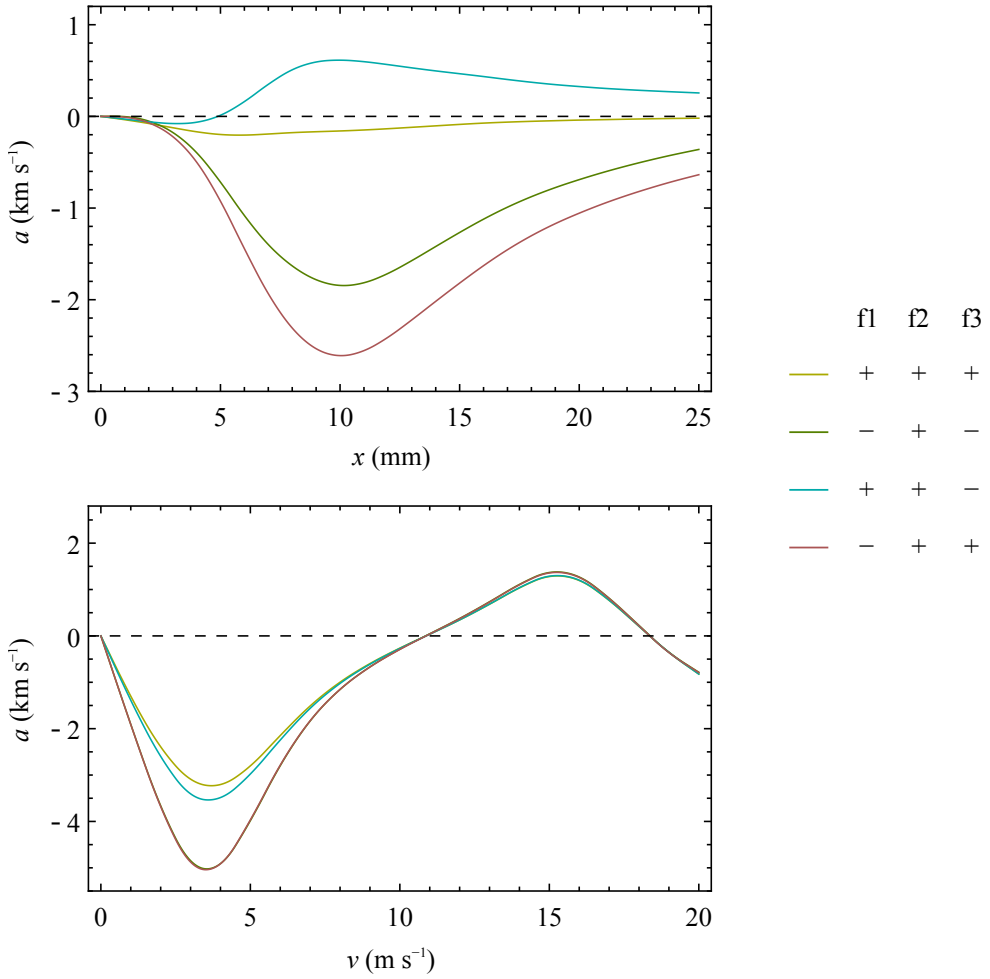

Figure 7.11: Acceleration versus displacement, and acceleration versus speed curves for YbF MOTs where the A(0)-X(0) transition is driven using three frequency components. The power per component, per beam is 80 mW.

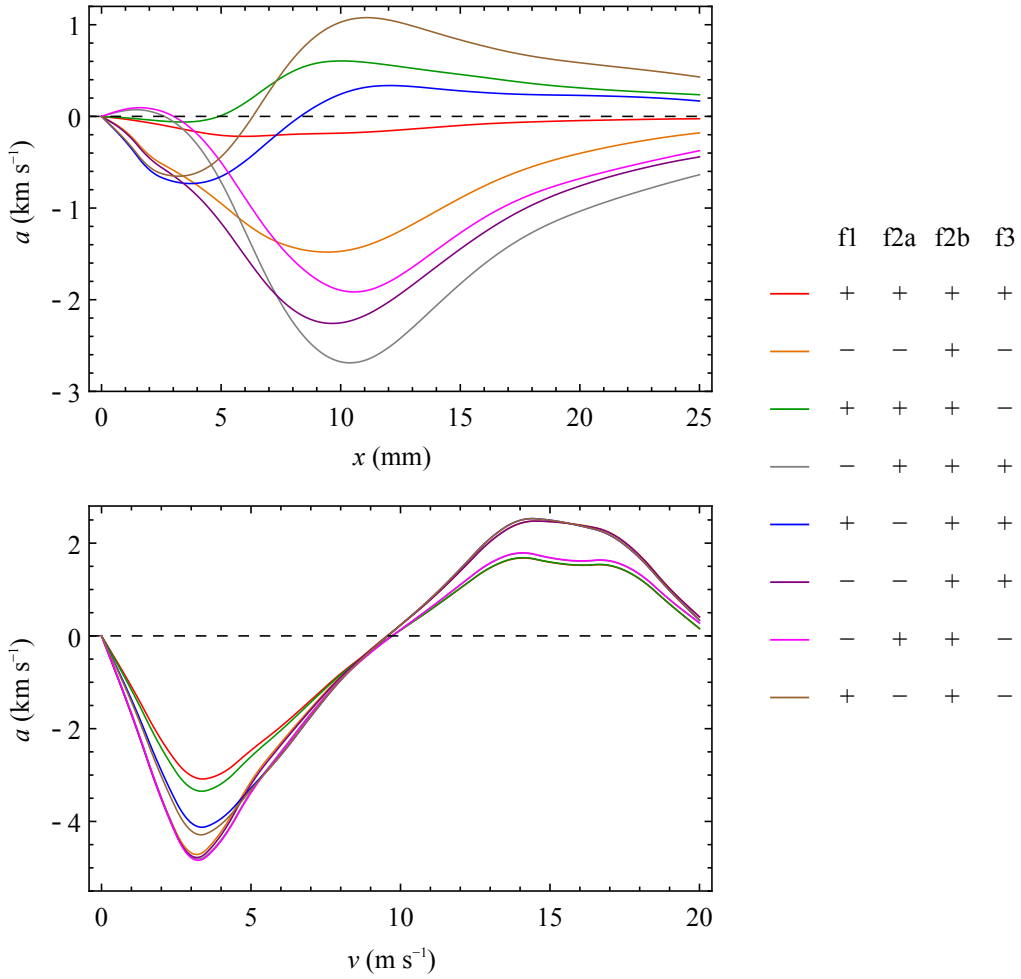

Figure 7.12: Acceleration versus displacement, and acceleration versus speed curves for YbF MOTs where the A(0)-X(0) transition is driven using four frequency components. The power per component, per beam is 60 mW.

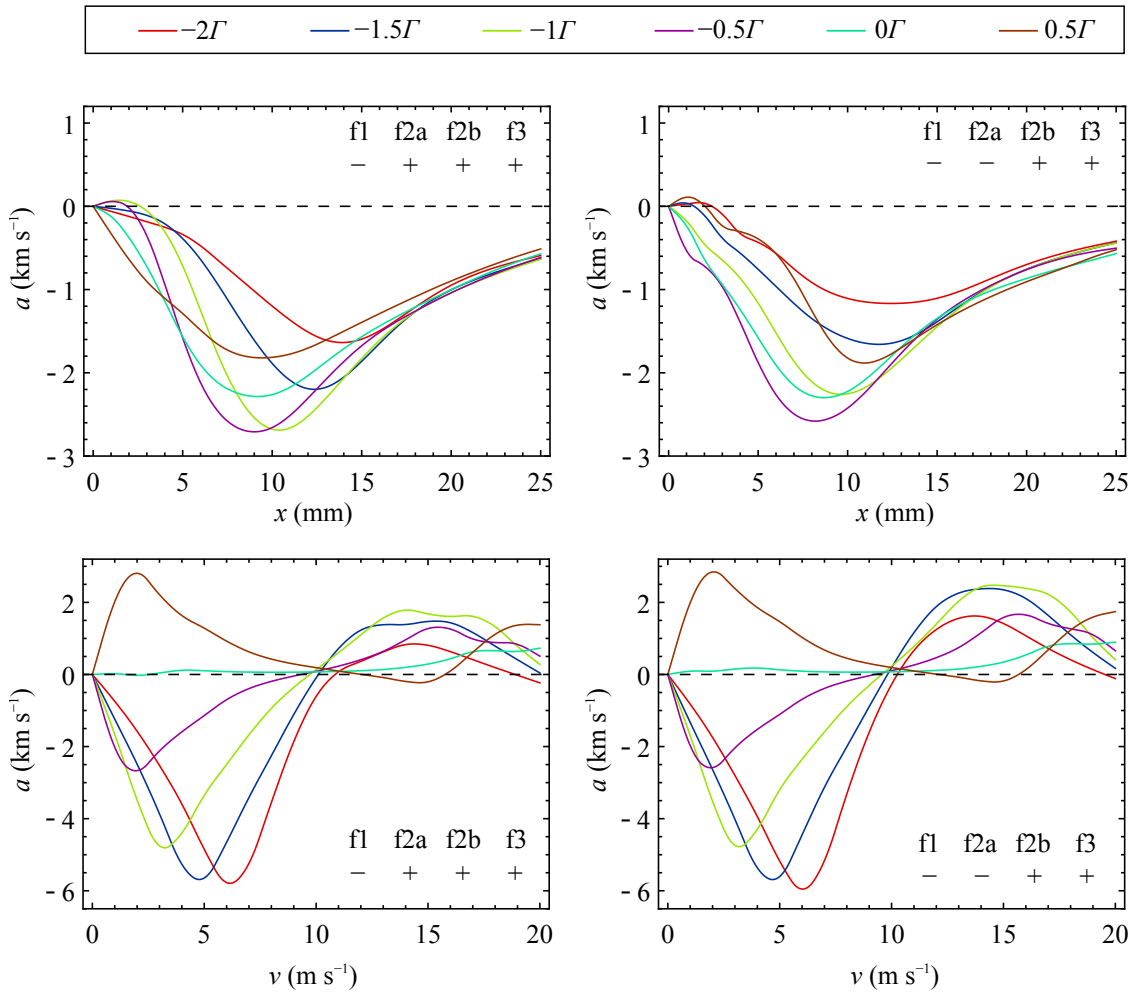

Figure 7.13: Acceleration curves where the A(0)-X(0) transition is driven using four frequency components for different global detuning δ. The power per component, per beam is 60 mW.

distribution is narrower for the case where $\delta = -\Gamma$. These observations are consistent with the acceleration curves in Fig. 7.13. For higher detunings, the capture velocity is not increased.

7.4.5 Summary

We have demonstrated that magneto-optical trapping forces can be produced for YbF using a rate equation model. Some possible options for the polarisations and frequencies for the MOT lasers have been discussed, and an optimised laser scheme has been suggested. The expected capture velocity for a YbF MOT which uses the A(0)-X(0) transition and the repump transition A(0)-X(1) is found to be approximately $10\,\mathrm{m\,s^{-1}}$.

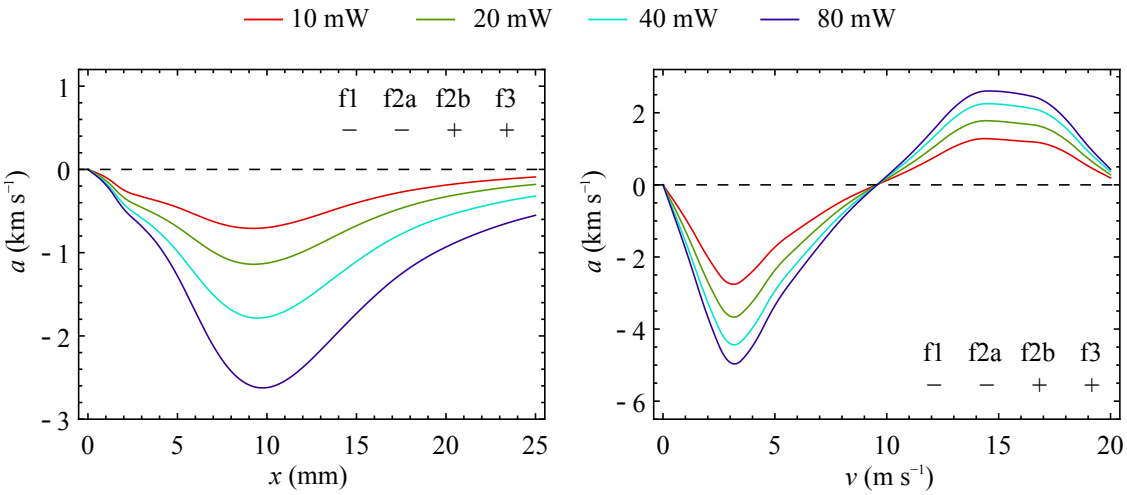

Figure 7.14: Acceleration curves where the A(0)-X(0) transition is driven using four frequency components for different powers per frequency component per beam.

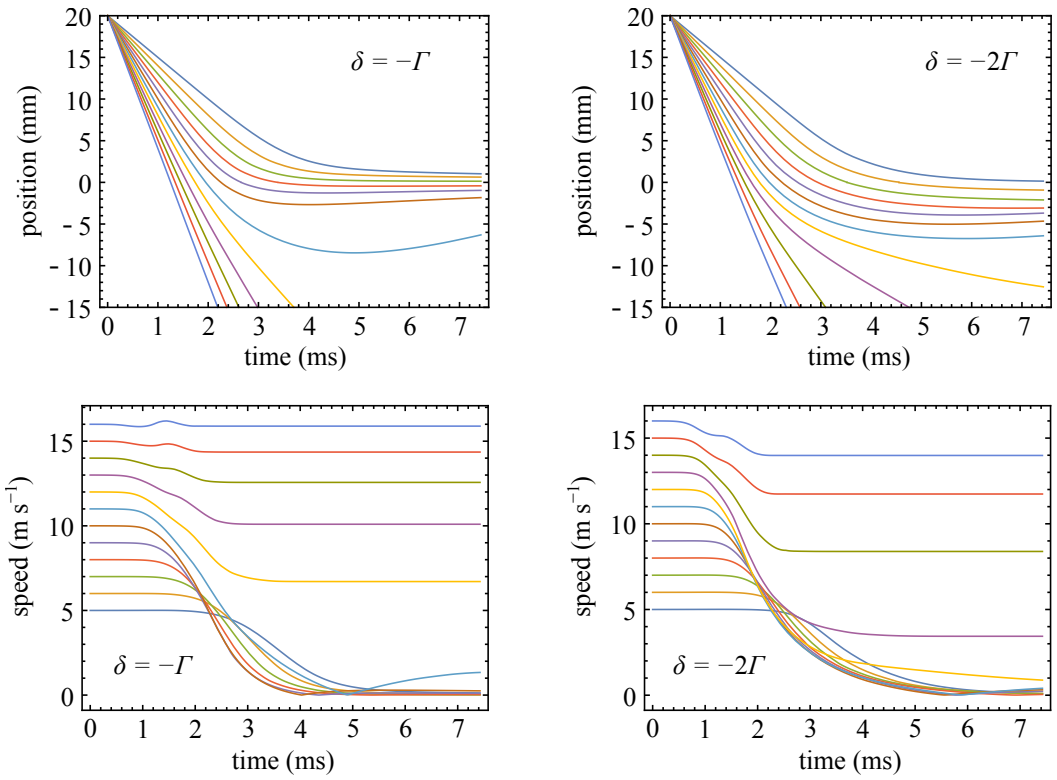

Figure 7.15: Trajectories of particles through the MOT.

7.5 Conclusion

This thesis has discussed the construction of an experiment to laser cool YbF, and presented the first evidence of laser cooling for this molecule. Whilst not an ideal choice for laser cooling, YbF is an interesting species to which to apply laser cooling because of its application in the measurement of the permanent electric dipole moment of the electron. In future, this laser cooling experiment can become part of the eEDM experiment, in order to improve its precision.

The temperature to which the molecular distribution was cooled is estimated to be $\sim 70\,\mathrm{mK}$. This temperature may be reduced towards the Doppler limit $\sim 200\,\mu\mathrm{K}$ through the addition of a fourth cooling laser, lengthening of the interaction region, and some optimisation of laser parameters. Evidence of Sisyphus laser cooling was also presented. Further experimental work may determine whether this cooling mechanism can play a useful role in beam collimation for the eEDM experiment. It may be beneficial to begin the laser cooling with the light red detuned, and chirp the frequency to be blue detuned in order to achieve the lowest transverse temperature.

Following the addition of the A(1)-X(3) laser, the branching to X($v > 3$) states can be determined. Should this be sufficiently low, molecules in a YbF buffer gas beam may be slowed to rest via radiation pressure. Otherwise, additional lasers may be used to repump higher vibrational states, such that this can be achieved. Molecules may then be captured in a MOT, which would enable the eEDM experiment to be performed using a molecular fountain.

Bibliography

[1] R. Frisch. Experimenteller Nachweis des Einsteinschen Strahlungsrückstoßes. *Zeitschrift für Physik* **86**, 42 (1933).

[2] P. Lebedew. Untersuchungen über die Druckkräfte des Lichtes. *Annalen der Physik* **311**, 433 (1901).

[3] E. F. Nichols & G. F. Hull. The Pressure Due to Radiation. *Proceedings of the American Academy of Arts and Sciences* **38**, 559 (1903).

[4] J. C. Maxwell. *A treatise on electricity and magnetism Vol. II* (Clarendon press, 1873).

[5] A. Ashkin. Atomic-beam deflection by resonance-radiation pressure. *Physical Review Letters* **25**, 1321 (1970).

[6] S. V. Andreev, V. I. Balykin, V. S. Letokhov & V. G. Minogin. Radiative slowing and reduction of the energy spread of a beam of sodium atoms to 1.5 K in an oppositely directed laser beam. *JETP Letters* **34**, 442 (1981).

[7] H. J. Metcalf & P. van der Straten. *Laser Cooling and Trapping* (Springer-Verlag, New York, 1999).

[8] S. Chu, L. Hollberg, J. E. Bjorkholm, A. Cable & A. Ashkin. Three-dimensional viscous confinement and cooling of atoms by resonance radiation pressure. *Physical Review Letters* **55**, 48 (1985).

[9] V. S. Letokhov, V. G. Minogin & B. D. Pavlik. Cooling and capture of atoms and molecules by a resonant light field. *Zeitschrift Fur Physik* **45**, 698 (1977).

[10] E. L. Raab, M. Prentiss, A. Cable, S. Chu & D. E. Pritchard. Trapping of Neutral Sodium Atoms with Radiation Pressure. *Physical Review Letters* **59**, 2631 (1987).

[11] P. D. Lett, R. N. Watts, C. I. Westbrook, W. D. Phillips, P. L. Gould & H. J. Metcalf. Observation of atoms laser cooled below the doppler limit. *Physical Review Letters* **61**, 169 (1988).

[12] J. Dalibard & C. Cohen-Tannoudji. Laser cooling below the Doppler limit by polarization gradients: simple theoretical models. *JOSA B* **6**, 2023 (1989).

[13] P. J. Ungar, D. S. Weiss, E. Riis & S. Chu. Optical molasses and multilevel atoms: theory. *JOSA B* **6**, 2058 (1989).

[14] A. Aspect, E. Arimondo, R. Kaiser, N. Vansteenkiste & C. Cohen-Tannoudji. Laser cooling below the one-photon recoil energy by velocity-selective coherent population trapping. *Physical Review Letters* **61**, 826 (1988).

[15] S. H. Autler & C. H. Townes. Stark effect in rapidly varying fields. *Physical Review* **100**, 703 (1955).

[16] G. A. Askar'yan. Effects of the gradient of a strong electromagnetic beam on electrons and atoms. *Soviet Physics JETP* **15** (1962).

[17] B. Sheehy, S. Q. Shang, P. van der Straten, S. Hatamian & H. Metcalf. Magnetic-field-induced laser cooling below the Doppler limit. *Physical Review Letters* **64**, 858 (1990).

[18] D. S. Weiss, E. Riis, Y. Shevy, P. J. Ungar & S. Chu. Optical molasses and multilevel atoms: experiment. *JOSA B* **6**, 2072 (1989).

[19] C. Valentin, M. Gagné, J. Yu & P. Pillet. One-Dimension Sub-Doppler Molasses in the Presence of Static Magnetic Field. *EPL (Europhysics Letters)* **17**, 133 (1992).

[20] O. Emile, R. Kaiser, C. Gerz, H. Wallis, A. Aspect & C. Cohen-Tannoudji. Magnetically assisted Sisyphus effect. *Journal de Physique II* **3**, 1709 (1993).

[21] M. D. Plimmer, N. Castagna, G. Di Domenico, P. Thomann, A. V. Taichenachev & V. I. Yudin. 2D laser collimation of a cold Cs beam induced by a transvers B-field. *JETP Letters* **82**, 18 (2005).

[22] J. A. Devlin & M. R. Tarbutt. Three-dimensional Doppler, polarization-gradient, and magneto-optical forces for atoms and molecules with dark states. *New Journal of Physics* **18**, 123017 (2016).

[23] E. S. Shuman, J. F. Barry & D. DeMille. Laser cooling of a diatomic molecule. *Nature* **467**, 820 (2010).

[24] D. DeMille. Quantum Computation with Trapped Polar Molecules. *Physical Review Letters* **88**, 067901 (2002).

[25] R. V. Krems. Cold controlled chemistry. *Physical chemistry chemical physics* **10**, 4079 (2008).

[26] L. D. Carr, D. DeMille, R. V. Krems & J. Ye. Cold and ultracold molecules: science, technology and applications. *New Journal of Physics* **11**, 055049 (2009).

[27] R. V. Krems, W. C. Stwalley & B. Friedrich. *COLD MOLECULES: Theory, Experiment, Applications* (CRC Press, 2009).

[28] T. E. Wall. Preparation of cold molecules for high-precision measurements. *Journal of Physics B* **49**, 243001 (2016).

[29] J. Doyle, B. Friedrich, R. V. Krems & F. Masnou-Seeuws. Editorial: Quo vadis, cold molecules? *The European Physical Journal D* **31**, 149 (2004).

[30] J. T. Bahns, W. C. Stwalley & P. L. Gould. Laser cooling of molecules: A sequential scheme for rotation, translation, and vibration. *The Journal of Chemical Physics* **104**, 9689 (1996).

[31] B. K. Stuhl, B. C. Sawyer, D. Wang & J. Ye. Magneto-optical Trap for Polar Molecules. *Physical Review Letters* **101**, 243002 (2008).

[32] J. F. Barry, E. S. Shuman, E. B. Norrgard & D. DeMille. Laser Radiation Pressure Slowing of a Molecular Beam. *Physical Review Letters* **108**, 103002 (2012).

[33] M. T. Hummon, M. Yeo, B. K. Stuhl, A. L. Collopy, Y. Xia & J. Ye. 2D Magneto-Optical Trapping of Diatomic Molecules. *Physical Review Letters* **110**, 143001 (2013).

[34] V. Zhelyazkova, A. Cournol, T. E. Wall, A. Matsushima, J. J. Hudson, E. A. Hinds, M. R. Tarbutt & B. E. Sauer. Laser cooling and slowing of CaF molecules. *Physical Review A* **89**, 053416 (2014).

[35] J. F. Barry, D. J. McCarron, E. B. Norrgard, M. H. Steinecker & D. DeMille. Magneto-optical trapping of a diatomic molecule. *Nature* **512**, 286 (2014).

[36] M. Prentiss, A. Cable, J. E. Bjorkholm, S. Chu, E. L. Raab & E. E. Pritchard. Atomic-density-dependent losses in an optical trap. *Optics Letters* **13**, 452 (1988).

[37] S. Q. Shang, Z. T. Lu & S. J. Freedman. Comparison of the cold-collision losses for laser-trapped sodium in different ground-state hyperfine sublevels. *Physical Review A* **50**, R4449 (1994).

[38] M. R. Tarbutt. Magneto-optical trapping forces for atoms and molecules with complex level structures. *New Journal of Physics* **17**, 015007 (2015).

[39] D. J. McCarron, E. B. Norrgard, M. H. Steinecker & D. DeMille. Improved magneto-optical trapping of a diatomic molecule. *New Journal of Physics* **17**, 1 (2015).

[40] E. B. Norrgard, D. J. McCarron, M. H. Steinecker, M. R. Tarbutt & D. DeMille. Submillikelvin Dipolar Molecules in a Radio-Frequency Magneto-Optical Trap. *Physical Review Letters* **116**, 063004 (2016).

[41] M. Yeo, M. T. Hummon, A. L. Collopy, B. Yan, B. Hemmerling, E. Chae, J. M. Doyle & J. Ye. Rotational State Microwave Mixing for Laser Cooling of Complex Diatomic Molecules. *Physical Review Letters* **114** (2015).

[42] S. Truppe, H. Williams, M. Hambach, N. Fitch, T. E. Wall, E. A. Hinds, B. E. Sauer & M. R. Tarbutt. A bright, cold, velocity-controlled molecular beam by frequency-chirped laser slowing. *arXiv* (2016). 1605.06055.

[43] B. Hemmerling, E. Chae, A. Ravi, L. Anderegg, G. K. Drayna, N. R. Hutzler, A. L. Collopy, J. Ye, W. Ketterle & J. M. Doyle. Laser slowing of CaF molecules to near the capture velocity of a molecular MOT. *Journal of Physics B* **49**, 174001 (2016).

[44] I. Kozyryev, L. Baum, K. Matsuda, B. L. Augenbraun, L. Anderegg, A. P. Sedlack & J. M. Doyle. Sisyphus Laser Cooling of a Polyatomic Molecule. *arXiv* (2016).

[45] T. A. Isaev & R. Berger. Polyatomic candidates for cooling of molecules with lasers from simple theoretical concepts. *Physical Review Letters* **116** (2016).

[46] C. M. Tesch, R. De Vivie-Riedle. Quantum computation with vibrationally excited molecules. *Physical review letters* **89**, 157901 (2002).

[47] P. Jansen, H. L. Bethlem & W. Ubachs. Perspective: Tipping the scales: Search for drifting constants from molecular spectra. *Journal of Chemical Physics* **140**, 010901 (2014).

[48] V. Vuletić & S. Chu. Laser Cooling of Atoms, Ions, or Molecules by Coherent Scattering. *Physical Review Letters* **84**, 3787 (2000).

[49] L. Aldridge, S. E. Galica & E. E. Eyler. Simulations of the bichromatic force in multilevel systems. *Physical Review A* **93** (2016).

[50] C. Corder, B. Arnold & H. Metcalf. Laser cooling without spontaneous emission. *Physical Review Letters* **114**, 043002 (2015).

[51] N. J. Fitch & M. R. Tarbutt. Principles and Design of a Zeeman-Sisyphus Decelerator for Molecular Beams. *ChemPhysChem* **17**, 3609 (2016).

[52] E. Purcell & N. Ramsey. On the Possibility of Electric Dipole Moments for Elementary Particles and Nuclei. *Physical Review* **78**, 807 (1950).

[53] J. H. Smith, E. M. Purcell & N. F. Ramsey. Experimental limit to the electric dipole moment of the neutron. *Physical Review* **108**, 120 (1957).

[54] T. D. Lee & C. N. Yang. Question of Parity Conservation in Weak Interactions. *Physical Review* **104**, 254 (1956).

[55] C. S. Wu, E. Ambler, R. W. Hayward, D. D. Hoppes & R. P. Hudson. Experimental Test of Parity Conservation in Beta Decay. *Physical Review Letters* **105**, 1413 (1957).

[56] L. Landau. On the conservation laws for weak interactions. *Nuclear Physics* **3**, 127 (1957).

[57] J. H. Christenson, J. W. Cronin, V. L. Fitch & R. Turlay. Evidence for the 2π Decay of the K_2^0 Meson. *Physical Review Letters* **13**, 138 (1964).

[58] BaBar Collaboration. Measurement of CP-Violating Asymmetries in B^0 Decays to CP Eigenstates. *Physical Review Letters* **86**, 2515 (2001).

[59] A. Abashian *et al.* Measurement of the CP Violation Parameter $\sin 2\phi_1$ in B_d^0 Meson Decays. *Physical Review Letters* **86**, 2509 (2001).

[60] LHCb Collaboration. Measurements of Indirect CP Asymmetries in $D^0 \to K^-K^+$ and $D^0 \to \pi^-\pi^+$ Decays. *Physical Review Letters* **112**, 041801 (2014).

[61] W. Pauli. *Niels Bohr and the development of physics* (Pergamon Press, Oxford, 1955).

[62] W. O. Greenberg. CPT violation implies violation of Lorentz invariance. *Physical Review Letters* **89**, 231602 (2002).

[63] CPLEAR collaboration. First direct observation of time-reversal non-invariance in the neutral-kaon system. *Physics Letters B* **444**, 43 (1998).

[64] BaBar Collaboration. Observation of time-reversal violation in the B^0 meson system. *Physical Review Letters* **109**, 211801 (2012).

[65] R. N. Zare. *Angular Momentum* (Wiley, 1988).

[66] K. Jungmann. Searching for electric dipole moments. *Annalen der Physik* **525**, 550 (2013).

[67] ATLAS Collaboration. Observation of a new particle in the search for the Standard Model Higgs boson with the ATLAS detector at the LHC. *Physics Letters B* **716**, 1 (2012).

[68] CMS Collaboration. Observation of a new boson at a mass of 125 GeV with the CMS experiment at the LHC. *Physics Letters B* **716**, 30 (2012).

[69] Planck Collaboration. Planck 2015 results. I. Overview of products and scientific results. *Astronomy & Astrophysics* **594** (2016).

[70] D. A. Sakharov. Violation of CP invariance, C asymmetry, and baryon asymmetry of the universe. *JETP Letters* **5**, 24 (1967).

[71] ACME Collaboration. Order of Magnitude Smaller Limit on the Electric Dipole Moment of the Electron. *Science* **343**, 269 (2014).

[72] M. R. Tarbutt, B. E. Sauer, J. J. Hudson & E. A. Hinds. Design for a fountain of YbF molecules to measure the electron's electric dipole moment. *New Journal of Physics* **15**, 053034 (2013).

[73] J. M. Pendlebury & E. A. Hinds. Particle electric dipole moments. *Nuclear Instruments and Methods in Physics Research A* **440**, 471 (2000).

[74] E. A. Hinds. Testing Time Reversal Symmetry Using Molecules. *Physica Scripta* **T70**, 34 (1997).

[75] D. F. Nelson, A. A. Schupp, R. W. Pidd & H. R. Crane. Search for an Electric Dipole Moment of the Electron. *Physical Review Letters* **2**, 492 (1959).

[76] A. Adelmann, K. Kirch, C. J. Onderwater & T. Schietinger. Compact storage ring to search for the muon electric dipole moment. *Journal of Physics G* **37**, 85001 (2010).

[77] L. Schiff. Measurability of Nuclear Electric Dipole Moments. *Physical Review* **132**, 2194 (1963).

[78] Roberts, B. L. & Marciano, W. J. *Lepton Dipole Moments*. Advanced Series on Directions in High Energy Physics (WORLD SCIENTIFIC, 2009).

[79] P. G. H. Sandars & E. Lipworth. Electric Dipole Moment of the Cesium Atom. A New Upper Limit to the Electric Dipole Moment of the Free Electron. *Physical Review Letters* **13**, 718 (1964).

[80] P. G. H. Sandars. The Electric Dipole Moment of an Atom. *Physics Letters* **14**, 194 (1965).

[81] E. S. Ensberg. Experimental Upper Limit for the Permanent Electric Dipole Moment of Rb^{85} by Optical-Pumping Techniques. *Physical Review* **157**, 270 (1967).

[82] M. Weisskopf, J. Carrico, H. Gould, E. Lipworth & T. Stein. Electric Dipole Moment of the Cesium Atom. A New Upper Limit to the Electric Dipole Moment of the Electron. *Physical Review Letters* **21**, 1645 (1968).

[83] K. Abdullah, C. Carlberg, E. D. Commins, H. Gould & S. B. Ross. New experimental limit on the electron electric dipole moment. *Physical Review Letters* **65**, 2347 (1990).

[84] E. D. Commins, J. D. Jackson & D. P. DeMille. The electric dipole moment of the electron: An intuitive explanation for the evasion of Schiff's theorem. *American Journal of Physics* **75**, 532 (2007).

[85] P. G. H. Sandars. Measurability of the Proton Electric Dipole Moment. *Physical Review Letters* **19**, 1396 (1967).

[86] P. G. H. Sandars. The search for violation of P or T invariance in atoms or molecules. In zu Putlitz, G. (ed.) *Atomic Physics 4*, 71–92 (Plenum Press, New York, 1975).

[87] O. P. Sushkov & V. V. Flambaum. Parity breaking effects in diatomic molecules. *Sov. Phys. JETP* **48**, 608 (1978).

[88] J. J. Hudson. *Measuring the electric dipole moment of the electron with YbF molecules*. Ph.D. thesis, University of Sussex (2001).

[89] I. B. Khriplovich & S. K. Lamoreaux. *CP Violation Without Strangeness* (Springer, 1997).

[90] J. J. Hudson, D. M. Kara, I. J. Smallman, B. E. Sauer, M. R. Tarbutt & E. A. Hinds. Improved measurement of the shape of the electron. *Nature* **473**, 493 (2011).

[91] S. Eckel, P. Hamilton, E. Kirilov, H. W. Smith & D. DeMille. Search for the electron electric dipole moment using Ω-doublet levels in PbO. *Physical Review A* **87**, 052130 (2013).

[92] M. G. Kozlov. Enhancement of the electric dipole moment of the electron in the YbF molecule. *Journal of Physics B* **30**, L607 (1997).

[93] A. N. Petrov, A. V. Titov, T. A. Isaev, N. S. Mosyagin & D. DeMille. Configuration-interaction calculation of hyperfine and P,T-odd constants on ^{207}PbO excited states for electron electric-dipole-moment experiments. *Physical Review A* **72**, 022505 (2005).

[94] L. V. Skripnikov, A. N. Petrov & A. V. Titov. Communication: Theoretical study of ThO for the electron electric dipole moment search. *Journal of Chemical Physics* **139**, 221103 (2013).

[95] D. M. Kara, I. J. Smallman, J. J. Hudson, B. E. Sauer, M. R. Tarbutt & E. A. Hinds. Measurement of the electron's electric dipole moment using YbF molecules: methods and data analysis. *New Journal of Physics* **14**, 103051 (2012).

[96] J. A. Devlin. *Progress towards a more sensitive measurement of the electron electric dipole moment with YbF*. Ph.D. thesis, Imperial College London (2015).

[97] I. M. Rabey. *Improved shot noise limit of the YbF EDM experiment*. Ph.D. thesis, Imperial College London (2017).

[98] W. J. Marciano. Time variation of the fundamental "constants" and kaluza-klein theories. *Physical Review Letters* **52**, 489 (1984).

[99] J. P. Uzan. Varying constants, gravitation and cosmology. *Living Reviews in Relativity* **14** (2011).

[100] C. Chin, V. V. Flambaum & M. G. Kozlov. Ultracold molecules: New probes on the variation of fundamental constants. *New Journal of Physics* **11**, 055048 (2009).

[101] E. Reinhold, R. Buning, U. Hollenstein, A. Ivanchik, P. Petitjean & W. Ubachs. Indication of a cosmological variation of the proton-electron mass ratio based on laboratory measurement and reanalysis of H_2 spectra. *Physical Review Letters* **96**, 151101 (2006).

[102] J. K. Webb, J. A. King, M. T. Murphy, V. V. Flambaum, R. F. Carswell & M. B. Bainbridge. Indications of a spatial variation of the fine structure constant. *Physical Review Letters* **107**, 191101 (2011).

[103] P. Molaro, D. Reimers, I. I. Agafonova & S. A. Levshakov. Bounds on the fine structure constant variability from Fe II absorption lines in QSO spectra. *The European Physical Journal Special Topics* **163**, 173 (2008).

[104] I. I. Agafonova, P. Molaro, S. A. Levshakov & J. L. Hou. First measurement of Mg isotope abundances at high redshifts and accurate estimate of $\Delta\alpha/\alpha$. *Astronomy and Astrophysics* **529**, 20 (2011).

[105] J. Bagdonaite, P. Jansen, C. Henkel, H. L. Bethlem, K. M. Menten & W. Ubachs. A stringent limit on a drifting proton-to-electron mass ratio from alcohol in the early universe. *Science* **339**, 46 (2013).

[106] S. Truppe, R. J. Hendricks, S. K. Tokunaga, H. J. Lewandowski, M. G. Kozlov, C. Henkel, E. A. Hinds & M. R. Tarbutt. A search for varying fundamental constants using hertz-level frequency measurements of cold CH molecules. *Nature communications* **4**, 2600 (2013).

[107] V. V. Flambaum, Y. V. Stadnik, M. G. Kozlov & A. N. Petrov. Enhanced effects of temporal variation of the fundamental constants in $2\Pi_{1/2}$-term diatomic molecules: ^{207}Pb ^{19}F. *Physical Review A* **88**, 052124 (2013).

[108] J Guéna, M. Abgrall, D. Rovera, P. Rosenbusch, M. E. Tobar, P. Laurent, A. Clairon & S. Bize. Improved Tests of Local Position Invariance Using ^{87}Rb and ^{133}Cs Fountains. *Physical Review Letters* **109**, 080801 (2012).

[109] C. Cheng, A. P. van der Poel, P. Jansen, M. Quintero-Pérez, T. E. Wall, W. Ubachs & H. L. Bethlem. Molecular Fountain. *Physical Review Letters* **117**, 253201 (2016).

[110] P. Schwerdtfeger & R. Bast. Large parity violation effects in the vibrational spectrum of organometallic compounds. *Journal of the American Chemical Society* **126**, 1652 (2004).

[111] C. Fábri, L. Horný & M. Quack. Tunneling and Parity Violation in Trisulfane (HSSSH): An Almost Ideal Molecule for Detecting Parity Violation in Chiral Molecules. *ChemPhysChem* **16**, 3584 (2015).

[112] B. Darquié *et al.* Progress toward the first observation of parity violation in chiral molecules by high-resolution laser spectroscopy. *Chirality* **22**, 870 (2010).

[113] S. Tokunaga, R. J. Hendricks, M. R. Tarbutt & B. Darquié. High-resolution mid-infrared spectroscopy of buffer-gas-cooled methyltrioxorhenium molecules. *arXiv* (2016). 1607.08741.

[114] A. J. Macdermott. Electro weak enantioselection and the origin of life. *Origins of Life and Evolution of the Biosphere* **25**, 191 (1995).

[115] M. Quack. How Important is Parity Violation for Molecular and Biomolecular Chirality? *Angewandte Chemie International Edition* **41**, 4618 (2002).

[116] J. Brown & A. Carrington. *Rotational Spectroscopy of Diatomic Molecules* (Cambridge University Press, 2003).

[117] J. Wang. *Laser and Radiofrequency Spectroscopy of Ytterbium Fluoride Ground State*. Ph.D. thesis, Yale University (1996).

[118] G. Herzberg. *Molecular Spectra and Molecular Structure Vol. 1, Spectra of Diatomic Molecules* (D. Van Nostrand Company, New York, 1950), second edition edn.

[119] B. E. Sauer, J. Wang & E. A. Hinds. Laser-rf double resonance spectroscopy of ^{174}YbF in the $X^2\Sigma^+$ state: Spin-rotation, hyperfine interactions, and the electric dipole moment. *The Journal of Chemical Physics* **105**, 7412 (1996).

[120] K. L. Dunfield, C. Linton, T. E. Clarke, J. McBride, A. G. Adam, J. R. Peers. Laser Spectroscopy of the Lanthanide Monofluorides: Analysis of the $A^2\Pi X^2\Sigma^+$ Transition of Ytterbium Monofluoride. *Journal of Molecular Spectroscopy* 433 (1995).

[121] B. E. Sauer, S. B. Cahn, M. G. Kozlov, G. D. Redgrave & E. A. Hinds. Perturbed hyperfine doubling in the $A\ ^2\Pi_{1/2}$ and [18.6]0.5 states of YbF. *The Journal of Chemical Physics* **110**, 8424 (1999).

[122] M. D. Di Rosa. Laser-cooling molecules. *The European Physical Journal D* **31**, 395 (2004).

[123] M. Dolg, H. Stoll & H. Preuss. Ab initio pseudopotential study of YbH and YbF. *Chemical Physics* **165**, 21 (1992).

[124] R. F. Barrow & A. H. Chojnicki. Analysis of the optical spectrum of gaseous ytterbium monofluoride. *Journal of the Chemical Society, Faraday Transactions 2* **71**, 728 (1975).

[125] K. N. Uttam & M. M. Joshi. A New Band System of the YbF Molecule. *Journal of Molecular Spectroscopy* **174**, 290 (1995).

[126] X. Zhuang, A. Le, T. C. Steimle, N. E. Bullied, I. J. Smallman, R. J. Hendricks, S. M. Skoff, J. J. Hudson, B. E. Sauer E. A. Hinds & M. R. Tarbutt. Franck-Condon factors and radiative lifetime of the $A^2\Pi_{1/2} - X^2\Sigma^+$ transition of ytterbium monofluoride, YbF. *Physical Chemistry Chemical Physics* **13**, 19013 (2011).

[127] I. J. Smallman, F. Wang, T. C. Steimle, M. R. Tarbutt & E. A. Hinds. Radiative branching ratios for excited states of YbF: Application to laser cooling. *Journal of Molecular Spectroscopy* **300**, 3 (2014).

[128] D. J. Berkeland & M. G. Boshier. Destabilization of dark states and optical spectroscopy in Zeeman-degenerate atomic systems. *Physical Review A* **65**, 033413 (2002).

[129] J. F. Barry. *Laser cooling and slowing of a diatomic molecule.* Ph.D. thesis, Yale University (2013).

[130] E. S. Shuman, J. F. Barry, D. R. Glenn & D. DeMille. Radiative Force from Optical Cycling on a Diatomic Molecule. *Physical Review Letters* **103**, 223001 (2009).

[131] J. S. Bumby. *Progress towards a source of cold, slow molecules for tests of fundamental physics.* Ph.D. thesis, Imperial College London (2016).

[132] N. E. Bulleid. *Slow, cold beams of polar molecules for precision measurements.* Ph.D. thesis, Imperial College London (2013).

[133] N. R. Hutzler, H. I. Lu & J. M. Doyle. The buffer gas beam: An intense, cold, and slow source for atoms and molecules. *Chemical Reviews* **112**, 4803 (2012).

[134] M. R. Tarbutt, J. J. Hudson, B. E. Sauer, E. A. Hinds, V. A. Ryzhov, V. L. Ryabov & V. F. Ezhov. A jet beam source of cold YbF radicals. *Journal of Physics B* **35**, 5013 (2002).

[135] P. C. Condylis. *Measuring the electron electric dipole moment using supersonic YbF*. Ph.D. thesis, Imperial College London (2006).

[136] S. M. Skoff, R. J. Hendricks, C. D. Sinclair, J. J. Hudson, D. M. Segal, B. E. Sauer, E. A. Hinds & M. R. Tarbutt. Diffusion, thermalization, and optical pumping of YbF molecules in a cold buffer-gas cell. *Physical Review A* **83**, 023418 (2011).

[137] D. Patterson, J. Rasmussen & J. M. Doyle. Intense atomic and molecular beams via neon buffer-gas cooling. *New Journal of Physics* **11**, 055018 (2009).

[138] J. K. Messer & F. C. De Lucia. Measurement of pressure-broadening parameters for the CO-He system at 4 K. *Physical Review Letters* **53**, 2555 (1984).

[139] J. M. Doyle, B. Friedrich, J. Kim & D. Patterson. Buffer-gas loading of atoms and molecules into a magnetic trap. *Physical Review A* **52**, R2515 (1995).

[140] D. Egorov, T. Lahaye, W. Schöllkopf, B. Friedrich & J. Doyle. Buffer-gas cooling of atomic and molecular beams. *Physical Review A* **66**, 1 (2002).

[141] S. M. Skoff. *Buffer gas cooling of YbF molecules*. Ph.D. thesis, Imperial College London (2011).

[142] D. Patterson. *Buffer Gas Cooled Beams and Cold Molecular Collisions*. Ph.D. thesis, Harvard University (2010).

[143] D. W. Sedgley, A. G. Tobin, T. H. Batzer & W. R Call. Characterization of charcoals for helium cryopumping in fusion devices. *Journal of Vacuum Science & Technology A* **5**, 2572 (1987).

[144] A. G. Tobin, D. W. Sedgley, T. H. Batzer & W. R. Call. Evaluation of charcoal sorbents for helium cryopumping in fusion reactors. *Journal of Vacuum Science & Technology A* **5**, 101 (1987).

[145] J. R. Olson. Thermal conductivity of some common cryostat materials between 0.05 and 2 K. *Cryogenics* **33**, 729 (1993).

[146] N. G. Aliev & N. V. Volkenshtein. Thermal conductivity of Tm, Yb and Lu at low temperatures. *Soviet Physics JETP* **22**, 997 (1966).

[147] A. S. Arnold, J. S. Wilson & M. G. Boshier. A simple extended-cavity diode laser. *Review of Scientific Instruments* **69**, 1236 (1998).

[148] P. Horowitz & W. Hill. *The Art of Electronics* (Cambridge University Press, Cambridge, 1989), second edn.

[149] X. Baillard, A. Gauguet, S. Bize, P. Lemonde, P. Laurent, A. Clairon & P. Rosenbusch. Interference-filter-stabilized external-cavity diode lasers. *Optics Communications* **266**, 609 (2006).

[150] D. J. Thompson & R. E. Scholten. Narrow linewidth tunable external cavity diode laser using wide bandwidth filter. *Review of Scientific Instruments* **83**, 023107 (2012).

[151] M. Fuchs. Development of a High Power Stabilized Diode Laser System. Tech. Rep., University of Oregon (2006).

[152] D. A. Bryan, R. Gerson & H. E. Tomaschke. Increased optical damage resistance in lithium niobate. *Applied Physics Letters* **44**, 847 (1984).

[153] C. Mok, M. Weel, E. Rotberg & A. Kumarakrishnan. Design and construction of an efficient electro-optic modulator for laser spectroscopy. *Canadian Journal of Physics* **84**, 775 (2006).

[154] D. R. Glenn. *Development of techniques for cooling and trapping polar diatomic molecules*. Ph.D. thesis, Yale University (2009).

[155] D. J. McCarron, S. A. King & S. L. Cornish. Modulation transfer spectroscopy in atomic rubidium. *Measurement Science and Technology* **19**, 105601 (2008).

[156] I. P. Kaminow & E. H. Turner. Electrooptic Light Modulators. *Applied Optics* **5**, 1612 (1966).

[157] A. W. Warner, M. Onoe & G. A. Coquin. Determination of Elastic and Piezoelectric Constants for Crystals in Class (3m). *Journal of the Acoustical Society of America* **42**, 1223 (1967).

[158] M. V. Hobden & J. Warner. The temperature dependence of the refractive indices of pure lithium niobate. *Physics Letters* **22**, 243 (1966).

[159] Members of the CCM. EDMSuite. http://github.com/ColdMatter/EDMSuite. Accessed: 10/02/2017.

[160] J. H. Burke, O. Garcia, K. J. Hughes, B. Livedalen & C. A. Sackett. Compact implementation of a scanning transfer cavity lock. *Review of Scientific Instruments* **76**, 1 (2005).

[161] C. P. Pearman, C. S. Adams, S. G. Cox, P. F. Griffin, D. A. Smith & I. G. Hughes. Polarization spectroscopy of a closed atomic transition: applications to laser frequency locking. *Journal of Physics B* **35**, 5141 (2002).

[162] T. Y. Fan. Laser beam combining for high-power, high-radiance sources. *IEEE Journal on Selected Topics in Quantum Electronics* **11**, 567 (2005).

[163] R. W. Drever, J. L. Hall, F. V. Kowalski, J. Hough, G. M. Ford, A. J. Munley & H. Ward. Laser phase and frequency stabilization using an optical resonator. *Applied Physics B* **31**, 97 (1983).

[164] G. Brooker. *Modern Classical Optics* (Oxford University Press, Oxford, 2003).

[165] A. E. Siegman. Defining, measuring, and optimizing laser beam quality. *Proc. SPIE 1868* **1868**, 2 (1993).

[166] L. S. Meng, J. K. Brasseur & D. K. Neumann. Damage threshold and surface distortion measurement for high-reflectance, low-loss mirrors to 100+ MW/cm^2 cw laser intensity. *Optics Express* **13**, 10085 (2005).

[167] T. W. Hansch & B. Couillaud. Laser frequency stabilization by polarization spectroscopy of a reflecting reference cavity. *Optics Communications* **35**, 441 (1980).

[168] J. M. Boon-Engering, W. E. van der Veer, E. A. Bente & W. Hogervorst. Stabilization of an optical cavity containing a birefringent element. *Optics Communications* **140**, 285 (1997).

[169] P. Asenbaum & M. Arndt. Cavity stabilization using the weak intrinsic birefringence of dielectric mirrors. *Optics Letters* **36**, 3720 (2011).

[170] T. C. Steimle, T. Ma & C. Linton. The hyperfine interaction in the $A^2\Pi_{1/2}$ and $X^2\Sigma^+$ states of ytterbium monofluoride. *The Journal of chemical physics* **127**, 234316 (2007).

[171] V. Zhelyazkova. *Laser Cooling of CaF Molecules*. Ph.D. thesis, Imperial College London (2014).

[172] R. V. Darnley. *Electrodynamic Guiding and Decelaration of Polar Diatomic Molecules*. Ph.D. thesis, University of London (2007).

[173] J. Lim, T. C. Steimle, *et al.* The $X^2\Sigma^+ - [557]$, [561] bands of ^{174}YbF (2017). Article in preparation.

[174] E. G. Gamaly, A. V. Rode, B. Luther-Davies & V. T. Tikhonchuk. Ablation of solids by femtosecond lasers: Ablation mechanism and ablation thresholds for metals and dielectrics. *Physics of Plasmas* **9**, 949 (2002).

[175] A. Wolski. Maxwell's Equations for Magnets. *arXiv* (2011). 1103.0713.

[176] T. V. Tscherbul, J. and Kłos, L. Rajchel & R. V. Krems. Fine and hyperfine interactions in cold YbF-He collisions in electromagnetic fields. *Physical Review A* **75**, 033416 (2007).

[177] H-I Lu, J. Rasmussen, M. J. Wright, D. Patterson & J. M. Doyle. A cold and slow molecular beam. *Physical chemistry chemical physics* **13**, 18986 (2011).

[178] H. L. Bethlem, G. Berden & G. Meijer. Decelerating Neutral Dipolar Molecules. *Physical Review Letters* **83**, 1558 (1999).

[179] N. Vanhaecke, U. Meier, M. Andrist, B. H. Meier & F. Merkt. Multistage Zeeman deceleration of hydrogen atoms. *Physical Review A* **75**, 031402 (2007).

[180] S. A. Meek, M. F. Parsons, G. Heyne, V. Platschkowski, H. Haak, G. Meijer & A. Osterwalder. A traveling wave decelerator for neutral polar molecules. *Review of scientific instruments* **82**, 093108 (2011).

[181] A. Trimeche, M. N. Bera, J-P Cromières, J. Robert & N. Vanhaecke. Trapping of a supersonic beam in a traveling magnetic wave. *European Physical Journal D* **65**, 263 (2011).

[182] M. R. Tarbutt & T. C. Steimle. Modeling magneto-optical trapping of CaF molecules. *Physical Review A* **92**, 053401 (2015).

List of Figures

List of Tables